METHOD FOR DESIGN AND OPTIMIZATION OF SURFACE MOUNT PERMANENT MAGNET MACHINES AND INDUCTION MACHINES

A Dissertation
Presented to
The Academic Faculty

by

Yao Duan

In Partial Fulfillment
Of the Requirements for the Degree
Doctor of Philosophy in the
School of Electrical and Computer Engineering

Georgia Institute of Technology
December 2010

METHOD FOR DESIGN AND OPTIMIZATION OF SURFACE MOUNT PERMANENT MAGNET MACHINES AND INDUCTION MACHINES

Approved by:

Dr. Ronald G. Harley, Advisor
School of ECE
Georgia Institute of Technology

Dr. David G. Taylor
School of ECE
Georgia Institute of Technology

Dr. Thomas G. Habetler
School of ECE
Georgia Institute of Technology

Dr. J. Rhett Mayor
School of ME
Georgia Institute of Technology

Dr. Deepak M. Divan
School of ECE
Georgia Institute of Technology

Date Approved: 11/14/2010

To

my dear parents, Xianxiang Duan, Xiaohong Han,

my dear parents-in-law, Xiangwu Sun, Linfang Wang,

my lovely wife, Qin Sun,

and my beloved daughter Wenzheng Duan,

for their support and love.

ACKNOWLEDGEMENTS

A doctoral dissertation is usually considered to be a personal accomplishment. However, it would not have been possible for me to finish this work without the inspiration, encouragement, and support from many people.

First of all, I would like to express my most sincere thanks to Dr. Ronald G. Harley. He has been a wise and trusted advisor throughout the entire process. It is due to his constant inspiration and encouragement that I have gained a deeper understanding of engineering and made progress toward solving problems and improving my communication skills as a researcher. Had it not been for his vision, encouragement, and his confidence in my ability, much of this work would not have been completed. I am deeply grateful for his guidance.

I would also like to express my gratitude to Dr. Thomas G. Habetler. His invaluable guidance and constant encouragement provide me with tremendous motivation.

I am indebted to Dr. Deepak M. Divan for his insightful suggestions on my research work and to Dr. David G. Taylor for being my dissertation committee member and for his support in completion of this work.

I would like to specially thank Dr. J. Rhett Mayor and Andrew Semidey for the close and continuous collaboration throughout our research. I have benefited a lot from our teamwork.

I am also indebted to Dr. Jose Restpetro for his help and assistance to my experimental work.

My gratitude are also given to Mr. Stephen Dellinger and Dr. Peter Wung, who gave me valuable inputs about the electrical machine design methods used in industry.

I was fortunate to work with many exceptional fellow colleagues in my research group. I would like to thank Yi Du, Pinjia Zhang, Jing Dai, Yi Yang, Siwei Cheng, Jiaqi Liang, Anish Prasai, Jyoti Sastry, Frank Kreikebaum, Dr. Youngkook Lee, Andrew Paquette, Debrup Das, Diogenes Molina, Dustin Howard, Jorge Hernandez, Rohit Moghe, Darshit Shar, Jacob Kuns,Sangtaek Han, Dr. Long Wu, Dr. Wei Zhou, Dr. Wei Qiao, Dr. Zhi Gao and Dr. Bin Lu for their friendship and support. A special thanks to Aristidis Zachas, who generously shared with me his valuable experience with Ansoft software and machine design experience.

There are numerous names of faculty, family and friends that I should mention here, who have helped me during my four year at Georgia Tech. I want to express my gratitude to all of the people I know.

Most of all, I owe the greatest debt of gratitude to my family. My parents and parents-in law have always been the source of encouragement and support throughout my life. My dear wife, Qin Sun, has shared every single step in this long journey with me. Without their great love, encouragement, and understanding, everything would not have been possible.

The financial supports from the following institutions/organizations are gratefully acknowledged:

- Office of Naval Research
- Grainger Center for Electric Machinery and Electromechanics, at the University of Illinois, Urbana Champaign

TABLE OF CONTENTS

Page

LIST OF TABLES

Page

LIST OF FIGURES

Page

NOMENCLATURE

A

ac	Specific electrical loading (A/m)
A_{cu}	Copper wire area of a stator coil (mm^2)
a_p	Number of parallel strands of one winding coil
A_s	Stator slot area per slot (mm^2)
A_{wire}	Cross sectional area of the copper wire (mm^2)

B

$\overline{B}$	Specific magnetic loading (T)
B_{airm}	Maximum value of the airgap flux density at rated condition (T)
B_d	The flux density value on the demagnetization curve where magnetic polarization vector collapses (T)
$B_{gap\text{-}mag}$	Radial component of the magnetic field in the airgap produced by the permanent magnet (T)
B_n	The n-th spatial harmonic component of the airgap flux density produced by the permanent magnet (T)
B_r	Residual flux density of the permanent magnet (T)
$B_{s0,}\ B_{s1,}\ B_{s2}$	Stator slot opening at the slot tip, wedge, and bottom (mm)
B_{sc} , B_{rc}	Flux densities in the stator core and rotor core (T)
B_{st} , B_{rt}	Flux density in the stator and rotor tooth (T)

B_{wd}	Armature reaction field produced by the three phase winding of SMPM machines (T)

C

c_1	Self-acceleration constant
c_2	Global-acceleration constant
CW	Concentrated winding

D

D	Stator diameter on the airgap side (mm)
D_{core}	Core loss density of steel (W/kg)
D_e	Rotor endring center line diameter (mm)
D_o	Stator outer diameter (mm)
D_r	Rotor diameter on the airgap side (mm)
D_{ri}	Rotor inner diameter (mm)
DW	Distributed winding
d_w	Stator wire diameter (mm)

E

E_1	The fundamental component of back EMF (V)
Eff	Machine efficiency
eff_a	*A priori* assumption of machine efficiency

EMF	Electro-Motive Force

F

f	Machine operating frequency (Hz)
f_f	Slot fill factor
F_m	MMF provided by the magnetizing current

G

g	Physical airgap length (mm)
g'	Effective airgap length (mm)
GA	Genetic Algorithm
g_{best}	Global best

H

H_d	The field intensity value on the demagnetization curve where magnetic polarization vector collapses (A/m)
h_m	Thickness of the permanent magnet in the radial direction (mm)
HPSO	Homogeneous Particle Swarm Optimization
H_{s0}, H_{s1}, H_{s2}	Height of stator tooth tip, slot wedge, and from wedge to slot bottom (mm)

I

I_{bar}	Rotor bar current referred to the rotor winding (A)
I_{ph}	RMS value of the stator phase current (A)
I_{dgmrm}	Maximum permitted value of steady state stator current before demagnetization (A)
I_{qs}^{e}, I_{ds}^{e}	Stator q-axis and d-axis current (A)
I_r	Rotor current referred to the stator (A)
I_{ring}	Rotor ring current referred to the rotor winding (A)

J

J_s	Stator current density (A/mm^2)
J_{rr}, J_r	Rotor ring and rotor bar current density (A/mm^2)

K

K_c	Carter coefficient
K_{lmrm}	Minimum ratio of stator leakage inductance to armature reaction inductance in SMPM machines to prevent demagnetization at three phase short circuit
k_{mg}	Ratio of MMF across the stator and rotor steel to the MMF across the airgap
K_r	Skin effect coefficient for rotor resistance
K_{sov}	Slot opening factor

K_{pv}	Winding pitch factor
K_{wn}	Winding factor for the n^{th} harmonic
K_{χ}	Skin effect coefficient for rotor slot leakage inductance

L

L	Machine axial length (mm)
l_c	Length of one turn of the winding coils (mm)
l_{cp}	Total length of series-connected winding coils per phase (mm)
l_{end}	Length of stator winding end-connection (mm)
L_{EX}	Expected winding insulation life
l_{ext}	Coil-end extension length (mm)
l_f	Lamination factor
L_{sls}	Stator slot leakage inductance (H)
L_{lsn}	Necessary leakage inductance to protect the magnet from damagnetization at short circuit (H)
L_m	Armature reaction inductance (H)
L_{msr}	Mutual inductance between the rotor and stator in the dq model (H)
L_r	Equivalent rotor self-inductance in the dq frame (H)
L_{sle}	Stator end winding leakage inductance (H)
L_{sl} ,L_{rl}	Stator and rotor leakage inductance (H)
L_T	Average expected winding insulation life at temperature T

M

MMF	Magneto-Motive Force
M_n	Magnetization vector of the permanent magnet
M_{rn}, $M_{\theta n}$	Radial and tangential component of the magnetization vector

N

N	Iteration number in particle swarm optimization
N_c	Number of turns per phase for stator winding
N_s	The number of stator slots
n	Rotational speed in rps (revolutions per second)
n_{phase}	The number of phases of a machine
n_s	Safety factor

O

OFV	Objective function value
$output$	Design objective function

P

p	Pole number
p_{aug}	Core loss augmentation coefficient
p_{best}	Personal best in PSO
P_{core}	Core loss of electrical machines (W)
P_{cu}	Stator copper loss (W)

$pelSat_t$	Penalty functions for design constraints of tooth saturation
pelTemp	Penalty functions for design constraints of winding temperature
$pelDmg_r$, $pelDmg_s$	Penalty functions for design constraints of magnet protection at rated and short circuit condition
pelD, pelL	Penalty functions for design constraints of airgap diameter and length
pf_a	*A priori* assumption of machine power factor
PI	Performance Index
P_{out}	Machine active output power (W)
P_{rc}	Rotor aluminum loss of induction machines (W)
PSO	Particle Swarm Optimization
P_{str}	Stray loss of induction machines (W)
P_{wf}	Windage and friction loss (W)

Q

q	Number of slots per pole per phase

R

R_{cu}	The armature resistance per phase
r	Airgap radius (mm)
R_{dc}, R_{ac}	DC and AC value of the armature resistance per phase (Ω)
R_h, R_w	Rotor ring height and width (mm)

R_m	Rotor radius on the airgap side (mm)
R_r	Rotor core outer radius (mm)
R_r'	Equivalent rotor resistance per phase referred to the stator side (Ω)
R_{rs}'	Equivalent rotor resistance per phase referred to the stator side at locked-rotor (Ω)
R_{se}	Effective stator inner radius considering the slotting effect (mm)

S

S	Machine apparent power (VA)
s	Slip of induction machines

T

t_{frame}	Thickness of the frame (mm)
T_{max}	Expected maximum shaft torque of the machine (Nm)
T_{out}	Output torque on the motor shaft (Nm)
$TperA$	Torque per ampere of electrical machines
T_{sc}, T_{rc}	Stator and rotor core thickness (mm)
T_{sw} , T_{rw}	Stator and rotor tooth width (mm)
T_{th}	Specified winding temperature that would achieve the required insulation life

U

U	Applied voltage per phase to the machine in RMS value (V)

V

VMOP	Vector Multi-Objective Optimization
Volume	Volume of a machine (mm^3)

W

W_{bar}	Weight of rotor bar (kg)
W_{fm}	Weight of machine frame (kg)
W_{pm}	Weight of permanent magnet (kg)
W_{sc}, W_{rc}	Weight of stator core and rotor core (kg)
W_{ring}	Weight of rotor ring (kg)
W_{st}, W_{rt},	Weight of stator teeth and rotor teeth (kg)
W_{sw}	Weight of stator winding (kg)
WSMOP	Weighted Sum Multi-Objective Optimization
W_t	Total weight of a machine (kg)

X

X_{sl}	Leakage reactance per phase (Ω)
X_m	Armature reaction reactance per phase for SMPM machines (Ω)

X_{mg}	Magnetizing reactance for induction machines (Ω)

Y

Y	Pole pitch (mm)

Greek Symbols

α_1	Stator tooth wedge angle
α_p	Pole coverage coefficient
α_t	Tooth pitch in electrical degrees
β	The ratio of coil pitch to pole pitch
δ	Skin depth (mm)
δ_1	Power angle
θ	Angular position with reference to the center of a magnet pole
λ	Aspect ratio
λ_{dr}^{e} , λ_{qr}^{e}	Rotor d-axis and q-axis flux linkage (Wb-turns)
λ_{sls}, λ_{ds}, and λ_{ecs}	Stator slot leakage coefficient, stator differential leakage coefficient, and stator end leakage coefficient
λ_{slr}, λ_{dr}, and λ_{er}	Rotor slot leakage coefficient, rotor differential leakage coefficient, and rotor end leakage coefficient
μ_0	Permeability of vacuum = $4\pi*10^{-7}$ (H/m)
μ_r, μ_{rc}	Permeability of the permanent magnet and conductor material
ξ	Thickness of the conductor foil normalized with respect to the

	skin depth
σ	Conductivity of winding conductors (S/m)
σ_{yield}	Yield strength (Pa)
ρ_c	Resistivity of stator conductor at its operating temperature (Ωm)
ρ_r	Resistivity of rotor conductor at its operating temperature (Ωm)
ρ_{cu}	Copper mass density (kg/m^3)
ρ_{pm}	Permanent magnet mass density (kg/m^3)
ρ_s	Steel mass density (kg/m^3)
τ_p	Pole pitch (mm)
τ_r	Rotor slot pitch (mm)
τ_t	Stator slot pitch (mm)
τ_y	Coil pitch (mm)
Φ	Flux per pole (Wb)
Φ_{tm}	Maximum stator tooth flux (Wb)

SUMMARY

Advances in electrical machinery with high efficiencies could significantly reduce the cost of industrial and residential energy systems, thereby reducing fossil fuel needs and emissions. Electrical machine design is a comprehensive process based on several factors, including economic factors, material limitations, specifications and special application-dependent factors. At the same time, machine design is a multi-physics task comprising of electric design, magnetic design, insulation design, thermal design and mechanical design. However, the out-of-date conventional machine design can neither reflect the advances in the past 30 years, nor exploit the trade-offs between design factors from the multi-physics nature of the electrical machine.

This work focus on the development a fast and efficient method for the design and optimization of Surface Mount Permanent Magnet (SMPM) machines and induction machines, as influenced by the energy source, mechanical loads, thermal effects, and the up-to-date developments in materials and manufacturing capabilities.

A new analytical design method is developed for the electromagnetic design of SMPM machines. Both distributed and concentrated winding types of SMPM machines are considered and compared. Based on the proposed electromagnetic analytical design method and a generic thermo-mechanical machine design model [1], an innovative and computationally efficient electromagnetic-thermo-mechanical integrated design method is developed for SMPM machines. Particle Swarm Optimization (PSO) is applied in a novel way based on this integrated design method for the multi-objective design optimization of SMPM machines. With the proposed method, the thermal and mechanical design is no longer treated separately and heuristically as in the traditional design, but has

been systemically integrated with the electromagnetic design; the effect of power source, cooling capability, thermal limits, and up-to-date material capabilities are also reflected in the design and optimization. Superior designs compared to traditional designs can be achieved with PSO based multi-objective optimization. The proposed integrated design approach also has the merit of good computational efficiency and provides a significant time reduction of the design cycle compared to finite element analysis.

A novel electromagnetic analytical design method of induction machines has been developed, which needs only six prime design variables but is able to design induction machines in fine details. The advantage over the traditional and other existing design method is that this proposed method does not have the heuristic selection of the design variables and does not need manual design iterations. The computing time is almost negligible and the design cycle is significantly reduced compared to the tradition machine design.

CHAPTER 1 Introduction and Objective of Research

1.1 Background

1.1.1 Electrical machine technology development

Electrical machines are fundamental energy conversion devices and are extensively used in energy conversion. They consume a significant part of the produced electrical energy and are essential components in the industrial process, transportation, and other aspects of modern life [2]. Therefore, advances in such electrical machines with high efficiencies could significantly reduce the cost of industrial and residential energy systems, thereby reducing fossil fuel needs and emissions.

Over the past 30 years, considerable effort has been spent on developing methods to improve the performance of electrical machines. In general, the developments have followed one of two paths. Along the first path, power electronics have been connected to machines to control excitation. Controls have been derived to maximize torque per unit of stator excitation current [3], maximize efficiency [4], mitigate torque ripple [5], etc. Along the second path, new materials and manufacturing technologies have been developed that have improved the mass per unit of delivered power [5]. Continuing improvements in permanent magnet materials [6-7] , the ability to work with thinner laminations, and other areas have opened up new possibilities.

Although there are numerous reasons for the incremental progress being observed in machine design, modern electrical machines are still designed based on engineering methods established more than half a century ago, long before modern materials, computing tools, and electric drives (supply a machine with non-sinusoidal waveforms) became available.

Therefore, it is important to develop machine design methods that reflect modern progress in electric drives, materials, and manufacturing. Ideally, a machine should be designed and optimized as the electromechanical actuator in a complete system, including the energy source, power electronics, mechanical loads, thermal considerations, and cost constraints. This objective of an ideal machine design has stimulated the proposed research work.

1.1.2 Machine design factors

Machine design is influenced by the following factors [8].

- Economics. Typically, machines are to be designed to have a minimum material cost and manufacturing cost. On the other hand, the trade-off between capital cost and operational cost should also be considered, especially for large machines.
- Material limitations. The physical limits of materials generally determine the performance and dimensions of the machine.
- Specifications and standards. The design, performance and materials used are often subject to specifications issued by NEMA or similar bodies.
- Special factors. In some applications, special considerations may exist that dominate the design. For example, aerospace motors require a design of minimum weight with maximum reliability. For the design of traction motors the emphasis is usually on reliability and the ability to satisfy a torque-speed curve.

Machine design is an area in which it is likely that suitable results can be obtained with a range of combinations of parameters. Depending on the factors of a particular

design that are deemed important, different designs could emerge. Even though several designs could provide similar performances, there may be a decided advantage to one design over another. Therefore, a good design and optimization method should be able to find either a unique design, or the optimums that actually represent a regime of possible solutions that satisfy a certain set of specifications.

1.1.3 Machine design features

Design features for electrical machines can be broken down into electromagnetic, thermal, and mechanical aspects [9]. Designs attempt to satisfy a certain duty cycle and torque-speed profile of the load, thermal requirements, and in some applications, constraints such as weight, volume and efficiency.

- Electrical design. The supply voltage, frequency, and number of phases of the machine are typically specified, and sometimes even the phase connection and number of poles. The slot numbers, winding layouts, turns per phase, and wire sizes are determined by the designer.
- Magnetic design. The airgap diameter and machine stack length, or active length, are calculated based on output power, speed, pole number, and cooling type. The slot sizing, core height, and external stator diameter are also calculated depending on various criteria.
- Insulation design. Insulation material choice and its thickness in various parts of the machine are designed based on supply voltage, thermal management, and the environment in which the machine operates.
- Thermal design. Extracting the heat caused by losses from the machine is imperative to keep the windings, core, and frame temperatures within safe

limits. Depending on the application or power level, various types of cooling are used. Calculating the loss and temperature distribution and the cooling system represents the thermal design.

- Mechanical design. Mechanical design refers to critical rotating speed, noise, and vibration modes, mechanical stress in the shaft and frame, and its deformation displacement, bearing design, inertia calculation, and forces on the winding end coils during the most severe current transients.

In the machine design problem, all the above design features are strongly coupled. For example, the allowable operating envelope for electrical machines depends largely on the ability of the machine to reject heat generated because of internal loss. The internally generated heat limits the maximum allowable current and flux density, which have a significant impact on the electric and magnetic designs of the machine. The electric and magnetic design determines the amount of copper loss and core loss, which both are major source of heat. However, the thermal considerations and mechanical considerations are often dealt with separately in present practice, despite the strong design coupling.

1.2 Problem Statement

As stated in the previous sections, machine design is a comprehensive process based on several factors, including economic factors, material limitations, specifications and special application-dependent factors. At the same time, machine design is a multi-physics task comprising of electric design, magnetic design, insulation design, thermal design and mechanical design. However, an out-of-date conventional machine design can neither reflect the advances in the past 30 years, nor exploit the trade-offs between design factors from the multi-physics nature of the electrical machine. Since induction machines

and Surface Mount Permanent Magnet (SMPM) machines are presently two of the widely used electrical machines, this research focus on these two machine types only.

The objective of the proposed research is to develop a fast and efficient method for the design and optimization of two types of electrical machines, as influenced by the energy source, mechanical loads, thermal effects, and the up-to-date developments in materials and manufacturing capabilities.

The ultimate goal of this research is to advance the currently outdated design practices and create a tool that would allow designers to optimize electromagnetic devices that meet the needs of any given specific application.

Because there are many special considerations in the design of very small or very large machines and in special purpose machines (high speed machines, axial flux machines, etc), the focus of this research is on general purpose, medium-sized (about 1 kW to 100 kW), low-voltage (typically below 1000 V) and three-phase machines. However, the proposed design and optimization framework still apply to those special designs.

1.3 Dissertation Outline

Chapter Two presents a comprehensive survey of the previous work on the design of SMPM machines and induction machines. The proposed new analytical design method and a novel Particle Swarm Optimization (PSO)[10] based optimization are presented in Chapter Three. A new method to compare the distributed winding and concentrated winding types of SMPM machines based on the analytical design method and PSO are proposed in Chapter Four. Chapter Five presents an innovative electromagnetic-thermo-mechanical integrated design approach that is able to reflect the multi-physics nature of

the electrical machines, including energy source, mechanical loads, thermal effects and materials. Chapter Six presents a sensitivity analysis about how the SMPM machine performance designed by the proposed method varies with variations of the machine parameters between the design calculation and the machine if actually manufactured. Chapter Seven proposes a novel electromagnetic design and optimization method for both mains-fed and inverter-fed induction machines. The conclusions, the contributions, and the recommendations for future work are summarized in Chapter Eight.

CHAPTER 2

Previous Work on Design and Optimization of Surface Mount Permanent Magnet Machine and Induction Machine

2.1 Overview

A comprehensive literature survey is presented to summarize the traditional design methods and recent progresses in the design and optimization of Surface Mount Permanent Magnet (SMPM) machines and induction machines. The traditional machine design methods, as reviewed, are dominated by heuristic rules of thumb that were established more than 30 years ago. Recent progress in SMPM machines and induction machines are also reviewed. In addition, the applications of optimization algorithms in the machine design are summarized. These design and optimization methods are evaluated with a focus on details of the accuracy of the design models, the computational efficiencies, and the abilities to reflect constraints and specifications. The summary of the previous work leads to a conclusion that there is a need for a novel machine design method that could reflect the effect of energy source, mechanical loads, thermal effects and up-to-date developments in materials and manufacturing capabilities.

2.2 The Traditional Machine Design Approach

The traditional design approach was established nearly half a century ago and is dominated by rules of thumb and empirical curves that reflect the experiences of manufacturers, sometimes passed down from generation to generation as the established "company policy" way of doing it. In the traditional design, designers start by heuristically selecting values of design parameters, and then follow an iterative tuning process trying to achieve design specifications.

2.2.1 The sizing equation

Traditional machine design usually starts from the famous sizing equation [11], as shown in

$$S = 11 K_{w1} * \overline{B} * ac * (\frac{D}{1000})^2 * \frac{L}{1000} * n \,, \tag{2.1}$$

where S is the motor rating in W, $\overline{B}$ is the specific magnetic loading in Tesla, ac is the specific electrical loading in A/m, D is the stator bore diameter in millimeter, L is the generator active length in millimeter, K_{w1} is the winding factor for the fundamental, and n is the rated speed in rps (revolutions per second).

Values for $\overline{B}$ and ac are selected by the designer at the start of the design process. The magnetic loading $\overline{B}$ is limited by the saturation point of the materials used, the hysteresis losses and eddy current losses, the stray losses, the effectiveness of the cooling strategy, the load profile, and the duty cycle. The specific electric loading ac is limited by the copper loss in the conductors, the effectiveness of the cooling strategy, the temperature limitation of the insulation material, the load profile, and the duty cycle. In the traditional design, the selection of $\overline{B}$ and ac is primarily based on the designer's experience. Some textbooks provide guides from previous design experiences, such as a scan from [11] shown in Figure 2.1.

D m.	$\frac{L}{D}$ max.	Slip-ring			Cage		
		$\overline{B}$ Wb./m.²	ac amp.-cond./m.	δ A./mm.²	$\overline{B}$ Wb./m.²	ac amp.-cond./m.	δ A./mm.²
0·1	0·8	0·3	6 000	3·8	0·3	11 000	4·0
0·15	0·75	0·35	10 000	3·6	0·35	15 000	3·8
0·2	0·7	0·4	13 000	3·4	0·4	18 000	3·6
0·3	0·65	0·43	17 500	3·3	0·43	22 500	3·5
0·4	0·62	0·45	21 500	3·2	0·45	26 000	3·5
0·5	0·6	0·46	25 000	3·2	0·46	29 000	3·5
0·75	0·5	0·47	30 000	3·2	0·47	33 000	3·5
1·0	0·42	0·48	32 500	3·2	0·48	35 000	3·5
1·5	0·33	0·5	34 000	3·2			
2·0	0·3	0·51	35 000	3·2			
3·0	0·3	0·53	37 000	3·2			

Figure 2.1: Table for the selection of magnetic and electric loading [11].

2.2.2 Selection of the aspect ratio

After $\overline{B}$ and ac are selected, the D^2L value of the machine is then calculated by (2.1). For a machine with its pole number denoted by p, an aspect ratio λ is defined as $\lambda = \frac{L}{\pi D / p} = \frac{L}{Y}$, where Y is the pole pitch in meters. By choosing a proper value for λ, D and L can be then calculated. Besides $\overline{B}$ and ac, λ is another design parameter that designers usually choose at the beginning of the design process. A good choice of λ helps to increase winding induced EMF with less coil length. With the same flux density, the induced EMF is proportional to the coil area. For highest induced EMF with the same coil length, the design of a rectangular coil shape with $\lambda = 1$ is desired. Besides this consideration, the selection of λ also depends on other factors, such as machine performance requirements, material consumptions, manufacturing feasibility and cooling.

In the traditional design, the selection of the aspect ratio is also guided by empirical curves, as illustrated in Figure 2.2 for induction machine design.

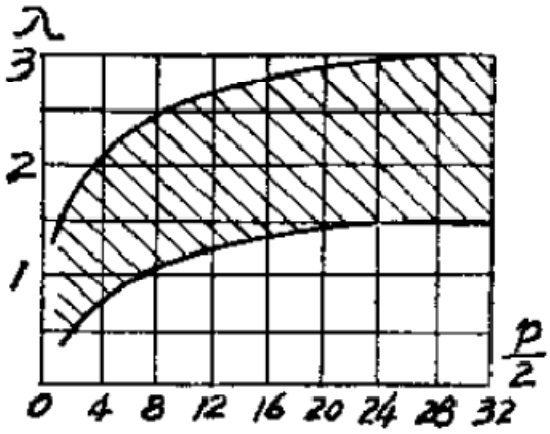

Figure 2.2: Heuristic curve for the selection of the aspect ratio [12].

2.2.3 Selection of current density

By selecting values for $\overline{B}$, *ac* and λ, another important design parameter to select is the stator current density J_s. For a certain rated current I, the current density J_s determines the cross sectional area of the copper wire A_{wire} used, as shown in (2.2)

$$A_{wire} = \frac{I}{J_s}. \tag{2.2}$$

Higher current density leads to smaller A_{wire} and then larger armature resistance. For the same stator current, the copper loss is increased. This higher copper loss not only leads to lower machine efficiency, but also increases the winding operating temperature because more heat is generated. Since the winding operating temperature is limited by the maximum allowable temperature of the insulation, the machine designer should select a current density low enough that the operating temperature is within limits. On the other hand, when thinner wire is used, with the same number of winding turns, the amount of

copper is reduced and less slot space is required to fit the wires. Accordingly, the teeth length can be reduced and the amount of steel is also reduced. The overall effect then leads to a reduction of the machine material cost and weight, which means that current density should not be too small in order to avoid a bulky machine.

In the traditional design, the current density is typically selected by rule of thumb or the designer's experience, as shown in Figure 2.1. According to certain empirical rules, the current density is generally selected in the range of 3 to 7 A/mm^2 [11-12]. In the traditional approach, many important factors in determining the temperature rise of machines cannot be easily taken into account, such as the ambient operating temperature, the available effective surface area for heat rejection, and the duty cycle of operation. For example, the recommended current density values in Figure 2.1 (represented by δ) are given just according to the selections of $\overline{B}$, *ac*, *D* and *L*. However, a machine designed to run continuously under full load with a 40^o C ambient temperature is expected to have much lower current density than a machine designed to run intermittently and at an ambient of 10^o C. In the traditional design, selecting the current density for both cases usually depends on a designer's experience and safety margin, which may often lead to over- or under-design of the electrical machines.

2.2.4 Selection of the flux density

To fully utilize the material, the flux densities in the teeth and cores are usually selected around the knee point of the B-H curve [8]. The traditional design rules were mostly developed based on silicon steel with a knee flux density around 1.4 T. However, with the improvement in magnetic material over the decades, core materials with saturation flux densities as high as 2.2 T have been produced, such as 'Hiperco' from

Carpenter steel for example [13]. Higher working flux density leads to smaller tooth width, thinner core, and thus smaller machines with the same rating. As a result, the empirical design curves that are based on a knee point of 1.4 T are inappropriate for machine designs using more modern magnetic materials.

2.2.5 The traditional electrical machine design process

The traditional electrical machine design process is an iterative process and is summarized by the flow chart in Figure 2.3. An *a priori* assumption of machine efficiency eff_a and power factor pf_a has to be made and the machine rating S in VA is calculated by equation(2.3),

$$S = \frac{P_{out}}{eff_a * pf_a}, \tag{2.3}$$

where P_{out} is the specified machine rated output power. After the value for S calculated, values for $\overline{B}$, ac and λ are selected to calculate D and L according to the sizing equation (2.1). Next, with the given rated voltage and current density, the number of coil turns and wire diameter of stator winding coils are determined for a given winding layout. At the same time, tooth width and core thickness are calculated with the selection of the flux density in the teeth and the core. The machine's outer diameter is then calculated from the slot area needed for the winding and the areas of the teeth and core. Rotor designs are also carried out with certain traditional rules, which can be found in the literature, such as [12].

After one complete trial design is produced, the performance of this trial design is calculated and verified against initially selected design parameters (primarily $\overline{B}$, ac, and J_s) and *a priori* assumptions of efficiency and power factor. If any of these parameters

does not agree with initially assumed values, modifications are made to either design parameters or *a priori* assumptions and the design process is repeated. This process is repeated as many times as needed until agreement is reached. Even if such agreement is achieved, there are also various performance requirements to meet, such as specified maximum winding temperature, minimum power factor, and maximum weight. For line start induction machines, there are also requirements about starting current and starting torque. If one of such design requirements is not met, the designer has to modify the selection of certain design parameters and start the design process over with even more iterations. What make this traditional design process more time-consuming are the inherently complicated interrelations between different components of the machine. No direct relation exists between design parameters and machine performance so as to inform the designer about how to change design parameters to improve the design at the next iteration. Moreover, the inherent trade-offs between different machine performance indexes make it often impossible to improve one performance index without degrading another. For example, to increase machine efficiency, thicker wires can be used but this choice increases the weight and cost of the machine at the same time. In the traditional design, it is totally depend on the designer's personal experience and skill to find good designs through this iterative and heuristic process. Not only tedious and inefficient, this experienced-based design process cannot guarantee optimal machine performance with respect to its design specifications and operating environment, and this is a disadvantage in today's increasing application and performance requirement and competitive market of electrical machines.

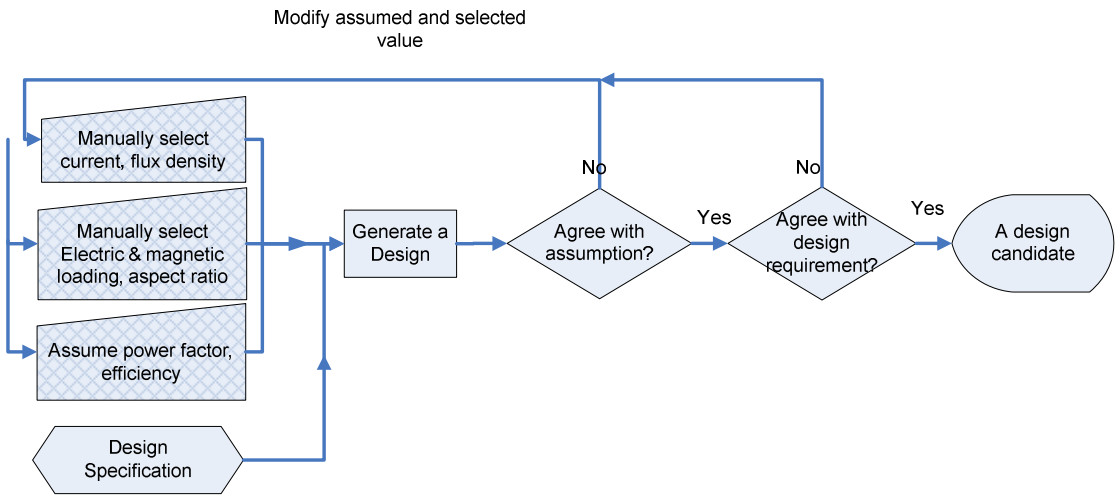

Figure 2.3: Illustration of the iterative design process in the traditional machine design

2.3 Previous work SMPM machine design

The development of the high energy density permanent magnet material, such as NdFeB and SmCo, accelerated the development and use of the permanent magnet machines in the mid 1980s. The design techniques of permanent magnet machines are newer compared to those for induction machines. The previous work on SMPM machine design methods generally follows two paths: analytical design and numerical design. For both design methods, the machine design has to start with certain design parameters pre-selected, either by the designer's experience, or certain algorithm.

2.3.1 SMPM machine *analytical* design

In the analytical design of SMPM machines, a set of analytical models is developed as the design basis, such as the magnetic equivalent circuit in [14] or a set of analytical design equations in [15-16].

2.3.1.1 Magnetic equivalent circuit based design

In [14], a magnetic equivalent circuit (MEC) of the SMPM machines is developed, as shown Figure 2.4. R_s, R_{ml}, R_g, R_m, and R_r are equivalent reluctances that represent the MMF drop on stator steel, leakage flux path, airgap, permanent magnet, and rotor steel. Φ_r, Φ_l and Φ_g are the flux produced by the permanent magnet, leakage flux, and flux that goes through the airgap and enters the stator. Analytical equations are developed to calculate the values of each element in the magnetic equivalent circuit. By assigning nonlinear properties to the reluctances based on the nonlinear B-H curve of the steel used for the machine, saturation effects can also be included.

Although the MEC method is a useful tool for analytical analysis of SMPM machines, it does not design a machine but analyzes an existing design. Hence, the MEC method cannot provide fundamental improvement to the traditional machine design method.

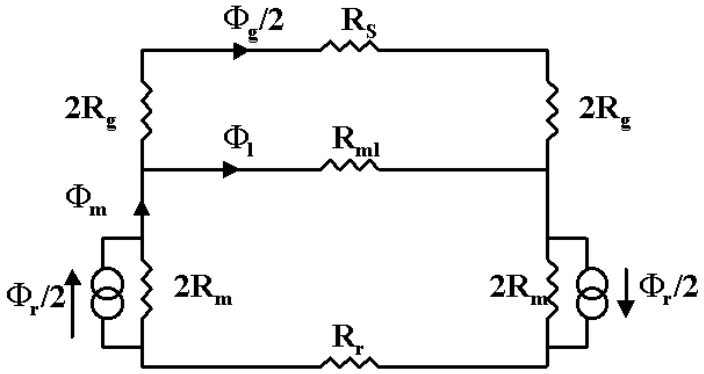

Figure 2.4: Magnetic equivalent circuit of the SMPM machine

2.3.1.2 Analytical design equation based design

As in [15-16], a large set of equations is created for the SMPM machine analytical design model, which includes geometrical equations, equations of the physical

characteristics, magnetic equations, electrical equations, and thermal equations. These equations include both equalities and inequalities to represent the physical relations and constraints. This large model includes 224 parameters linked by 124 equations and shows good accuracy compared to finite element analysis.

With this comprehensive analytical design model, the designer can input values for certain design variables and calculate the others. Optimization algorithms can also be developed based on this model.

The challenge with this design model is the huge number of design variables and the complicated relationships between them. Optimizing a model with hundreds of variables is extremely difficult. These challenges have not been sufficiently addressed in [15-16]. It is thus desired to find a way to identify key design variables and thus reduce the dimension of the optimization.

2.3.2 Numerical method based PM machine design

Numerical methods, such as finite element analysis (FEA), are widely applied to the design of electrical machines [17-19]. FEA has good accuracy in saturation calculation and is also good at capturing performance in detail. In [17-18], FEA is used to determine the optimum shape and magnetization of a set of discrete anisotropic magnet blocks or arcs on SMPM machines. In [19], FEA is used to find the relationships between the induced harmonic current and the magnet shape to optimize the magnetic shape design. In all those designs, the design parameters must first be given to the FEA apriori and then the FEA carries out the analysis. In fact, FEA is not a design tool, but an analysis tool.

FEA combined with certain computational optimization methods has been applied in PM machine design and optimization. Such FEA based design optimization is well

illustrated in [17-18]. First, a set of design variables is defined, such as the machine geometry variable definition in Figure 2.5.

Although the optimized results show improvement from an existing design, significant computational effort is needed. With a very conservative estimate of 30 seconds per FEA simulation and a basic design space search assumed, the necessary time for the design simulation is summarized and shown in Table 2.1, where *n* is the number of machine design parameters and *Hours* is the estimated time needed for FEA based design optimization.

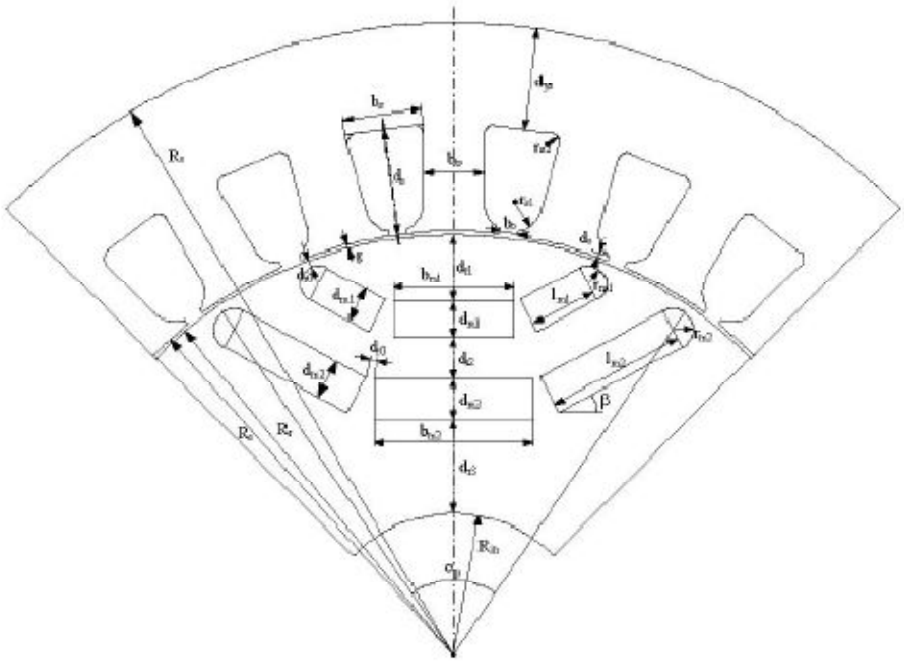

Figure 2.5: Geometrical design variables

Table 2.1: Computational cost with parameter dimension

n	10	15	20
Hours	8.53	273.1	8783.1

The number of design parameters for a SMPM machine or an induction machine can easily be more than 20. It is not realistic to spend 365 days (8783.1 hours) for a basic search of one optimized machine design.

With the development of faster computers, the FEA simulation needs less and less time. However, FEA simulations can still easily take several hours or even days. FEA can be a useful tool to evaluate an optimal design, but is not a good candidate as a design and optimization method.

2.3.3 Summary of previous work on SMPM machine design

A significant amount of previous work has been done on the SMPM machine design. On the analytical side, different analytical design methods have been developed that are able to design SMPM machines with input of certain design parameters. On the numerical side, FEA has been applied to analyze machine performances and also design machines when combined with certain intelligent algorithms. However, neither of the two has enough work on identifying which are the key machine design parameters and how to choose optimal values for them. As a result, their design processes end up with solving a problem with a large number of dimensions, which makes design optimization difficult and time-consuming. Moreover, thermal design is usually treated separately from electromagnetic design and with not enough attention. As a result, the current density selection is either based on heuristic rules or crude temperature evaluations. The effect of the energy, thermal environment, mechanical loads and material properties are not fully considered.

2.4 Previous work on induction machine design

Most induction machines are designed using traditional design rules with strong emphasis on line-fed machines. More recent work in the last decade has put more emphasis on the design of induction machines driven by modern variable speed drives. In addition, there are some works on using modern numerical-based electromagnetic analysis tools to improve traditional empirical curve-based design calculations. Despite those developments, the traditional iterative design process has not been improved.

2.4.1 Previous work on inverter driven induction machine design

The operating conditions of induction machines change significantly from traditional mains-fed to inverter-fed applications. In traditional design strategy, an important concern is the start-up characteristics, which includes limiting inrush current, generating sufficient starting torque, and ensuring a high starting efficiency. To meet such start-up requirements, the design strategy is to utilize the skin effect optimally to have proper rotor resistance during starting.

In designing an inverter-driven induction machine, the strategies are different. First, the start-up characteristics of a mains-fed machine can be completely ignored. Second, the most favorable slip frequency can be selected to maximize efficiency at any speed and load. Third, the machine operating frequency is variable, which brings the designer a certain degree of freedom to choose the number of poles.

On the other hand, for the design of an inverter-fed induction motor, the negative impact of an inverter should be considered. The harmonics introduced by the variable frequency non-sinusoidal voltages produce additional losses and torque pulsations, which add to the cooling requirements. The voltage spikes from the PWM and the impedance

mismatch can cause early failure of the insulation; this requires special attention to the insulation design.

2.4.1.1 Rotor slot shape design[20-22]

In the traditional mains-fed induction machine, the primary concern in designing the rotor shape is to simultaneously limit the starting current and ensure good performance. Hence, different rotor slot shapes have been developed, especially the double cage rotor. Without such starting requirement, the rotor slot shape can be optimized solely to maximize machine efficiency in the small slip region in which the machine is mostly operated. In [21] and [22], generic rotor slot shapes are developed and the machine design is optimized with the efficiency in the small slip region as the target. The optimized result of [22] is compared with the traditional rotor slot, as shown in Figure 2.6 and a 48% reduction of the rotor loss is achieved. Although the slot shape design is only part of the total design process, this reduction indicates that design optimization can possibly bring great improvement to the traditional machines.

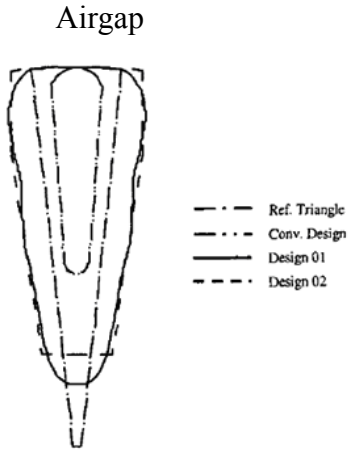

Figure 2.6: The comparison of the optimized rotor slot for inverter driven induction machine with the rotor slot for traditional line start induction machine[22]

2.4.1.2 The selection of pole number

The selection of the pole number for induction motors supplied from a constant frequency source is straightforward because the pole number is determined solely by the synchronous speed required for the application. However, the selection of the pole number for inverter-driven induction motors is much more complicated because the pole number is not determined by a single, dominating factor in these cases. Theoretically, any even number can be chosen as the pole number since the frequency can be adjusted. Numerous factors and trade-offs hence have to be made. In [23], the authors compare 2 pole and 4 pole induction motors with the same overall outside dimensions in terms of the efficiency, power factor, etc. Some qualitative results show that compared to 2 pole machines, 4 pole machines have lower copper losses, lower power factor, higher time harmonic losses, higher iron losses, higher power density and are easier to manufacture.

It is thus important to include the pole number selection in the design optimization, which has until now not been fully explored.

2.4.1.3 Impact of the harmonics on the induction machine design

The harmonics induced by the inverter cause an increase of the core loss and stray loss. If a traditionally designed, mains-fed induction motor is driven by an inverter, de-rating of the machine is usually applied because of the higher temperature rise due to such additional losses. Induction machine design methods that consider the increased harmonic losses are promoted, such as [24], where a heuristic term is added to the traditional sizing equation to consider the harmonics. The induction machine design can also be optimized with the known spectrum of the harmonics in the inverter [25-26]. It is

thus important to consider these additional losses in the design and optimization of inverter-fed induction machines.

2.4.1.4 Voltage spikes on the insulation

Motor windings, when fed by PWM inverters, are exposed to voltage spikes thousands of times per second during operation. The machine winding layout and insulation design should be adjusted accordingly to maximize the winding insulation lifetime. Several reports describe improved insulation material [27] and even so-called partial discharge resistance wires [28]. Some authors also propose that the insulation design is a system approach, not a component approach [29]. It is clearly important to include the modification of the insulation design into the machine design. However, different insulation thicknesses will lead to different slot fill factors and may have an impact on the machine's overall size.

2.4.2 Previous work on induction machine design method and process

Induction machine design methods based on solutions of electromagnetic fields are proposed in [30-31] so that the performance calculations are not based on the empirical curves and the accuracy of calculating the machine's equivalent circuit parameters, such as magnetizing inductances and leakage inductances, can be improved. Optimization algorithms are applied [32] to the design of these machines for the methods of [31] or for traditional methods based on empirical equations [33] in order to automate the design process. However, similar to SMPM machine analytical design methods, the induction machine design method involves a large number of design variables, which makes the optimization process inefficient and time-consuming.

2.4.3 Summary of previous work on induction machine design

The previous work on induction machine design for both mains-fed and inverter-fed applications provides valuable insights regarding the effects of different power supplies on the rotor slot design, winding insulation design, loss calculation, and pole number selection. Improved induction machine performance calculation methods have been developed by previous researchers. What is needed now is a novel design strategy that would utilize these insights and at the same time run fast and efficiently to find optimal designs with respect to given machine operating environments and design specifications.

2.5 Electrical machine Computer-Aided-Design

With the development of computer technology, Computer-Aided-Design (CAD) software tools for the design of electrical machines have become more and more popular. CAD software tools are able to carry out machine design calculations, provide certain levels of optimization and provide links to FEA analysis. The RMxprt by Ansoft [34] and SPEED [35] are two examples. These CAD tools save much time and effort for the machine designer.

However, the presently commercially available CAD software tools can still be called analysis tools, rather than machine design tools. For example, in RMxprt, the designer has to input the inner and outer diameter for stator and rotor, and the machine axial length. For a PM machine, magnet thickness, magnet pole coverages, and magnetization are also needed. For an induction machine, the rotor slot shape and geometry are needed. Hence, even with the CAD software, the designer still has to make his or her own selections on certain key design parameters, and this selection may still be

mostly based on certain heuristic rules or the designer's experience. Thus, the tedious and inefficient nature of the iterative process cannot be improved by CAD software.

A computer-based design assistant for induction motors is proposed in [36] where the design assistant is able to synthesize new designs with Monte Carlo method. The design assistant essentially produces a large number of machine design trials with randomly generated machine design parameters. The assistant ends up with extremely long design cycles because no approach is taken to reduce the number of machine design dimensions and no approach is taken to intelligently find the optimal design frontier.

2.6 Previous work on the machine design optimizations

The complexity of the electrical machine structure makes an optimal design a difficult and challenging task. In many instances the specifications of the design conflict with one another, for example high power density and low magnet volume [18]. The nonlinearities in materials and the complex relationships between many of the geometrical parameters truly make optimal machine design a multi-objective optimization. This renders most classic optimization algorithms ineffective [18] and the optimization problem needs to be formulated as a nonlinear, non-gradient, constrained minimization problem [15] using techniques that are suited for this type of problem.

In general the optimization problem can be stated as follows [15, 37]:

Starting from the initial design parameter vector

$$\bar{X}_0 = [x_{01}, x_{02}, ..., x_{0D}],\ \bar{X}_0 \in R^D,$$

find the final design parameter vector

$$\bar{X}_m = [x_{m1}, x_{m2}, ..., x_{mD}],\ \bar{X}_m \in R^D,$$

which satisfies the objective function set

$$f(\bar{X}_m) = [f_1(\bar{X}_m), f_2(\bar{X}_m), ..., f_k(\bar{X}_m)],$$

and which is subject to the design constraints

$$g_i(\bar{X}_m) \leq 0 \text{ for } i = 1, 2, ..., n,$$

where the boundaries of the design parameters are defined as

$$x_j^{(L)} \leq x_j \leq x_j^{(U)} \text{ for } j = 1, 2, ..., D.$$

Various optimization methods have been published for the design of electrical machines and is briefly summarized.

2.6.1 Sequential Unconstrained Minimization Technique (SUMT) [15]

The SUMT converts the original constrained problem into an unconstrained one, which can be solved using a direct search method requiring only values of the objective function and not the derivatives. The main idea of SUMT is to add a term to the constrained objective function $f(\bar{X})$, which depends on the degree to which the constraints are violated and vanishes if the constraints are satisfied. This added term is called a "penalty function" and is sequentially modified in such a way that the optimum solution of successive unconstrained problems approaches the optimum solution of the constrained problem. In [15], efficiency is set as the objective function and the optimized motor shows an improvement of 26% in the efficiency with a 13.8% increase in the motor active weight, but with the same volume.

2.6.2 Genetic algorithms[17, 38]

Genetic Algorithm (GA) is a search procedure that emulates the mechanics of natural selection and genetics. The algorithms explore the motor parameter space using mechanisms of reproduction, crossover, and mutation, with the aim of optimizing machine design. The steps of using a GA can be summarized as follows:

1. Encode any potential solution of the optimization problem into a binary string, called a chromosome.
2. Create an initial population of chromosomes
3. Evaluate the chromosomes by the objective function and assign a fitness score accordingly.
4. Select members from the current population to produce offspring.
5. Perform crossover
6. Perform mutation
7. Repeat 3) to 6) until terminating criterion is met

Reference [17] uses a genetic algorithm-based optimization in order to design a SM PM brushless DC motor. A steady state analysis of a brushless motor is used to support the design and provide expressions of the main electrical, magnetic, mechanical, and thermal quantities as functions of the machine dimensions and operating conditions. Results indicate that the GA performs well in optimizing the machine.

2.6.3 Vector optimization algorithm[39]

A vector optimization problem consists of several objectives that need to be maximized or minimized at the same time. One method of solving these problems is to transform the multi-objective problem into a scalar problem using weighting methods or

restriction formulations. The main challenge in using this approach is the choice of a suitable transformation method and the selection of the parameters of the transformation.

The vector optimization algorithm (VEKOPT) [39] is a method that finds an approximation of the whole PARETO-set, which is defined by (2.4). The optimality condition for vector optimization was first introduced by the Italian scientist V. PARETO (1848 – 1923) and is based on a condition for several objectives. The so-called PARETO-optimal solution occurs if the improvement of one objective function simultaneously decreases at least one of the other objective functions. A parameter vector $\vec{x}^*$ is called PARETO-optimal, if no other vector $\vec{x}$ exists that holds both conditions

$$f_j\left(\vec{x}\right) \le f_j\left(\vec{x}^*\right) \quad \text{for all} \quad j \in \{1,\ldots,m\}$$

$$f_j\left(\vec{x}\right) < f_j\left(\vec{x}^*\right) \quad \text{for at least one} \quad j \in \{1,\ldots,m\} \tag{2.4}$$

In [39], VEKOPT is applied to a 4 pole synchronous machine and the target is to maximize the output power and minimize the volume of the magnet used at the same time with certain constraints. When compared with a previously built machine, the solution provided by this optimization method results in a design with 16% less magnet volume.

2.6.4 Particle Swarm Optimization [39]

PSO is an evolutionary computation technique that was developed in 1995 by Kennedy and Eberhart [10] and is based on the behavioral patterns of swarms of bees in a field trying to locate the area with the highest density of flowers. PSO has been shown to be effective in optimizing difficult multidimensional problems in a variety of fields [10,

40]. A more detailed description of PSO and the proposed novel application of PSO in electrical machine design are presented in Chapter 3.

2.6.5 Summary on optimization methods

The challenge in machine design optimization is that electrical machines are complicated and nonlinear systems, which require the optimization algorithm to have good ability to avoid local minimums. In addition, since machine design calculations are usually computationally intense, the optimization algorithm should also have a good searching efficiency in order to have shorter design cycles.

Traditional gradient-based methods do not work because the gradients in the complicated machine design problem are difficult to calculate. The SUMP converts a constrained problem to an unconstrained problem, but cannot help the search. Hence, computational-based optimization methods are good candidates for machine design optimization. According to preliminary research in [41], the performance of GA is sensitive to the running coefficients, while PSO is not. Hence, PSO may be a good candidate for machine design optimization.

2.7 Chapter summary

In this chapter, the design and optimization methods for induction machines and SMPM machines are summarized.

The traditional design is strongly based on the heuristic selection of parameters and empirical curves and cannot reflect the modern development in materials, power electronics, etc. In addition, the traditional design process is an inefficient iterative process, which makes it difficult to optimize a design.

The more recent development of the SMPM machine and induction machine design and optimization methods, including CAD software tools, can incorporate the modern techniques at some level, but are still far from ideal. The selection of key design parameters by the designer, such as the magnetic loading, electric loading, and current density, still plays an important role in the design. Though thermal analysis is applied in some of the design processes, thermal design is typically treated separately and is only used to check the temperature distribution of a completed design.

The literature review presented in this chapter shows that most of the existing design and optimization methods cannot fully reflect the interactions of the energy source, power electronics, load profile, thermal constraints, and material properties, which is the reason for this research.

CHAPTER 3
Surface Mount Permanent Magnet Machine Electromagnetic Design and Optimization

3.1 Overview

The complexity of the PM machine structure makes a manual optimal design a difficult and challenging task unless some optimization algorithm is used. A manual design consists of first designing from first principles and then subjecting the design to a Finite Element Analysis (FEA) to confirm flux densities. FEA itself does not design a machine but evaluates a given design. The nonlinearities in materials and the complex relationships between many of the geometric parameters make optimal machine design a truly multi-objective optimization [42]. This chapter presents a novel analytical design method and a PSO based optimization algorithm, which are able to design and optimize SMPM machines with respect to different users' specific requirements.

3.2 SMPM Machine Analytical Design Method

3.2.1 Sizing of SMPM machines

The design of an electrical machine usually starts from the classical sizing equation [11], as shown below:

$$S = 11 K_{w1} * \overline{B} * ac * \left(\frac{D}{1000}\right)^2 * \frac{L}{1000} * n, \tag{3.1}$$

where S is the motor rating in VA, $\overline{B}$ is the specific magnetic loading in Tesla, ac is the specific electrical loading in A/m, D is the stator bore diameter in millimeter, L is the machine active length in millimeter, K_{w1} is the winding factor for the fundamental, and n is the rated speed in rps (revolutions per second).

As described in Chapter 2, the selection of $\overline{B}$ and *ac* is heuristic in a traditional design, but is crucial to the overall performance of the machine. However, there is no universal solution that is able to start from a specific design specification and directly tell the optimum values of $\overline{B}$ and *ac* to use in (3.1). Moreover, no physical constraints exist that are able to define an exact domain for the values of $\overline{B}$ and *ac*. Hence, the values for $\overline{B}$ and *ac* are usually selected based on the designer's experience. This heuristic approach can be inaccurate and inefficient. Moreover, it is also difficult to develop optimization algorithms based on such an approach. A different sizing approach is thus developed in this chapter for the design of SMPM machines based on the availability of the analytical field solution of the airgap flux densities.

For the SMPM machine design, [43] provides an analytical calculation of the magnetic field solution in the airgap region. The radial component of the magnetic field in the airgap produced by the permanent magnet can be solved and expressed in a Fourier series as follows:

$$B_{gap-mag}(\theta, r) = \sum_{n=1,3,5...}^{\infty} B_n(r)\cos(\frac{np}{2}\theta) \tag{3.2}$$

where B_n is the *n*-th spatial harmonic component of the airgap flux density distribution, *r* is the airgap radius, θ is the angular position with reference to the center of a magnet pole and *p* is the number of poles. By first assuming the stator has a slotless structure (slotting effect is considered later) and infinite permeability, the B_n's are only functions of the stator bore diameter *D*, the effective airgap length *g'*, and the magnetic properties of the permanent magnets. The effective airgap length *g'* is expressed as

$$g' = g + \frac{h_m}{\mu_r} \tag{3.3}$$

where g is the physical airgap length, h_m is the thickness of the permanent magnet in the radial direction and μ_r is the permeability of the permanent magnet, which is slightly larger than 1. For most general purpose SMPM machines designed, g is usually much smaller than h_m and does not have a significant influence on the overall performance of the machine. Hence, the airgap length g can be fixed to a typical value for a 15 kW, 60 Hz machine, say 1 mm. The selection of g depends on several factors, mostly on the manufacturing methods. As a result, the magnetic loading $\overline{B}$ in the SMPM machine is determined by the stator bore diameter D and the magnet thickness h_m, which gives rise to a new sizing approach for SMPM machines.

Instead of choosing $\overline{B}$ and ac, the designer chooses values for the stator bore diameter D, the magnet thickness h_m, and the machine axial length L. $\overline{B}$ can be computed from the analytical equations provided in [43], which is discussed in detail later in section 3.2.3. The sizing equation in (3.1) still holds and ac is thus determined. As a result, there is no iterative process in this new sizing approach. Moreover, the variables to be selected are the machine geometry parameters, not the heuristic variables. Hence, optimization algorithms can be applied more efficiently to the machine design with this new sizing approach.

3.2.2 Magnetic design of SMPM machines

The SMPM machine is reported to have relatively high torque pulsations, which are mainly composed of the cogging and ripple torque. Torque pulsations in general degrade the machine performance and are thus not desirable. Various methods to minimize those

torque pulsations have been proposed and illustrated in the literature [44-45]. Instead of focusing on the detailed tuning of the machine geometries to minimize the torque pulsations, this work seeks to find a general solution for the magnetic pole coverage and the magnetization that will decrease the cogging torque and the ripple torque to low levels. Hence, it is not necessary to include the design of the magnet Pole Coverage Coefficient (α_p) and magnetization direction in the optimization, and the dimension of the optimization problem can be reduced.

The α_p defines how much the magnet covers the total pole pitch and has a value between 0 and 1, where 1 means the magnet covers the total pole area. Two commonly used directions of magnetization are radial magnetization and parallel magnetization.

Assuming infinite permeability of the steel core and neglecting the slotting effect, the MMF waveform produced by a permanent magnet for typical SMPM machines can be calculated according to [43]. The magnitudes for the fundamental, 3rd, 5th and 7th harmonics are plotted in Figure 3.1 for different values of α_p and directions of magnetization:

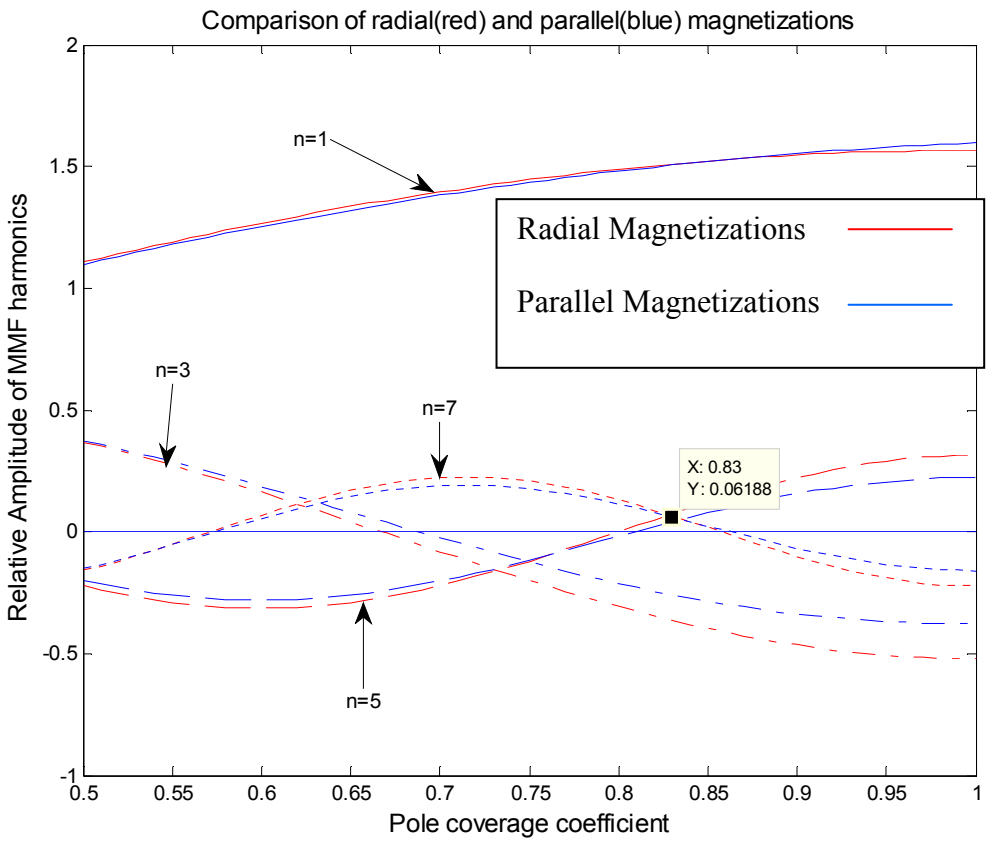

Figure 3.1: Relative magnitude of MMF harmonics [43]

Figure 3.1 shows that as the α_p increases, the magnitude of the fundamental increases slowly. When the α_p is around 0.83, the magnitudes of the 5th and 7th harmonics are close to zero. In addition, the parallel and radial magnetization produce approximately the same magnitude for the fundamental, while the parallel magnetization has a much smaller 3rd harmonic than the radial magnetization when the α_p is equal to 0.83. Fewer harmonics in the MMF waveform means there will be fewer harmonics in the airgap flux density waveform, and eventually there will be less torque ripple with a near sinusoidal excitation. For the above reasons, a α_p of 0.83 and parallel magnetization are chosen for the purpose of minimizing the torque ripple. Since the above analysis is

not related to the diameter and length of the machine, this conclusion can be a general design guide for all SMPM machines within the scope of this research. A typical 15 kW, 1800 rpm and 60 Hz SMPM machine with pole coverage of 0.83 and parallel magnetization is simulated in FEA. As shown in Figure 3.2 (a), the cogging torque has a peak value of only 3 Nm (note that the two irregular peaks are due to numerical errors), which corresponds to 3.8 % of the rated torque (80 Nm). In the FEA simulation of torque ripples, the rotor speed is forced constant at its rated speed with sinusoidal excitation. Since there is no damping on the mechanical side in the simulation, the simulated torque ripples, which are 12.5% of the rated torque as shown in Figure 3.2 (b), can be considered reasonably small.

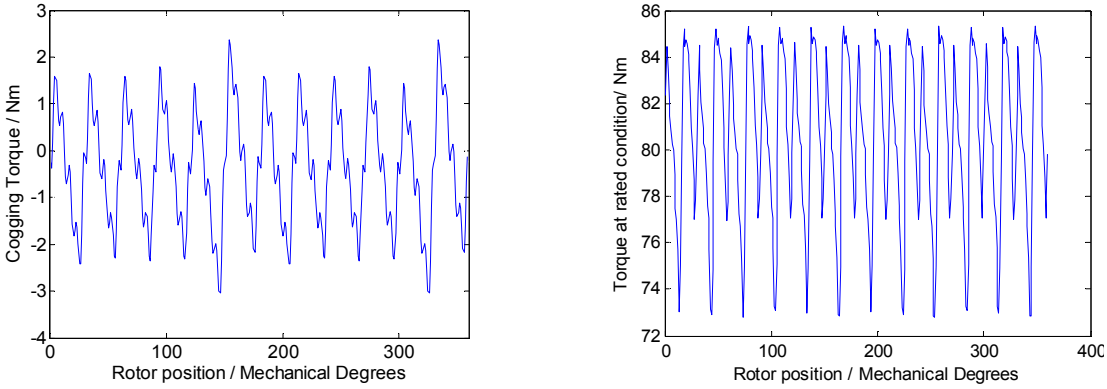

(a) (b)

Figure 3.2: FEA simulated cogging torque and torque ripples at rated condition
(a) Cogging torque (b) Torque ripples at rated condition with sinusoidal voltage excitation (Rated torque is 79.6 kW)

If lower cogging or ripple torque is desired for certain applications, detailed teeth shoe and tip shape designs are needed. Since the detailed teeth shoe and tip shape design generally do not have a significant impact on the overall machine performance, this

detailed design process may only be applied to the completed optimized machine and thus does not need to be included in the analytical design method.

3.2.3 Analytical design method

In this section, an analytical design method for SMPM machines is proposed. With certain design parameters as input, this analytical design method outputs a detailed design of a machine design trial, including the sizing of the machine (all the geometry parameters shown in Figure 3.3), the winding layout, and machine performance. Note that the machine geometry shown in Figure 3.3 is just for a specific slot type and slot number. Other slot types and slot numbers can be also included in the proposed analytical design method.

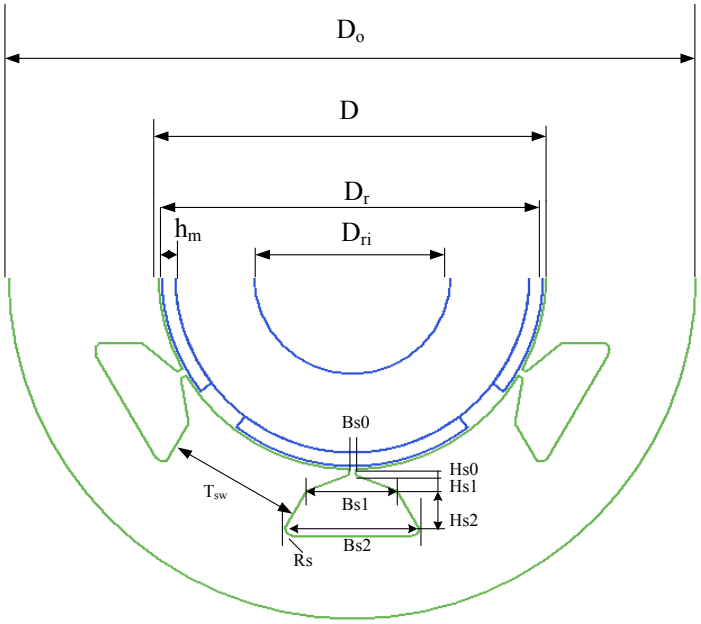

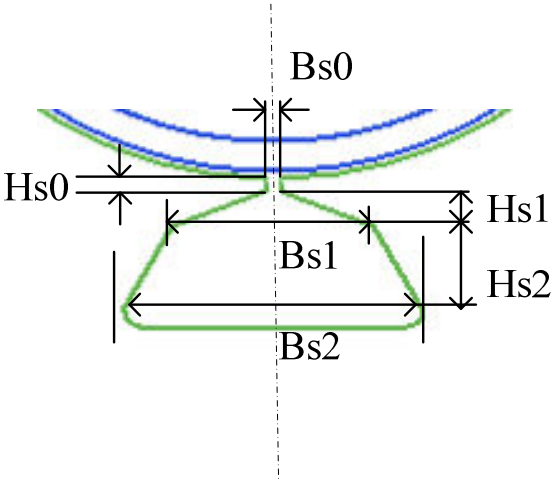

Figure 3.3: Definition of the SMPM machine geometry parameters

With the given stator bore diameter D, the machine active length L (axial stack length of stator lamination), the airgap length g, the magnet thickness, the α_p and the magnetization direction, the magnitudes of the B_n (n=1,3,5…) in (3.2) can be calculated based on the analytical equations provided in [43] as shown in (3.4)

$$B_{mag}(r,\theta)=\sum_{n=1,3,5,\ldots}^{\infty}B_n\cos(n\frac{p}{2}\theta)=\left(\sum_{n=1,3,5,\ldots}^{\infty}\frac{\mu_0 M_n}{\mu_r}\frac{n\frac{p}{2}}{(n\frac{p}{2})^2-1}R_m^{-(n\frac{p}{2}-1)}\right)$$
$$\cdot\left\{\frac{(n\frac{p}{2}-1)R_m^{np}+2R_r^{n\frac{p}{2}+1}R_m^{n\frac{p}{2}-1}-(n\frac{p}{2}+1)R_r^{np}}{\frac{\mu_r+1}{\mu_r}[R_{se}^{np}-R_r^{np}]-\frac{\mu_r-1}{\mu_r}[R_m^{np}-R_{se}^{np}(\frac{R_r}{R_{se}})^{np}]}\right\} \quad , \quad (3.4)$$
$$\cdot\left[r^{n\frac{p}{2}-1}+R_{se}^{np}r^{-(n\frac{p}{2}+1)}\right]\cos(n\frac{p}{2}\theta)$$

where $B_{mag}(r,\ \theta)$ is the flux density at point $(r,\ \theta)$ defined by the polar coordinates with center of the rotor to be the origin, p is the number of poles, n is the order in Fourier series of the flux density waveform. R_r and R_m are geometry parameters and their

definitions are shown in Figure 3.4. R_{se} is the effective stator inner radius considering the slotting effect and is expressed as [46]

$$R_{se} = R_s + (K_c - 1)g', \tag{3.5}$$

where g' is the effective airgap length and K_c is commonly referred to as Carter coefficient [8]. The effective airgap length g' is used to consider the MMF drop on the permanent magnet (relative permeability given by μ_r) and is expressed as:

$$g' = g + \frac{h_m}{\mu_r}. \tag{3.6}$$

To calculate the carter coefficient K_c, the slot opening B_{s0} is first determined. The choice of slot opening depends primarily on the manufacturing method of stator core, the winding method, and machine performance. A small value of B_{s0} leads to higher fundamental flux density, but at the same time increases the leakage flux. According to [9], past experience shows that B_{s0} is usually 2 to 3 mm for medium-sized machines (about 1 kW to 100 kW). After the value for B_{s0} is chosen, the carter coefficient K_c is derived as in [46]:

$$K_c = \frac{\tau_t}{\tau_t - \gamma g'}, \tag{3.7}$$

where

$$\gamma = \frac{4}{\pi}\left[\frac{B_{s0}}{2g'}\tan^{-1}\left(\frac{B_{s0}}{2g'}\right) - \ln\sqrt{1+\left(\frac{B_{s0}}{2g'}\right)^2}\right], \tag{3.8}$$

and

$$\tau_t = \frac{2\pi R_s}{N_s}. \tag{3.9}$$

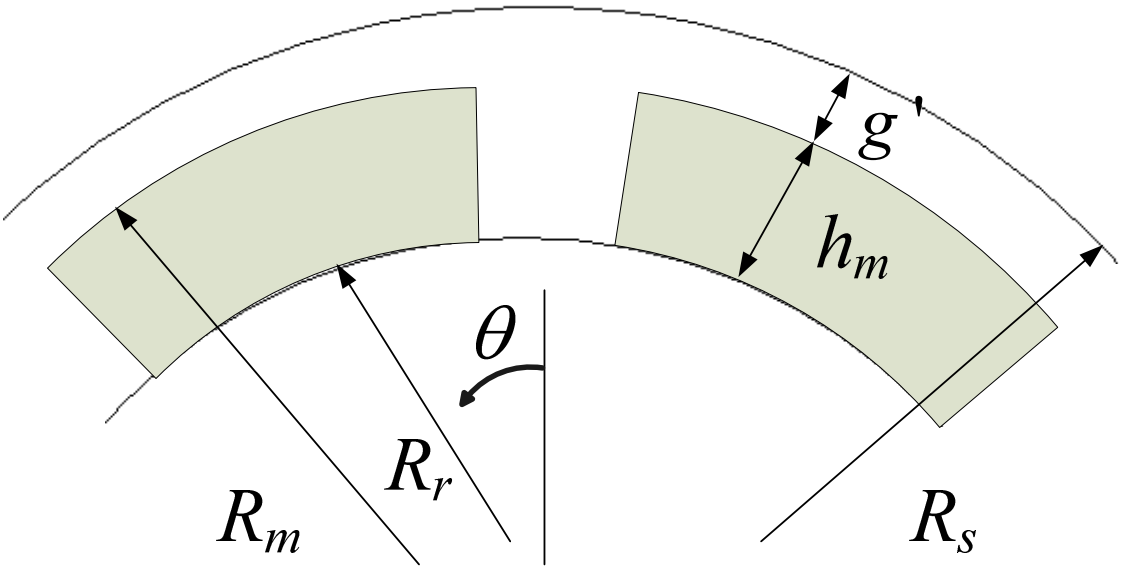

Figure 3.4: The definition of R_r, R_s, and R_m

M_n is the magnetization vector of the permanent magnet and is expressed as

$$M_n = M_{rn} + n\frac{p}{2}M_{\theta n}, \tag{3.10}$$

where M_{rn} is the radial component of the magnetization vector and $M_{\theta n}$ is the tangential component. For parallel magnetization, they are expressed [46] in (3.11)

$$\begin{aligned} M_{rn} &= \frac{B_r}{\mu_0}\alpha_p(A_{1n} + A_{2n}) \\ M_{\theta n} &= \frac{B_r}{\mu_0}\alpha_p(A_{1n} - A_{2n}) \end{aligned}, \tag{3.11}$$

where

$$A_{1n} = \frac{\sin[(n\frac{p}{2}+1)\alpha_p \frac{\pi}{p}]}{(n\frac{p}{2}+1)\alpha_p \frac{\pi}{p}}$$

$$A_{2n} = 1 \text{ for } n\frac{p}{2} = 1 \quad . \tag{3.12}$$

$$A_{2n} = \frac{\sin[(n\frac{p}{2}-1)\alpha_p \frac{\pi}{p}]}{(n\frac{p}{2}-1)\alpha_p \frac{\pi}{p}} \text{ for } n\frac{p}{2} \neq 1$$

For radial magnetization, they are expressed [46] in (3.13) as

$$M_{rn} = 2(\frac{B_r}{\mu_0})\alpha_p \frac{\sin(\frac{n\pi\alpha_p}{2})}{\frac{n\pi\alpha_p}{2}}. \tag{3.13}$$

$$M_{\theta n} = 0$$

When the rotor rotates at a speed ω_r, the rotating flux produced by the permanent magnet induces voltages in the stator winding, which is back EMF. Assuming all the flux produced by the permanent magnet is linked with a stator winding, the fundamental component of back EMF E_1 can be expressed by (3.14)

$$E_1 = 4.44 f N_c B_1 K_{w1} \frac{2}{\pi} \frac{\pi D}{p} L, \tag{3.14}$$

where N_c is the number of turns per phase and K_{w1} is the winding factor for the fundamental. The calculation of winding factor can be found in many textbooks, such as [8]. How to determine the value of N_c is explained later.

The overall effect of proper magnet design and the three phase winding leads to small magnitudes of harmonics and a dominant fundamental in the back EMF waveform. As a result, the calculation of output power can be approximated by only considering the fundamental of the back EMF. Therefore, assuming the PM machines are designed to be

inverter-driven and field-oriented control is applied, the machine output power can then be estimated as:

$$P_{out} = n_{phase} E_1 I_{ph} \tag{3.15}$$

where n_{phase} is the number of phases of the machine, I_{ph} is the RMS value of the winding current, and E_1 is the RMS value of the fundamental component of the back EMF. Since the output power is specified, the magnitude of the winding current I_{ph} is then computed by (3.15).

Since the SMPM machines and induction machines have the same type of stator structure and winding layout, the stator winding inductances for SMPM machines can be calculated similarly to induction machines. The armature reaction inductance L_m is calculated as [9]:

$$L_m = \frac{3}{\pi}\left(\frac{K_{w1} N_c}{p/2}\right)^2 \frac{\mu_0}{g' K_c} DL\,. \tag{3.16}$$

Because the SMPM machine has a large effective airgap, the differential leakage inductance is almost zero and can be neglected [9]. Hence, the stator leakage inductance L_{sl} only has two components: the slot leakage inductance L_{sls} and the end leakage inductance L_{sle}. The slot leakage inductance L_{sls} is expressed as [9]

$$L_{sls} = 2\mu_0 L \frac{N_c^{\,2}}{pq} \lambda_{sls}\,, \tag{3.17}$$

where q is the number of slots per pole per phase and λ_{sls} is

$$\lambda_{ls} = \left[\frac{2}{3}\frac{H_{s2}}{B_{s1}+B_{s2}} + 2\frac{H_{s1}}{B_{s0}+B_{s1}} + \frac{H_{s0}}{B_{s0}}\right]\frac{1+3\beta}{4} \tag{3.18}$$

where β is the ratio of coil pitch to pole pitch. The end winding leakage inductance L_{sle} is calculated as [47]

$$L_{sle} = \frac{1}{2} pq\mu_0 * (T_{sw} + \frac{B_{s1} + B_{s2}}{2}) * (\frac{3N_c}{N_s})^2 \log(\frac{(T_{sw} + \frac{B_{s1} + B_{s2}}{2})\sqrt{\pi}}{\sqrt{2A_s}}) \qquad (3.19)$$

where T_{sw} is the tooth width, N_s is the number of stator slots, and A_s is the stator slot area per slot. Although the exact slot size is unknown at this step, typical values of B_{s2}, A_s, and H_{s2} can be used at first. After the exact slot size is calculated in later steps, the correct values can then used to recalculate the inductance values. Since the armature reaction inductance is much larger than the leakage inductance, the error in the leakage inductance calculation caused by using the approximate values of B_{s2}, A_s, and H_{s2} do not affect machine performance calculation in a significant way. Hence, an iterative calculation for leakage inductance is not necessary.

When the machine rated voltage is specified, a phasor diagram at the rated operation condition of the SMPM machine is drawn as shown in Figure 3.5, assuming operation under field oriented control. In this phasor diagram, U is the applied voltage per phase to the machine and is known, R_{cu} is the armature resistance per phase, X_m and X_{sl} are the armature reactance and the leakage reactance per phase, respectively. The armature resistance R_{cu} is usually small compared to the armature reactance and thus can be neglected in this phasor diagram. Hence, the number of turns per phase is the only unknown in this phasor diagram and thus can be solved.

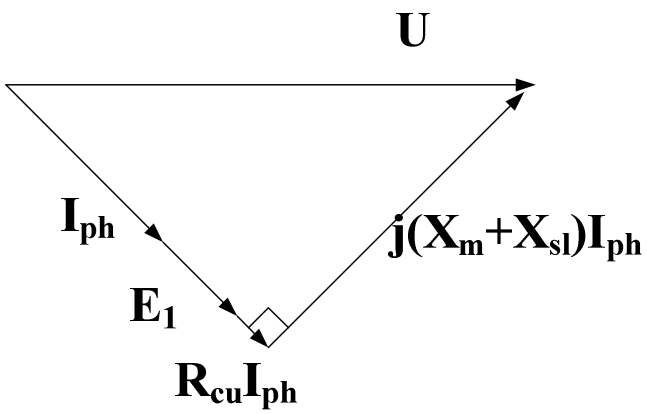

Figure 3.5: Phasor Diagram of the SMPM machine at the rated operation condition

If the machine is controlled by other methods or fed from other sources, equation (3.15) and the phasor diagram of Figure 3.5 may no longer be valid. However, the stator current can still be determined depending on how the machine is controlled. Once the relationship between the stator current and the number of stator winding turns is determined with respect to how the machine is controlled, the proposed design method can still work. For the Matlab code in the Appendix, only function *ampturn* needs to be modified when other control methods are used.

After the phase current is calculated, the copper wire area of a stator coil is found from

$$A_{cu} = \frac{I_{ph}}{J_s}. \tag{3.20}$$

where J_s is the coil current density. How to choose appropriate current density values is explained later when the thermal model is integrated with the electromagnetic design method. Right now a typical value between 4 and 7 A/mm^2 can be assumed.

The next design steps are to calculate the geometrical parameters as defined in Figure 3.3 for a typical stator slot shape. The airgap flux density is integrated along a pole to get the flux per pole Φ. When the flux densities in the stator core B_{sc} and rotor core B_{rc} are chosen, the stator core thickness T_{sc} and rotor core thickness T_{rc} can be calculated by:

$$T_{sc} = \frac{\Phi}{2B_{sc}Ll_f} \tag{3.21}$$

$$T_{rc} = \frac{\Phi}{2B_{rc}Ll_f} \tag{3.22}$$

where l_f is the lamination factor and is usually between 0.95 and 1. If the rotor of SMPM machines is not laminated, then l_f= 1. When the center line of a rotor pole is aligned with a stator tooth, the flux into this stator tooth reaches its maximum (denoted by Φ_{tm}). The stator tooth width can then be calculated based on the assumed stator tooth flux density (B_{st}) as:

$$T_{sw} = \frac{\Phi_{tm}}{B_{st}Ll_f}. \tag{3.23}$$

The stator tooth tip height H_{s0} and wedge angle α_1 are determined mostly by the manufacturing method and their typical values are given in [12] and listed in the Appendix I. By specifying a value for the slot fill factor f_f (typically 0.6 to 0.7 for bare wire slot fill factor), the slot area A_s needed to fit the stator coils can be calculated:

$$A_s = \frac{6N_cA_{cu}}{N_sf_f}. \tag{3.24}$$

Assuming parallel tooth sides, B_{s1} and B_{s2} can be estimated as:

$$B_{s1} = \frac{\pi(D + 2*(H_{s0} + H_{s1}))}{N_s} - T_{sw}, \tag{3.25}$$

$$B_{s2} = \frac{\pi(D + 2*(H_{s0} + H_{s1} + H_{s2}))}{N_s} - T_{sw}. \quad (3.26)$$

The area of the trapezoidal-shaped slot is expressed as:

$$A_s = \frac{B_{s1} + B_{s2}}{2} H_{s2}. \quad (3.27)$$

The values for H_{s2} and B_{s2} can be thus calculated from equations (3.25) to (3.27).

3.2.4 Performance calculation

After all the geometry and electrical design parameters are calculated, the machine performance is analyzed, including the weight, volume and efficiency.

3.2.4.1 Weight and volume

The weight of the machine is comprised of the active weight (the sum of the stator core, rotor core, magnets and the winding) and the inactive weight (primarily including the weight of machine frame, shaft and bearing). Since only the electromagnetic design is considered in this chapter, the weight considered in the design objective is only the active weight. The total weight of the machine is included in the design in later chapters. The volume is estimated by the cylinder with the same cross sectional area of the motor but larger axial length, due the extra space needed by the end windings.

3.2.4.2 Loss and efficiency

The copper loss P_{cop} is given by $3I^2R_{cu}$, where R_{cu} is the stator armature resistance per phase. For low frequencies, such as 60 Hz machines, the skin effect is not significant. Hence, the stator winding resistance (at 60 Hz) can be estimated as its dc resistance R_{dc} and given by:

$$R_{dc} = \rho_c \frac{l_c N_c}{A_{cu}} \tag{3.28}$$

where ρ_c is the resistivity of the wire at its operating temperature (the winding temperature at the machine rated condition can be used as an estimation), l_c is the length of one turn of the winding coils and includes the active part $2L$ and the end connection part $2l_{end}$

$$l_c = 2(L + l_{end}) \tag{3.29}$$

The end connection length depends on the coil pitch, shape of coils, number of layers in the winding, and also the manufacturing method. Machine manufacturers usually have developed their own equations or look-up tables based on their past experience [12]. In this work, a general estimation is developed by taking the average length of the end connection path for double-layer windings, as shown in Figure 3.6. The center line of the end connection path is shown in Figure 3.6 (a) and (b) and is modeled as a rectangular shown in Figure 3.6 (c).

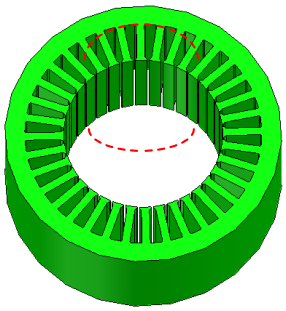

(a)

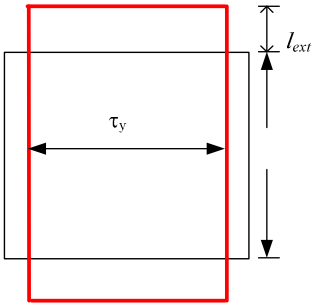

(c)

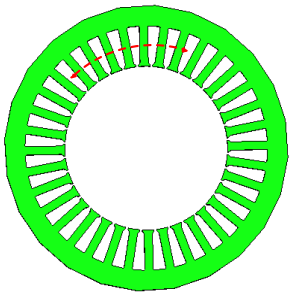

(b)

Figure 3.6: Illustration of coil length estimation

The average end connection length is thus given by

$$l_{end} = 2l_{ext} + \tau_y , \tag{3.30}$$

where l_{ext} is the coil-end extension length and is a value generally between 10 and 30 mm, depending on machine size [12]. τ_y is the coil pitch in mm and given by

$$\tau_y = \frac{\pi(D + 2(H_{s0} + H_{s1}) + H_{s2}))}{p}\beta , \tag{3.31}$$

where β is the short pitch ratio. For example, if the coil pitch is 7 slots and the pole pitch is 9 slots, then β=7/9.

For higher frequencies or more accurate copper loss calculation, the stator winding ac resistance, R_{ac}, is calculated as suggested by [48]:

$$R_{ac} = R_{dc}\frac{\xi}{2}\frac{\sinh\xi + \sin\xi}{\cosh\xi + \cos\xi}(1 + \sum_{m=1,2..}\frac{2}{3}(m^2 - 1)) \tag{3.32}$$

where m is the coil layer number and its definition is illustrated in Figure 3.7. The conductor layers are modeled as continuous conductor foils, which fill the full core-window breadth, and the conductor foil has the same equivalent dc resistance of the

round conductors[48]. ξ is the thickness of the conductor foil normalized with respect to the skin depth δ and is given by

$$\xi = \frac{\sqrt{A_{cu}}}{4\delta}, \tag{3.33}$$

The skin depth δ is given by

$$\delta = \frac{1}{\sqrt{\pi \mu_0 \mu_{rc} \sigma f}} \tag{3.34}$$

where μ_{rc} is relative permeability of the conductor material (μ_{rc} = 1 for copper) and σ is conductor conductivity.

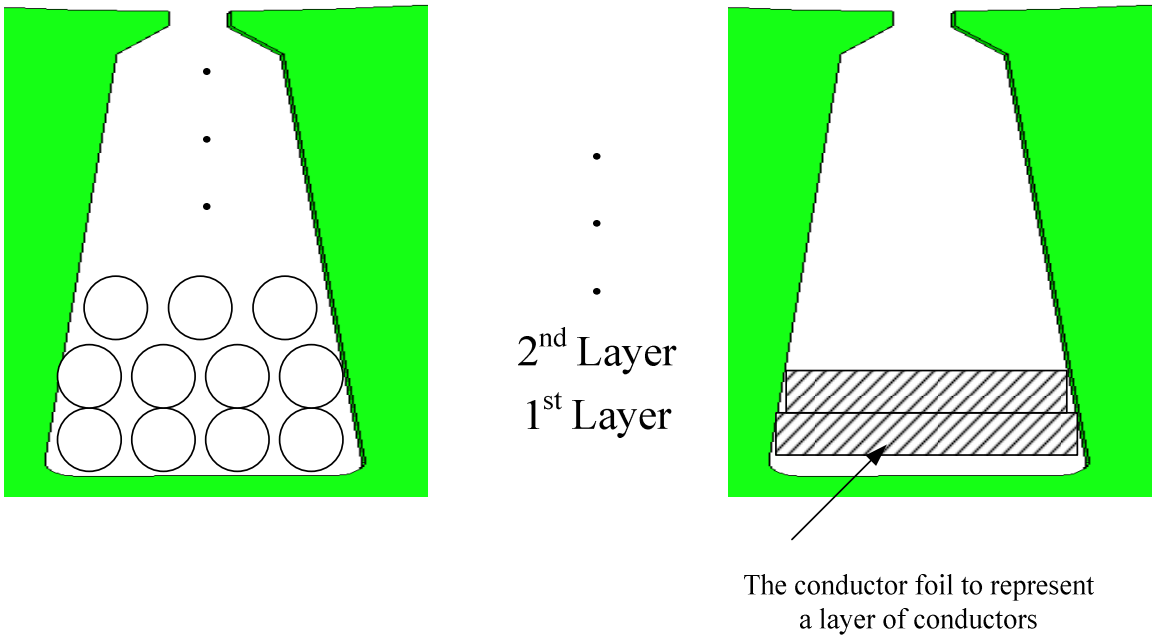

Figure 3.7: Illustration of layer number definition in ac resistance calculation

The core loss P_{core} can be estimated by using the material loss curve from the data sheet given by the supplier. A typical core loss curve is shown in Figure 3.8 for Hiperco 50[49]. In the rotor of SMPM machines, the flux produced by the magnet does not induce core loss. At steady state, the armature reaction field rotates synchronously with the rotor

and hence does not induce rotor core loss either. As a result, only the harmonic armature reaction field induces core loss in the rotor. Since this harmonic armature reaction field is small in the rotor due to the large relative airgap of SMPM machines, the rotor core loss can be neglected for low and medium speed machines.

For the stator core loss, since the harmonics in airgap flux density is reduced by proper selection of magnet pole coverage and magnetization as described in 3.2.2, the fundamental component of airgap flux is the dominating component for stator core loss. Based on the machine operating frequency f, stator teeth flux density B_{st}, and stator core flux density B_{sc}, the core loss density in the stator teeth and core can be found from the core loss curve. Due to mechanical machining (stamping value depends on the quality of the material, sharpness of the cutting tools, etc.), the steel core loss density after manufacturing may be increase from its catalog data by a factor of the so-called core loss augmentation p_{aug}[9]. A typical value of p_{aug} according to [9] is between 1.6 to 1.8.

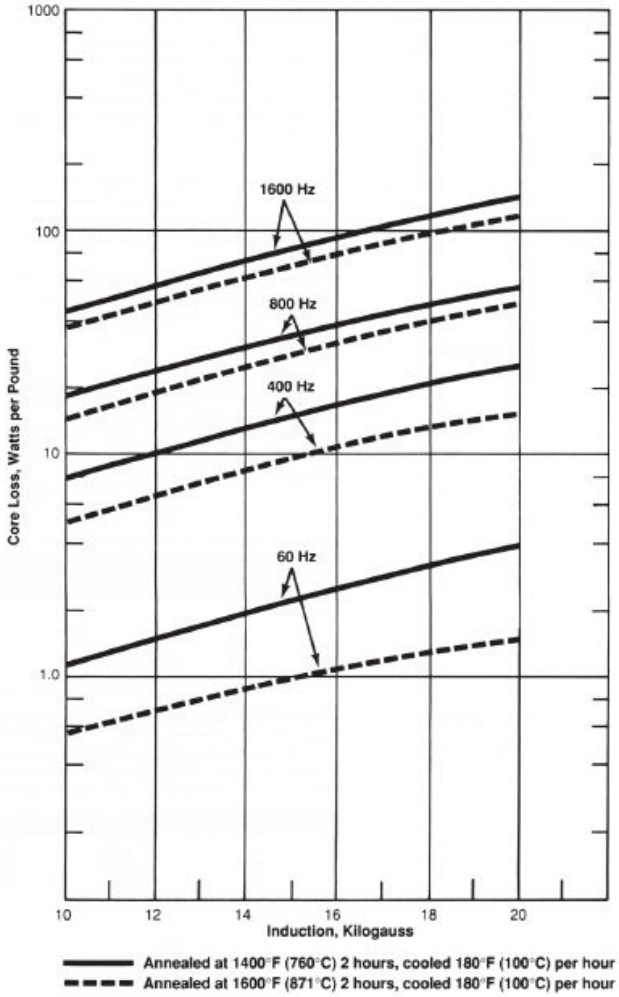

Figure 3.8: A typical core loss curve for Hiperco 50 Alloy with 0.15 mm thickness [49]

With an estimated value of windage and friction loss P_{wf} (1% of total output power, for example), the efficiency can then be calculated as (3.35)

$$eff = \frac{P_{out}}{P_{out} + P_{core} + P_{cu} + P_{wf}} \tag{3.35}$$

3.2.5 Effect of armature reaction

Due to the large effective airgap of the SMPM machine, the armature reaction magnetic field is usually small. However, SMPM machine designs with small magnet thicknesses sometimes may have unexpected performances due to their larger armature reaction magnetic field. In developing design optimization algorithms, a good accuracy of the analytical design method is desired throughout the whole solution space, but the use of the time-consuming FEA should be minimized. Hence, it is necessary to consider and include designs with small magnet thicknesses in the analytical design method for optimization purpose.

When the magnet thickness is small, the effective airgap length is small and the average airgap flux density is also small, which means more stator current is needed to produce the rated torque. As a result of the larger stator current MMF and smaller effective airgap, a significantly larger armature reaction magnetic field is induced. This higher armature reaction magnetic field may cause two unexpected problems: the risk of demagnetization and the unexpected saturation in the stator teeth, stator yoke and the rotor yoke. Demagnetization damages the permanent magnets and should be avoided under all machine operation conditions. Saturation of the magnetic circuits significantly increases the current needed to produce the rated torque and should also be avoided.

3.2.5.1 Consideration of saturation

The higher armature reaction magnetic field may cause unexpected saturation in the stator teeth, stator yoke and the rotor yoke, and will significantly increase the current needed to produce the rated torque. If this phenomenon is neglected, it will cause a large difference between the predicted and the actual machine performance for a SMPM motor

with a small magnet thickness. Table 3.1 contains parameters of two example designs, one with a magnet thickness of 3.5 mm and the other with a thickness of 5.38 mm. The resultant phase current at the rated output torque in the small airgap machine, calculated by (3.15), is compared with the one obtained from a FEA solution and it shows a significant error.

Table 3.1: Comparison of two designs of the 15 kW, 1800 rpm, 60 Hz SMPM motor

	D(mm)	L(mm)	h_m(mm)	Stator Current/ A	
				Proposed method	FEA
Des. 1	74.2	143.2	3.5	38.0	58.1
Des. 2	80	121.2	5.38	32.4	34.0

Reference [50] provides an accurate analytical calculation of the airgap magnetic field produced by the armature reaction and its good accuracy is shown by comparison with FEA. Instead of using the complicated nonlinear sum of two field solutions, an alternative solution is used. The linear sum of the magnetic fields produced by the permanent magnets and the armature winding are calculated to determine the maximum flux density value in the stator teeth (B_{stm}), stator core (B_{scm}) and rotor core (B_{rcm}) under certain load conditions. These values should not exceed a certain level ($B_{stm,th}$, $B_{scm,th}$, and $B_{rcm,th}$ respectively) based on the property of steel used for the machine. With the B-H curve of steel chosen for the stator teeth and back iron, it is not difficult to evaluate whether saturation occurs under certain load conditions using this approach. For non-oriented silicon steels, 1.6 T can be used as typical values for $B_{stm,th}$, $B_{scm,th}$, and $B_{rcm,th}$. This is formally defined in (3.36)

$$\begin{aligned} B_{stm} &< B_{tm,th} \\ B_{scm} &< B_{scm,th} \\ B_{rcm} &< B_{rcm,th} \end{aligned} \quad . \tag{3.36}$$

3.2.5.2 Magnet protection

A typical demagnetization characteristic for the NdFeB magnet material (NdFeB/N3575) appears in Figure 3.9[51]. The B-H curve is linear and repeatable for negative values of field intensity H up to the value H_d at which point the magnetic polarization vector M collapses [8]. The corresponding value of flux density is B_d. Both B_d and H_d are temperature-dependent.

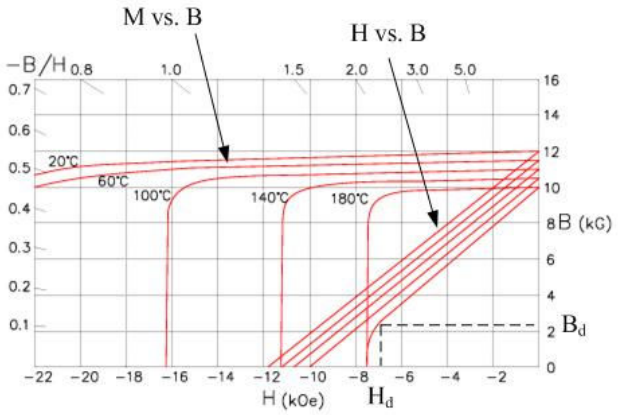

Figure 3.9: Demagnetization characteristic of NdFeB / N3575 [51]

(1 T = 10 kG, 1 kA/m = 79.577472 kOe)

To protect the permanent magnet from demagnetization, it must be protected against reverse fields exceeding the value H_d. For normal steady state operation, the maximum permitted value of steady state stator current before the reverse field exceeds H_d is derived in [8] and given by

$$I_{dgmr} \le I_{dgmrm} = \frac{p\pi}{6\mu_0 (K_{w1} N_c)} (B_r h_m - B_d (g + h_m)) , \tag{3.37}$$

where p is the number of stator poles, K_{w1} is the winding factor for the fundamental, N_c is the number of turns per phase, g is the air gap length in m and B_r is the residual flux density in Tesla at the operating temperature of the magnet.

In addition, the magnet should be protected against a possible short circuit of the stator terminals [52]. During a three phase short circuit, the peak stator current should not exceed I_{dgmr}. When a short circuit happens, the rotating permanent magnets continue to induce a normal voltage in the stator and the stator current is only limited by primarily the leakage inductance and the armature resistance. Hence, the leakage inductance should be designed to be large enough to limit the stator current. As described in [52], the necessary leakage inductance L_{lsn} to protect the magnet from damage is given by

$$\frac{L_{lsn}}{L_m} \geq K_{lmrm} = \left(\frac{\frac{8}{\pi} B_r h_m * \alpha_p}{B_r h_m - B_d g'} \right) - 1 \tag{3.38}$$

3.2.6 Flowchart of analytical design method

A flowchart is drawn to summarize the design steps of the proposed analytical design method, as shown in Figure 3.10. The input variables to this flowchart (called "design specification variables" in this work) for the design of SMPM machines are summarized as follows (values do not change during optimization):

1. The rated speed, rated frequency, output power, and applied voltage. These variables define the machine operating condition and are specified by the designers.
2. Current density J_s, flux densities (B_{st}, B_{sc}, B_{rc}), and slot fill factor. These values depend on the limitations of materials and manufacturing capabilities.

3. Slot number and winding configurations. How to select slot number and define proper winding configurations for SMPM machines are explained in greater detail in Chapter 4 and are selected by the designer.
4. Permanent magnet material properties (demagnetization curve, mass density), pole coverage, and magnetization.
5. Airgap length, slot opening, slot wedge width and depth. These values depend mostly on the manufacturing methods. Typical values can be found in [8-9].
6. Steel material properties, which include B-H curve, lamination factor, core loss curve, and mass density. Values are obtained from manufacturer's datasheet.
7. Coil properties, which include conductor resistivity at certain operating temperature, conductor mass density, wire insulation thickness and slot liner thickness. Values are obtained from manufacturer's datasheet.

After the values of the design specification variables are selected, for each combination of three design variables D, L and h_m (called "prime design variables" in this work), a SMPM machine is designed by running this flowchart. The values of the three prime design variables do not need to be selected by the designer, but to be found by the optimization algorithm in this research. Each arrow in Figure 3.10 indicates an equation as described in previous sections. With the input of design specification variables that represent the design specifications and constraints, only three parameters (the three prime design variables) are needed to represent a candidate machine design; other machine design parameters are calculated by running this flowchart. At the end of the flowchart, the machine performances and the saturation level under certain load condition are calculated.

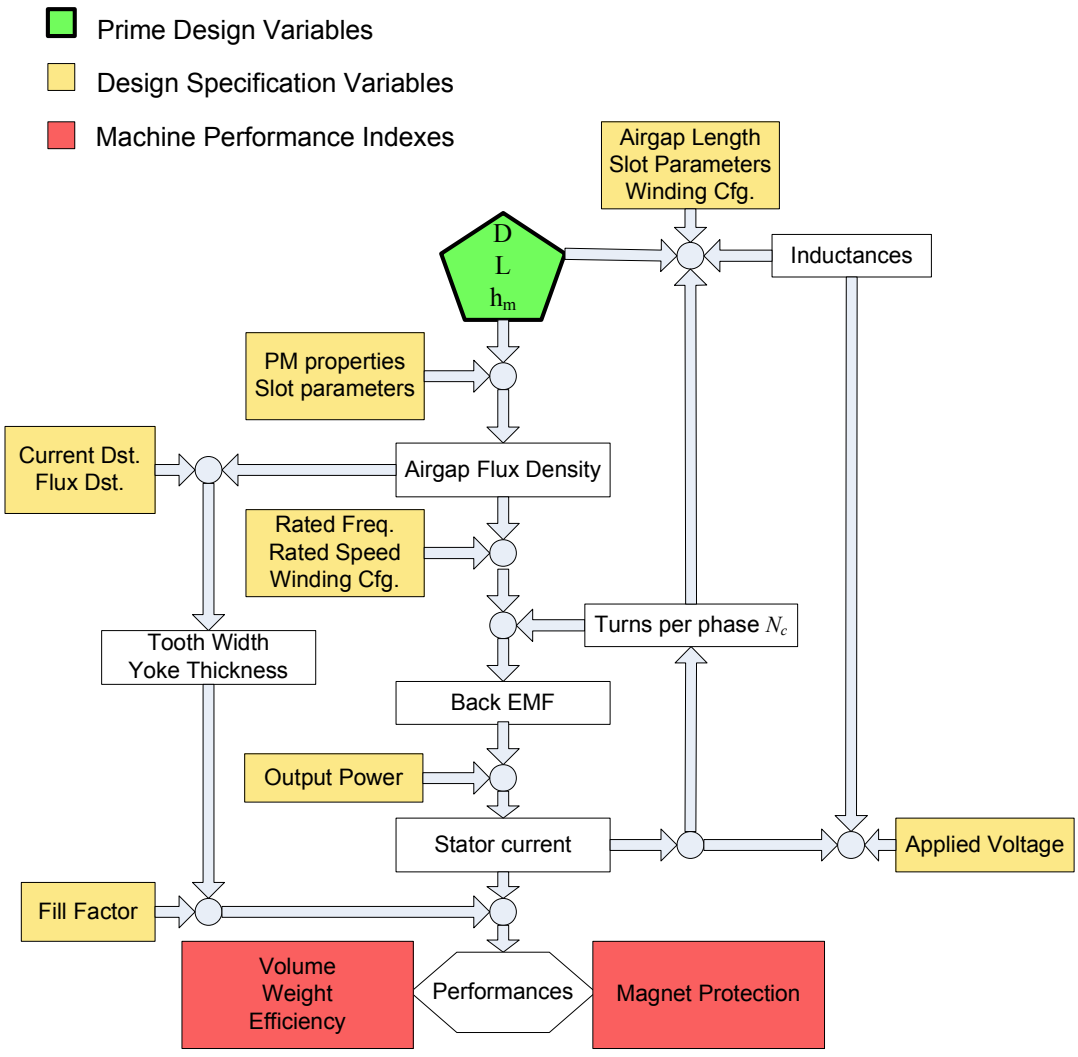

Figure 3.10: Flowchart of the SMPM analytical design method

The proposed SMPM design method is comprised of two stages. The first stage is the magnetic design, where the cogging and ripple torque is minimized by proper choice of magnet pole coverage, the magnetization and the stator tooth tip. The second stage is to run the flowchart in Figure 3.10 to generate machine design prototypes and calculate the machine performances. Because the analysis and conclusion in the first design stage generally does not change much for different machine diameters and lengths, the

optimization only needs to start from stage 2 and the goal is to find the optimal combination of the D, L and h_m which will give a machine design prototype subject to the constraints and specifications. FEA analysis is thus only required for the optimal prototype from the analytical design for the purpose of verification or fine tuning.

In some situations, the machine rated voltage is not specified but needs to be selected by the designer. The number of stator turns per phase N_c is now treated as another prime design variable. With the number of turns selected, the excitation voltage and phase current are calculated using the phasor diagram in Figure 3.5 and their feasibility are checked against design constraints, which includes the capability of the power source, the ratings of available power electronic devices, the ratings of insulation materials, safety concerns, cost, and other practical considerations.

3.2.7 Accuracy of analytical design method

A typical 15 kW, 1800 rpm and 60 Hz SMPM machine design without severe saturation is simulated under no load and rated condition to illustrate the actual performance of the motor using FEA. For FEA simulation under no load, zero stator current is imposed and the rotor is set to rotate at the rated speed. For rated condition, the rated voltage (480 V) is applied to the three phase stator winding, a constant rated speed is applied to the rotor, and the machine then reaches a steady state condition after certain numerical and electrical transients.

The analytical calculation of airgap flux density produced by permanent magnet (equations (3.4) to (3.13)) is compared with FEA in Figure 3.11. The result shows that the analytical calculation has good agreement with FEA.

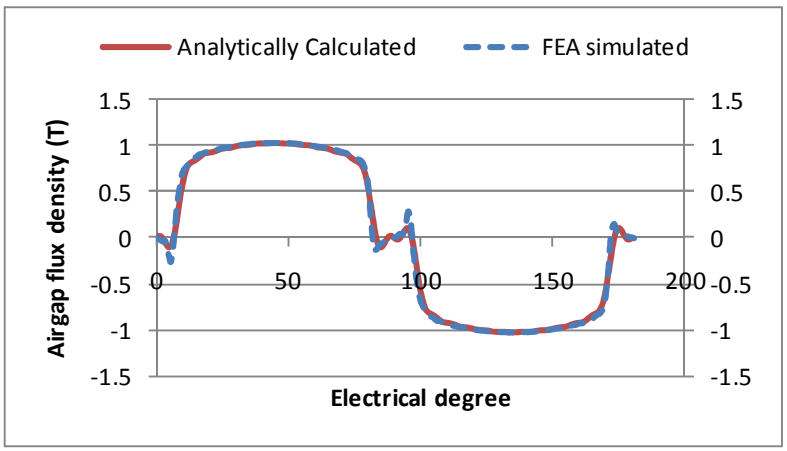

Figure 3.11: Comparison of airgap flux density calculation by analytical design method and FEA

The flux densities calculated by FEA are plotted in Figure 3.12 for both no load and full load operating conditions. The flux densities in stator teeth, stator core and rotor core are specified to be 1.45 T in the analytical design method and FEA result shows that this flux density specification is achieved correctly. The flux lines in Figure 3.12 show that nearly all the permanent magnet flux enters the stator and links with the stator. Hence, it is valid to assume negligible leakage permanent magnet flux and to use (3.14) to calculate back EMF.

The FEA simulation result also shows that the assumption of no leakage flux is valid for this design. Leakage flux indicates that there are flux lines that goes out from one magnet, enters the stator tooth, but goes back to another magnet without coupling with the winding. In Figure 3.12, no such flux lines are observed, which means the leakage flux is negligible.

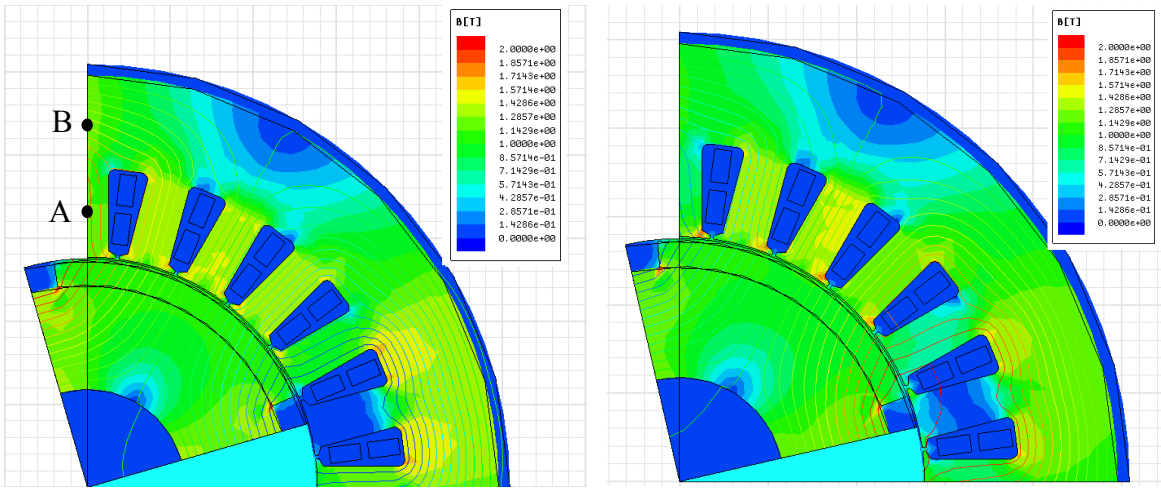

(a) No load (b) Full load

Figure 3.12: Plot of flux densities calculated by FEA at (a) no load and (b) full load operating condition

A comparison of calculating the phase current and the output torque by the analytical design method and the FEA is shown in Figure 3.13. Notice that the analytical design method only considers the fundamental thus the resulting torque has a constant value. However, the average torque by the FEA and the analytical design method agrees with each other as shown in Figure 3.13 (b). Figure 3.13 (a) shows the good accuracy of predicting the phase current by the analytical design method. With the phase current calculation verified, the copper loss calculation is expected to also have good accuracy compared to FEA. The normalized current calculation difference between the analytical design method and FEA with respect to the peak of the FEA calculated stator current as the reference is plotted in Figure 3.13 (c). In the analytical design model, only the fundament component of the stator current is calculated. On the hand, harmonics are

calculated in FEA, which is the major source for the differences between the analytical and FEA result.

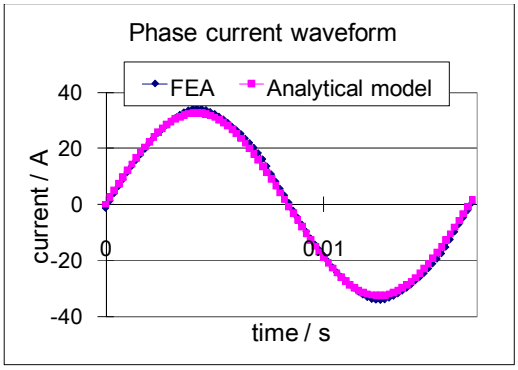

(a)

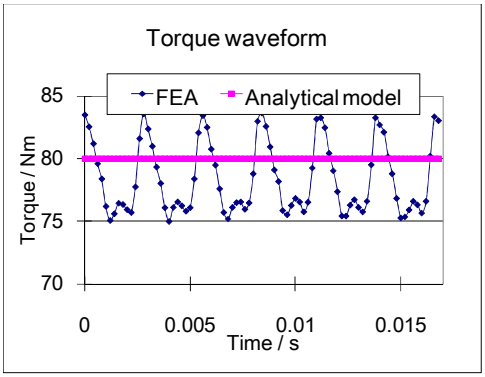

(b)

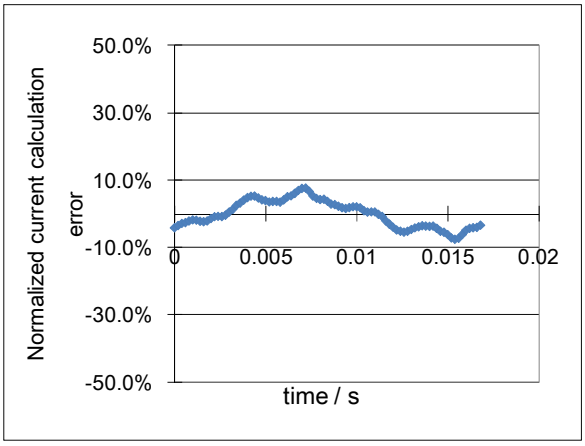

(c)

Figure 3.13: FEA result of a typical design of the 15 kW, 1800 rpm motor by the analytical design method (a) Phase current waveform at rated condition (b) Output torque waveform at rated condition (c) Difference between analytically calculated stator current and FEA simulated stator current normalized to the peak of the FEA simulated current

The flux density waveforms in stator teeth and core are also plotted for verification of core loss calculation. As seen in Figure 3.12, the flux densities in the stator teeth and

core are not exactly evenly distributed across the whole stator region. It would be impossible to plot the flux density waveform for each point in the stator. For stator teeth, as seen Figure 3.12, the flux densities are almost evenly distributed except for some small regions in the tooth root and tip. Hence, the flux density at point A, the center of a stator tooth, can be used to represent the stator teeth flux density. Similarly, the flux density at point B is used to represent the stator core flux density. The flux densities at points A and B as a function of time when the machine is running at (a) no load and (b) rated load condition, are shown in Figure 3.14 and Figure 3.15, respectively. The FEA results shows that both the flux density at stator teeth and core are nearly sinusoidal with a peak value close to the design specified value of 1.45 T, especially for rated conditions. Hence, the core loss calculation in the analytical design method is expected to have good accuracy compared to FEA.

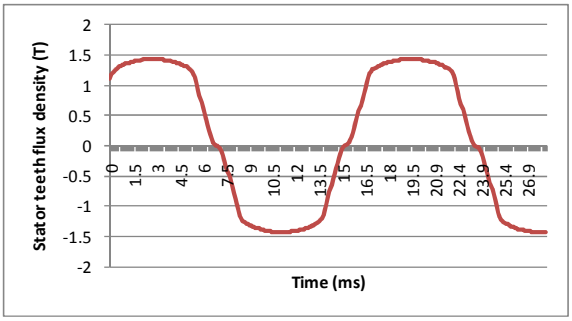

(c) No load

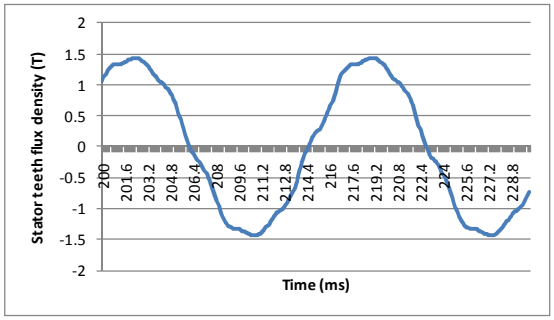

(d) Full load

Figure 3.14: Flux density waveform in stator teeth (point A) calculated by FEA at (a) no load and (b) full load operating condition

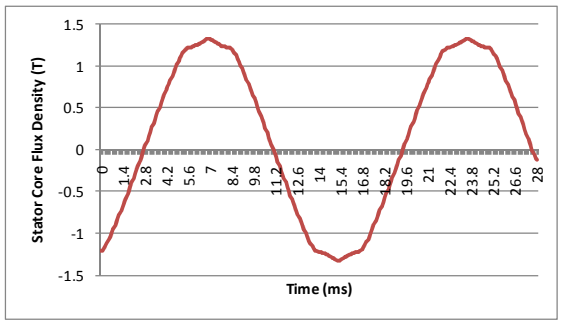

(e) No load

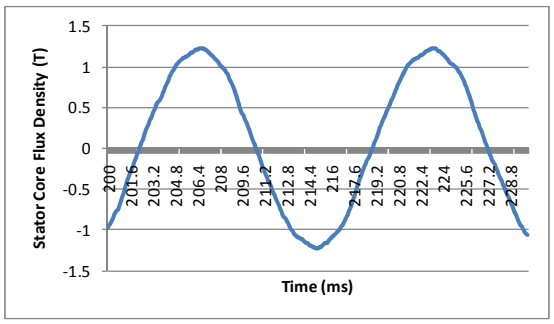

(f) Full load

Figure 3.15: Flux density waveform in stator core (point B) calculated by FEA at (a) no load and (b) full load operating condition

As described above, the analytical design method has good accuracy in the calculation of output torque, copper loss, and core loss. The analytical performance calculation, including efficiency, torque per ampere, and power factor, can thus be expected to have good accuracy as well. By using the proposed analytical design method, most of the computation time can be saved with no sacrifice of accuracy.

Table 3.2: Summary of accuracy of the proposed design method

	Analytical	FEA	Difference normalized with respect to FEA
Peak stator current	32.6 A	34.2 A	-4.68 %
Average torque	80 Nm	77 Nm	3.9 %
Peak flux density in stator tooth	1.45 T	1.48 T	-2.03 %
Peak flux density in stator core	1.45 T	1.35 T	7.41 %

3.2.8 Summary of assumptions in the proposed method

1. Assumption of infinite permeability in the steel. In SMPM machines, the permeability of the permanent magnet is close to that for air, which leads to a large airgap consisting of the physical airgap plus the thickness of the magnet. Hence, most of the MMF appears across the airgap and the MMF across the steel is negligible unless there is severe saturation somewhere in the steel. However, as described in section 3.2.5.1, severe saturation is avoided in the proposed design method. To have an accurate evaluation of the MMF across the steel, a FEA is necessary.
2. Assumption of no leakage flux. As observed earlier, this assumption is valid for the SMPM machines designed in this research with a pole coverage coefficient of 0.83. With a higher value of pole coverage coefficient, the leakage flux may increase but it means inefficient use of the permanent magnet and is to be avoided. Furthermore, the leakage flux can only be accurately evaluated by a FEA. Hence, in the analytical design and optimization stage, it is practical to assume no leakage flux and this assumption can be validated later by FEA only for the optimized design.
3. Assumption of field-oriented-control. An assumption of control method has to be made in order to calculate the value of stator current for certain speed and torque conditions. The assumption of field-oriented-control is made on the basis that it is a widely-used control method for SMPM machines. If the machine is controlled by other methods or fed from other sources, equation (3.15) and the phasor diagram of Figure 3.5 may no longer be applicable. However, the stator

current can be still determined depending on how the machine is controlled. Once the relationship between the stator current and the number of stator winding turns is determined with respect to how the machine is controlled, the proposed design method can still work. For the Matlab code in the Appendix, only function *ampturn* needs to be modified for other control methods.

3.3 PSO based design optimization

In the analytical design method as indicated in Figure 3.10, the number of turns per phase is obtained by solving phasor diagrams with numerical methods and it is difficult to get a solution in direct analytical form. Furthermore, this method is actually a hybrid nonlinear method of continuous and discrete variables because the number of turns can only be integer and the wire size needs to be one of the standard AWG sizes. The above reasons make it impossible to calculate the gradient, which is essential in traditional nonlinear optimizing techniques, such as the Newton method [53], and computational techniques are therefore required. Particle Swarm Optimization (PSO)[10] is proposed and applied in this design optimization and is effective in solving such problems as hybrid methods.

3.3.1 Objective function

Before the optimization algorithm is run, the objective function needs to be defined, as in (3.39). To account for various requirements in the permanent magnet motor design, the objective functions used here have five performance indexes, namely: volume (m^3), weight (kg), efficiency (0-100%), weight of the magnets (kg) and the torque per ampere at the rated condition (Nm/Arms). For the machines to be designed, the weight, volume, efficiency, torque/ampere and magnet weight have typical values that range around 20-50

kg, 0.002-0.005 m^3, 0.5-1, 2-5 Nm/Arms and 0.5-2 kg, respectively. Each term in the objective function in (3.39) is thus first normalized to have about the same magnitude, and then the weighting factors or coefficients before each index are further tuned to represent how much importance is attached to a particular index. One example of such an objective function, called *output*, is defined in (3.39), as

$$output = Volume*10000 + Weight + (1 - Eff)*1000 + WtMgt*2 - TperA*10 \quad (3.39)$$

3.3.2 Introduction of the Particle Swarm Optimization (PSO)

PSO is an evolutionary computation technique developed in 1995 by Kennedy and Eberhart [10] and the procedures are as summarized by the following steps:

1) Define the solution space: select the parameters that need to be optimized and select the number of particles. Here, the parameters are D, L and h_m.
2) Define a fitness function, which is the objective function defined in (3.39).
3) Initialize Random Swarm Location and Velocities.
4) Systematically "fly" the particles through the solution space: The following steps are performed on each particle individually:
   a) Evaluate particle fitness: compare to "global best" (g_{best}) and "personal best" (p_{best}).
   b) Update the particles' velocity according to the relative values of p_{best} and g_{best}, using the following expression:

$$v_n = \omega * v_n + c_1 rand() * (p_{best,n} - x_n) + c_2 rand() * (g_{best,n} - x_n) \quad (3.40)$$

5) Move the particle: The velocity is applied for a given time-step Δt, which is usually chosen to be 1, and the position is updated to

$$x_n = x_n + \Delta t * v_n \tag{3.41}$$

6) Repeat process starting at step 4). In this way each particle moves for discrete time intervals until the termination criteria are met.

3.3.3 PSO implementation

Six particles are used by the PSO algorithm to search for the combination of all the Performance Indexes (PIs) which yield a minimum value of *output* (objective function, such as (3.39)), and each particle is a 3-dimensional vector of the three input variables: D, L and h_m. Each particle therefore represents a candidate or trial design of the SMPM motor which is then evaluated by the objective function *output*. The evaluations of the magnetic saturation in the stator teeth and back iron as described in earlier sections are added in the PSO program as constraints. When the flux density of a particular design exceeds a certain threshold, a large penalty function is added to its objective function in order to signal to all particles that this design is a poor candidate and drive them away from this point in the solution space [54]. The flux density threshold that triggers the penalty function depends on the B-H curve of the steel used for the core material. A typical penalty function and a typical B-H curve of non-oriented steel are shown in Figure 3.16. Figure 3.17 shows how the 6 particles start from random positions in Figure 3.17 (a) and after 100 iterations all converge to the correct optimal solution in Figure 3.17 (d).

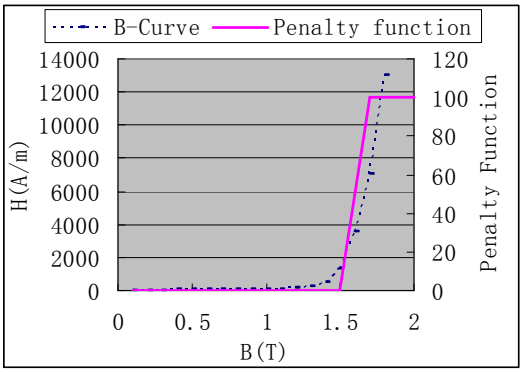

Figure 3.16: A typical penalty function and silicon steel B-H curve for designs with flux density saturation

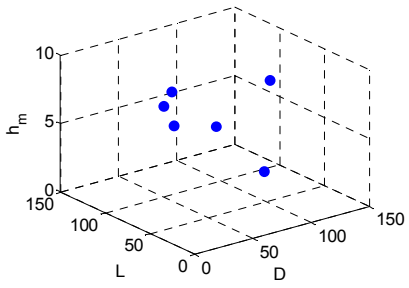

(a) *N*=0, min(*output*)=171.2

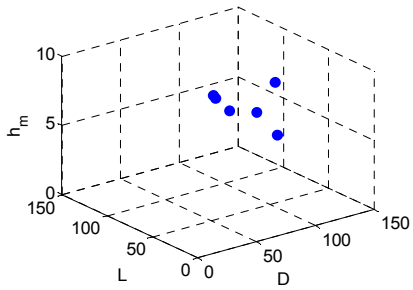

(b)*N*=32, min(*output*)=82.3

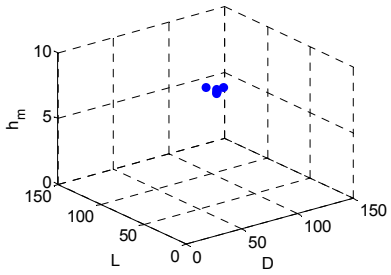

(c) *N*=75, min(*output*)=78.2

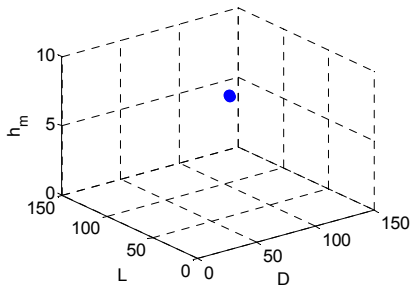

(d) *N*=100,min(*output*)=78.2

Figure 3.17: Particle positions as iteration *N* increases

3.3.4 Design optimization result

After running the PSO several times, a series of solutions are found that differ slightly from one another and have approximately the same optimal objective function

value. Data for a selection of two typical solutions appear in Table 3.3. The first three rows in the table contain the values for the final choices of the three input variables D, L and h_m; the next five rows are the PI values, and the final row is the value of the objective function. This all shows that the previous design 1 in Table 3.1 with the very thin 3.5 mm magnet, has been eliminated and does not appear as one of the optimal solutions due to the saturation as described earlier.

Table 3.3 shows that there are different combinations of the three input variables D, L and h_m that yield near-optimal solutions, and each of the performance indexes fall into certain ranges. For example, the weight is around 30-40 kg, the volume is around 0.0047 m^3 and the efficiency is about 95.6 % for the two designs.

Table 3.3: Optimal design found by PSO

	Design A	**Design B**
***D* (mm)**	112	70.5
***L* (mm)**	90.7	154.6
h_m (mm)	5.6	5.3
Weight (kg)	36.5	31.6
Volume (m^3)	0.0047	0.0048
Efficiency	95.7%	95.6%
Torque per Ampere (Nm/A)	3.8	3.5
Magnetic weight (kg)	1.02	1.0
***Output* (equation (3.39))**	91.2	90.9

Another important merit of this method is time-saving. The analytical method is much faster than FEA and PSO is also a fast and efficient optimization method. Running

one PSO with 100 iterations and 6 particles (trying to evaluate 600 potential designs) takes no more than 30 seconds on an ordinary desktop computer.

This design optimization program can also be adjusted to fit different requirements. For example, if less weight is the most important target, the objective function can be defined to contain only the weight, with other performance indexes to be in the constraints, together with the saturation level. In this case, only the penalty function needs to be redefined to include more constraints. Furthermore, more performance indexes, such as the price of the motor, can be added to the objective function to include more design requirements.

3.4 Chapter summary

In this chapter, an analytical design method of SMPM machines with good accuracy and considerations of the nonlinearity in the material is developed. PSO is applied to find the optimal solutions with respect to a certain user defined objective function. The advantage with this proposed analytical design method and PSO optimization is that the heuristic selection of the design variables, including the electric loading, magnetic loading and aspect ratio, are no longer necessary. The computing time is almost negligible. The results will provide useful insight for the drive system designers or the machine designers at the initial design stage.

CHAPTER 4

Comparison of the Distributed and Concentrated Winding for Surface Mount Permanent Magnet Machines

4.1 Introduction

Recently there has been a growing interest in PM motors with concentrated windings, mainly due to low cost of manufacture. However, these designs give rise to harmonics and torque ripple. In certain applications this may be acceptable, but in others not. Comparisons of the SMPM motors with distributed windings (Fig 1(b)) and concentrated windings (Fig 1(a)) have been reported either by designing two motors with exactly the same rotors [55], or by qualitative analysis [56]. However, the design of PM machines, as in the case of any machine, is an area where suitable results can be obtained with an almost infinite number of combinations of design parameters, and depending on such factors as the intended application, different designs could be generated. A fast, efficient and comprehensive analysis tool of the two winding types, and with optimization in terms of the user's requirements, is therefore a more useful tool for a machine designer, particularly for initial designs.

In this chapter, the design optimization method for SMPM machines with a distributed winding as described in Chapter 3, is first adapted for the concentrated winding SMPM. Optimization results are then compared between machines with distributed winding and concentrated windings. The example machine designs have the same rated condition: 15 kW, 60 Hz and 1800 rpm. The merits and disadvantages of the two winding types can thus be comprehensively understood from the quantitative comparison of results.

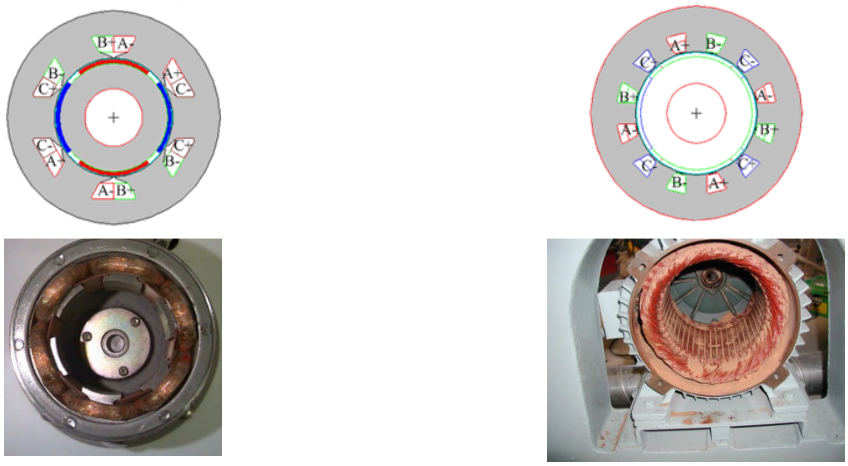

(a) (b)

Figure 4.1: Illustration of the (a) Concentrated Winding (CW) and (b) Distributed Winding (DW)

4.2 Introduction of the concentrated winding (CW) for PM machines

As seen in Figure 4.1, a coil is wound around one wide tooth in a CW machine, which features a modular manufacturing process. Each *tooth module*, comprised of a stator tooth and the coil wound around the tooth, is manufactured separately. When the stator core is manufactured, the tooth modules are inserted into the core. This modular design significantly simplifies the winding process and a copper slot fill factor as high as 65% can be achieved. In addition, if there is an insulation failure, the machine can be simply repaired by replacing the faulty module.

Since the coil span is only one slot pitch, the end winding length is short and the resulting stator armature resistance is relatively small. On the other hand, the CW may have a lower winding factor than the DW machine because the DW machine can be either full-pitched or short-pitched, and there are different combinations of winding patterns available. The CW machine, however, can only have 1 slot pitch. In a three phase machine where the pole pitch is usually larger than one, the CW machine winding

are mostly short pitched. Moreover, acceptable windings can only be achieved with a limited combinations of pole numbers[57].

4.3 Analytical design method of SMPM machines with concentrated winding (CW)

4.3.1 Magnet design

Similar to DW SMPM machines, the magnet thickness is an important factor to determine the machine performance and is thus chosen to be one of the design input variables. The conclusion from the DW SMPM machine about the magnet pole coverage and magnetization in the last chapter can be applied here. Hence, a α_p of 0.83 and parallel magnetization are chosen. For comparison purposes, the same rated conditions (15 kW, 1800 rpm and 60 Hz) of the CW machine are chosen as a design example. The stator slot numbers for the DW and CW motors are selected to be 24 and 6, respectively. For DW machines in general, according to [8], it is desirable to keep the slot number as small as possible to reduce the manufacture cost. Furthermore, the winding factor decreases with the increase of the number of slots per pole per phase. For this four pole machine, two slots per pole per phase are selected for DW design, which gives a stator slot number of 24. If only one slot per pole per phase is used, there will be large amount of harmonics, which is not desired. For CW machines, there is only limited combination of slot number and pole number that are able to produce balanced three phase MMF and have relatively large winding factor. A slot number of 6 is the only practical choice for this four pole CW machine [57].

Figure 4.2 shows the typical FEA simulated cogging torque and torque ripple at rated condition with sinusoidal excitation after careful design of the pole coverage coefficient, magnetization direction, slot opening and tooth tip. The cogging torque has been

effectively reduced to a peak-to-peak value of around ±5% of the rated torque of 79.6 Nm. The peak to peak torque ripples are also reduced to as low as 15% for both DW and CW machines.

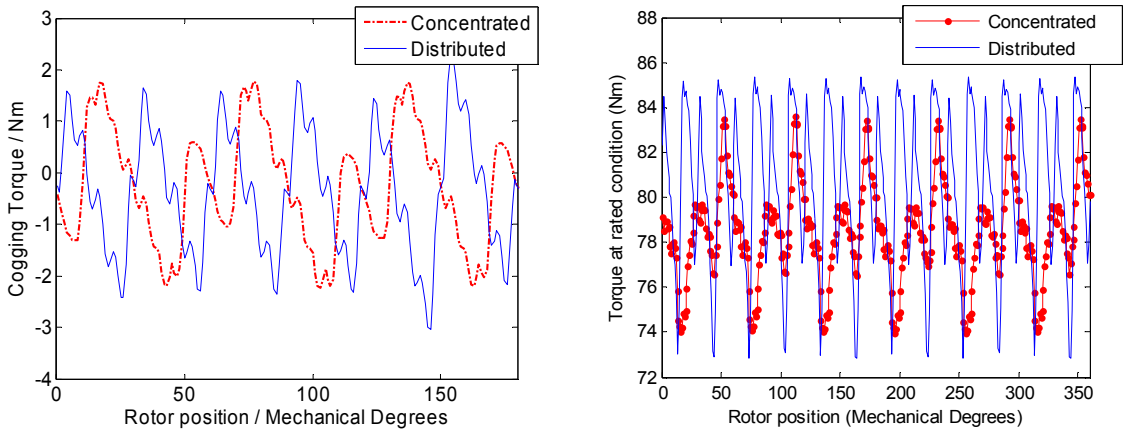

(a) (b)

Figure 4.2: Comparison of (a) Cogging torque waveforms and (b) Torque ripple waveforms

4.3.2 Analytical design method

From the design method point of view, the major difference between the DW and the CW machines is the way in which the coils are wound. Other aspects, such as the machine geometry definitions as in Figure 3.3, the analytical electromagnetic equations as from (3.4) to (3.11) and the analytical design flowchart as in Figure 3.10, are all basically the same. The differences in the design between the two winding types are highlighted below.

For the CW design, the 1800 rpm and 60 Hz machine has four poles (p = 120*60/1800 = 4), thus this machine can only have either 3 slots or 6 slots. For example, for a 3 slot design, there is only 1/4 slot per pole per phase, which is too low for the stator winding to produce a 4 pole sinusoidal MMF [57]. As a result, the 6 slots design is

chosen and the winding factor is 0.867. On the contrary, a full pitched DW for a 3 phase, 4 pole and 24 slots machine has a higher winding factor of 0.95.

The modeling of the end winding is shown in Figure 4.3. The total length of the wire and the stator winding resistance can then be calculated accordingly once the end winding is defined.

(a) (b)

Figure 4.3: Modeling of the end winding for (a) Distributed winding and (b) Concentrated winding for SMPM machines

4.3.3 Verification of the analytical design method in FEA

The FEA simulation and the analytical design method for a typical 15 kW, 1800 rpm and 60 Hz concentrated winding machine are compared below:

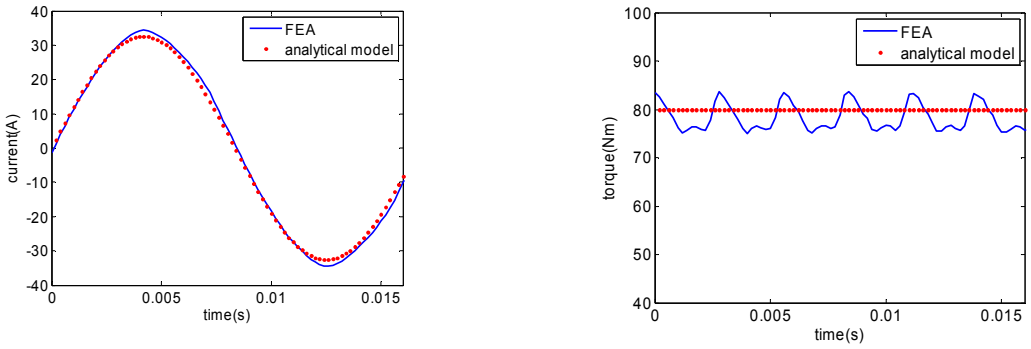

(a) (b)

Figure 4.4: FEA result of the motor with concentrated winding designed by the analytical method (a) Phase current waveform at rated condition (b) Output torque waveform at rated condition

Notice that the analytical design method only considers the fundamental of the airgap magnetic field and thus the resulting torque is an average value without pulsations (Figure 4.4 (b)). However, this average agrees with the average value of the FEA method. The current waveform in Figure 4.4 (a) shows good agreement between the analytical design method and FEA methods. This in turn yields good agreement of the efficiency calculation.

4.4 Optimization and comparison result

4.4.1 Objective function

The same concept for the objective function is used as described in CHAPTER 3. Two objective functions are defined in (4.1), where *obj1* pays more attention to the weight and volume and *obj2* gives more importance to the efficiency and torque per ampere.

$$\begin{aligned} obj1 \quad & output = volume*20000 + 2*Weight + (1-Eff)*200 + WtMagnet*5 - TperA*5 \\ obj2 \quad & output = volume*10000 + Weight + (1-Eff)*1000 + WtMagnet*5 - TperA*20 \end{aligned} \tag{4.1}$$

4.4.2 Optimization results

A distributed winding (DW) and a concentrated winding (CW) machine are optimized to have the same rating of 15 kW, 60 Hz, 1800 rpm and a supply voltage of 480 V (line to line). The DW motor has 24 slots and a double layer, full pitch stator winding. The CW motor has 6 slots and a double layer winding with a 120 electrical degree coil pitch. For comparison reasons, the airgap length for both machine types is 1 mm; NdFeB with a residual flux density of 1.23 T and relative permeability of 1.01 is used as the rotor magnet material; the magnet pole coverage is 0.83 and parallel magnetization is used; no skew is applied to the magnet.

PSO is run for both machine types with *obj1* and *obj2*, respectively. The optimized solution for each machine lies in a region and the particles converge to one of the solution points in the region. This optimal region indicates that in the machine design, different choices of design parameters could lead to designs with the same objective. Because the particles are initialized at random positions and their travel velocities are regulated by random variables, the optimal point in which the particles converge is random. This randomness provides particles with a good ability to explore the optimal solution region, which is a great advantage of PSO in solving the optimization problem.

The columns under Design 1 and Design 2 in Table 4.1 are two typical PSO results for each machine type and the respective objective function. The table shows that while values of each of the objective functions fall within a close range, the differences between the CW and DW designs are clear. When more importance is given to weight and volume as in *obj1*, the CW motor has a significantly better overall performance than the DW machine. However, the opposite is true where a higher efficiency and torque per ampere are desired. These results are a helpful guide for the designer to understand and make decisions on winding choices and tradeoffs.Table 4.2 shows the detailed machine design information of Design 1 for each winding type and objective function. Comparing the CW and DW design in Table 4.2, it is observed that the CW motor has a much smaller outer diameter for both designs under *obj1* and *obj2*, which leads to less use of stator steel and thus less weight and volume. This is due to the higher slot fill factor. The short end-winding, another advantage of the CW, helps to reduce the phase resistance; this effect is observed in Table 4.2 under *obj2* when the efficiency is given importance.

Although the CW has a lower winding factor, its design is only slightly worse (less than 1% of efficiency) than the DW design.

The comparison results in Table 4.2 show that the CW designs are superior in terms of weight and volume. In addition, the lower phase resistance helps to diminish the negative impact of the relatively low winding factor. These PSO optimization results agree with the physics reasoning behind the analytical equations. The result also shows that the particle swarm intelligence is able to correctly understand the underlying physical behavior of the objective system in the searching process and find the best solution.

Table 4.1: Multi-objective optimization design result

	Objective Function 1				**Objective Function 2**			
	CW		**DW**		**CW**		**DW**	
	Des. 1	**Des. 2**	**Des. 1**	**Des. 2**	**Des. 1**	**Des. 2**	**Des. 1**	**Des. 2**
Wt. / kg	28.5	27.9	30.0	29.4	32.12	32.39	32.02	33.23
Vol. / m^3	0.0031	0.0032	0.0038	0.0037	0.0043	0.0041	0.0048	0.0047
Eff.	93.31%	93.34%	94.69%	93.68%	95.08%	94.89%	95.88%	95.85%
T./A. (Nm/Arms)	2.79	2.79	3.54	2.79	3.79	3.74	3.73	3.75
Mgt. Wt. / kg	0.685	0.780	0.95	0.600	1.48	1.26	1.12	1.04
Objective	122.5	123.2	134.3	134.4	56.38	56.42	52.39	52.17

Table 4.2: Concentrated and distributed winding machine optimized design

	***Obj1*, CW**	***Obj1*, DW**	***Obj2*, CW**	***Obj2*, DW**
***D* (mm)**	82.7	83.3	84.8	77.1
***L* (mm)**	82.3	88.1	139.9	148.1
h_m(mm)	5.76	7.56	7.63	5.62
Stator outer diameter (mm)	220.1	235.0	198.9	203.3
Number of turns per phase	208	218	158	154
Winding Factor	0.866	0.9659	0.866	0.9659
Tooth width (mm)	27.0	7.19	28.8	6.25
Slot opening(mm)	3	1	3	1
Phase resistance(Ω)	0.33	0.42	0.39	0.31
Synchronous Reactance(Ω)	7.31	6.82	6.23	6.41
Armature Leakage Reactance(Ω)	3.37	2.30	3.18	1.92

4.5 Vector multi-objective optimization and comparison

4.5.1 Vector multi-objective optimization

In Weighted Sum Multi-Objective Optimization (WSMOP) [58] , the optimization result depends on the weighting coefficients. However, how much attention should be paid to each performance index is often based on a conceptual understanding of the problem. In many situations, there is no mathematical approach that can precisely quantify those conceptual objectives into numerical weight coefficients. This disadvantage makes the WSMOP results less informative. Another disadvantage is that WSMOP is not good at providing information on trade-offs between performance indexes. The observations from a few design samples, such as Table 4.2, cannot be safely extended as general trends.

A different formulation of the multi-objective optimization problem is to define the objective function to be a vector where each element represents a performance index. The optimization problem then becomes the so-called Vector Multi-Objective Optimization (VMOP) [58] and can be formally defined as:

Find the vector $\vec{x}^* = [x_1^*, x_2^*, ..., x_n^*]^T$ which will satisfy the *m* inequality constraints:

$$g_i(\vec{x}) \geq 0 \qquad i = 1, 2, ..., m\,, \tag{4.2}$$

the *p* equality constraints:

$$h_i(\vec{x}) = 0 \qquad i = 1, 2, ..., p\,, \tag{4.3}$$

and will optimize the vector function:

$$\vec{f}(\vec{x}) = [f_1(\vec{x}), f_2(\vec{x}), ..., f_k(\vec{x})]^T \tag{4.4}$$

In VMOP, the meaning of optimality needs to be re-defined. First, the way to compare two vectors is defined. Without loss of generality, if the minimization problem is assumed, a decision vector $\vec{x}$ is said to dominate a decision vector $\vec{y}$ (denoted $\vec{x} \prec \vec{y}$) only when satisfying the following two conditions:

$$\begin{aligned} f_i(\vec{x}) &\le f_i(\vec{y}) \quad \forall i = 1,...k \\ f_i(\vec{x}) &< f_i(\vec{y}) \quad \text{for at least one } i = 1,...k \end{aligned} \tag{4.5}$$

The optimal solutions of VMOP are called Pareto Optimals. The vector $\vec{x}^*$ is Pareto optimal if there does not exist another decision vector $\vec{y}$ that dominates it. The entire set of Pareto optimal solutions is called the Pareto optimal set. When plotted in the objective space, the corresponding vectors in the Pareto optimal set are collectively known as the Pareto front [58].

To better illustrate the above definitions, suppose a machine design VMOP problem has the following two-dimensional objective function:

$$\vec{f}(\vec{x}) = [f_1(\vec{x}), f_2(\vec{x})]^T \tag{4.6}$$

where $f_1(\vec{x})$ and $f_2(\vec{x})$ can be any performance indexes, such as weight, volume, efficiency (1-efficiency in a minimization problem), and so on. A typical Pareto front of this problem is plotted in Figure 4.5 and the symbol "+" represents feasible designs. In Figure 4.5, design C has smaller values of both $f_1(x)$ and $f_2(x)$ than design E. Hence, design C is said to dominate design E. As seen in Figure 4.5, no designs are able to dominate designs A, B, C and D. Hence, designs A, B, C and D are Pareto optimals and lie on the Pareto front.

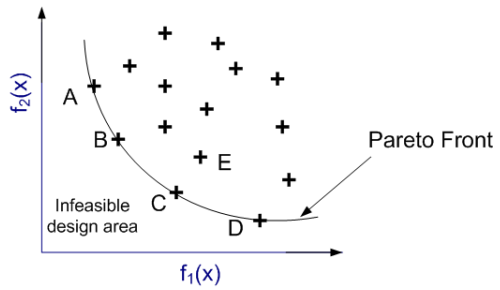

Figure 4.5: Plot of a typical Pareto front

The Pareto front, as seen in Figure 4.5, can be regarded as a boundary between the feasible designs and infeasible designs. Moreover, design trade-offs between performance indexes can be clearly shown by the Pareto front: designs on the Pareto front cannot improve one performance index without degrading another. For example, going from design A to design D, although $f_2(x)$ becomes smaller, $f_1(x)$ unavoidably becomes larger at the same time. After the Pareto front is constructed, the designer can clearly identify the design trade-offs between performance indexes and then select points from the Pareto front to meet specific design requirements. Those selected optimal designs are then good candidates for further detailed designs and evaluations.

In most cases, there is no easy way to find an analytical expression of the lines or surfaces that contain the points in the Pareto front. Alternatively, the usual procedure to generate the Pareto front is to compute many points of the objective vector functions in the problem solution domain and find the non-dominated points. Non-dominated points are the points which are not dominated by others in the solution domain, such as A, B, C, and D in Figure 4.5. When sufficient points in the entire solution space have been computed, the non-dominated points can be regarded as Pareto optimals and it is then possible to produce the Pareto front based on those non-dominated points [58].

4.5.2 Multi-objective particle swarm optimization

When solving a Single-Objective Optimization (SOP) or WSMOP problem, the process is stopped when the global optimal is found. For a VMOP problem, however, the process is not stopped until sufficient Pareto optimals are found and the Pareto front is plotted. The traditional gradient based methods are not designed to find multiple optimal solutions and are thus difficult to convert to solve the VMOP problem. PSO, on the other hand, can be re-defined to solve the VMOP problem [58-59].

How to determine the global best particle is a major issue when applying PSO to VMOP problems. In the Single-Objective PSO (SOPSO), the global best is simply the position which has been found by all particles to have the best objective function value. In Vector Multi-Objective PSO (VMOPSO), however, there is a set of Pareto optimals which form the optimum solutions. This raises the problem of how to select the g_{best} for each particle in the swarm population because all the Pareto optimal solutions are equally good. Since there is no reason to rank between Pareto optimals, a logical solution is to randomly choose one of the Pareto optimals as the g_{best}, which leads to the Homogeneous Particle Swarm Optimization (HPSO) [59]. Similarly, the p_{best} is also randomly chosen from one of the Pareto optimals. Therefore, each particle is treated as an equal identity in the swarm and HPSO is reported to give more exploration ability [59].

The procedure of applying the HPSO for the SMPM design optimization is as follows:

1) Define the solution space. Select the parameters to be optimized. Here, the parameters are *D, L,* and h_m, which is the same as the SOPSO

2) Define a vector multi-objective function. Suppose the minimum volume and highest efficiency are both the design objectives, the vector multi-objective function can be defined as

$$\vec{f}(\vec{x}) = [Volume,\ 1\text{-}Eff]^T \tag{4.7}$$

3) Initialize with random swarm locations and velocities.

4) Create a Pareto repository, which is a set of Pareto Optimals found by the swarm. At the initialization, the Pareto repository is the non-dominated solutions among the initial particles.

5) Systematically "fly" the particles through the solution space. The following steps are performed on each particle individually:

   - Evaluate each particle's Vector Multi-Objective function and check its Pareto optimality with the Pareto repository. Update the Pareto repository with the non-dominated particles and discard the ones that are being dominated.
   - Randomly select two Pareto solutions from the Pareto repository as the p_{best} and g_{best}.
   - Move the particle according to (3.40) and (3.41), which is the same way as the single objective PSO.

6) Repeat the process starting at step 5). In this way the particle moves for discrete time intervals until the termination criteria are met.

4.5.3 Results and comparisons

The HPSO described above is run for both CW and DW designs with the vector multi-objective function (4.7). In order to better explore the solution domain, the number

of particles is increased from 6 in the WSMOP to 100 and the number of iterations is kept the same.

The Pareto front found by HPSO for DW and CW SMPM machines are shown in Figure 4.6 (a) and (b), respectively. The trade-offs between the efficiencies and the volumes of these machines are clearly seen from the plotted Pareto front. In order to increase the efficiency, the volume of the machine must be allowed to increase accordingly. This is because when the volume increases, the machine can be designed with lower electrical or magnetic loading, which leads to reduced losses. However, as shown in Figure 4.6 this effect diminishes once efficiency reaches a certain level. The reason is that with the increase of volume, the length of the coils also increases and the resistance of the winding increases, especially for the end-winding, which leads to more copper loss.

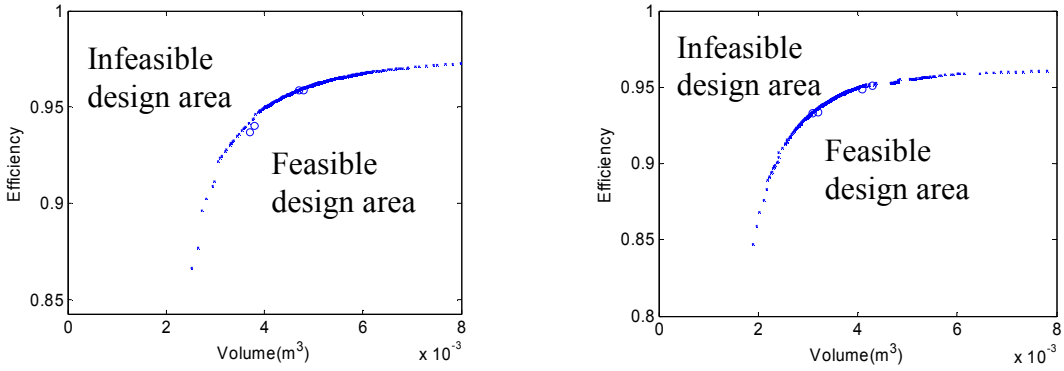

(a) (b)

Figure 4.6: Pareto front by HPSO for design with (a) Distributed Winding (b) Concentrated Winding

The Pareto front in Figure 4.6 is actually a boundary which indicates that for certain volumes of the machine, the efficiency cannot be higher than the Pareto front. The

volume and efficiency of the optimized machines in Table 1 found by the SOPSO with weighted sum objective functions are also marked on Figure 4.6 with the symbol "O". Because the volume and efficiency are two important performance indexes in *obj1* and *obj2*, the resulting optimal design of SOPSO should be close to the Pareto front boundary. In addition, the SOPSO optimal designs cannot reach the Pareto boundary because compromises have to be made for other performance indexes of *obj1* and *obj2*. Figure 4.6 shows that the optimal designs in Table 4.2 lie close to but within the Pareto front of the VMOPSO, which agrees well with the above analysis. If there are only volume and efficiency in the weighted sum objective function, then the WSMOP will find the optimal that lies on the Pareto front.

A comparison of the Pareto front of the CW and DW is shown in Figure 4.7 which indicates that when the volume is a constraint, the concentrated winding machines have a better efficiency. In addition, even for designs with very large volumes, the DW machines only have slightly better efficiencies than the CW machines. This result not only agrees with the observation made from the WSMOP, but also reinforces the conclusion that the CW machine has a better performance than the DW machine in terms of volume and efficiency.

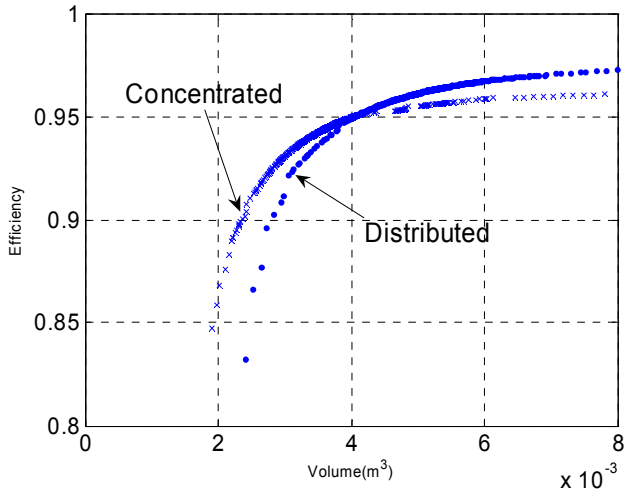

Figure 4.7: Comparison of Pareto front for DW and CW machines

Another important aspect of the proposed comparison method described in this work is the computational time. The Pareto front calculation is a time-consuming process because it needs a large number of computations of the design candidates. The proposed analytical design method and the particle swarm based optimization method are therefore even more useful as time-saving tools in such a calculation; using FEA techniques would be impossible. A desktop computation with Pentium 4 CPU and 4GB RAM takes no more than 15 minutes to evaluate 100 particles and 100 iterations, and is able to generate enough non-dominated points for the Pareto front.

4.6 Chapter summary

An analytical method is developed for a SMPM motor with either distributed or concentrated stator windings and PSO is applied to optimize the design of each motor for both WSMOP and VMOP. The optimized designs with the two winding types are compared quantitatively for certain objective functions, which can be defined by the designer according to the application. The Pareto front of the two winding designs are

found and compared. Optimization results show that the concentrated winding machines generally have a better performance than the distributed winding machines, in terms of active volume and efficiency. The proposed SMPM machine electromagnetic design tool provides optimized designs of a SMPM motor with both types of windings in minutes on an ordinary desktop computer, which saves significant time and energy for the machine designer, compared to using FEA for every choice of parameter.

CHAPTER 5 Electromagnetic and Thermo-mechanical Integrated Design and Optimization

5.1 Overview

The electromagnetic design is only a part of the design of an electrical machine. A well designed machine not only delivers the required power and torque at a required speed with good efficiency, but also has enough heat rejection ability to keep the temperature within limits at certain operating conditions, and mechanically ensures successful transmission of the machine's electromagnetic torque to the load, as well [8]. The machine design is thus a truly multi-physics task and has complicated trade-offs among electromagnetic, mechanical and thermal effects. This chapter starts with a brief introduction of the electrical machine structure, and then shows a fast and generic thermal method for calculating the temperature distribution of SMPM machines developed by Dr. J. R. Mayor and A. Semidey [60]. Based on the analytical design method and the generic thermal model, a novel electromagnetic-thermo-mechanical integrated design approach for SMPM machines is proposed in order to generate realistic machine designs with both the active part (core and winding) and the inactive part (frame) considered. Particle Swarm Optimization (PSO) is then applied to this integrated electromagnetic-thermo-mechanical design method in order to correctly and efficiently find designs which optimize certain requirements such as weight, efficiency, etc for example.

5.2 Electrical machine structure and heat convection path

Electrical machines have mechanical structures, or frames and end shields to support and enclose the core and windings. The machine frames mainly have two purposes: First,

to ensure successful transmission of the shaft torque to the motor supports and withstand the twisting forces and shocks. For this purpose, the frame is designed with sufficient thickness and mechanical strength. Besides the purpose of providing mechanical support and protection of moving parts, the machine frame also serves as a ventilating housing, or means of guiding the cooling medium into effective channels. Taking an open drip proof (ODP) motor as an example, the machine frame and the ventilation channel are shown in Figure 5.1 [9], where the arrows show the paths of ventilation. A thicker frame is mechanically stronger, but is thermally more difficult for the internal heat to get out, and the machine is built with more material and has more weight. Hence, the thermal and mechanical designs are strongly coupled and good designs should find proper trade-offs between them.

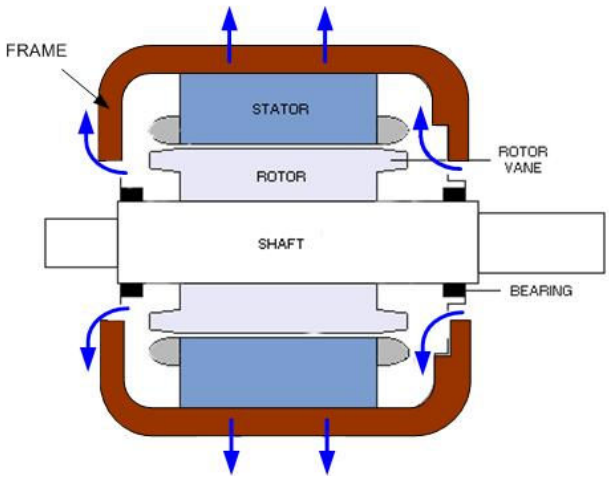

Figure 5.1: Frame and ventilation of an ODP motor[9]

To enhance cooling capability, it is common to use fins on the surface of the frame or use forced cooling. Fins on the frame surface increases the effective area for better heat transfer, but on the other hand increases the overall weight of the machine by a large portion. Forced cooling can be primarily divided into two methods. One is to use certain

external equipment to provide the flow of the cooling media. However, the extra cooling equipment needs addition space, which may not be available in many applications. Another way is self-cooling, where there is usually a cooling fan installed on the same shaft of the machine and provides ventilation as the machine rotates. The self-cooling capability highly depends on the shaft speed and is not effective at low speed at high torque conditions. In addition, the cooling fan on the shaft takes energy from the machine shaft and thus decreases the efficiency.

To sum up, the electrical machine frame design is a trade-off among the mechanical strength, the cooling capability and the overall machine performance in terms of weight, efficiency, cost, etc. Different choices can be made on the frame design but they all have advantages and disadvantages. Unavoidably, this frame design is also strongly coupled with the electromagnetic design of the machine. All the above trade-offs raise the need of a tool which is able to accurately include the electromagnetic, thermal and mechanical design of electric machines in a systematical way.

5.3 Determination of the frame thickness [61]

The primary factor to determine the thickness of the frame is the expected maximum shaft torque of the machine (T_{max}) and the material property used for the frame. If the support screws of the frame are assumed to be on the outer perimeter of the stator, the necessary frame thickness to successfully transmit the T_{max} should satisfy the following equation, given by a study of the author's partner group in mechanical engineering,

$$\frac{\pi}{2}\left(\left(\frac{D_o}{2}+t_{frame}\right)^4-\left(\frac{D_o}{2}\right)^4\right)=\frac{n_s * T_{\max} * \left(\frac{D_o}{2}+t_{frame}\right)}{\sigma_{yield}}, \qquad (5.1)$$

where D_o is the stator outer radius, t_{frame} is the thickness of the frame, n is the safety factor, and σ_{yield} is a coefficient representing the property of the frame material.

5.4 Thermal analysis of electrical machines

For good machine design, it is extremely important to have good knowledge of the temperature distribution in the machine. Classical thermal electrical machine designs use various simplifications to approximate the motor as a cylinder in order to carry out a thermal analysis. This conservative approach has low accuracy and can not be applied to design optimizations. Contemporary methods include thermal circuits [62] and finite element analysis techniques [63] to represent the flow of heat through the machine. While the thermal circuit based analysis requires minimal computational time, it requires experimental data to fit the model to specific machines and is therefore not generic. FEA is accurate and generic, but requires a large amount of computational time. This large time requirement limits its use in the design cycle. What is truly useful in the design and optimization process is a generic and computationally efficient thermal analysis tool that can be integrated with the electromagnetic design and optimization and used over and over for every candidate design. To meet this need, the author's partner group in mechanical engineering developed a generic electrical machine thermal model using an automated 2D finite difference approach and the details can be found in [1]. According to the partner group in mechanical engineering, the heat produced in the end winding is assumed to dissipate through the stator core and frame to the ambient in this thermal model.

Briefly summarized, the generic electrical machine thermal model is able to calculate temperature distributions under both steady state and transient condition. The

accuracy is comparable to FEA but the computation time is significantly reduced. The thermal model is also able to consider the six combinations of cooling conditions as shown in Figure 5.2.

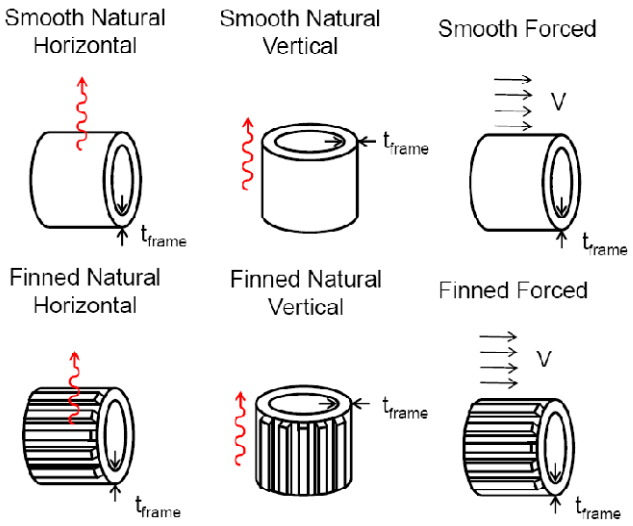

Figure 5.2: Machine heat rejection path choices [64]

5.5 Integration of the electromagnetic and thermal-mechanical design

5.5.1 Current density selection

As described in Chapter 2, the current density selection is important to the machine design but is done heuristically in conventional designs, which often leads to over- or under- design. With a combination of the electromagnetic design method and thermo-mechanical model, the selection of current density can be truly based on the specific machine performance and cooling capability.

5.5.2 Simulation of the effect of current density to the temperature distribution

The effect of choosing different current densities on the designs of the electrical machines is first studied. As an example, the electromagnetic analytical design method

generates three designs with the same set of values for three prime design variables (D=80 mm, L=130 mm and h_m=7 mm), but with different current densities. The thermo-mechanical model is then applied to the three electromagnetic designs to calculate the temperature distribution. The exterior boundary condition for this study is horizontal orientation, smooth surface and forced cooling, where the coolant flow speed is constant. The result is compared in Table 5.1 and the temperature distributions for the three designs are shown in Figure 5.3.

As the current density increases from 4 A/mm^2 to 7 A/mm^2, the design results in Table 5.1 shows how the active weight of the machine decreases from 38 kg to 29.9 kg and the stator core outer diameter decreases from 232 to 206 mm. A higher current density leads to machine designs with lower weight and volume, which is desirable, but on the other hand, the maximum winding temperature increases from 79.8 ^{o}C to 106.5 ^{o}C due to increased copper losses. This winding temperature increase leads to higher thermal stress on the winding insulation material and a reduction in insulation life. Again the design trade-offs as illustrated in Table 5.1 demonstrate the need for an electromagnetic and thermo-mechanical integrated design procedure.

Table 5.1: Comparison of designs with different current density

	Design 1	**Design 2**	**Design 3**
Current Density (A/mm^2)	4	5.5	7
Max. Winding Temperature (^{o}C)	79.4	89.1	101.1
Stator outer diameter (mm)	232	218	206
Machine active weight (kg)	38.8	33.9	29.9
Total machine weight (kg)	41	36.2	32.4

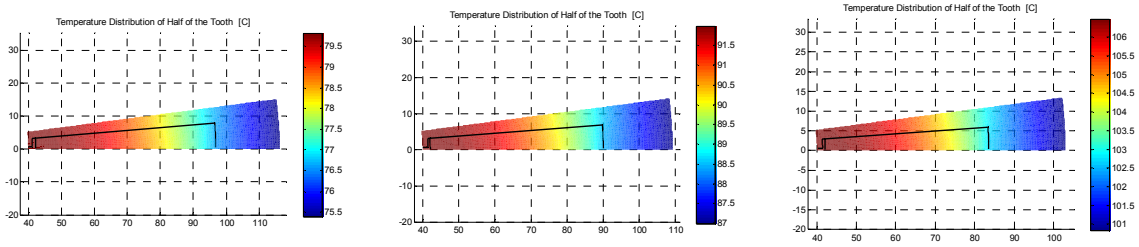

Design 1 Design 2 Design 3

Figure 5.3: Temperature distribution of three different designs (Created by Andrew Semidy in the School of Mechanical Engineering, Gatech [1])

5.5.3 Temperature limit

For 60 Hz SMPM operation, the dominating heat sources are the stator copper loss and the stator core loss. The stator winding temperature rise is limited by the choice of winding insulation material. The insulation life in turn strongly depends on the operating temperature. According to IEEE standard 101[65], winding insulation expected life is doubled for every 10 ^{o}C reduction in operating temperature. Hence, for a specific insulation class, the average expected life L_T at winding temperature T can be expressed as

$$L_T = L_{140} * 10^{k(T-140)}, \tag{5.2}$$

where L_{140} is the winding insulation life at 140 ^{o}C and k is a constant. The winding temperature is therefore limited by the required life of the insulation system, as described by

$$T < T_{th}, \tag{5.3}$$

where T_{th} is the specified winding temperature that would achieve the required insulation life. When a higher temperature is allowed than T_{th}, the machine can be designed with a higher value of stator current density, which leads to a smaller machine with more torque per ampere. However, the price paid is a reduced insulation life, or the use of a higher temperature class of insulation.

5.5.4 EM-TM design integration

When the thermo-mechanical design is considered, the current density J_s can be viewed as another prime design variable besides D, L and h_m. The integrated EM-TM design calculation flowchart in Figure 5.4 illustrates the various steps.

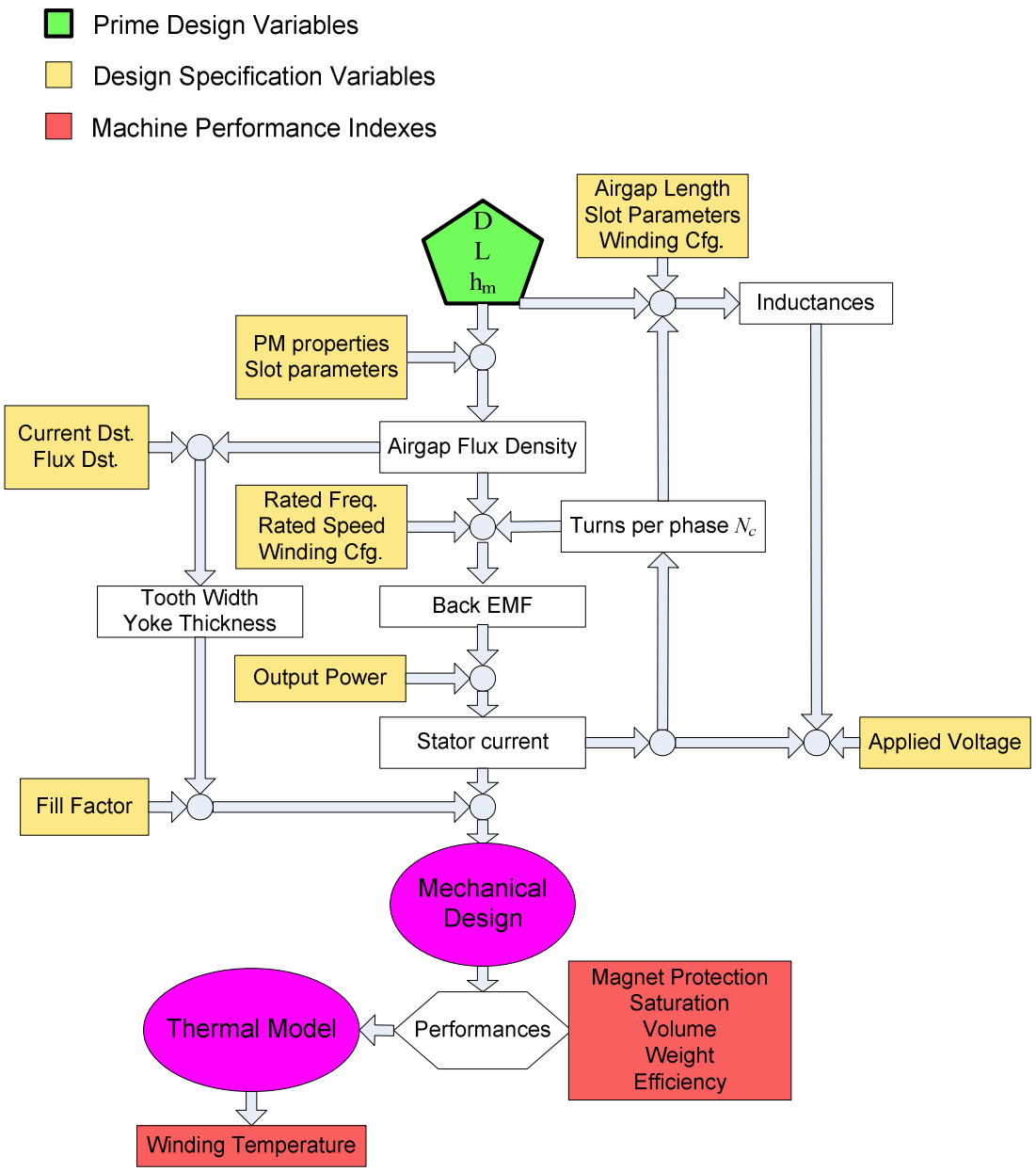

Figure 5.4: EM-TM integrated design calculation flowchart

5.6 Numerical design example

5.6.1 Numerical design example introduction

A numerical design example of a 15 kW, 1800 rpm, 60 Hz SMPM machine is presented in this section to illustrate how the proposed method starts from 4 prime design variables and produces a machine design. The 15 kW example SMPM machine is designed to have N_s = 24 stator slots and a full pitched winding. The ambient temperature is 27 ^{o}C. The materials used for the machine appear in Table 5.2. In this example, the values of the four prime design variables are chosen as: D = 215 mm. L = 160 mm, h_m = 8.5 mm, J_s = 4 A/mm^2. In fact, and the proposed design method is able to produce a trial design of the SMPM machine based on the values chosen for the four prime design variables.

Table 5.2: Materials for the example SMPM machine design

Component	**Material Type and Description**
Stator Core	non-oriented steel M-15 from AK Steel [66]
Rotor Core	non-oriented steel M-15 from AK [66]
Permanent Magnet	NdFeB (Sintered) N3575 [51]
Insulation Class	Class F
Frame	Aluminum

5.6.2 Example design flow and result

5.6.2.1 Airgap flux density calculation

The values of the four prime design variables are first input to the electromagnetic analytical design method. The electromagnetic airgap length g for this machine is chosen to be 1 mm, which is a typical value for 15 kW, 1800 rpm SMPM machine [67]. For class F insulation to have an expected insulation life of over 20,000 hours, the maximum winding temperature is 153 ^{o}C [8]. As described in chapter 3, the PM operating temperature can be estimated to also 153 ^{o}C. From the datasheet of permanent magnet N3575 [51] (Figure 5.5), the residual flux density B_r at 153 ^{o}C is read off to be about 1.04 T and the relatively permeability (recoil permeability in the datasheet) is read off to be 1.05.

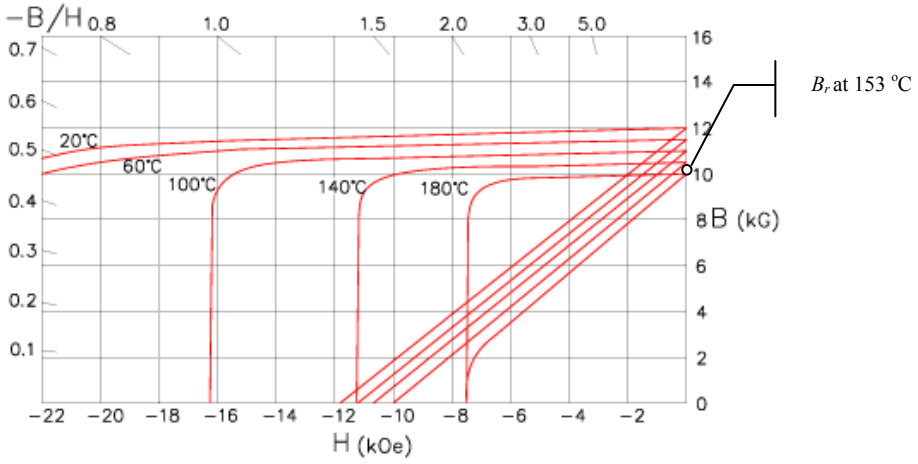

Relative permeability

Magnetic Properties	Nom.	Min.
Br (Gauss)	12,000	11,700
Hc (Oersted)	11,600	11,000
Hk (Oersted)	14,000	12,600
Hci (Oersted)	27,000	25,000
BHmax (MGOe)	35.0	33.0
Temp Coeff of Br (%/°C)	-0.11	N/A
Recoil Permeability (µrec)	1.05	N/A
Tc, Curie Temperature (°C)	310	N/A
Maximum Operating Temperature (°C)	180	N/A

1 kOe = 79577.4 A/m, 1 kG = 0.1 T

Figure 5.5: Datasheet of N3575[51]

A typical value of 2 mm is chosen for the slot opening B_{s0} [9]. From Figure 3.4,

$$\begin{aligned} R_m &= D/2 - g = 107.5 - 1 = 106.5 \text{ mm} \\ R_r &= R_m - h_m = 106.5 - 8.5 = 98 \text{ mm} \end{aligned} \quad . \tag{5.4}$$

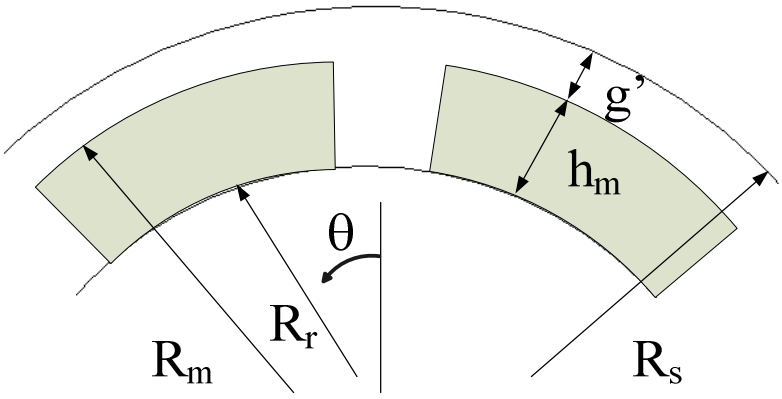

Figure 3.4 The definition of R_r, R_s, and R_m

According to (3.6), the effective airgap length g' is:

$$g' = g + \frac{h_m}{\mu_r} = 1 + \frac{8.5}{1.05} = 9.0952 \text{ mm}. \tag{5.5}$$

According to (3.9), the tooth pitch τ_t is

$$\tau_t = \frac{2\pi R_s}{N_s} = \frac{\pi D}{N_s} = \frac{\pi * 215}{24} = 28.14 \text{ mm}, \tag{5.6}$$

and from (3.8),

$$\begin{aligned} \gamma &= \frac{4}{\pi}\{\frac{B_{s0}}{2g'}\tan^{-1}(\frac{B_{s0}}{2g'}) - \ln\sqrt{1+(\frac{B_{s0}}{2g'})^2}\} \\ &= \frac{4}{\pi}\{\frac{2}{2*9.0952}\tan^{-1}(\frac{2}{2*9.0952}) - \ln\sqrt{1+(\frac{2}{2*9.0952})^2}\} = 0.0019 \end{aligned} \tag{5.7}$$

The Carter coefficient K_c is then calculated based on (3.7):

$$K_c = \frac{\tau_t}{\tau_t - \gamma g'} = \frac{28.14}{28.14 - 0.0019 * 9.0952} = 1.0000, \tag{5.8}$$

and then according to (3.5), the equivalent stator inner radius is

$$R_{se} = R_s + (K_c - 1)g' = \frac{215}{2} + (1.0000 - 1) * 90.952 = 107.5 \text{ mm}. \tag{5.9}$$

As described in Chapter 3, the pole coverage α_p is selected to be 0.83 and the magnetization direction is parallel. The magnetization vector of the permanent magnet M_n is calculated according to (3.10) to (3.12):

$$\begin{aligned} A_{1n} &= \frac{\sin[(n\frac{p}{2}+1)\alpha_p\frac{\pi}{p}]}{(n\frac{p}{2}+1)\alpha_p\frac{\pi}{p}} = \frac{\sin[(2n+1)0.83\frac{\pi}{4}]}{(2n+1)0.83\frac{\pi}{4}} \\ A_{2n} &= \frac{\sin[(n\frac{p}{2}-1)\alpha_p\frac{\pi}{p}]}{(n\frac{p}{2}-1)\alpha_p\frac{\pi}{p}} = \frac{\sin[(2n-1)0.83\frac{\pi}{4}]}{(2n-1)0.83\frac{\pi}{4}} \end{aligned} \tag{5.10}$$

$$M_{rn} = \frac{B_r}{\mu_0}\alpha_p(A_{1n} + A_{2n}) = \frac{1.04}{4\pi * 10^{-7}}\alpha_p\left(\frac{\sin[(2n+1)0.83\frac{\pi}{4}]}{(2n+1)0.83\frac{\pi}{4}} + \frac{\sin[(2n-1)0.83\frac{\pi}{4}]}{(2n-1)0.83\frac{\pi}{4}}\right)$$
$$M_{\theta n} = \frac{B_r}{\mu_0}\alpha_p(A_{1n} - A_{2n}) = \frac{1.04}{4\pi * 10^{-7}}\alpha_p\left(\frac{\sin[(2n+1)0.83\frac{\pi}{4}]}{(2n+1)0.83\frac{\pi}{4}} - \frac{\sin[(2n-1)0.83\frac{\pi}{4}]}{(2n-1)0.83\frac{\pi}{4}}\right) \quad (5.11)$$

These values are then input to (3.4) to find the airgap flux density distribution with $r = D/2$, which corresponds to the magnetic flux density distribution at the inner surface of the stator. Values of B_n are calculated by (3.4) and shown in Table 5.3 for n=1 to n=17.

Table 5.3: Values of B_n for the example design

n	1	3	5	7	9	11	13	15	17
B_n	1.072	-0.151	-0.022	0.091	-0.104	0.083	-0.046	0.008	0.022

5.6.2.2 Back EMF calculation

For a distributed, full-pitch winding with the number of slots per pole per phase q = 24/4/3 = 2, the winding factor K_{w1} is

$$K_{w1} = \frac{1}{q}\frac{\sin(\frac{\pi}{6})}{\sin(\frac{\pi}{6*q})} = 0.9659 \quad (5.12)$$

The fundamental component of back EMF E_1 can be the calculated according to (3.14), as

$$E_1 = 4.44 f N_c B_1 K_{w1} \frac{2}{\pi} \frac{\pi D}{p} L$$
$$= 4.44 * 60 * N_c * 1.072 * 0.9659 * \frac{2}{\pi} \frac{\pi * 215/1000}{4} * 160/1000 \text{ (V)} \quad . \qquad (5.13)$$

5.6.2.3 Winding current calculation

The winding current to produce the rated output power of 15200 W (15 kW plus an estimate of winding and friction loss of 200 W [8]) is calculated according to (3.15),

$$I_{ph} = \frac{P_{out}}{n_{phase} E_1} = \frac{15200}{3 * E_1} \text{ (A)} \qquad (5.14)$$

5.6.2.4 Tooth width and core thickness calculation

The next step is to calculate the stator tooth width, stator and rotor core thickness. The total flux per pole produced by the permanent magnet is found by integrating the airgap flux density calculated in section 5.6.2.1:

$$\Phi = \pi \frac{D}{p} L \int_{-\frac{\pi}{2}}^{\frac{\pi}{2}} \sum_{n=1,3,5,..}^{\infty} B_n \cos(n\theta) d\theta = 2.11 * 10^{-2} Wb \,. \qquad (5.15)$$

The maximum stator tooth flux Φ_{tm} is reached when the center line of a rotor pole is aligned with a stator tooth. The tooth pitch α_t of this 4 pole, 24 stator slot machine is

$$\alpha_t = \frac{p\pi}{N_s} = \frac{4\pi}{24} = \frac{\pi}{6} \,. \qquad (5.16)$$

Hence, the maximum stator tooth flux Φ_{tm} is calculated by integrating the airgap flux density over one tooth width, i.e., replacing $\pi/2$ and p of (5.15) by $\alpha_t/2$ and N_s:

$$\Phi_{tm} = \pi \frac{D}{N_s} L \int_{-\frac{\alpha_t}{2}}^{\frac{\alpha_t}{2}} \sum_{n=1,3,5,..}^{\infty} B_n \cos(n\theta) d\theta = 4.1 * 10^{-3} \ Wb \qquad (5.17)$$

The steel used in the machine is type NO 007 from Cogent Steel [68] and from its typical DC magnetization curve shown in Figure 5.6, a value of 1.45 T is chosen because 1.45 T is just around the knee point of this B-H curve. Higher flux density values in teeth and cores reduce the steel use but at the same they cannot exceed knee point to avoid saturation. The tooth width, stator and rotor core thickness are calculated according to (3.21) to (3.23) with a lamination factor of 0.95:

$$T_{sc} = \frac{\Phi}{2B_{sc}Ll_f} = \frac{2.11*10^{-2}}{2*1.45*160/1000*0.95}*1000 = 47.9\ mm$$
$$T_{rc} = \frac{\Phi}{2B_{rc}Ll_f} = \frac{2.11*10^{-2}}{2*1.45*160/1000*0.95}*1000 = 47.9\ mm \quad (5.18)$$
$$T_{sw} = \frac{\Phi_{tm}}{B_{st}Ll_f} = \frac{4.1*10^{-3}}{1.45**160/1000*0.95}*1000 = 18.6\ mm$$

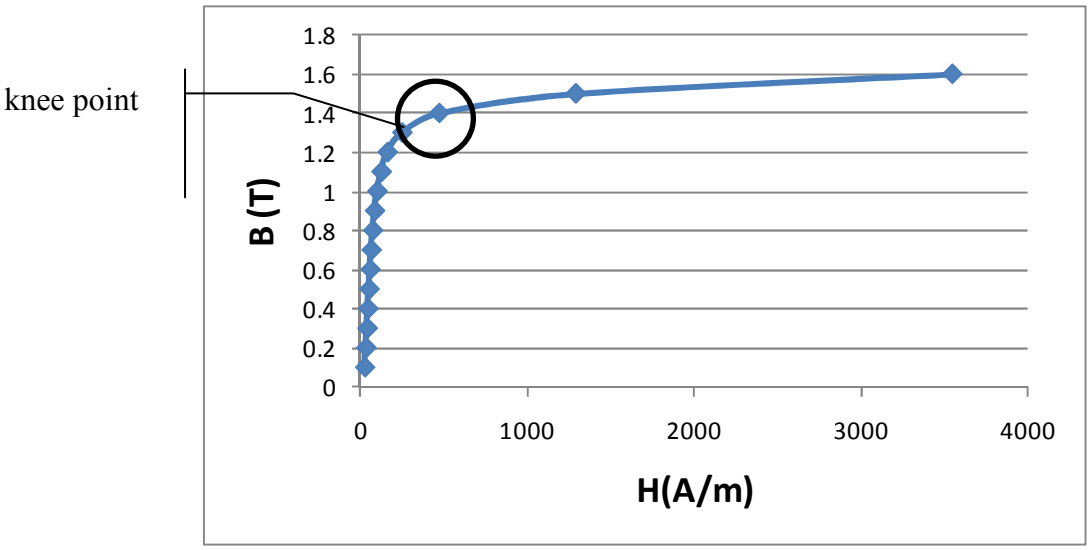

Figure 5.6: Typical DC magnetization curve of NO 007 [68]

The rotor inner diameter D_{ri} is calculated according to geometrical relations as shown in Figure 3.3

$$D_{ri} = D - 2*(g + h_m + T_{rc}) = 215 - 2*(1 + 8.5 + 47.85) = 100.3 \text{ (mm)}. \quad (5.19)$$

5.6.2.5 Inductance calculation

According to (3.16), the armature reaction inductance L_m is calculated as

$$\begin{aligned} L_m &= \frac{3}{\pi} * (\frac{K_w N_c}{p/2})^2 \frac{\mu_0}{g' K_c} DL \\ &= \frac{3}{\pi} * (\frac{0.9659 N_c}{2})^2 \frac{4\pi * 10^{-7}}{9.0952/1000 * 1.0000} * 215 * 160 * 10^{-6} \text{ (H)}. \end{aligned} \quad (5.20)$$

In this example, H_{s0} and H_{s1} of Figure 3.3 are chosen to be both 1 mm. B_{s1} can be estimated as:

$$\begin{aligned} B_{s1} &= \pi(D + 2(H_{s0} + H_{s1})) / N_s - T_{sw} \\ &= \pi(215 + 2(1+1)) / 24 - 18.6 = 10.06 \text{ (mm)}. \end{aligned} \quad (5.21)$$

For the calculation of leakage inductance, B_{s2} can be temporarily assumed to be $2B_{s1}$ and H_{s2} can be assumed to be $2T_{sw}$ at this stage. Their actual values will be calculated later when the number of stator winding turns is solved and the leakage inductance calculation will be also updated with the actual values. Since the armature reaction is the major inductance component, the calculation of the number of stator winding turns is generally not affected by this assumption of B_{s2} and H_{s2}. According to (3.17) and (3.18), the stator slot leakage inductance is calculated as:

$$\begin{aligned} L_{sls} &= 2\mu_0 L \frac{N_c^2}{pq} ([\frac{2}{3}\frac{H_{s2}}{B_{s1} + B_{s2}} + 2\frac{H_{s1}}{B_{s0} + B_{s1}} + \frac{H_{s0}}{B_{s0}}]\frac{1 + 3\beta}{4}) \\ &= 2 * 4\pi * 10^{-7} * \frac{160}{1000} \frac{N_c^2}{4\frac{24}{4*3}} ([\frac{2}{3}\frac{2*18.6}{10.1 + 2*10.1} + 2\frac{1}{2+1} + \frac{1}{2}]/1000\frac{1+3}{4}) \text{ (H)}. \end{aligned} \quad (5.22)$$

The slot shape is approximated as trapezoid and the slot area A_s is estimated as:

$$A_s = \frac{B_{s1} + B_{s2}}{2} * H_{s2} \quad (5.23)$$

Hence, the end winding leakage is calculated based on (3.19) and is expressed as:

$$L_{sle} = \frac{1}{2} pq\mu_0 * (T_w + \frac{B_{s1} + B_{s2}}{2}) * (\frac{3N_c}{N_s})^2 \log(\frac{(T_w + \frac{B_{s1} + B_{s2}}{2})\sqrt{\pi}}{\sqrt{2A_s}})$$
$$= \frac{1}{2} 4 \frac{24}{4*3} 4\pi * 10^{-7} (18.6 + \frac{10.1 + 2*10.1}{2*1000}) * (\frac{3N_c}{24})^2 \log(\frac{(18.1 + \frac{10.1 + 2*10.1}{2})\sqrt{\pi}}{\sqrt{2\frac{10.1 + 2*10.1}{2} * 2*18.1}}) \text{ (H).} \quad (5.24)$$

5.6.2.6 Number of stator turns calculation

The supply voltage U of the example machine is 480 V (line-to-line). Hence, the number of stator winding turns can be solved to have the phasor diagram of Figure 3.5, which is represented analytically as:

$$(E_1 + I_{ph} R_{cu})^2 + (I_{ph}(X_m + X_{sl}))^2 = U^2. \quad (5.25)$$

Since all the terms in (5.25) are represented as function of N_c, the value of N_c can thus be solved to meet this equation. For this example, N_c is calculated to be 57. However, for this machine with a double layer stator winding, the number of conductors per half slot should be an integer. Hence, N_c should be multiples of $2*q/2 = 8$. The closest number to meet this requirement is 56, which means the actually applied voltage to the machine to produce the rated output power is slightly different from the specified 480 V (approximately 56/57*480 = 471 V) . Since SMPM machines are supplied by inverters with adjustable voltage, this small variation of supply voltage is achievable. With $N_c = 56$, the back EMF and stator current per phase is calculated based on (5.13) and (5.14) to be:

$$E_1 = 265.7 \text{ (V), or 460.2 V (line-line)}$$
$$I_{ph} = I_{ph} = \frac{P_{out}}{n_{phase} E_1} = \frac{15200}{3*265.7} = 19.1 \text{ (A).} \quad (5.26)$$

The armature reaction inductance and leakage inductance are calculated to be:

$$L_m = \frac{3}{\pi} * (\frac{0.9659 N_c}{2})^2 \frac{4\pi * 10^{-7}}{9.0952/1000 * 1.0000} * 215 * 160 * 10^{-6} \text{ (H)}$$
$$= 3.3 \text{ (mH).} \quad (5.27)$$
$$L_{sl} = 0.35 \text{ (mH).}$$

5.6.2.7 Slot depth calculation

For the phase current calculated in the previous step and the current density selected at the beginning, the wire cross sectional area is calculated as:

$$A_{cu,i} = \frac{I_{ph}}{J_s} = \frac{19.1}{4} = 4.77 \text{ (mm}^2\text{)} \quad (5.28)$$

The closest standard gauge wire has a diameter of d_w = 2.5873 mm. In general, if d_w >1.3 mm in low power machines, such as this 15 kW machine, a few conductors with smaller diameters is used in parallel [9]. When winding the coils, the two or more wires are held together and wound as one wire [69]. In this example, a_p = 4 wires are used in parallel and the wire diameter is then:

$$d_{w2} = \sqrt{\frac{4A_{cu,i}}{\pi a_p}} = \sqrt{\frac{4 * 4.77}{\pi * 4}} = 1.23 \text{ (mm)} \quad (5.29)$$

The closest standard AWG wire has a diameter of 1.29 mm and four of these wires in parallel have a total cross sectional area of A_{cu} = 5.23 mm^2. This wire diameter is then smaller than 1.3 mm and also smaller than the slot opening of 2 mm, which enables the wires to fit through the slot through slot opening. With a slot fill factor of 40%, the slot area needed to fit such wires is:

$$A_s = \frac{6 N_c A_{cu}}{N_s f_f} = \frac{6 * 56 * 5.23}{24 * 0.4} = 183.1 \text{ (mm}^2\text{)}. \quad (5.30)$$

From equations (3.25) to (3.27), H_{s2} and B_{s2} can be found as:

$H_{s2} = 19.2$ (mm), $B_{s2} = 15.1$ (mm).

The current density is recalculated when the standard wire gauge is selected:

$$J_s = J_{sini} * \frac{A_{cu,i}}{A_{cu}} = 3.63 \text{ (A/mm}^2\text{)}. \tag{5.31}$$

5.6.2.8 Stator outer diameter calculation

After the tooth height is determined, the stator outer diameter D_o is then given by:

$$\begin{aligned} D_o &= D + 2*(H_{s0} + H_{s1} + H_{s2} + T_{cs}) \\ &= 215 + 2*(1+1+19.2+47.85) = 353.2 \text{ (mm)}. \end{aligned} \tag{5.32}$$

At this point, the electromagnetic trial design of the SMPM machine is complete. The next step is to calculate the performance of this trial design.

5.6.2.9 Frame thickness calculation

The frame thickness is calculated by solving (5.1). The term T_{max} is the maximum torque that could be applied to the shaft and varies by application. In this example, a value of 300 Nm (about 4 times the rated torque for illustration purposes) is used. A value of 50 is assigned to the safety factor n, which indicates a fairly rigid frame structure [70]. Steel is used as the frame material and hence σ_{yield} is $120*10^6$ Pa. With the above input, the frame thickness is calculated to be:

$$t_{frame} = 1.27 \text{ (mm)}. \tag{5.33}$$

5.6.2.10 Weight and volume calculation

The weight of the SMPM machine is comprised of the weight of the stator core, stator winding, permanent magnets, rotor core, and the frame. With a ρ_s = 7.8 kg/m^3 estimated as the mass density for the stator and rotor cores, the weight of the stator core is:

$$W_{sc} = \frac{\pi}{4}(D_o^2 - (D_o - 2*T_{sc})^2)*L*\rho_s$$
$$= \frac{\pi}{4}(353.2^2 - (353.2 - 2*47.85)^2)*160*10^{-9}*7.8*10^3 \quad (5.34)$$
$$= 57.3 \text{ (kg)},$$

the total weight of the stator teeth is

$$W_{st} = N_s*T_w*(H_{s0} + H_{s1} + H_{s2})*L*\rho_s$$
$$= 24*18.6*(1+1+17.2)*160*10^{-9}*7.8*10^3 \quad (5.35)$$
$$= 11.8 \text{ (kg)},$$

and the weight of the rotor core is

$$W_{rc} = \frac{\pi}{4}((D_{ri} + 2*T_{rc})^2 - D_{ri}^2)*L*\rho_s$$
$$= \frac{\pi}{4}((100.3 + 2*47.85)^2 - 100.3^2)*160*10^{-9}*7.8*10^3 \quad (5.36)$$
$$= 27.8 \text{ (kg)}.$$

The permanent magnets used in this machine have a mass density of ρ_{pm} = 7.4 kg/m^3. The weight of the permanent magnets therefore given by

$$W_{pm} = \frac{\pi}{4}(D^2 - (D - 2h_m)^2)*\alpha_p*L*\rho_{pm}$$
$$= \frac{\pi}{4}(215^2 - (215 - 2*8.5)^2)*0.83*160*10^{-9}*7474 \quad (5.37)$$
$$= 5.4 \text{ (kg)}.$$

With an estimate of the coil-end extension length to be 10 mm at each end (a typical value given by [12]), the total length of winding coils per phase is estimated to be

$$l_c = 2(L + l_{end})N_c = 2(L + 2l_{ext} + \frac{\pi(D + 2(H_{s0} + H_{s1}) + H_{s2}))}{p}\beta)$$
$$= 2(160 + 2*10 + \frac{\pi(215 + 2(1+1) + 17.2))}{4})N_c \quad (5.38)$$
$$= 3.06*10^4 \text{ (mm)}.$$

Hence, the weight of the stator winding is (neglecting the weight of insulation components):

$$W_{sw} = 3\rho_{cu} A_{wire} l_c = 3*8.96*10^3 *5.23*3.06*10^4 *10^{-9} = 4.3 \text{ (kg)}. \quad (5.39)$$

The weight of the machine frame is (assuming the machine frame has an additional length of 30% of the core length to allow for end winding clearances) :

$$\begin{aligned} W_{fm} &= \frac{\pi}{4}\rho_s((D_o + 2*t_{frame})^2 - D_o^2)L(1+30\%) \\ &= \frac{\pi}{4}((353.2+2*1.27)^2 - 353.2^2)*160*10^{-9}*7.8*10^3(1+30\%) \\ &= 2.3 \text{ (kg).} \end{aligned} \quad (5.40)$$

The total weight of the SMPM machine finally comes to be

$$W_t = W_{sc} + W_{st} + W_{rc} + W_{pm} + W_{sw} + W_{fm} = 108.9 \text{ (kg)} \quad (5.41)$$

Allowing for the additional length of 30%, the volume of the machine is:

$$\begin{aligned} Volume &= \frac{\pi}{4}(D_o + 2*t_{frame})^2 *(1+30\%)L \\ &= \frac{\pi}{4}((353.2+2*1.27)^2 *1.3*160*10^{-9} \\ &= 0.02 \text{ (m}^3\text{)} \end{aligned} \quad (5.42)$$

5.6.2.11 Loss and efficiency calculation

The resistivity at the expected temperature of 150 ^oC has a resistivity of $2.52*10^{-8}$ Ωm. The dc resistance of this example machine design is:

$$R_{dc} = \rho_c \frac{l_c}{A_{cu}} = 2.52*10^{-8} * \frac{3.05*10^4}{5.23} *10^3 = 0.15 \text{ (}\Omega\text{)}. \quad (5.43)$$

The skin depth of copper at 60 Hz is:

$$\delta = \frac{1}{\sqrt{\pi\mu_0\mu_r\sigma f}} = \frac{1}{\sqrt{\pi*4\pi*10^{-7}/(1.68*10^{-8})*60}} = 8.4 \text{ (mm)} \quad (5.44)$$

Since the wire diameter is 2.58 mm, which is much smaller than the skin depth of 8.4 mm. The skin effect can be safely neglected and the ac resistance is approximately the same as dc resistance. The copper loss of the trial design is:

$$P_{cu} = 3 * I_{ph}{}^2 * R_{cu} = 3 * 19.1^2 * 0.15 = 159.2 \text{ (W)} \tag{5.45}$$

From the core loss data shown in Table 5.4, the non-oriented steel NO 007 at 0.007 inch nominal thickness has a core loss density of approximately D_{core} = 3.03 W/kg at 60 Hz. Hence, the core loss of this machine at rated condition is:

$$P_{core} = D_{core} * (W_{sc} + W_{st}) = 3.03 * (11.8 + 57.3) = 198.95 \text{ (W)} \tag{5.46}$$

Table 5.4: Core loss data of NO 007 [68]

Flux density (T)	0.1	0.2	0.3	0.4	0.5	0.6	0.7	0.8	0.9
Specific core loss (W/kg)	0.022	0.088	0.198	0.308	0.44	0.572	0.726	0.902	1.1
Flux density (T)	1	1.1	1.2	1.3	1.4	1.5	1.6	1.7	1.8
Specific core loss (W/kg)	1.32	1.562	1.87	2.266	2.75	3.3	3.828	4.334	4.796

As explained previously in section 5.6.2.3, the windage and friction loss is assumed to be P_{wf} = 200 W, the machine efficiency is

$$Eff = \frac{P_{out}}{P_{out} + P_{cu} + P_{core} + P_{fw}} = \frac{15000}{15000 + 159.2 + 198.95 + 200} = 95.2\% \tag{5.47}$$

5.6.2.12 Armature reaction calculation

Neglecting the harmonics in the stator phase current, the armature reaction field produced by the three phase winding is derived based on [50] as:

$$B_{wd}(r,t) = \mu_0 \frac{N_c}{\pi} \frac{1}{g'} I_{ph} \sum_v \frac{1}{v} K_{sov} K_{pv} F_v(r) * \sin(\frac{p}{2} \omega_r t + \theta_1), \tag{5.48}$$

where t is time and at $t = 0$ the phase A current has a phase angle of zero, g' is effective airgap length as calculated in (5.5), v is the order of the spatial harmonics produced by the three phase windings and only has values as follows for symmetrical three phase windings when only the fundamental component of the phase current is considered

$$v = 6c \pm 1, \; c = 1, 2, 3, \ldots . \tag{5.49}$$

K_{sov} is called the slot-opening factor and is expressed as:

$$K_{sov} = \frac{\sin v \frac{B_{s0}}{2R_s}}{v \frac{B_{s0}}{2R_s}} = \frac{\sin v \frac{2}{215}}{v \frac{2}{215}}. \tag{5.50}$$

K_{pv} is the winding pitch factor and is expressed as:

$$K_{pv} = \sin(\beta \frac{\pi}{2}) = \sin(1 * \frac{\pi}{2}) = 1. \tag{5.51}$$

The function $F_v(r)$ is given as:

$$F_v(r) = g' \frac{v}{r} (\frac{r}{R_s})^v \frac{1 + (\frac{R_r}{r})^v}{1 - (\frac{R_r}{R_s})^v} = 9.0952 * \frac{v}{r} (\frac{r}{215/2})^v \frac{1 + (\frac{215/2 - 1}{r})^v}{1 - (\frac{215/2 - 1}{215/2})^v}. \tag{5.52}$$

When the stator current is aligned with back EMF as Figure 3.5, $\theta_1 = \pi/2$. Since the focus is the effect of the armature reaction field upon the flux density in the stator, the armature reaction field is calculated at $r = R_s$. The calculated armature reaction magnetic field in the airgap is shown in Figure 5.7. This field B_{wd} is added arithmetically to the airgap magnetic field $B_{gap\text{-}mag}$ produced by the permanent magnet calculated in section 5.6.2.1

and the resulting maximum airgap flux density B_{airm} is found. The maximum flux in a stator tooth is then approximately given by:

$$\Phi_{tm} = B_{airm} * \frac{\pi D}{N_s} L = 0.9768 * \frac{\pi * 215}{24} * 160 = 4.4 * 10^{-3} \text{ (Wb)}. \qquad (5.53)$$

The maximum tooth flux density is then calculated as:

$$B_{stm} = \frac{\Phi_{tm}}{T_w L l_f} = B_{airm} * \frac{\pi D}{N_s l_f T_{sw}} = 0.9768 * \frac{\pi * 215}{24 * 0.95 * 18.6} = 1.56 \text{ (T)} \qquad (5.54)$$

B_{stm} is then compared to steel B-H curve to determine whether the armature reaction is causing excessive saturation. In this case, according to the B-H curve of NO 007 (Figure 5.6), 1.56 T is not too high and the flux density saturation in the stator teeth is not severe.

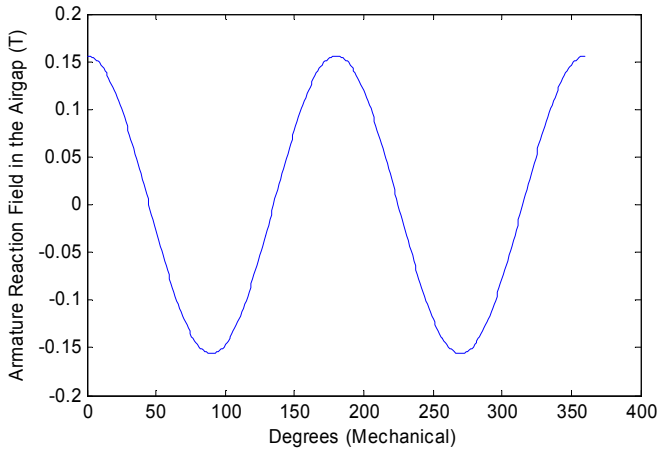

Figure 5.7: Calculation result of the armature reaction field in the airgap

As described earlier, the operating temperature of the permanent magnets is assumed to be the same as the maximum stator winding temperature. As shown in Figure 3.9, at an expected operating temperature of 153 ^{o}C, B_d is found to be approximately zero. Hence, the maximum permitted value of steady state stator current before the reverse field exceeds H_d is

$$I_{dgmrm} = \frac{P\pi}{6\mu_0(K_w N_c)}(B_r h_m - B_d(g + h_m))$$
$$= \frac{4\pi}{6*4\pi*10^{-7}(0.9659*56)}(1.04*8.5 - 0*(1+8.5))*10^{-3} \qquad (5.55)$$
$$= 272.2 \text{ (A)}.$$

The rated current I_{ph} = 19.77 A, which is smaller than I_{dgmrm} and hence there is no demagnetization at rated condition.

To protect the permanent magnets at short-circuit, the necessary leakage inductance is:

$$\frac{L_{lsn}}{L_m} \geq \left(\frac{\frac{8}{\pi} B_r h_m * PCC}{B_r h_m - B_d g'} \right) - 1 = \left(\frac{\frac{8}{\pi} 1.04*8.5*0.833}{1.04*8.5 - 0*9.0952} \right) - 1 = 1.11 . \qquad (5.56)$$

For this example machine, L_s/L_m = 0.1 <1.11, which means there is a risk of demagnetization if there is a three-phase short circuit. To protect the permanent magnets at short circuit, the stator design can be modified to increase the leakage inductance (increase slot height and decrease slot width), or additional series inductance may be added to limit the short circuit current during inverter faults[52].

5.6.2.13 Winding temperature calculation

The calculated copper loss, core loss and machine geometry are inputs to the generic thermal model described in section 5.4 and the winding temperature distribution is calculated for a certain ambient temperature and boundary condition. In this example design, the ambient temperature is 27 ^{o}C and the boundary condition is: horizontal configuration, smooth surface, natural convection. With the input of loss distribution in the stator and the boundary conditions, the generic thermal model automatically generates meshes for the stator and uses finite-difference approach to solve the temperature

distribution of the stator. For this example, the maximum winding temperature is calculated to be 161.1 ^{o}C, which is about 8 ^{o}C higher than the specified 153 ^{o}C.

5.6.3 Summary of example design

An example design is illustrated in this section using the proposed Electromagnetic-Thermo-Mechanical design model with detailed numerical results. The MATLAB scripts for this example are attached in Appendix II.

Before the optimization process starts, a few parameters are manually chosen and held fixed during optimization. The fixed values chosen for these parameters are listed in Table 5.5. These values are selected by the designers based on material and manufacturing constraints and in any case may only vary within a small range. Hence, the values of parameters listed in Table 5.5 are not determined by PSO. This helps to reduce the dimensions of the optimization problem. If the designer is interested to see the effect of those parameters to the machine performances, case studies can simply be performed by comparing several designs with different values chosen for such parameters. For example, if the designer wants to see how the machine performance is improved by increasing the slot fill factor, the slot fill factor can be chosen to be 40%, 50 %, 60% and 70%, and PSO is run the to find the optimal design for each of the four slot fill factor values and compare them. This will show whether an investment in improving the slot fill factor will be worthwhile.

Table 5.5: List of parameter values chosen and fixed during optimization

Parameter name	**Values chosen**
Slot opening B_{s0}	2 mm

Slot tip height H_{s0}	1 mm
Slot wedge height H_{s1}	1 mm
Steel lamination factor	0.95
Slot fill factor	40% (distributed winding)
Airgap	1 mm

5.7 Optimization result and discussion

5.7.1 Objective function

To account for various requirements in the permanent magnet motor design, the objective functions used here have three performance indexes, namely: weight (kg), efficiency (0-100%), and the torque per ampere at the rated condition (Nm/Arms). Because the frame calculation is included in the EM-TM design method, the machine weight is not the active weight as proposed in [71] but a realistic estimation of the weight of a completed manufactured machine product. Such an objective function is defined in (5.57).

The candidate designs have weights, efficiencies, and torque/ampere values that range around 20-50 kg, 50%-100% and 2-5 Nm/Arms, respectively. The terms in the objective function in (5.57) are first normalized to all have about the same magnitude, and then the weighting factors or coefficients before each term (called an index) index are adjusted to afford different levels of importance to each index.

$$output = Weight + (1 - Eff) * 100 - TperA * 10 \tag{5.57}$$

If this machine is to be designed for applications where the weight of machine is critical, then the objective is defined to contain *Weight* only, and other objectives then become design constraints, such as minimum efficiency, maximum length, and so on.

5.7.2 Design constraints and penalty function

The machine design have several constrains, such as the maximum armature reaction field and maximum winding temperature. In addition, there often are constraints in the dimensions of the machine. For certain applications, there are also other specific constrains, such the maximum rotor inertia, maximum cost, and so on. Those design constraints add more complexity to the nonlinear machine design optimization problem. To simplify the optimization process, a penalty function is introduced to convert a constrained problem to an unconstrained problem whose solutions ideally converge to the original constrained problem. The main idea of a penalty function is that when there is a violation of certain constraints in a candidate design, a large value is added to the objective function to indicate that this is a poor candidate. Various forms of penalty functions have been proposed and the penalty function in this paper is defined based on the physics of the machine and the application requirement of the design problem.

5.7.2.1 Penalty function for armature reaction

As described earlier by (3.36), (3.37), and (3.38), a large armature reaction magnetic field may saturate the rotor and stator steel as well as risk demagnetization of the magnets. Hence, linear distance based penalty functions are used to penalize large currents. A distance function d(x) to represent the distance to a feasible design is defined in general as (5.58):

$$d(x)=\begin{cases}0 & \text{when } x<0\\ 1 & \text{when } x\geq 0\end{cases} \tag{5.58}$$

For the steel saturation, the flux density to saturate the steel depends on the B-H curve of the steel used. The linear distance based penalty function for the saturation in the teeth $pelSat_t$ is defined by (5.59)

$$pelSat_t = (B_{tm} - B_{tm,th}) * d(B_{tm} - B_{tm,th}), \tag{5.59}$$

An example of $pelSat_t$ for a typical B-H curve of non-oriented steel is illustrated in Figure 5.8. Similar penalty functions for the saturation in the stator core $pelSat_{sc}$ and the rotor core $pelSat_{rc}$ can also be defined.

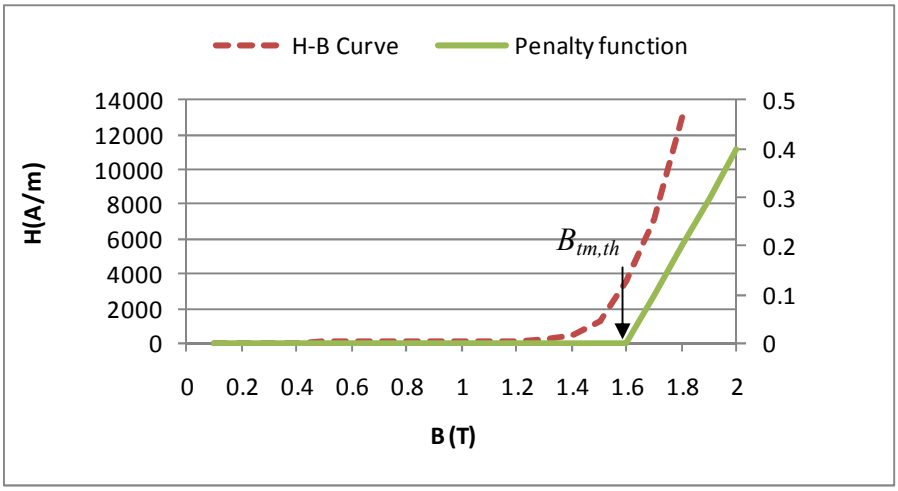

Figure 5.8: A typical penalty function and silicon steel B-H curve for designs with flux density saturation

For the magnet protection from demagnetization, two similar linear distanced based penalty functions are defined in (5.60) and (5.61).

$$pelDmg_r = \frac{(I_{ph} - I_{dgrm})}{I_{dgrm}} * d(I_{ph} - I_{dgrm}) \tag{5.60}$$

$$pelDmg_s = \frac{(K_{lmrm} - \frac{L_{ls}}{L_m})}{K_{lmrm}} * d(K_{lmrm} - \frac{L_{ls}}{L_m}) \tag{5.61}$$

5.7.2.2 Penalty function for winding temperature

As described earlier, a machine designed with a higher winding temperature will have less weight but shorter insulation life for the same insulation class. To consider this trade-off in the machine design objective, a penalty function for temperature rise is defined as (5.62)

$$pelTemp = \max(\frac{L_{EX} - L_T}{L_{EX}}, 0), \tag{5.62}$$

where L_{EX} is the expected winding insulation life. For example, if a class B winding insulation is used and the expected insulation life is 20,000 hours, the value of *pelTemp* is plotted in Figure 5.9 according to the following equation:

$$pelTemp = \max(0, \frac{20000 - 10000 * 10^{-0.03(T-140)}}{20000})$$

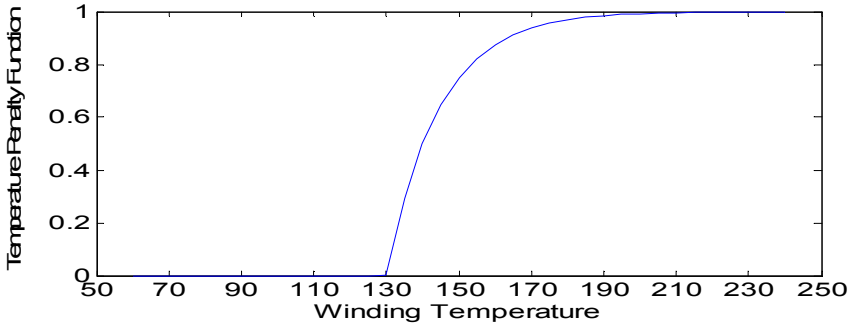

Figure 5.9: Plot of *pelTemp* for insulation class B and L_{EX} = 20000 hours

5.7.2.3 Penalty function for spatial constraints

In many applications, the machine size spatial constraint is not simply the volume of the machine, but rather a limit on length, or width, or height, or a combination of these.

As a result, the maximum outer diameter and length of the machine including the frame are defined as the problem constraints. The machine outer diameter is the sum of the stator core diameter, the thickness of the frame and some margin for cooling fins and clearances. For the machine length, it is necessary to leave extra space for end windings, end cap, bearing and other necessary components in addition to the active core length. Hence, any machine spatial constraint can be represented as a certain allowable range for the machine active length and/or active diameter. Penalty functions similar to (5.59) can be used (denoted as *pelD* and *pelL*) to penalize the diameter or length when they approach their respective constraints.

5.7.2.4 Penalty function for a combination of all constraints

The various penalty functions described above can be added to represent all the design constraints. The design objective function is then modified from (5.57) to (5.63) to include the penalty function

$$output = Weight + (1 - Eff) * 100 - TperA * 10 + penalty \tag{5.63}$$

An example of such a penalty function is illustrated in (5.64)

$$\begin{aligned} penalty = {} & k_1 * pelSat_t + k_2 * pelDmg_r + k_3 * pelTemp \\ & + k_4 * pelD + k_5 * pelL \end{aligned}, \tag{5.64}$$

where k_i (i=1,2,3,4,...) represents the importance of violating certain constraints. First a set of values for k_i is chosen to scale each term in (5.64) to have a value of 1 when the limit is exceeded by 10%. For example, k_1 before $pelSat_t$ and k_3 before $pelTemp_t$ are calculated as:

$$k_1 = \frac{1}{pelSat_t \mid_{B_{tm}=110\%B_{tm,th}}} = \frac{1}{(110\%B_{tm,th} - B_{tm,th})} \tag{5.65}$$

$$k_3 = \frac{1}{pelTemp\,|_{L_T=90\%L_{EX}}} = \frac{1}{\max(\frac{L_{EX} - 90\%L_{EX}}{L_{EX}}, 0)}. \tag{5.66}$$

Then the values of k_i are adjusted to represent the severeness of violating certain design constraints. For example, if there is a strict constraint on the machine size, k_4 or k_5 are then assigned very large values, and vice versa. More penalty functions can be added into *penalty* to include additional specific design constraints.

In this design of the 15 kW, 1800 rpm, 60 Hz SMPM machines, the constraints considered are: minimum winding insulation life of 20,000 hours for a class F insulation, no demagnetization at rated condition, the maximum stator tooth flux density of 1.6 T including the armature reaction magnetic field, maximum stator outer diameter of D_{om} = 500 mm, and maximum length (not including spaces for end-winding) of 300 mm. To scale each term in (5.64) to have a value of 1 when the limit is exceeded by 10%, values of k_i's are calculated as:

$$\begin{aligned}
k_1 &= \frac{1}{pelSat_t\,|_{B_{tm}=110\%B_{tm,th}}} = \frac{1}{(110\%B_{tm,th} - B_{tm,th})} = \frac{1}{(110\%*1.6-1.6)} = 6.25 \\
k_2 &= \frac{1}{pelDmg_r\,|_{I_{ph}=110\%I_{dgrm}}} = \frac{1}{\frac{(110\%I_{dgrm} - I_{dgrm})}{I_{dgrm}}} = 10 \\
k_3 &= \frac{1}{pelTemp\,|_{L_T=90\%L_{EX}}} = \frac{1}{\max(\frac{L_{EX} - 90\%L_{EX}}{L_{EX}}, 0)} = 10 \\
k_4 &= \frac{1}{pel_D\,|_{D_o=110\%D_{om}}} = \frac{1}{\frac{(110\%D_{om} - D_{om})}{D_{om}}} = 10 \\
k_5 &= \frac{1}{pel_L\,|_{L=110\%L_m}} = \frac{1}{\frac{(110\%L_m - L_m)}{L_m}} = 10
\end{aligned} \tag{5.67}$$

Prior design experience gives an approximate range of *output* in (5.57) to be around 50. To make all design constraints relatively strict, when any of the constraints is violated, a value of 2 times of the *output* is assigned *penalty*. Hence, all the k_i's are increased by 50*2 = 100 from (5.67), which gives $k_1 = 625$, $k_2 = k_3 = k_4 = k_5 = 1000$.

5.7.3 Optimization result

PSO is run with a swarm of 6 particles to find the optimal design subject to the objective function defined in (5.63). The particles start from random positions at the beginning and for this example design find the correct *final optimal design* (FOD) after 120 iterations (or trial designs). The FOD in Table 5.6 has a current density of 3.63 A/mm^2 that gives the desired winding temperature (153 ^oC corresponds to a life 20,000 hours for class F insulation) to fully utilize the material capabilities.

On an ordinary desktop computer with 3GB memory and Intel Pentium 4 CPU, running this PSO with 120 iterations for 6 particles takes only 15 minutes. On the other hand, on the same computer, the 15 minutes is just enough to run a single transient FEA to evaluate a single machine's electromagnetic performance. It would therefore eventually take several days for 6 particles with 120 iterations if FEA were to be used for each iteration. Hence, the machine design cycle is reduced significantly by the proposed method.

Table 5.6: Optimal design found by PSO

D (mm)	154.8	Wt. (kg)	56.6	*pelDmgr*	0
L (mm)	113.9	Eff.	95.7 %	*pelSat*	0
h_m (mm)	8.7	T. per Amp (Nm/Arms)	4.31	*pelTemp*	0
J_s (A/mm2)	3.63	Temp. (^{o}C)	152.6		
Objective function			17.8		

5.7.4 Comparison with FEA

To verify the proposed SMPM design method, the final optimal machine design (FOD) is simulated by both electromagnetic FEA (Maxwell 12) and thermal FEA.

The phase current waveforms simulated by Maxwell FEA and calculated by the proposed analytical design method are compared in Figure 8 that shows that the results from the two methods agree closely. The FEA calculated flux densities in the machine appear in Figure 5.11 and show that all the values are correct as specified by the chosen type of steel. Since the proposed analytical design method has good accuracy in calculating the phase current and flux density for certain operating condition, it can be expected that the efficiency and torque per ampere calculation results are also accurate.

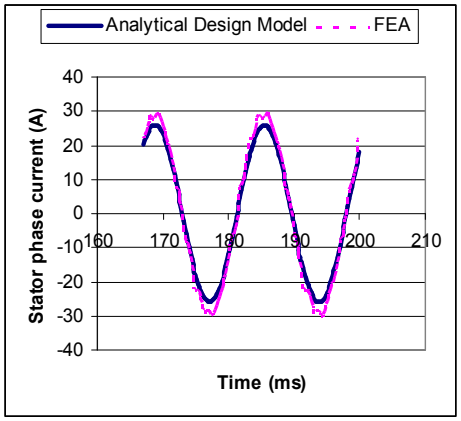

Figure 5.10: Comparison of the stator phase current calculation

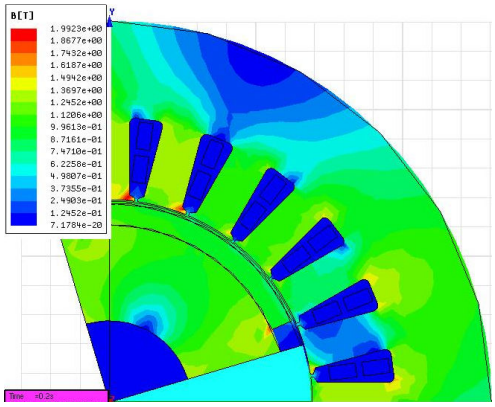

Figure 5.11: Flux densities in stator and rotor calculated by FEA

A thermal 3D FEA is also performed on the optimized motor to validate the FD thermal simulation used in the opitimization algorithm developed in section 5.4.

5.7.5 Discussion

One significant advantage of the proposed EM-TM integrated design and optimization is that the current density value is no longer chosen heuristically but is found by the PSO solution based on the machine design objectives and constraints. This advantage is illustrated in Table 5.7 below. Design A is the optimal design in Table 5.6. Designs B-D are also optimal designs found by PSO but the current densities are pre-

selected and then held fixed by the designer as in the traditional design process. The results in Table 5.7 show that the integrated EM-TM design is able to find machine designs with superior performance than the machines designed with traditional heuristic methods.

Table 5.7: Comparison of EM-TM design and traditional design

	Des. A	**Des. B**	**Des. C**	**Des. D**
J_s **(A/mm2)**	*3.63*	4.5	4	3
Wt. (kg)	*56.6*	81	64	59.8
Eff.	*95.7*	95.5%	95.6%	95.9%
T. per A. (Nm/Arms)	*4.31*	4.26	3.99	4.39
Winding Temp. (^{o}C)	*152.6*	153.3	152.9	152.8
Output	*17.8*	44.8	28.5	20.1

5.8 EM-TM integrated design considering load profiles

In many situations, electrical machines are used to drive a load with a specific load profile and duty cycle. It is important to consider the load profile in the machine design process. In the traditional machine design, however, this is done often with designer's experience or by using safety margins. Since both the electromagnetic and thermo-mechanical design model are able to consider machine transients, the load profiles can be fully considered in the proposed EM-TM integrated design and SMPM machines can be

optimized for a given specific load profile. This merit is illustrated by using the proposed design and optimization method to design three machines with the same duty cycle but three load profiles A, B, and C as shown in Figure 5.12, respectively. All the three machines have the same rated condition: 15 kW (full load), 1800 rpm and 60 Hz. At different load levels, the speed of the machines is constant at 1800 rpm at all times.

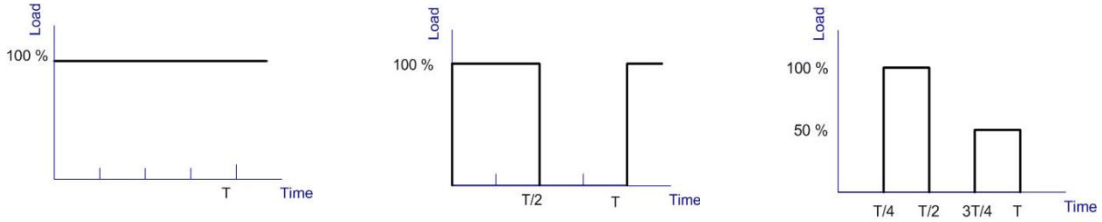

A B C

Figure 5.12: Three example load profiles

5.8.1 Loss estimation at transient

Given vector control for SMPM machines, the controller is trying to control the machine to follow the speed and torque reference command from the requirement of the load profile. A well-designed controller today has small steady-state error and fast response to changes in the speed or torque command. It is then valid to assume that the machine is able to exactly follow the speed and torque command of the load profile. Hence, under this assumption, the machine frequency f profile can simply determined from the load profile with the following equation:

$$f = \frac{n}{60} * \frac{p}{2}, \tag{5.68}$$

where n is the rotor speed in rpm and p is the number of the poles. Winding current is proportional to the output torque given no flux weakening below the rated speed and thus

can be also calculated. With the frequency and current determined, the core loss and copper loss can be then calculated with respect to a specific load profile.

5.8.2 Design and optimization result

As described in [1], the thermal model is able to analyze the transient distribution of machine temperature using given copper and core loss data. The same flowchart as Figure 5.4 can be used with the loss and temperature in transient included. From comparison purpose, the winding temperature limit is that the maximum winding temperature should not be over 150^{o} at any time for all the three load profiles. Aluminum is used for machine frames. All three designs have smooth surface, natural cooling and an ambient temperature of 27 ^{o}C. Different choices of materials, insulation systems, cooling conditions and design constraints can be used for different applications. Same materials as shown in Table 5.2 are used. The objective function is defined as (5.69)

$$output = Wt + (1 - Eff) * 500 + penalty, \tag{5.69}$$

where *penalty* is the penalty function to consider the design constraints, similarly to (5.64).

The same PSO used in section 5.7 is applied. The particles start from random positions at the beginning and for this example design find the correct optimal design after 120 iterations (or trial designs), which are shown in Table 5.8, where the Design A, B and C correspond to the three load profiles, respectively. The maximum winding temperatures for all three optimal designs are all close to their given limit (150 ^{o}C), which indicates that the material capabilities and cooling capabilities are fully utilized by the proposed method. The maximum winding temperatures as a function of time for Design B and C plotted by the TM model are shown in Figure 4 (a) and (b), respectively.

Table 5.8: Optimal Design found by PSO for three load profiles

	Design A	**Design B**	**Design C**
***D* (mm)**	184	163.3	114.4
***L* (mm)**	165.8	170.8	162.8
h_m (mm)	5.91	6.26	6.71
***Js* (A/mm2)**	4.14	4.11	3.65
Weight *(kg)*	93.9	83	58.8
Efficiency	97.3 %	97.2 %	97.1 %
Torque per Amp.* *(Nm/Arms)	4.58	4.71	4.44
Temp. (^{o}C)	150	148.6	149.4
output	75.1	63.3	43.2

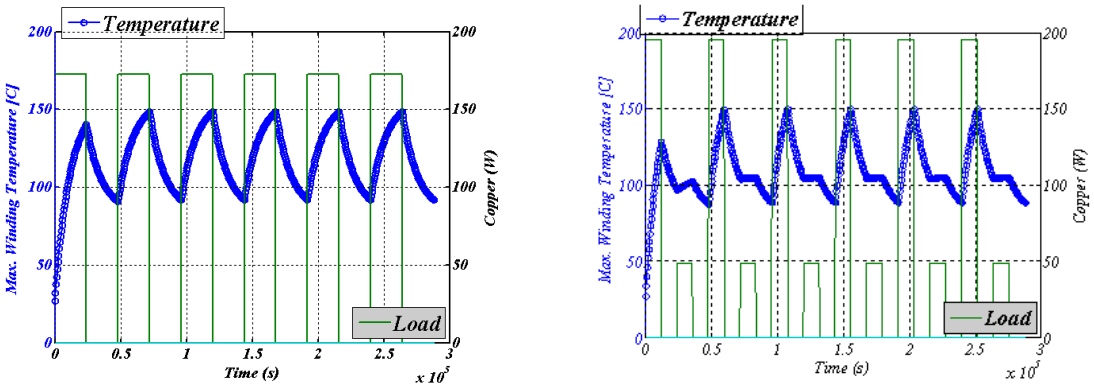

(a) Design B (b) Design C

Figure 5.13: The maximum winding temperature as a function of time for Design B and C

A comparison of the three optimal designs shows that the effect of different load profiles is an important factor to be considered in the design process. Design A runs with full load at all times, which means it generates the largest amount of losses among the three, hence Design A uses more materials than the other two. Design C has the least amount of losses and hence has a 37 % weight reduction compared to Design A.

A comparison of the current densities in the three designs shows that simply choosing a lower current density for machines with a lighter load profile is not an optimal choice. In this design example, Design C has the lightest load profile but its current density is the lowest (3.65 A/mm^2 compared to 4.14 and 4.11 A/mm^2 of Designs A and B). As mentioned earlier, the optimal selection of current density is a complicated, multi-physics problem, which needs a comprehensive machine design tool, such as the proposed integrated EM-TM method.

Although transient thermal simulation is run for each trial design with at least three load cycles in order to get the steady-state temperature information, running this PSO with 120 iterations for 6 particles (720 trial designs evaluated) takes only two hours on an ordinary desktop computer with 3GB memory and Intel Pentium 4 CPU. On the other hand, these two hours is even not enough for the transient simulation of a single machine design if multi-physics FEA is used. Hence, the machine design cycle is reduced significantly by the proposed method.

5.9 Chapter summary

A novel integrated Electromagnetic-Thermo-Mechanical design method for the design of Surface Mount Permanent Magnet machines is explained. In this integrated approach the current density is no longer heuristically selected and the thermal and

mechanical designs are no longer treated separately as is often done in traditional design. Particle Swarm Optimization is used to find designs that minimize user defined cost functions. The optimization results show that the integrated design approach is able to find optimal designs with systematical consideration of both electromagnetic and mechanical design factors, cooling capability and thermal limits. The proposed integrated design approach also has the merit of good computational efficiency and provides a significant time reduction of the design cycle compared to FEA.

CHAPTER 6
Sensitivity Analysis of the SMPM Machine EM-TM Integrated Design and Optimization

6.1 Introduction

Due to various reasons, the performances of manufactured machines sometimes vary from the design calculations. Common causes for those variations include deviations of material properties from datasheets, modeling errors, and manufacturing tolerances. It would thus be useful to carry out a sensitivity analysis to analyze how those variations affect machine performances. If the system can be fully representated by analytical equations and all the equations are differentiable, the sensitivity analysis is normally carried out by calculating the partial derivatives with respect to certain variables. However, not all the machine equations in this proposed research are differentiable. For example, the thermal model that calculates the winding temperature rise is based on a finite difference approach. For this purpose, certain machine parameters are therefore varied by small amounts around their nominal values used in the design calculations and the resulting machine performance variations are evaluated. This estimates the sensitivity by a numerical technique. The sensitivity analysis result gives indication on the robustness of the design modeling technique and helps machine designers to identify which machine parameters are important to ensure robust designs.

6.2 Sensitivity Analysis Problem Formulation

6.2.1 Parameter variations

The foremost task in sensitivity analysis is to discover the sources of variations. Three major sources of machine parameter variations are identified and explained in this section.

The first source of machine parameter variations comes from the material properties. The actual permanent magnets and steels used to build the machine usually do not have exactly the same property as specified by their catalog datasheets. These include the variations of demagnetization curves of the permanent magnets and B-H curves of steels. In addition, the steel loss density may increase from its catalog data by a factor of 1.6 to 1.8 [9], which is called core loss augmentation [9] and is due to mechanical machining (stamping value depends on the quality of the material, wear of the cutting tools, die cutting edges, etc.).

The second source of design parameters variations - machine modeling errors, is mainly due to the unavoidable assumptions and approximations made during the modeling. To obtain analytical solutions of magnetic fields, the stator and rotor are simplified to have some ideal properties and shapes. For example, the analytical solution of the airgap density waveform is solved based on assumptions of infinite permeability of the steel and a simplified shape of the stator slot. Otherwise, those design details will consume too much unnecessary modeling and computational effort and the design cycles will be slowed down. In addition to the simplifications for the purpose of obtaining analytical solutions, some other assumptions have to be made in the modeling calculations regarding how the machine is built. For example, the end-winding layout and

lengths depend on how the coils are wound, which is actually different for different machine manufacturing methods. This assumption leads to variations of stator resistances and end-winding leakage inductances.

The third source of design parameter variations is the manufacturing tolerances. The geometry parameters of the stator and rotor cannot be made to be exactly the same as the design specifications. These variations of the geometry parameters include tooth width, slot shape, core thickness, machine axial length, airgap length, magnet thickness and pole coverage. Lower tolerances in general mean higher manufacturing costs.

6.2.2 Sensitivity analysis approach

When one or some of the machine parameters vary from their design specifications, the physical operating condition of the machine changes and then machine performance indexes vary from design calculations, including efficiency, weight and winding temperature rise. For example, if the magnet used in the machine is actually stronger than specified by the catalog datasheet, less current is needed to produce the same output torque but the flux densities in the steel are higher. This machine then has a lower copper loss and higher core loss. Depending on how much those two loss components are affected, the machine efficiency and winding temperature will vary accordingly.

Hence, a good strategy is to first identify how the variations of certain parameters affect the machine operating conditions, and then relate such change of machine operating conditions to the variations of machine performance indexes. Figure 6.1 shows this proposed sensitivity analysis strategy.

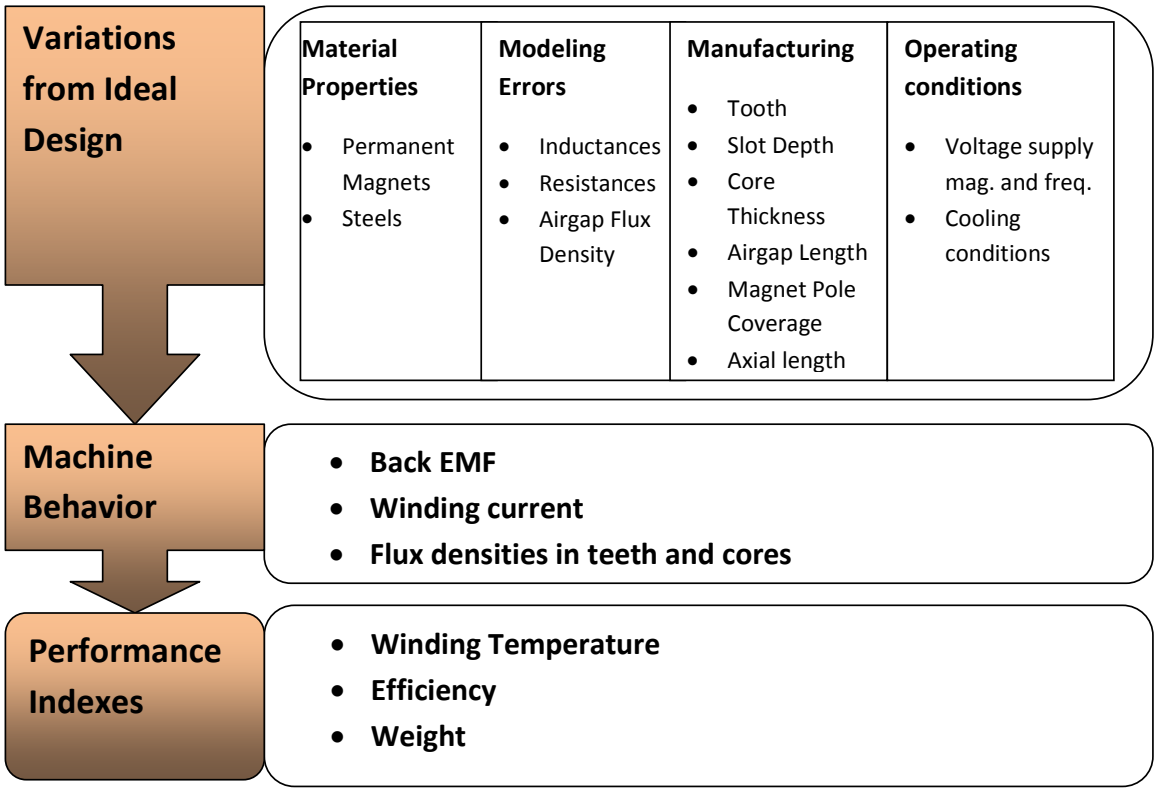

Figure 6.1: Flowchart of the sensitivity analysis.

Each machine parameter listed in Figure 6.1 is varied one by one around its original value used in the ideal design and the resulting variations of machine operating conditions (machine behavior) are first calculated. At the same time, another sensitivity analysis is carried out to study how the machine performance indexes change with variations of machine operating conditions. The sensitivity of machine performance indexes to the design parameters can be directly identified by combining the results of the above two sensitivity analyses. Less computation is needed to save some repetitive work in this way. More importantly, the physics reasoning behind the variation of performance indexes is revealed.

6.3 Sensitivity Analysis Approaches and Results

In this section, each machine parameter shown in Figure 6.1 is varied within a certain range around a nominal value. The effect of such parameter variations to the machine behaviors is first determined, and then the variation of the performance indexes is calculated. The benchmark machine design is the optimized design found in Table 5.6 of the previous chapter.

6.3.1 Variation of machine active weight

The active weight of an SMPM machines can be generally broken down into four components, weight of stator core, weight of stator winding, weight of magnets, and weight of rotor core. The variation of total machine weight is caused by the differences between the estimated and actual amount of materials to build the machine, primarily due to manufacturing tolerances. As the rotor has a relatively simple shape and only takes a small portion of the total machine active weight, the sensitivity analysis of the machine active weight is focused on the weight variation of stator core and winding.

The parameters that affect stator weight primarily are: tooth width, slot depth, core thickness, machine axial length and the length of the winding. The equations to calculate the machine weight in terms of these parameters are differentiable. Hence, how the machine weight varies with these parameters can be directly calculated. The results showing here is to illustrate how large the weight variations are. Modern machining tools are able to produce core laminations in relatively good agreement with the specified design geometry, and hence the variations of core geometry parameters are expected to be small (usually less than 5%). On the other hand, because the length of the end coils varies with the winding process, the actual total length of machine coils is expected to

have large variations. Figure 6.2 and Figure 6.3 shows the sensitivity analysis results of machine active weight to variations of machine parameters, which indicate that the stator active weight is more sensitive to variations in the axial length of the stator and not much affected by the tooth width, slot depth, core thickness and end-winding configuration. But overall, this sensitivity analysis result shows that the stator weight is not expected to differ significantly between the design calculation and the measured result of the manufactured stator.

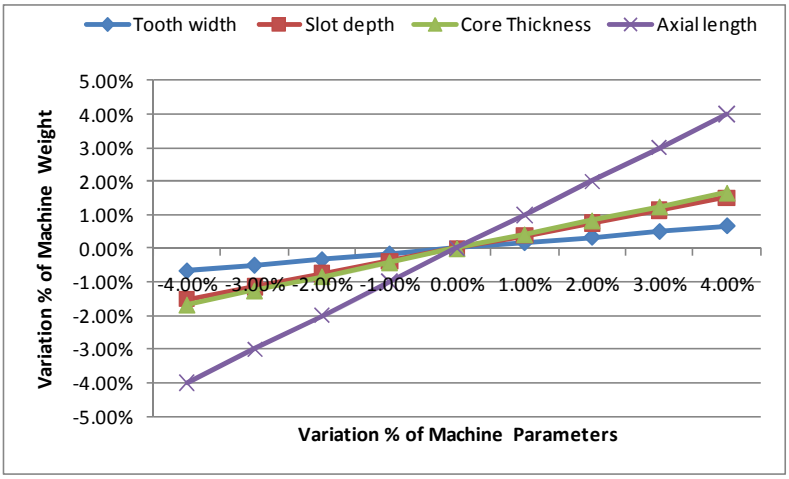

Figure 6.2: Variation of stator weight due to variations of geometry parameters.

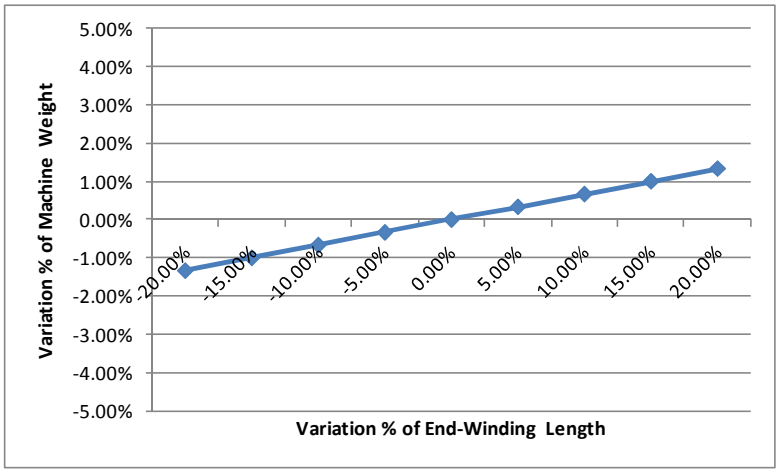

Figure 6.3: Variation of stator weight due to variations of end-winding length.

6.3.2 Variation of efficiency and winding temperature

6.3.2.1 From variations of machine parameters to variations of machine behavior

In this section, the sensitivity analysis is carried out for variations of material properties, modeling errors and manufacturing tolerances, respectively.

a) Variation of material properties- permanent magnet

The PM material property is characterized by the demagnetization curve, which is usually a line in the second quadrant of the B-H space for rare-earth PM's, such NdFeB and SmCo. A typical demagnetization curve is shown in Figure 6.4.

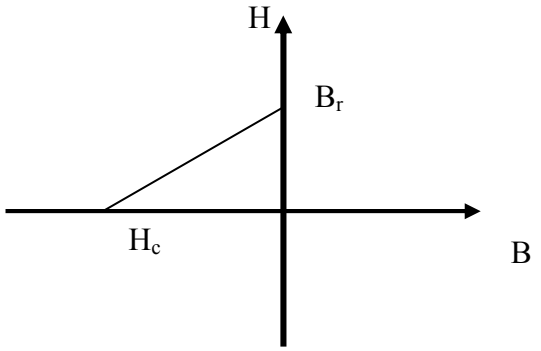

Figure 6.4: A typical B-H curve of rare-earth permanent magnets.

The B-H curve is defined by the residual flux density B_r and the relative permeability $\mu_r = \frac{B_r}{H_c}$. Hence, the variations of PM material properties can be represented by the variations of the values of B_r and μ_r. According to (3.4) to (3.13), the effect of variations of B_r and μ_r on the airgap flux density can be first calculated by getting the derivative of the airgap flux density with respect to B_r and μ_r. The variation of fundamental back EMF is directly proportional to the magnitude of the variation of the fundamental airgap flux density. With a given machine control method, for example, vector control, the variation

of winding current can be further identified. Under vector control, the machine output power P_{out} is given by (6.1) and the variation of phase current I_{ph} can be calculated accordingly.

$$P_{out} = 3E_1 I_{ph} \tag{6.1}$$

The sensitivity analysis result of the machine behavior to the variations of residual flux density and relative permeability is shown in Figure 6.5 and Figure 6.6, respectively. For both variations of 25% from their nominal values, the sensitivity analysis result shows that the residual flux density has a much larger effect on the machine performance than the relative permeability.

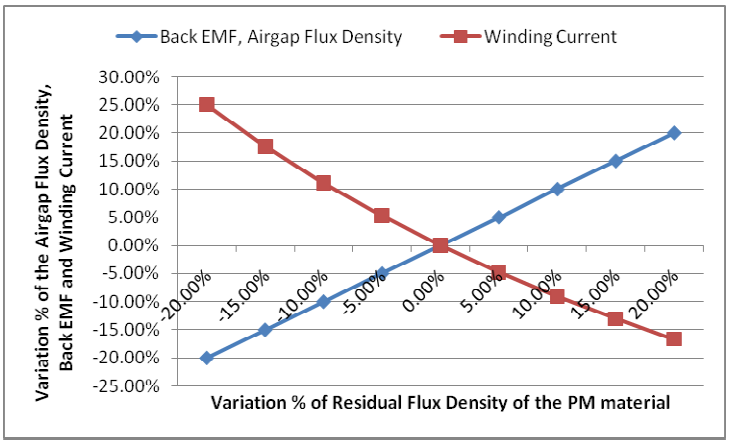

Figure 6.5: Sensitivity analysis result of residual flux density to machine behavior.

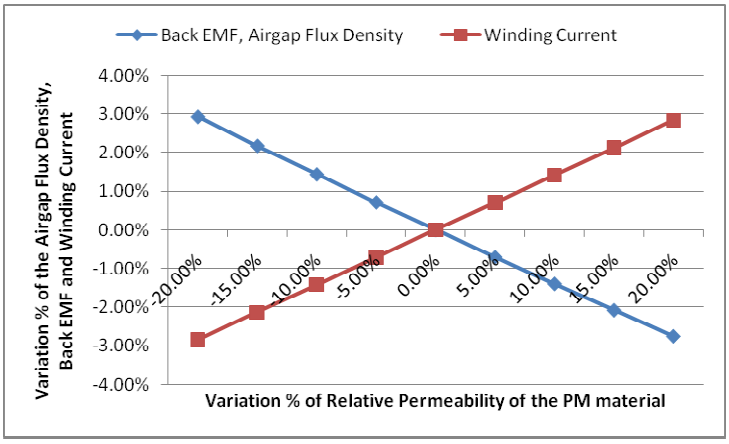

Figure 6.6: Sensitivity analysis result of relative permeability to machine behavior.

b) Variation of material properties - steel

The material property of an electric steel is mainly represented by its B-H curve and core loss curve. Since the analytical design method does not consider machine designs with deep saturation, the steel permeability is close to infinity for the optimized machine. Hence, the variation of B-H curve variation does not affect machine performance in a notable way. As a result, it is only necessary to investigate the variations of steel core loss densities, which is done later in this chapter.

c) Variations of modeling errors – inductance calculation

Again the machine is assumed to be under vector control. Figure 6.7 shows the phasor diagram of the SMPM machine under vector control. When the armature reaction inductance L_m and stator leakage inductance L_l vary, the angle δ between the back EMF E and terminal voltage U varies and is given by (6.2)

$$P_{out} = 3\frac{E_1 U}{X_m + X_{sl}} \sin \delta_1 . \tag{6.2}$$

With the machine output power P_{out}, back EMF E and terminal voltage U constant, the variation of (X_m+X_{sl}) leads to variations of the power angle δ_1, but the magnitude of the phase current I_{ph} is not affected.

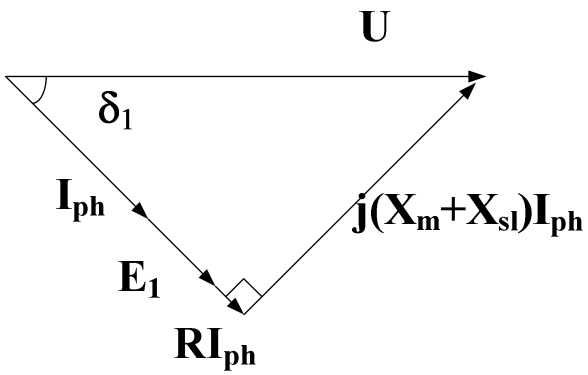

Figure 6.7: Phasor diagram of SMPM machine under vector control.

Although the variation of inductance leads to a change in the armature reaction magnetic field and stator leakage magnet field, those magnetic fields are generally small compared to the main magnetic field produced by the permanent magnet. Hence, the effect of the variation of the inductance to the flux density in the steel can be neglected.

d) Modeling errors – stator resistance

Because the stator resistance is generally much smaller than the armature reactance, the effect of the variation of stator resistance upon the stator current can be safely neglected. Hence, the effect of a variation of the stator resistance is only allowed for as a proportional variation of stator copper losses.

e) Modeling errors – airgap flux density

The modeling error of the airgap flux density as equations (3.4) to (3.13) can be generally divided into two aspects: the error in the fundamental flux density waveform and the error of the harmonic flux density waveform. The fundament flux density error leads to variations of fundamental component of the back EMF and can thus be treated the same way as the PM material property. The effect of the modeling errors in harmonic airgap flux density is primarily on the current harmonics and torque ripples, which is not

part of the optimization and does not need to be analyzed at this stage. Detailed finite element analysis of the optimized machine and a further detailed design will reduce the harmonics and torque ripples.

f) Manufacturing tolerances – stator core

As described earlier, the manufacturing tolerances of stator core, including tooth width, slot depth, core thickness and axial length, are relatively small. Hence, those manufacturing tolerances do not lead a significant change of the electromagnetic field of the machine and their effects on the efficiency and winding temperature variations can be safely neglected.

g) Manufacturing tolerances – permanent magnet

Although the manufacturing tolerances of the permanent magnet thickness and pole coverage are also relatively small, their effects to the machine performance cannot be neglected. According to equations (3.4) to (3.13), the effect of the variations of magnet thickness and pole coverage to the fundament airgap flux density can be calculated. The variation of winding current can also be determined, similar to the method used in the PM material property. On the hand, the variation of PM thickness also varies effective airgap length and hence affects the armature reaction inductance, but as mentioned previously, this does not affect the winding current.

Based on the above analysis, the sensitivity analysis result of the airgap flux density and winding current to the magnet thickness and pole coverage are calculated and shown in Figure 6.8 and Figure 6.9, respectively. The result shows that the magnet pole coverage variation has a much larger effect to the airgap flux density and phase current

than the magnet thickness. Hence, more attention is needed to reduce the manufacturing tolerances for magnet pole coverage rather than the magnet thickness.

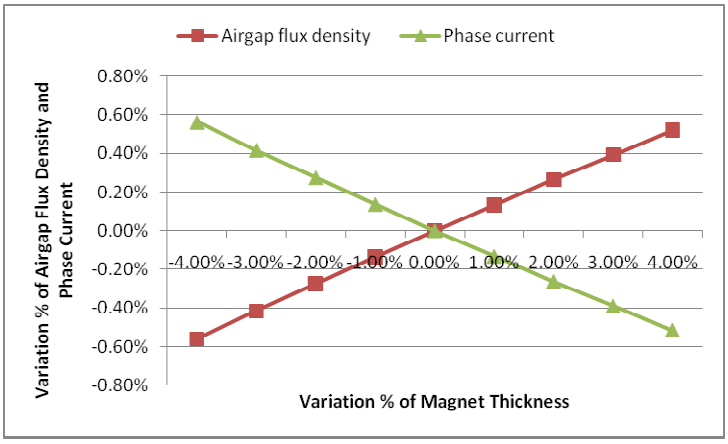

Figure 6.8: Variation of magnet thickness to airgap flux density and winding current.

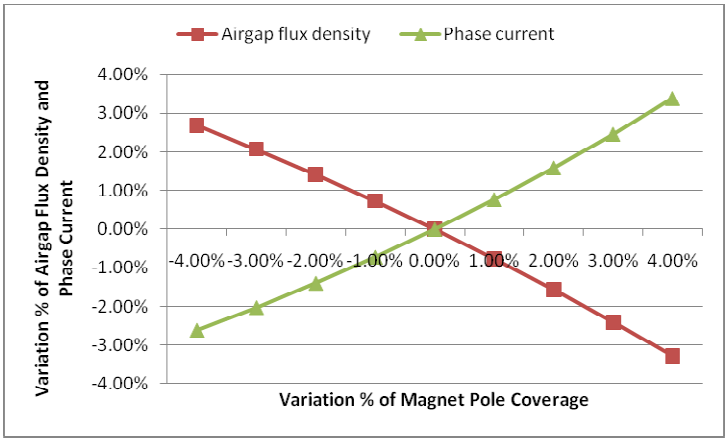

Figure 6.9: Variation of magnet pole coverage to airgap flux density and winding current.

h) Manufacturing tolerances – Airgap length

The variation of airgap length changes the MMF drop across the airgap and thus affects the airgap flux density and then the winding current. According to equations (3.4) to (3.13), the sensitivity analysis result of the airgap flux density and winding current to

airgap length are calculated by calculating the derivative of airgap flux density with respect to airgap length and shown in Figure 6.10.

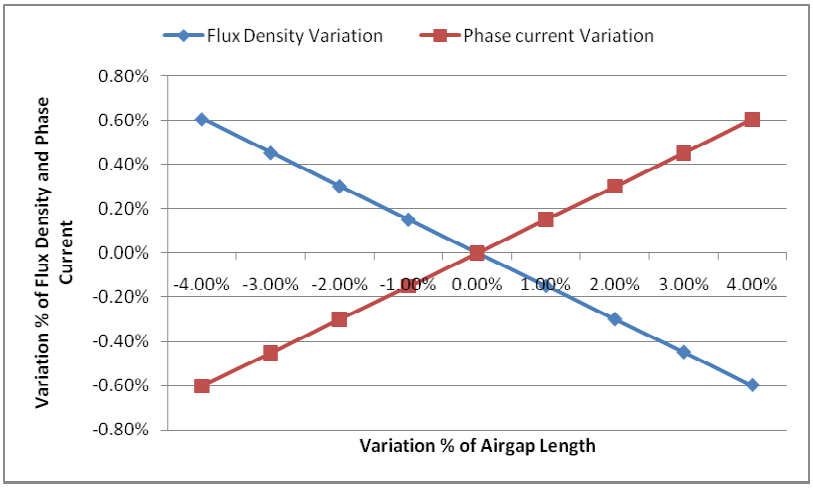

Figure 6.10: Variation of airgap length to airgap flux density and winding current.

6.3.2.2 From machine behavior to machine performance index

Efficiency and winding temperature rise are two of the most important performance indexes and their sensitivity with parameter variations are studied in this section, which presents a sensitivity analysis due to variations of the winding current and flux densities in the steel.

The SMPM machine efficiency *eff* is given by (6.3)

$$eff = \frac{P_{out}}{P_{out} + P_{copper} + P_{core}} = \frac{P_{out}}{P_{out} + 3I_{ph}^2 R_{cu} + P_{core}(B_{st}, B_{sc})}, \quad (6.3)$$

where $P_{core}(B_{st}, B_{sc})$ is the machine core loss, which is a function of stator teeth flux density B_{st} and the stator core flux density B_{sc}, for a given machine geometry at a given operating frequency. This core loss function $P_{core}(B_{st}, B_{sc})$ can be constructed as a look-up table using core loss curves found from the datasheet of the steel used to build the

machine, such as [72]. Hence, equation (6.3) becomes differentiable and the sensitivity is calculated analytically.

The sensitivity analysis result of the machine efficiency to variations of winding current and flux densities is shown in Figure 6.11, where the tooth and core flux density are assumed to vary at same rate. The number along each curve is the percent rate of the machine efficiency variation. For example, point A in Figure 6.11 indicates that when the winding current is decreased by 20% and the flux density is increased by 10%, the machine efficiency increases by 0.2 %.

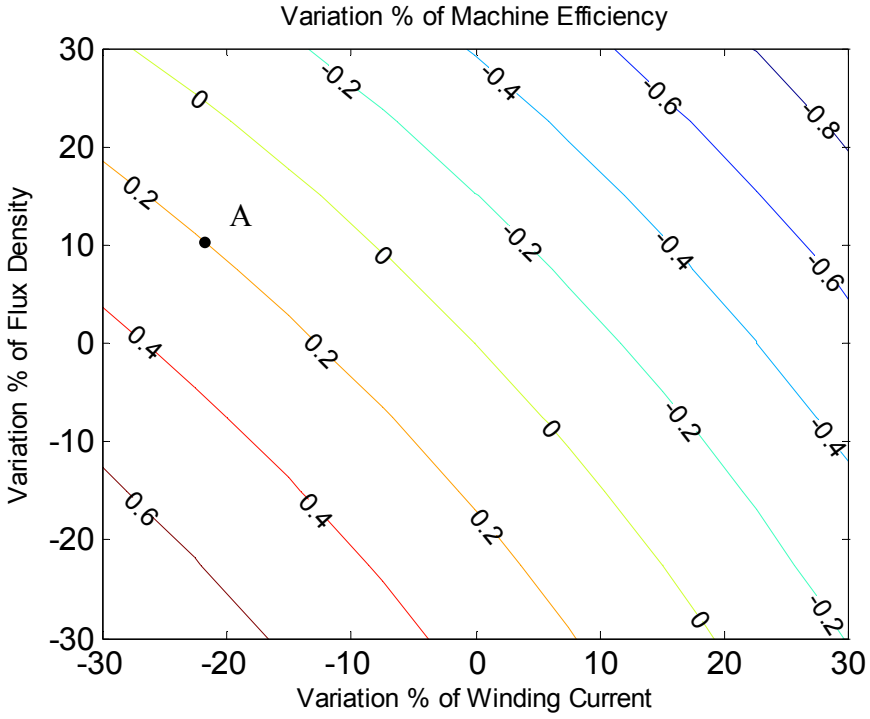

Figure 6.11: Sensitivity analysis result of machine efficiency to the variations of winding current and flux density.

The core loss and copper loss are inputs to the thermal program described in section 5.4. By varying the values of flux densities and winding current, the sensitivity analysis result of the winding temperature is also calculated and shown in Figure 6.12, where the tooth and core flux density are also assumed to vary at the same rate. Similar to Figure 6.11, the number along each curve is the percent rate of the winding temperature variation. For example, point B of Figure 6.12 indicates that when the winding current is decreased by -10% and the flux density is decreased by -10%, the winding temperature decreases by 15 %. The thermal model is numerical-based and is not differentiable, so the sensitivity can be only analyzed on numerically.

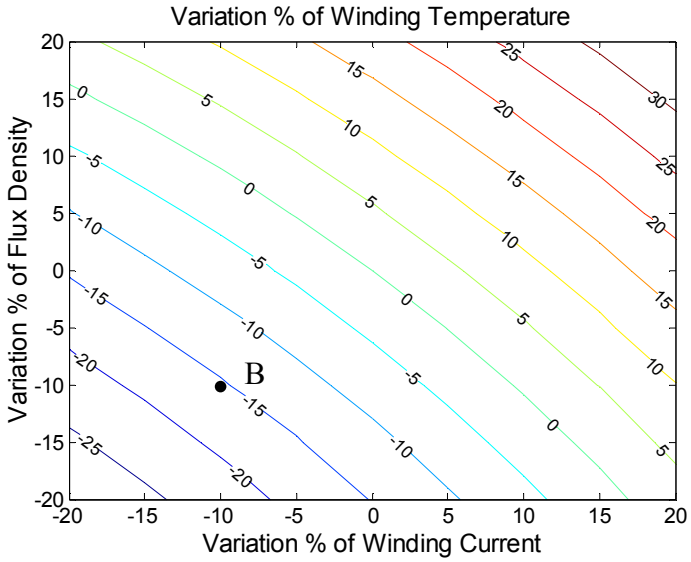

Figure 6.12: Sensitivity analysis result of winding temperature to the variations of winding current and flux density.

6.3.3 Sensitivity analysis result of efficiency and winding temperature

Based on the sensitivity analysis results in the previous two sections, the sensitivity of machine efficiency and winding temperature to design parameter variations can be determined. The effect of the variations of the material property of steel, resistance

calculation, and airgap flux density calculation can be directly read from Figure 6.11 and Figure 6.12. The effects of other parameters are illustrated with more details below.

6.3.3.1 Material properties – PM material

By combining Figure 6.5 and Figure 6.6 into Figure 6.11 and Figure 6.12, the sensitivity results of efficiency and winding temperature to PM material properties are shown in Figure 6.13 and Figure 6.14, respectively. When the residual flux varies by ±20%, the machine efficiency variation is within 2 % and the winding temperature variation is within 10 %. The sensitivity analysis result shows that although the variation of the PM material properties leads to relatively remarkable changes in the winding currents and flux densities, their overall effect to the efficiency and winding temperature are small. This is because the variation in the residual flux density or relatively permeability leads to the copper loss and core loss to change in the opposite direction. Hence, the variations of PM material properties are not likely to produce another design that is significantly better than the original optimal design found in the previous chapter.

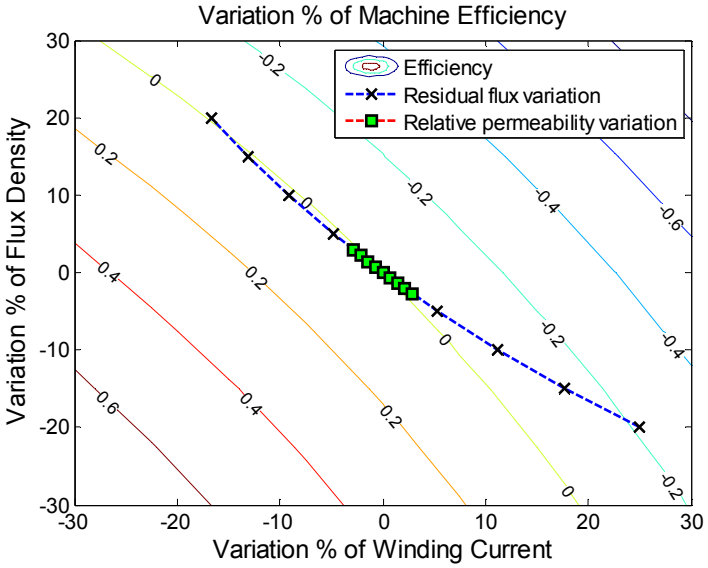

Figure 6.13: Sensitivity analysis result of machine efficiency to PM material properties.

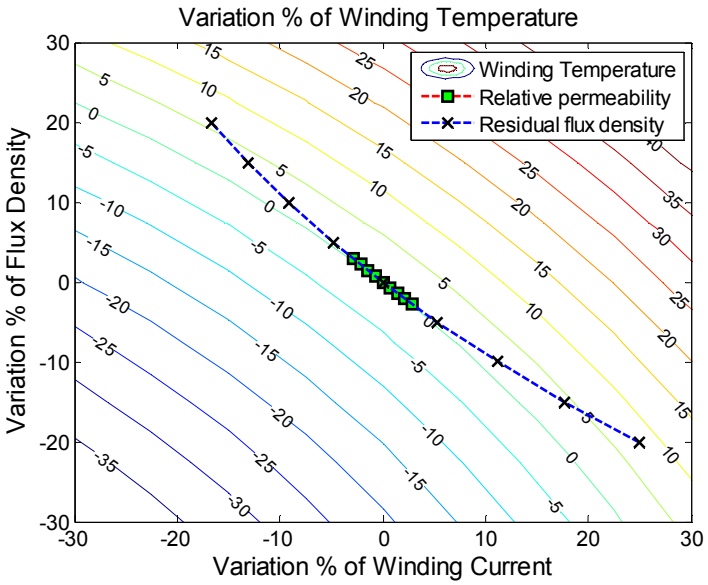

Figure 6.14: Sensitivity analysis result of winding temperature to PM material properties.

6.3.3.2 Manufacturing tolerances-permanent magnet

The effect of manufacturing tolerances of the PM thickness and pole coverage to the efficiency and winding temperature rise of the SMPM machines are shown in Figure 6.15 and Figure 6.16. These results show that for both ±5 % variations, the pole coverage has a much larger effect on the machine performance than the magnet thickness. Nevertheless, both of their effects on the machine performance are small, especially on the efficiency and winding temperature.

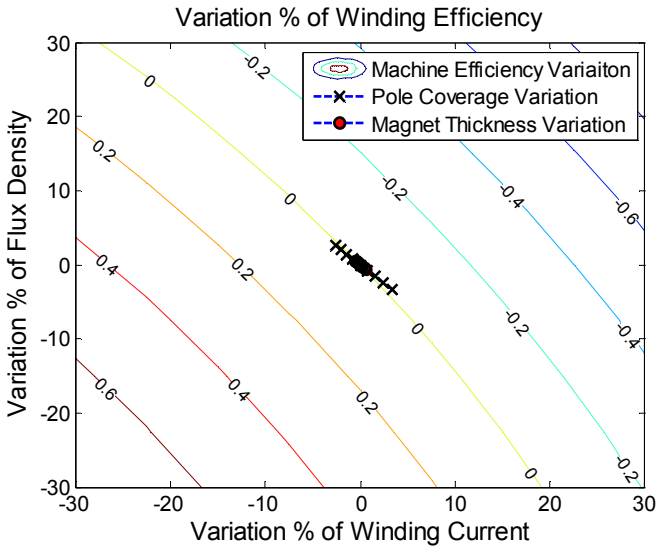

Figure 6.15: Sensitivity analysis result of machine efficiency to magnet manufacturing tolerances.

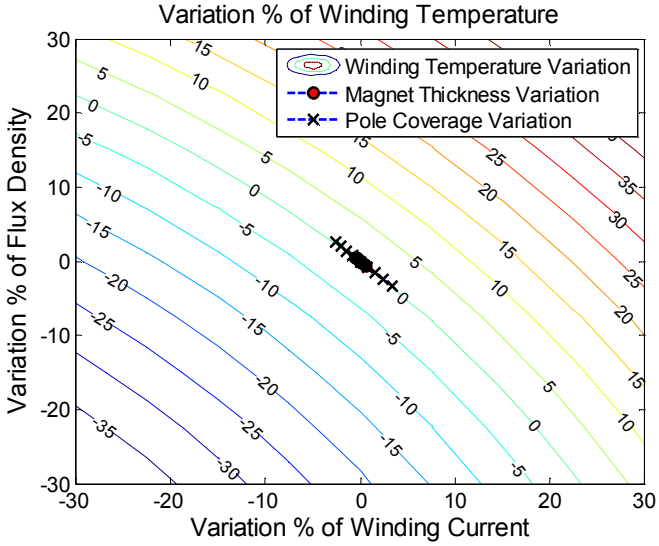

Figure 6.16: Sensitivity analysis result of winding temperature to magnet manufacturing tolerances.

6.3.3.3 Manufacturing tolerances - airgap

The effect of the manufacturing tolerances of the airgap length to the efficiency and winding temperature rise of the SMPM machines are shown in Figure 6.17 and Figure

6.18. Both of their effects on the machine performance are small, especially on the efficiency and winding temperature.

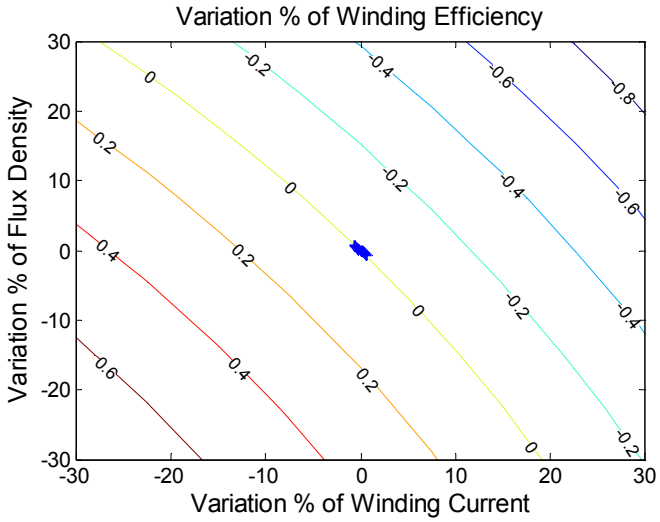

Figure 6.17: Sensitivity analysis result of machine efficiency to airgap length tolerances.

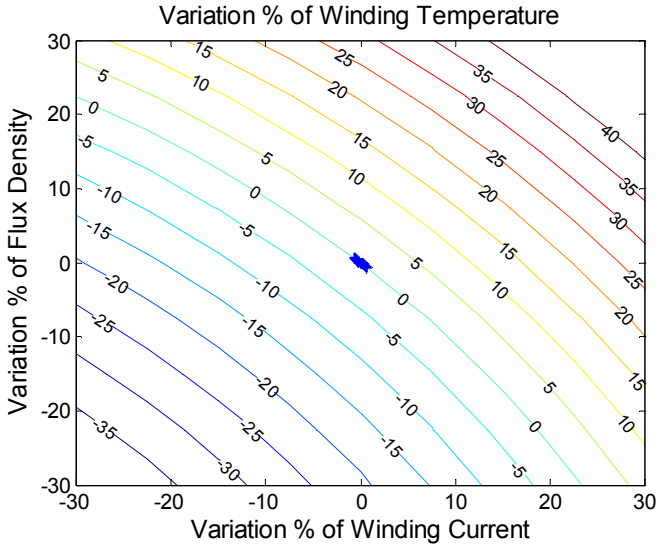

Figure 6.18: Sensitivity analysis result of winding temperature to airgap length tolerances.

6.4 Chapter Summary

This chapter carries out a sensitivity analysis to evaluate how the machine performance varies with variations of the machine parameters between the design calculation and the actual manufactured machine. All the common machine parameter variations are considered and their effect to the machine winding current and steel flux density are identified and summarized in Table 6.1 .

Table 6.1: Sensitivity of machine winding current and steel flux density to variations of machine parameters.

Source	**Machine parameters**	**Parameter variations**	**Winding current variations**	**Steel flux density variations**
Material properties	PM residual flux density	-20 %~20 %	25% ~ -16.67%	-20 % ~ +20 %
	PM relative permeability	-20 %~20 %	-2.85 % ~ 2.83 %	2.93% ~ -2.75%
	Steel B-H curve	-20 %~20 %	Negligible	Negligible
	Steel core loss density	-20 %~20 %	Zero	Zero
Modeling errors	Inductance	-20 %~20 %	Nearly zero	Nearly zero
	Resistance	-20 %~20 %	Nearly zero	Nearly zero
	Airgap flux density	-20 %~20 %	25% ~ -16.67%	-20 % ~ +20 %
Manufacturing tolerances	Tooth width	-4 %~4 %	Negligible	Negligible
	Slot depth	-4 %~4 %	Negligible	Negligible
	Core thickness	-4 %~4 %	Negligible	Negligible
	Airgap length	-4 %~4 %	-0.6 % ~ 0.6 %	0.6 % ~ -0.6 %
	PM thickness	-4 %~4 %	-0.56 % ~ 0.56 %	0.56% ~ -0.56%
	PM pole coverage	-4 %~4 %	-2.61 % ~ 3.39 %	2.68% ~ -3.28 %

The sensitivity analysis result in Table 6.1 indicates that machine operating conditions (primarily winding current and steel flux density) are more sensitive to the PM material property, the modeling error of airgap flux density, and the PM pole coverage tolerances. Hence, more attention should be paid to those three machine parameters in order to ensure good agreement between the design calculation and the actual operating condition of the manufactured machine.

Another sensitivity analysis is carried out into how the variation of machine operating conditions affect the machine performance indexes used in the objective function. This result is then combined with the sensitivity analysis result of the machine operating condition to machine parameter variations. The combined sensitivity analysis result provides designers useful information on how the optimal design is affected by variations of machine parameters. Although the variations in the PM material property, the modeling error of airgap flux density, and the PM pole coverage tolerances have notable effects on the machine operating condition, since they lead to the change of copper and core loss in the opposite direction, their effect on the performance index is actually small and does not lead to a significant change in the optimal solution. Hence, more attention is needed on the accuracy of the steel core loss density and end-winding modeling, which can be obtained from the manufacturer.

To summarize, in an imperfect world where the machine parameters may vary from their original values used in the design calculation and optimization, the effects of such variations to the machine performances can be determined and can be used by machine designers to decide which parameters require more attention to reduce such variations.

The sensitivity analysis result also shows that the optimal solution can still hold if parameter variations are within a certain range.

CHAPTER 7 Induction Machine Electromagnetic Design and Optimization

7.1 Overview

The complexity of the induction machine structure makes a manual optimal design a difficult and challenging task unless some optimization algorithm is used. A manual design consists of first designing from first principles and then subjecting the design to a Finite Element Analysis (FEA) to confirm flux densities. FEA itself does not design a machine but evaluates a given design. The nonlinearities in materials and the complex relationships between many of the geometric parameters make optimal machine design a truly multi-objective optimization [33]. This chapter presents a novel analytical design model and a PSO based optimization algorithm, which together are able to design and optimize induction machines with respect to different users' specified requirements. A comparative study of PSO and Genetic Algorithm (GA) is also performed in this paper to see which algorithm is more successful in finding the global optima and has better computational efficiency.

7.2 Design optimization for mains-fed induction machines

7.2.1 Mains-fed induction machine standards

For mains-fed induction machines, the supply voltage has a fixed frequency and magnitude. There are industry standards, such as the USA NEMA standard [73] that clarify mains-fed machines according to their torque-speed curves and starting performances. For motors with 60 Hz, 460 V supply voltage for example, the performance requirements are summarized in Table 7.1 for NEMA Design B motors:

Table 7.1: Performance requirements of NEMA B single-speed polyphase squirrel cage medium sized motors with continuous ratings (20 HP, 60 Hz, 460 V supply voltage, 1800 rpm, NEMA Design B) [73]

Performance terms	Minimum locked-rotor torque	Minimum breakdown torque	Minimum pull-up torque	Maximum locked-rotor current	Slip at rated load
Values	150 Nm	200 Nm	105 Nm	580 A	Less than 5 %

Besides performance requirements, the frame sizes are also specified by the NEMA standard. However, the NEMA frame size is only for mounting purposes and is not for machine sizing during the design stage. A 20 HP, 60 Hz, 1800 rpm, and design B squirrel-cage induction machine for example has a NEMA frame size of 256T (foot mount), which indicates that the centerline of the shaft to the bottom of the foot is 6.25 inches, or 258.75 mm. From the machine design point of view, this indicates the machine outer diameter cannot exceed 258.75 mm. The other NEMA frame size specifications do not limit the size of induction machines.

7.2.2 Induction machine airgap length

In the traditional induction machine design, the selection of the airgap length is determined by empirical equations and there are different versions of them, illustrated by equations (7.1) [8] and (7.2) [11]:

$$g = 5(r\tau_p)^{1/2}$$
$$g = 9r(\frac{p}{2})^{-1/2}, \tag{7.1}$$
$$g = 3\tau_p(\frac{p}{2})^{1/2}$$

$$g = 0.2 + 2\sqrt{\frac{D}{1000}\frac{L}{1000}} \tag{7.2}$$

where τ_p is the pole pitch in millimeters, r is the airgap radius in millimeters, D is the airgap diameter is millimeters, and L is machine active length in millimeters. These equations indicate that the selection of the airgap length, from past experience, is related to the airgap diameter, number of poles, machine length, and maybe more.

The airgap length of induction machines is determined by both mechanical and electromagnetic factors. On the mechanical side, a larger airgap is desired and the limiting factors include the mechanical tolerances, the bearings, shaft deflection, unbalanced magnetic pull, manufacturing tolerances, etc. On the electromagnetic side, a small airgap length helps to reduce the magnetizing current and improve the power factor. From the view of lower copper loss and higher power factor, a small airgap length always seems desirable. However, if the airgap length is too small, the stator and rotor differential leakage inductances may increase [8, 74]. For mains-fed induction machines, the starting torque, starting current, and breakdown torque are also affected. If the airgap length is not selected correctly, the mains-fed machine performance may not meet design requirement. In [75], the authors also show that if the airgap is too small, the efficiency decreases. Possible reasons could be the increase of pulsation losses in copper and iron due to the relative movement of the slotted surface on both sides of the airgap.

Hence, the optimal selection of the airgap length is not a case of the smaller the better, but is a decision strongly coupled with other machine design parameters on the electromagnetic design side and should be determined by optimization algorithms.

The mechanical considerations give the lower bound for the selection of airgap length. According to [8], the minimum airgap length to maintain the required spacing between the stator and rotor due to mechanical tolerances is

$$g = 10^{-3} r \,. \tag{7.3}$$

A longer airgap may be required depending on practical considerations, such as bearing, shaft bending, and mechanical load [8].

7.2.3 Proposed induction machine design algorithm

In contrast to the conventional sizing equation, the induction machine design method proposed in this research starts from the machine output equation in the dq rotor reference frame. However, this does not mean that the proposed method is only for field-oriented controlled induction machines. The dq frame is just a way of modeling the operation of an induction machine. When the induction machine runs at steady state and has a rated output speed and torque, whether mains-fed or field-oriented-controlled, this machine has almost the same operating condition (stator current, power factor, frequency, etc.)[9]. Since the dq equations in the proposed method are used only to calculate the steady-state performances at the rated condition, they can be safely used for mains-fed induction machines. When the d-axis is aligned with the rotor flux, the output torque on the motor shaft [76] is:

$$T_{out} = \frac{3}{4} p \lambda_{dr}^{e} I_{qs}^{e} \,, \tag{7.4}$$

where p is the number of poles, λ_{dr}^{e} is the rotor d-axis flux linkage and I_{qs}^{e} is the stator q-axis current. When the rotor flux is aligned with the d-axis, the rotor d- and q-axis flux linkage can be expressed as

$$\begin{aligned} \lambda_{dr}^{e} &= \overline{B}\frac{\pi DL}{p}T_{ph} = L_{msr}I_{ds}^{e} \\ \lambda_{qr}^{e} &= 0 \end{aligned}, \tag{7.5}$$

where L_{msr} is the mutual inductance between the rotor and stator in the dq model.

To achieve an average airgap flux density $\overline{B}$, the MMF provided by the magnetizing current [9] is:

$$F_m = 2(1+k_{mg})K_c g\overline{B}/\mu_0 \tag{7.6}$$

where K_c is the Carter coefficient which represents the effective increase of the physical airgap by the slot opening, g is the physical airgap, μ_0 is the permeability of vacuum, and k_{mg} is the ratio of MMF across the stator and rotor steel to the MMF across the airgap. When the flux density in the rotor and stator steel is not heavily saturated, k_{mg} is small and close to zero. Neglecting the voltage drop across the stator resistance and leakage inductance, the magnetizing reactance X_{mg} can thus be represented as:

$$X_{mg} = \frac{U}{I_{mg}} = \frac{2U}{F_m p(1.35K_w N_c)} \tag{7.7}$$

where U is the phase excitation voltage. It is also known that

$$X_{mg} = 2\pi f L_{msr} \tag{7.8}$$

With equations (7.4) to (7.8), the number of turns per phase N_c can be calculated to satisfy the machine rated operating condition. When the number of stator slots is selected, the winding layout design can proceed with the calculated value of N_c.

Furthermore, by putting the solved N_c value into equations (7.4) to (7.8), the q- and d- axis current and flux linkage can be calculated for both stator and rotor. The next step is to choose the stator teeth flux density B_{st}, stator core density B_{sc}, and the stator current density J_s, and thus the stator geometry is obtained. The rotor can be designed similarly by selecting the rotor teeth flux density B_{rt}, rotor core flux density B_{rc}, and rotor bar current density J_r (rotor ring current density J_{rr} can be chosen to be a constant multiplied by the rotor bar current density). All the main geometry parameters as shown in Figure 7.1 can therefore be calculated. Note that different rotor slot shapes can be included in the design method and Figure 7.1 shows only the specific case of a rotor with rectangular teeth and a trapezoidal slot shape.

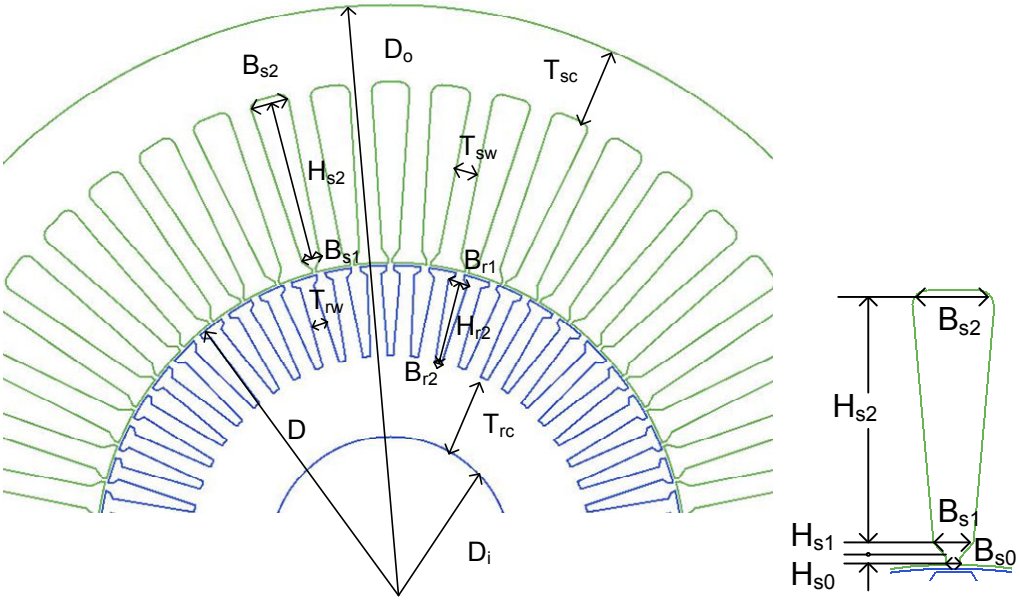

Figure 7.1: Geometry parameters of induction machines.

This new algorithm is more efficient than the traditional design process because it does not require design iterations to meet the assumption of efficiency and power factor made at the start of the traditional design. As explained earlier, dq frame is just a way to

calculate the machine operations. Equations (7.4) to (7.8) are valid at the rated operating condition no matter the machine is mains-fed or field-oriented-controlled. Hence, the algorithm works for both inverter-fed induction machines and mains-fed induction machines. Differences in design requirements of inverter-fed and mains-fed machines can be reflected in performance calculation and the design objective function.

7.2.4 Performance calculation

After the machine geometry and winding layout has been designed, the machine performance is then calculated, including the efficiency, power factor, weight, volume, and so on. Different induction machine modeling tools can be used for the performance calculation, such as the Finite Element Analysis [77], Magnetic Equivalent Circuit [78], and so on. In this research, the classical equivalent circuit (Figure 7.2) based analytical calculation is applied in order to minimize the computational burden.

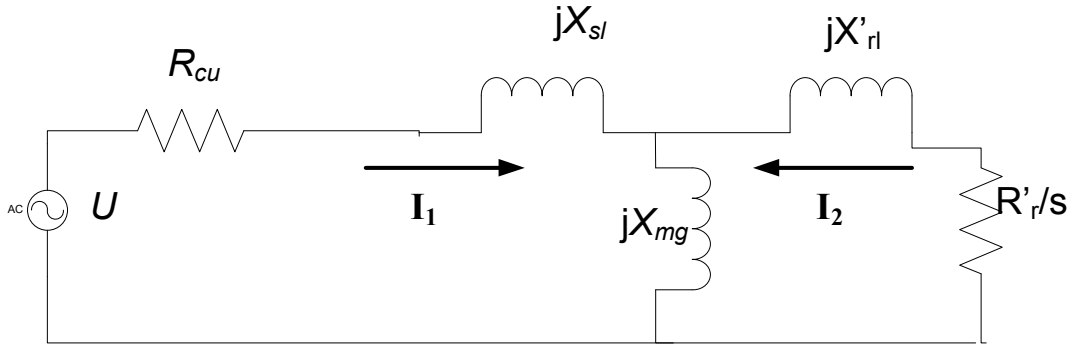

Figure 7.2: Classical equivalent circuit of induction machines

The magnetizing inductance of X_{mg} in Figure 7.2 is calculated by (7.7). The stator resistance R_{cu} is calculated in the same way as for the SMPM machine explained in Chapter 3. The stator leakage inductance L_{sl} consists of three components [9], namely the stator slot leakage inductance L_{sls}, the stator differential leakage inductance L_{ds}, and the

stator end-winding leakage inductance L_{ecs}. The calculation of stator leakage inductance is given by

$$L_{sl} = L_{sls} + L_{ds} + L_{ecs} = \mu_0 L \frac{N_c^2}{pq}(\lambda_{sls} + \lambda_{ds} + \lambda_{ecs}), \tag{7.9}$$

where λ_{sls}, λ_{ds}, and λ_{ecs} are called the stator slot leakage coefficient, stator differential leakage coefficient, and stator end leakage coefficient, respectively. Since the values of axial length L, pole number p, and the number of stator slot per pole per phase q are selected at the beginning; the number of turns per phase N_c has been calculated earlier; and μ_0 is the vacuum permeability ($4\pi*10^{-7}$ N•A^{-2}), only these leakage coefficients needs to be calculated. There are extensive researches in the literature about the calculation of such coefficients and the equations developed in [9] are used.

The equation to calculate the stator slot leakage coefficient is given by[9]:

$$\begin{aligned} &K_{sl1} = (\frac{1}{4} + \frac{1}{4}\beta),\ K_{sl2} = \frac{1}{4} + \frac{3}{4}K_{sl1} \\ &\lambda_{sls} = \frac{2}{3}\frac{H_{s2}}{(B_{s1} + B_{s2})}K_{sl2} + (\frac{H_{s0}}{B_{s0}} + \frac{H_{s1}}{B_{s1}} - \frac{B_{s0}}{2B_{s1}} + 0.785) * K_{sl1}. \end{aligned}, \tag{7.10}$$

where is the β the ratio of coil pitch over pole pitch and the definitions of other symbols are shown in Figure 7.1.

The equation to calculate the stator differential leakage coefficient is given by[9]:

$$\begin{aligned} &C_{sdiff} = 1 - 0.033B_{s0}^2 / g / \tau_t \\ &\gamma_{diff} = (0.18\sin(\pi(6\beta - 5.5)) + 1.24)/100 \\ &\lambda_{sdiff} = 0.9 y_s Spp^2 K_w{}^2 C_{sdiff}\gamma_{sdiff} / K_c / g / (1 + (F_{mts} + F_{mtr})/F_{mg}) \end{aligned}, \tag{7.11}$$

where τ_t is the stator slot pitch in mm, q is the stator per pole per phase, and K_{w1} is the stator winding factor for the fundamental.

The equation to calculate the stator end leakage coefficient is given by

$$\lambda_{end} = \frac{0.34q}{L}(2l_{end} - 0.64\beta\frac{\pi D}{p}).,\tag{7.12}$$

where τ_p is the stator pole pitch in mm and l_{end} is the length of end extension of the stator winding, as shown in Figure 3.6 (c).

The rotor leakage inductance also has three components [9], namely the rotor slot leakage inductance L_{slr}, the rotor differential leakage inductance L_{dr}, and the rotor end-winding leakage inductance L_{er}. The calculation of stator leakage inductance L_{rl} is given by

$$L_{rl} = L_{slr} + L_{dr} + L_{ecr} = \mu_0 L(\lambda_{slr}K_x + \lambda_{dr} + \lambda_{ecr}),\tag{7.13}$$

where K_x is the skin effect coefficient for rotor slot leakage inductance; λ_{slr}, λ_{dr}, and λ_{er} are the rotor slot leakage coefficient, rotor differential leakage coefficient, and rotor end leakage coefficient, respectively. The skin effect coefficient for rotor slot leakage inductance is given by [9]

$$K_x = \frac{3}{2\xi}\frac{(\sinh(2\xi) - \sin(2\xi))}{(\cosh(2\xi) - \cos(2\xi))},\tag{7.14}$$

and

$$\xi = \beta_s H_{r2}\sqrt{S_1};\ \ \beta_s = \sqrt{\frac{2\pi f\mu_0}{2\rho_r}},\tag{7.15}$$

where S_1 has an approximate value of one, ρ_r is the conductivity of the rotor bar material, and H_{r2} is defined in Figure 7.1. The rotor slot leakage coefficient is similar to the stator slot leakage coefficient. If the rotor slot has a trapezoidal shape as in Figure 7.1, then (7.10) can be used.

The equation to calculate the stator differential leakage coefficient is given by

$$\lambda_{dr} = \frac{0.9\tau_r}{K_c g}(\frac{N_r}{12p})^2 \tag{7.16}$$

where τ_r is the rotor slot pitch in mm, N_r is the number of rotor slots, and K_c is the Carter coefficient calculated earlier.

The equation to calculate the rotor end leakage coefficient is given by

$$\lambda_{er} = \frac{2.3(D_{er} - b)}{N_r L * 4\sin^2(\frac{2\pi p}{N_r})} \log \frac{4.7(D_{er} - b)}{b + 2a}, \tag{7.17}$$

where the symbols are defined in Figure 7.3.

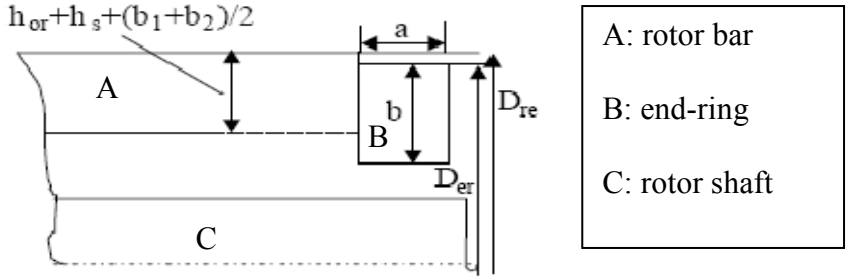

Figure 7.3: Definition of symbols used in the rotor end leakage coefficient calculation.

The rotor resistance is calculated [9] by the ohm's law considering the skin effect and is given by

$$R_r = \rho_r(\frac{L}{A_b}K_r + \frac{l_{er}}{2A_{er}\sin(\frac{2\pi p}{N_r})}) \tag{7.18}$$

where A_b is the rotor bar area, K_r is the skin effect coefficient for rotor resistance, l_{er} is the rotor endring length, and A_{er} is the rotor endring cross sectional area. The skin effect coefficient for rotor resistance is given by

$$K_r = \xi \frac{(\sinh(2\xi) + \sin(2\xi))}{(\cosh(2\xi) - \cos(2\xi))}. \tag{7.19}$$

The above calculations for the rotor resistance and rotor leakage inductance yield values referred to the rotor winding. To be used in the equivalent circuit of Figure 7.2, they have to be transformed to values referred to the stator winding as follows:

$$\begin{aligned} R_r' &= \frac{4*3}{N_r}(N_c K_{w1})^2 R_r \\ L_{rl}' &= \frac{4*3}{N_r}(N_c K_{w1})^2 L_{rl} \end{aligned} . \tag{7.20}$$

Note that the skin effect coefficients K_x and K_r are only used for locked-rotor performance calculations. At rated operation condition, the rotor bar current has a very low frequency and the skin effect can be neglected.

The rotor slip s at the rated steady-state condition is given by the following equation [76]:

$$s = \frac{R_r}{X_{rl} + X_{mg}} \frac{I_{qs}^{\ e}}{I_{ds}^{\ e}} . \tag{7.21}$$

Again this equation is valid for both main-fed and inverter-fed induction machines. Since all the parameters of (7.21) are known, the rotor slip at the rated steady-state condition can be calculated and other performance parameters can thus be obtained, such as stator loss, rotor loss, efficiency, and so on. The stator and rotor Watt losses on the winding and bars are calculated by $I_1^2 R_s$ and $I_2^2 R_r$' and skin effects are considered at the locked-rotor performance calculation for mains-fed induction machines. The stator core loss is estimated from the catalog data given by the steel manufacturer, or from test done by the designer. The stray loss, windage, and friction loss are estimated to have a total of 3% of the output power.

7.2.5 Flowchart of the proposed induction machine design method

Figure 7.4 shows the flowchart of the proposed induction machine design method, which has two advantages over the classical design process. First, the proposed method starts from six prime design variables and directly finds a machine design which satisfies the specifications with no iterations. This significantly saves the excessive calculations needed for the design iterations in the traditional design process. Second, there are six prime design variables in the proposed method; D and L are limited by the spatial limits; $\overline{B}$ is limited by the B-H curve of the steel; J_s and J_r are limited by thermal and cooling constraints. Hence, the domain of design variables to be searched is limited, in contrary to a much larger search domain in the traditional design method. Due to the above two advantages, the proposed design method is able to run more efficiently and faster than the traditional machine design method, which significantly reduces the machine design cycles.

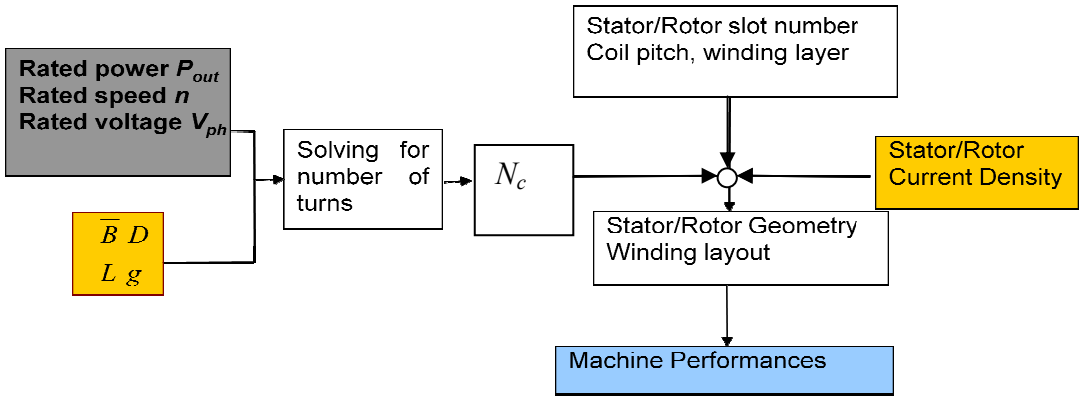

Figure 7.4: Flowchart of the proposed induction machine method

7.2.6 Numerical design example

A numerical design example is presented in this section to illustrate the proposed induction machine design method in detail. The example machine is rated at 15 kW, 60 Hz, 1800 rpm (synchronous speed) and is supplied by a balanced three phase voltage of 460 V(line-to-line voltage). The values of the six prime design variables chosen for this numerical example are: D = 150 mm, L = 120 mm, $\overline{B}$ = 0.5 T, g = 0.4 mm, J_s = 5 A/mm^2, and J_r = 5 A/mm^2. Similar to the SMPM machine design, the proposed design method is able to produce a trial design based on the values chosen for the six prime design variables.

For the NO 007 steel from Cogent Steel [68](Typical DC magnetization curve appears in Figure 5.6), the flux densities chosen for the stator teeth and core are $B_{st} = B_{sc}$ = 1.4 T, and for the rotor teeth and core are $B_{rt} = B_{rc}$ = 1.5 T. Both these flux densities are chosen around the knee point of the B-H curve. Since the flux densities vary at a very low frequency in the rotor at rated condition, the core loss is very small and relatively higher values of flux density can be chosen for the rotor.

7.2.6.1 Selection of stator and rotor slot number

The stator slot number is selected to be 48 (4 slots per pole per phase, a common choice for small and medium induction machines) for this 4 pole machine and the winding is double-layer and short-pitched by one stator slot to reduce harmonics in the stator MMF. The rotor bars and endrings are cast-aluminum and the rotor has 42 slots with a cage winding. If the number of rotor slots is too small, the MMF produced by the rotor winding may contain excessive harmonics, which leads to increase of the torque ripple. If the number of rotor slots is too large, the rotor bars and teeth are too thin to

manufacture. There are numerous researches in the literature about the choices of rotor slot numbers. Some choices may cause vibrations or make the machine noisy, some may lead to a cusp in the torque-speed curve, and some may cause starting difficulties [8]. According to [74], there are no perfect choices and each choice of the rotor slot number has its own advantages and disadvantages. The choice of the rotor slot number actually depends on the application of the machine. The number of rotor slot of 42 is thus selected based on several reasons: 1) 42 is less than the stator slot number; 2) Cusps in torque-speed curve and cogging problem are avoided.

7.2.6.2 Calculation of Carter coefficient

The rotor and stator slot openings are chosen to be B_{s0} = B_{r0} = 2 mm, which are typical values as given in [9]. For the closed rotor slots, the value of B_{r0} is set to zero and the equations do not need to be changed. The rotor outer diameter is

$$D_r = D - 2*g = 150 - 2*0.4 = 149.2 \text{ (mm)}. \tag{7.22}$$

The stator and rotor slot pitches are:

$$\begin{aligned} \tau_t &= \frac{\pi D}{N_s} = \frac{\pi*150}{4*4*3} = 9.82 \text{ (mm)} \\ \tau_r &= \frac{\pi D_r}{N_r} = \frac{\pi*149.2}{42} = 11.16 \text{ (mm)}. \end{aligned} \tag{7.23}$$

According to equations given in [7], the Carter coefficient to represent the stator and rotor slot effects upon the airgap length is calculated as:

$$K_c = K_{cs}K_{cr} = \frac{\tau_t}{\tau_t - \frac{B_{s0}{}^2}{5g + B_{s0}}} \frac{\tau_r}{\tau_r - \frac{B_{r0}{}^2}{5g + B_{r0}}}$$
$$= \frac{9.82}{9.82 - \frac{2^2}{5*0.4+2}} \frac{11.16}{11.16 - \frac{2^2}{5*0.4+2}} \quad . \tag{7.24}$$
$$= 1.22$$

7.2.6.3 Calculation of winding factor

For this example of q = 4, the winding distribution factor for the fundamental MMF is

$$K_{wd1} = \frac{1}{q} \frac{\sin(\frac{\pi}{6})}{\sin(\frac{\pi}{6*q})} = 0.9577 . \tag{7.25}$$

For the winding coil to be short-pitched by one stator slot (sp = 1), the pitch factor for the fundament MMF is

$$\beta = (N_s / p - sp) / (N_s / p) = (12-1)/12 = 11/12$$
$$K_{wp1} = \sin(11/12 * \pi / 2) = 0.9914 \quad . \tag{7.26}$$

Hence, the winding factor for the fundament MMF is

$$K_{w1} = K_{wd1}K_{wp1} = 0.9577 * 0.9914 = 0.9495 . \tag{7.27}$$

7.2.6.4 Solving for the number of stator turns

Assuming the windage and friction loss P_{wf} to be $0.012P_{out}$ (a typical estimation given by [8]), the rated electromagnetic torque of this machine is approximated as:

$$T_r = \frac{(1+0.012)P_{out}}{n_s} = \frac{1.012 * 15000}{1800/60 * 2\pi} = 80.53 \text{ Nm.} \tag{7.28}$$

When the rotor flux is aligned with the d-axis, the rotor d- and q-axis flux linkages are calculated as based on (7.5)

$$\begin{aligned}\lambda_{dr}^{e} &= \overline{B}\frac{\pi DL}{p}T_{ph} = 0.5*\frac{\pi*150*120}{4}*10^{-6}*T_{ph} = I_{ds}L_{m}\\ \lambda_{qr}^{e} &= 0\end{aligned}. \tag{7.29}$$

Expressed in the dq frame, at the rated condition, the electromagnetic torque on the motor shaft is:

$$T_{out} = \frac{3}{4}p\lambda_{dr}^{e}I_{qs}^{e} = \frac{3}{4}*4*\lambda_{dr}^{e}I_{qs}^{e} = T_{r} = 80.53 \text{ (Nm)}. \tag{7.30}$$

In the example design, the flux densities in the stator and rotor are not heavily saturated and thus the ratio of MMF drop along the stator and rotor steel to the MMF drop across the airgap can be assumed to be a relatively small value (less than one), for example, 0.5. The actual value of this ratio is calculated in the later steps and compared with this selection of 0.5. Hence, according to (7.6), the MMF provided by the magnetizing current is:

$$\begin{aligned}F_{m} &= 2(1+k_{mg})K_{c}g\overline{B}/\mu_{0}\\ &= 2*(1+0.5)*1.22*0.4*0.5/(4\pi*10^{-7})\\ &= 291.97 \text{ (A-t)}.\end{aligned} \tag{7.31}$$

Neglecting the voltage drop across the stator resistance and leakage inductance, according to (7.7), the magnetizing reactance X_{mg} is calculated as:

$$X_{mg} = \frac{V_{ph}}{I_{mg}} = \frac{2V_{ph}}{F_{m}p(1.35K_{w}T_{ph})} = \frac{2*460/\sqrt{3}}{291.97*4(1.35*0.9495T_{ph})} \tag{7.32}$$

The magnetizing reactance is also expressed as:

$$X_{mg} = 2\pi fL_{msr} = 2\pi*60*L_{msr}. \tag{7.33}$$

From (7.28) to (7.33), the number of stator turns per phase N_c is solved. For this example design, N_c becomes 141. However, the number of conductors per half slot should be an integer for a double-layer winding, which indicates that the number of turns per phase should be multiples of $N_s/3$ = 48/3=16. Hence, N_c is rounded up to 144. To keep (7.28) to (7.33) valid, the airgap flux density $\overline{B}$ needs to be adjusted to:

$$B_a = \overline{B} * \frac{T_{ph,before\ rounding}}{T_{ph,after\ rounding}} = 0.5 * \frac{141}{144} = 0.4894 \text{ (T)}. \tag{7.34}$$

B_a and N_c are then used to calculate the values of the other variables in (7.28) to (7.33)

$$\lambda_{dr}^e = B_a * \frac{\pi * 150 * 120}{4} * 10^{-6} * N_c = 0.4984 * \frac{\pi * 150 * 120}{4} * 10^{-6} * 144 = 0.9963 \text{ (Wb)} \tag{7.35}$$
$$\lambda_{qr}^e = 0$$

$$I_{qs}^e = \frac{T_{out}}{\frac{3}{4} p \lambda_{dr}^e} = \frac{80.53}{\frac{3}{4} * 4 * 0.9963} = 26.94 \text{ (A)} \tag{7.36}$$

$$I_{mg} = F_m p(1.35 K_w T_{ph}) = 291.97 * 4(1.35 * 0.9495 * 144) = 6.2 \text{ (A)} \tag{7.37}$$

$$I_{ds}^e = \sqrt{2} * I_{mag} = \sqrt{2} * 6.2 = 8.76 \text{ (A)}. \tag{7.38}$$

Hence, the stator current I_{ph} (RMS value) at rated condition is

$$I_{ph} = \frac{1}{\sqrt{2}} \sqrt{(I_{ds}^{e\,2} + I_{qs}^{e\,2})} = \frac{1}{\sqrt{2}} \sqrt{(8.76^2 + 26.94^2)} = 20 \text{ (A)}. \tag{7.39}$$

7.2.6.5 Stator design calculation

The magnetizing flux per pole is calculated as

$$\Phi = B_a \frac{\pi D}{p} L = 0.4984 * \frac{\pi * 150 * 120}{4} * 10^{-6} = 0.0069 \text{ (Wb)}. \tag{7.40}$$

With a lamination stacking factor of 0.95 (a typical value of the stacking factor [8]) , the stator tooth width T_{sw} and core thickness T_{sc} are calculated as

$$T_{sw} = \frac{\frac{\pi}{2}\Phi}{(N_s / p)Lk_j B_{st}} = \frac{\frac{\pi}{2} * 0.0069}{(48/4) * 120/1000 * 0.95 * 1.4} * 1000 = 5.68 \text{ (mm)} \quad (7.41)$$

$$T_{sc} = \frac{\Phi / 2}{Lk_j B_{sc}} = \frac{0.0069/2}{120/1000 * 0.95 * 1.4} * 1000 = 21.67 \text{ (mm)}. \quad (7.42)$$

For the phase current calculated in the last step and the current density selected at the beginning, the wire cross sectional area is calculated as:

$$A_{cu} = \frac{I_{ph}}{J_s} = \frac{20}{5} = 4 \text{ (mm}^2\text{)}. \quad (7.43)$$

The closest standard gauge wire has a diameter d_w of 2.3041 mm. Similar to SMPM machine design, if d_w >1.3 mm in lower power machines, such as this 15 kW machine, a few conductors with smaller diameters is used in parallel [9]. In this example, a_p = 4 wires are used in parallel and the individual wire diameter is:

$$d_{w2} = \sqrt{\frac{4A_{cu}}{\pi a_p}} = \sqrt{\frac{4 * 3.94}{\pi * 4}} = 1.13 \text{ (mm)} \quad (7.44)$$

The closest standard AWG wire has a diameter of 1.15 mm and three of these wires in parallel have a total cross sectional area of A_{cu} = 4.15 mm^2. This wire diameter of 1.15 mm is smaller than 1.3 mm and also smaller than the slot opening of 2 mm, which enables the wires to fit through the slot opening into the slot. With a slot fill factor of 40% , the slot area needed to fit such wires is:

$$A_s = \frac{6N_c A_{cu}}{N_s f_f} = \frac{6 * 144 * 4.15}{48 * 0.4} = 186.7 \text{ (mm}^2\text{)}. \quad (7.45)$$

The slot sizing of induction machines can be done similarly to the SMPM machine. In this example, H_{s0} and H_{s1} of Figure 7.1 are chosen to be 1 mm and 2 mm, respectively. B_{s1} can be estimated as:

$$\begin{aligned} B_{s1} &= \pi(D + 2(H_{s0} + H_{s1})) / N_s - T_{sw} \\ &= \pi(150 + 2(1+2)) / 48 - 5.68 = 4.54 \text{ (mm)}. \end{aligned} \tag{7.46}$$

From equations (3.25) to (3.27), H_{s2} and B_{s2} can be solved to be:

$$H_{s2} = 41.9 \text{ (mm)}, B_{s2} = 10 \text{ (mm)}.$$

The stator outer diameter is then:

$$\begin{aligned} D_o &= D + 2(H_{s0} + H_{s1} + H_{s2} + T_{cs}) \\ &= 150 + 2(1 + 2 + 41.9 + 21.67) = 283.1 \text{ (mm)}. \end{aligned} \tag{7.47}$$

Similarly to the SMPM machine design calculation, with an estimate of the coil overhang extension length to be 10 mm, the total length of winding coils per phase is estimated to be

$$\begin{aligned} l_{cp} &= 2(L + l_{end})N_c = 2(L + 2l_{ext} + \frac{\pi(D + 2(H_{s0} + H_{s1}) + H_{s2}))}{p}\beta)N_c \\ &= 2(120 + 2*10 + \frac{\pi(150 + 2(1+2) + 41.9))}{4}\frac{11}{12})*144 \\ &= 8.46*10^4 \text{ (mm)}. \end{aligned} \tag{7.48}$$

At 20 ^{o}C, the dc resistance of this example machine design is:

$$R_{dc} = \rho_{cu}\frac{l_{cp}}{A_{cu}} = 1.78*10^{-8}*\frac{8.46*10^4}{4.15}*10^3 = 0.36 \text{ } (\Omega). \tag{7.49}$$

As calculated in the SMPM machine design, the dc resistance is approximately the same as the ac resistance and the stator resistance in the equivalent circuit $R_{cu} = R_{dc}$.

7.2.6.6 Rotor design calculation

The flux densities in the rotor tooth and core are selected to be both $B_{rt} = B_{rc}$ =1.5 T. With a lamination factor of 0.95, the rotor tooth width T_{rw} and core thickness T_{rc} are hence calculated as

$$T_{rw} = \frac{\frac{\pi}{2}\Phi}{(N_r / p)Ll_f B_{rt}} = \frac{\frac{\pi}{2} * 0.0069}{(42/4) * 120/1000 * 0.95 * 1.5} * 1000 = 6.05 \text{ (mm)} \quad (7.50)$$

$$T_{rc} = \frac{\Phi / 2}{Ll_f B_{rc}} = \frac{0.0069/2}{120/1000 * 0.95 * 1.5} * 1000 = 20.23 \text{ (mm)}. \quad (7.51)$$

Assume L_{msr}/L_r = 0.95, where L_r is the equivalent rotor self-inductance in the dq frame and L_{msr} is equivalent mutual-inductance between the stator and rotor winding in the dq frame. Since the rotor leakage is much smaller than the magnetizing inductance, L_{msr}/L_r = 0.95 is generally a good choice. According to [76], the rotor current is then calculated as:

$$\begin{aligned} I_{qr}^e &= -\frac{L_{msr}}{L_r} I_{qs}^e = \text{-0.95*26.62=-25.6 (A)} \\ I_{dr}^e &= 0 \end{aligned} \quad (7.52)$$

The rotor current referred to the stator at rated condition is:

$$I_r = \frac{1}{\sqrt{2}} \sqrt{(I_{dr}^{e\,2} + I_{qr}^{e\,2})} = \frac{1}{\sqrt{2}} \sqrt{(0^2 + 25.6^2)} = 18.3 \text{ (A)}. \quad (7.53)$$

The rotor bar current referred to the rotor winding is [8]

$$I_{bar} = K_w \frac{N_s}{N_r} \frac{3N_c}{N_s} I_r = 0.945 \frac{48}{42} \frac{3*144}{48} 18.3 = 353.5 \text{ (A)}. \quad (7.54)$$

The actual rotor end ring current is:

$$I_{ring} = \frac{I_{bar}}{2\sin(\frac{\pi p}{2N_r})} = \frac{353.5}{2\sin(\frac{4\pi}{2*42})} = 1186 \text{ (A)}. \tag{7.55}$$

The rotor bar current density J_r is assumed to be the same as that of the stator current J_s and equal to 5 A/mm2. Thus the rotor bar area is:

$$A_{bar} = \frac{I_{bar}}{J_r} = \frac{353.5}{5} = 70.7 \text{ (mm}^2\text{)}. \tag{7.56}$$

Similarly to the stator slot sizing, the rotor slot width and depth are calculated as:

$$\begin{aligned} B_{r1} &= \pi(D_r - 2H_{r0} - 2H_{r1}) / N_r - T_{rw} \\ &= \pi(149.2 - 2*1 - 2*1) / 42 - 6.05 = 4.81 \text{ (mm)} \end{aligned} \tag{7.57}$$

$$\begin{aligned} B_{r2} &= 1.4 \text{ (mm)} \\ H_{r2} &= 22.8 \text{ (mm)}. \end{aligned} \tag{7.58}$$

Assume the rotor bar has an extension of l_{bext} = 15 mm at each end, the resistance per bar is

$$R_{bar} = \rho_{al} \frac{(L + 2l_{bext})}{A_{bar}} = 2.82*10^{-8} * \frac{(120 + 2*15)}{70.7} * 10^3 = 5.98*10^{-5} \text{ (}\Omega\text{)}. \tag{7.59}$$

Selecting the rotor end-winding current density to be J_{ring} = 1.2J_r, the rotor endring area is calculated as:

$$A_{ring} = \frac{I_{ring}}{J_{ring}} = \frac{1186}{1.2*5} = 197.7 \text{ (mm}^2\text{)}. \tag{7.60}$$

Assuming the cross section of the end ring is square, as illustrated in Figure 7.3, the end ring height and width are:

$$R_h = R_w = \sqrt{A_{ring}} = \sqrt{197.7} = 14.1 \text{ (mm)}. \tag{7.61}$$

The rotor end ring has a center line diameter of (referring to Figure 7.3):

$$D_e = D_r - 2H_{r2} - R_w = 149.2 - 22.8*2 - 14.1 = 89.6 \text{ (mm)}. \tag{7.62}$$

The rotor end ring resistance is:

$$R_{ring} = \rho_{al} \frac{\pi D_e}{A_{ring}} = 2.82*10^{-8} * \frac{\pi * 89.6}{197.7} * 10^3 = 4.02*10^{-5} \ (\Omega). \tag{7.63}$$

The total Joule loss in the rotor is:

$$\begin{aligned} P_{al} &= P_{albar} + P_{alring} = N_r {I_{bar}}^2 R_{bar} + 2 * {I_{ring}}^2 R_{ring} \\ &= 42*353.5^2 * 5.98*10^{-5} + 2*1186^2 * 4.02*10^{-5} \\ &= 427 \ (\text{W}). \end{aligned} \tag{7.64}$$

The equivalent rotor resistance per phase referred to the stator side is:

$$R_r' = \frac{P_{al}}{{I_r}^2} = \frac{427}{18.3^2} = 0.43 \ (\Omega). \tag{7.65}$$

7.2.6.7 Magnetizing inductance calculation

To calculate the magnetizing inductance, the total MMF drop along the main flux path (illustrated by the dashed line in Figure 7.5) is calculated as:

$$\begin{aligned} F_m &= F_g + 2F_{ts} + 2F_{tr} + F_{cs} + F_{cr} \\ &= K_c g B_a / \mu_0 + 2H_{ts}(H_{s0} + H_{s1} + H_{s2}) + 2H_{tr}(H_{r0} + H_{r1} + H_{r2}), \\ &\quad + H_{cs}\left(\frac{\pi(D_o - T_{sc})}{p}\frac{2}{3}\right) + H_{cr}\left(\frac{\pi(D_i + T_{sc})}{p}\frac{2}{3}\right), \end{aligned} \tag{7.66}$$

where H_{ts}, H_{tr}, H_{cs}, and H_{cr} are the electromagnetic field strengths and their values can be found from the steel B-H curve for their respective flux densities. In this example design, the steel used is N007 from Cogent Steel and its B-H curve can be found in [68] (Figure 5.6) . The total MMF drop then comes to be:

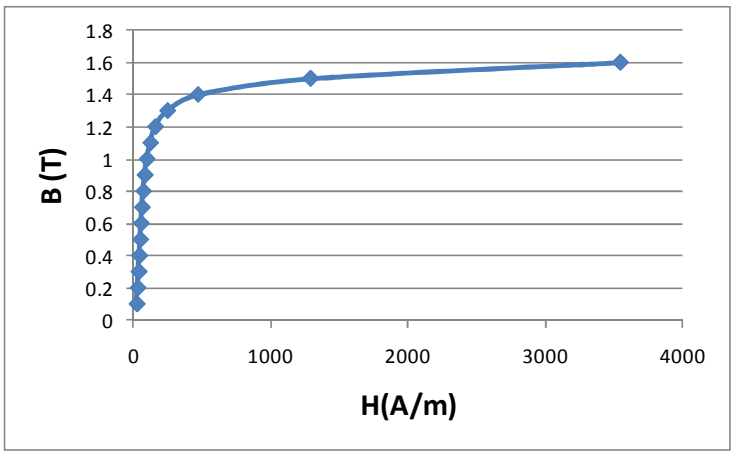

Repeating Figure 5.6: Typical DC magnetization curve of NO 007 [68]

$$
\begin{aligned}
F_m &= K_c g B_a / \mu_0 + 2H_{ts}(H_{s0} + H_{s1} + H_{s2}) + 2H_{tr}(H_{r0} + H_{r1} + H_{r2}) \\
&\quad + H_{cs}\left(\frac{\pi(D_o - T_{sc})}{p}\frac{2}{3}\right) + H_{cr}\left(\frac{\pi(D_i + T_{sc})}{p}\frac{2}{3}\right) \\
&= 1.223 * 0.4 / 1000 * 0.4996 / (4\pi * 10^{-7}) + 2 * 470 * (1 + 2 + 41.9) / 1000 \\
&\quad + 2 * 470 * (1 + 1 + 22.2) / 1000 + 1290 * \left(\frac{\pi(283.1 - 21.67)}{4}\frac{2}{3}\right) / 1000 \\
&\quad + 1290 * \left(\frac{\pi(61.2 + 21.67)}{4}\frac{2}{3}\right) / 1000 \\
&= 566.4 \ (\mathrm{A \cdot t}).
\end{aligned}
\tag{7.67}
$$

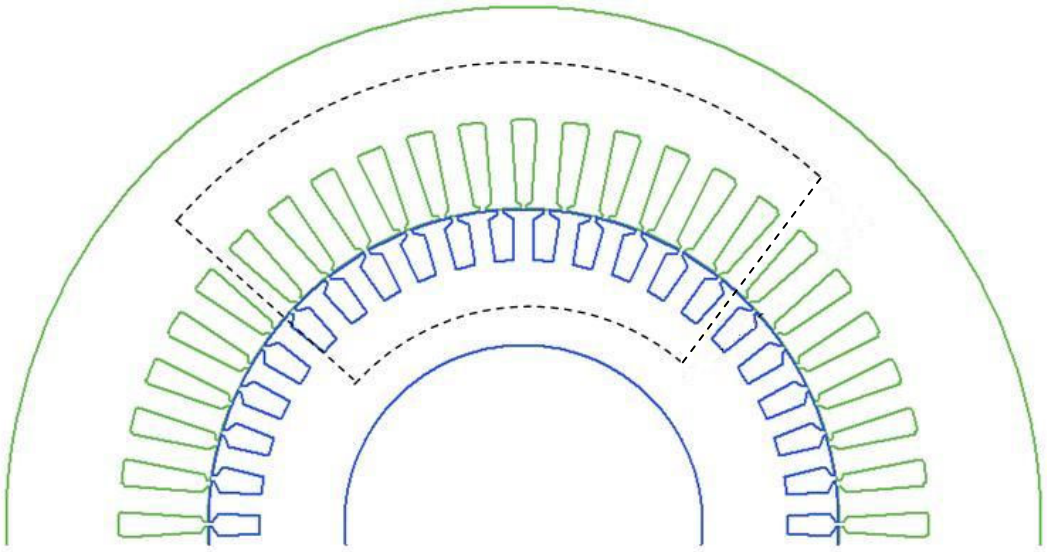

Figure 7.5: Illustration of a typical main flux path

The ratio of MMF drop along the stator and rotor steel to the MMF drop across the airgap is:

$$k_{mg} = \frac{F_{lm}}{F_g} - 1 = 0.49, \tag{7.68}$$

which is close to the assumption made at the beginning. This new value of k_{mg} is then used to repeat the step of 7.2.6.4 to calculate the revised number of stator winding turns. If a different value of N_c is found after rounding, the new value of k_{mg} and N_c will be used to revise the stator and rotor design. However, because N_c is rounded to multiples of integers, if the steel is not heavily saturated, this estimate of k_{mg} = 0.5 is found through the author's experience to be generally agrees with the calculated k_{mg} values for 15 kW, 60 Hz induction machines and yields induction machine designs with good performances (high efficiency, high power factor, etc.). For given flux density in the steel, k_{mg} equivalently represents the ratio of the total length of the main flux path (illustrated in Figure 7.5) in the steel over the airgap length. For normal airgap lengths, a lower value of k_{mg}, such as 0.3, indicates a shorter main flux path in the steel, which is not achievable because there has to be certain slot space; a higher value of k_{mg}, such as 0.7, indicates a longer main flux path in the steel, which often leads to a bulky design. In many cases, if a much lower or higher value of k_{mg} is chosen at the beginning, the value of N_c and k_{mg} more likely needs to be revised after repeating step 7.2.6.4 and eventually k_{mg} will become a value around 0.5. For induction machines with other power ratings or steel types, this value of 0.5 may change but can be easily identified by manually running some trial designs.

The magnetizing current is:

$$I_{mag} = \frac{F_{lm}}{2/p * 1.35 K_w N_c} = 6.1 \text{ (A)}. \quad (7.69)$$

7.2.6.8 Stator leakage inductance calculation

The equations presented in section 7.2.4 are used to calculate the stator leakage inductance. The permeance for the stator slot leakage inductance is

$$\begin{aligned}\lambda_{sls} &= \frac{2}{3}\frac{H_{s2}}{(B_{s1}+B_{s2})}\left(\frac{1}{4}+\frac{3}{4}\left(\frac{1}{4}+\frac{1}{4}\beta\right)\right)+\left(\frac{H_{s0}}{B_{s0}}+\frac{H_{s1}}{B_{s1}}-\frac{B_{s0}}{2B_{s1}}+0.785\right)*\left(\frac{1}{4}+\frac{1}{4}\beta\right)\\ &= \frac{2}{3}\frac{40.5}{(4.54+8.88)}\left(\frac{1}{4}+\frac{3}{4}\left(\frac{1}{4}+\frac{1}{4}\frac{11}{12}\right)\right)+\left(\frac{1}{1}+\frac{2}{4.54}-\frac{1}{2*4.54}+0.785\right)*\left(\frac{1}{4}+\frac{1}{4}\frac{11}{12}\right) \quad (7.70)\\ &= 3.2\ .\end{aligned}$$

The permeance for the stator end leakage inductance is

$$\lambda_{end} = \frac{0.34 Spp}{L}\left(2 l_{end} - 0.64\frac{\pi D}{p}\right) = \frac{0.34*4}{120}\left(2*162.7 - 0.64\frac{\pi*150}{4}\right) = 2.8. \quad (7.71)$$

The permeance for the stator differential leakage inductance is

$$\begin{aligned}C_{sdiff} &= 1 - 0.033 B_{s0}^2 / g / ys = 0.9664\\ \gamma_{diff} &= (0.18\sin(\pi(6\beta - 5.5)) + 1.24)/100 = 0.0124 \quad (7.72)\\ \lambda_{sdiff} &= 0.9 y_s Spp^2 K_w{}^2 C_{sdiff}\gamma_{sdiff} / K_c / g / (1 + (F_{mts} + F_{mtr})/F_{mg}) = 2.5\ .\end{aligned}$$

Hence, the stator leakage inductance is:

$$L_{sl} = \frac{\mu_0 L T_{ph}^2}{p * Spp}(\lambda_{sslot} + \lambda_{sdiff} + \lambda_{send}) = 0.0017 \text{ (H)}. \quad (7.73)$$

7.2.6.9 Rotor leakage inductance calculation

The equations presented in section 7.2.4 are used to calculate the rotor leakage inductance. The permeance for the rotor slot leakage inductance is

$$\lambda_{rls} = \frac{2}{3}\frac{H_{r2}}{(B_{r1}+B_{r2})}(\frac{1}{4}+\frac{3}{4}(\frac{1}{4}+\frac{1}{4}\beta)) + (\frac{H_{r0}}{B_{r0}}+\frac{H_{r1}}{B_{r1}}-\frac{B_{r0}}{2B_{r1}}+0.785)*(\frac{1}{4}+\frac{1}{4}\beta)$$
$$= \frac{2}{3}\frac{22.2}{(4.54+8.88)}(\frac{1}{4}+\frac{3}{4}(\frac{1}{4}+\frac{1}{4}\frac{11}{12})) + (\frac{1}{1}+\frac{1}{4.54}-\frac{1}{2*4.54}+0.785)*(\frac{1}{4}+\frac{1}{4}\frac{11}{12}) \quad (7.74)$$
$$= 3.54\ .$$

The permeance for the stator end leakage inductance is

$$\lambda_{rend} = \frac{2.3D_e}{4N_r \sin^2(\frac{p\pi}{2N_r})}\log(\frac{4.7D_e}{3R_w}) = 0.25. \quad (7.75)$$

The permeance for the stator differential leakage inductance is

$$\gamma_{diff} = 9(\frac{3p}{N_r})10^{-2} = 0.0073$$
$$\lambda_{rdiff} = 0.9\pi\frac{D_r\gamma_{diff}}{N_r K_c g}(\frac{N_r}{3p})^2 = 1.8479. \quad (7.76)$$

Hence, the rotor leakage inductance referred to the rotor side is:

$$L_{rbe} = \mu_0 L(\lambda_{rls}+\lambda_{rend}+\lambda_{rdiff}) = 8.51*10^{-7}\ \text{(H)}. \quad (7.77)$$

The rotor leakage inductance referred to the stator side is:

$$L_{rl}' = 4*3*(\frac{N_c K_{dp1}}{N_r})^2 L_{rbe} = 4.5\ \text{(mH)}. \quad (7.78)$$

The values of all the parameters in Figure 7.2 have now been calculated. The next steps calculate the machine performance.

7.2.6.10 Weight calculation

Only the active weight of induction machines are calculated here, which is comprised of stator core, stator winding, rotor core, and rotor winding. The weight calculations of the stator core and stator winding are similar to those for SMPM machines. The weight of the stator core is:

$$W_{sc} = \frac{\pi}{4}(D_o^2 - (D_o - 2*T_{sc})^2)*L*\rho_s = 17.2 \text{ (kg)}, \tag{7.79}$$

the total weight of the stator teeth is

$$W_{st} = N_s*T_{ws}*(H_{s0} + H_{s1} + H_{s2})*L*\rho_s = 11.6 \text{ (kg)}, \tag{7.80}$$

and the weight of the stator winding is

$$W_{sw} = 3\rho_{cu}A_{wire}l_c = 8.87 \text{ (kg)}. \tag{7.81}$$

The weight of the rotor core and teeth calculation is similar to those for the stator and are

$$W_{rc} = \frac{\pi}{4}(D_i^2 - (D_i + 2*T_{sc})^2)*L*\rho_s = 5.11 \text{ (kg)} \tag{7.82}$$

$$W_{rt} = N_r*T_{rw}*(H_{r0} + H_{r1} + H_{r2})*L*\rho_s = 6.09 \text{ (kg)}. \tag{7.83}$$

The total weight of the rotor bars and rings are:

$$W_{bar} = N_r*A_{bar}*(L + 2l_{bext})*\rho_s = 3.94 \text{ (kg)} \tag{7.84}$$

$$W_{ring} = 2*A_{ring}*\pi D_e*\rho_s = 1 \text{ (kg)}. \tag{7.85}$$

Hence, the total active weight of the example induction machine is;

$$W_t = W_{sc} + W_{st} + W_{sw} + W_{rc} + W_{rt} + W_{bar} + W_{ring} = 53.7 \text{ (kg)}. \tag{7.86}$$

7.2.6.11 Performance calculation at rated condition

The rotor slip at the rated condition is:

$$s = \frac{R_r'}{X_{rl} + X_{mg}}\frac{I_{qs}^e}{I_{ds}^e} = 0.0297, \tag{7.87}$$

The stator copper loss is:

$$P_{cu} = 3I_{ph}{}^2R_{cu} = 449.4 \text{ (W)}. \tag{7.88}$$

The rotor aluminum loss is:

$$P_{rc} = 3I_r^2 R_r' = 435 \text{ (W)}. \tag{7.89}$$

Since the flux in the rotor alternates at a frequency of as low as 60*0.029 = 1.74 (Hz), the core loss in the rotor can be safely neglected. The core loss density of N007 at 1.4 T and 60 Hz is read off from Table 5.4 to be D_c = 2.75 W/kg [68]. Hence, the core loss of the induction machine is calculated as:

$$P_{core} = D_c(W_{sc} + W_{st}) = 80 \text{ (W)}. \tag{7.90}$$

Assuming the windage and friction loss P_{wf} to be $0.012P_{out}$ and the stray loss P_{str} to be 0.01 P_{out}, the machine efficiency is

$$eff = \frac{P_{out}}{P_{rout} + P_{wf} + P_{str} + P_{sc} + P_{rc} + P_{core}} = 92.07\%. \tag{7.91}$$

7.2.6.12 Locked rotor performance calculation

When the rotor is at standstill, the rotor current has a frequency of 60 Hz and the skin effect has to be considered. According to equations in section 7.2.4, the magnitudes of the rotor resistance and rotor leakage inductance vary by ratios of K_r and K_x, respectively. K_r and K_x are calculated as:

$$\begin{aligned}
&\beta_s = \sqrt{\frac{2\pi f \mu_0}{\rho_{al}} \frac{B_{r1}}{2B_{r2}}} = 164.74 \text{ (m}^{-1}\text{)} \\
&\xi = \beta_s H_{r2} = 3.66 \\
&K_r = \xi \frac{\sinh(2\xi) + \sin(2\xi)}{\cosh(2\xi) - \cos(2\xi)} = 3.66 \\
&K_x = \frac{3}{2\xi} \frac{\sinh(2\xi) - \sin(2\xi)}{\cosh(2\xi) - \cos(2\xi)} = 0.41.
\end{aligned} \tag{7.92}$$

The rotor leakage inductance considering the skin effect is:

$$X_{rls}' = K_x X_{rls}' = 0.7 \text{ (H)}. \tag{7.93}$$

The rotor resistance considering the skin effect (referred to rotor) is:

$$R_{bes} = (R_{bar}K_r + \frac{R_{ring}}{2\sin^2(\frac{\pi p}{2N_r})}) = 0.0011\ (\Omega). \tag{7.94}$$

The rotor resistance referred to the stator side is:

$$R_{rs}' = 4*3*(\frac{N_c K_{w1}}{N_r})^2 R_{bes} = 6.13\ (\Omega). \tag{7.95}$$

The locked-rotor current I_{st} and torque T_{st} are then calculated as:

$$I_{st} = \frac{U}{\sqrt{(R'_{rs} + R_s)^2 + (X_{sl} + X'_{rl}K_x)^2}} = 40\ (\text{A}) \tag{7.96}$$

$$T_{st} = 3I_{st}^2 R'_{rs} \frac{p}{2} \frac{1}{2\pi f} = 155.6\ (\text{Nm}). \tag{7.97}$$

7.2.6.13 Breakdown torque calculation

When the torque is at its maximum, the rotor slip is:

$$s_{bk} = \frac{R'_r}{\sqrt{R_s^2 + (X_{rl} + X_{sl})^2}} = 0.186. \tag{7.98}$$

The stator current at breakdown torque is:

$$I_{bk} = \frac{V_{ph}}{\sqrt{(\frac{R'_r}{s_{bk}} + R_s)^2 + (X_{sl} + X'_{rl})^2}} = 73.5\ (\text{A}). \tag{7.99}$$

The breakdown torque is:

$$T_{bk} = \frac{3}{2} \frac{V_{ph}^2}{(R_s + \sqrt{R_s^2 + (X'_{rl} + X_{sl})^2})} \frac{p}{2} \frac{1}{2\pi f} = 203.8\ (\text{Nm}). \tag{7.100}$$

7.2.7 PSO design optimization for mains-fed induction machines

7.2.7.1 Design objectives

Similar to SMPM machine design in previous chapters, the design objective for the induction machine is represented by a function that is the weighted sum of various machine performance indexes (PI), such as weight (*Wt*, in kg), efficiency (*Eff*, a fractional number), power factor (*pf*, a fractional number), and so on. An example of such a weighted-sum based design objective function appears in (7.101)

$$output = Wt + 200 * (1 - Eff) + 200 * (1 - pf) . \tag{7.101}$$

Also similar to SMPM machine design, the use of coefficients before each PI has two purposes. First, they normalize each of the terms in the objective function to have approximately the same magnitude. Second, after normalization, designers can adjust those coefficients to represent how much importance each PI has with respect to the other PI values.

7.2.7.2 Design constraints

Machine designs have to meet design constraints from various aspects, including spatial constraints, material constraints, manufacturing constraints, thermal constraints, and other constraints in terms of machine performance. For mains-fed induction machines, they also have to meet the performance requirements specified by various standards, such as the NEMA standard if the machines are to be used in the US. A NEMA design B is designed here as an example and the constraints consider are summarized in Table 7.2.

Table 7.2: List of constraints used for example induction machine design (including NEMA B specifications)

Max. Stator Outer Diameter D_{sout}	250 mm	Max. rotor bar current density J_s	10 A/mm^2
Min. Rotor Inner Diameter D_{rin}	20 mm	Minimum locked-rotor torque T_{st}	150 Nm
Min. stator tooth width T_{sw}	5 mm	Min. breakdown torque T_{blc}	200 Nm
Min. rotor slot depth B_{r2}	2 mm	Maximum locked-rotor current I_{st}	580 A
Min. rotor slot width T_{rw}	1 mm	Slip s at rated load	< 5 %
Max. stator current density J_s	10 A/mm^2		

To include design constraints in the optimization, the penalty function approach [79] is used to convert constrained optimization problems into unconstrained optimization problems and a term penalty is added to the objective function, as shown in (7.102)

$$output = Wt + 200 * (1 - Eff) + 200 * (1 - pf) + penalty\,. \tag{7.102}$$

When any design constraint is violated, a large penalty function is added to its objective function in order to signal that this design is a poor candidate and drives the solution away from this point in the solution space.

Similar to SMPM machine design, linear distance based penalty functions (defined in (5.58)) are used to penalize the violation of design constraints. The linear distance based penalty function for the minimum stator tooth width is defined by

$$pelT_{sw} = \frac{(T_{sw,\min} - T_{sw})}{T_{sw,\min}} * d(T_{sw,\min} - T_{sw}) \tag{7.103}$$

If the stator tooth width (T_{sw}) is larger than the minimum tooth width $T_{sw,min}$ (5 mm), pel_{Tsw} is zero. When T_{sw} is smaller than $T_{sw,min}$, pel_{Tsw} increases linearly with the decrease of T_w. This penalty function of pel_{Tsw} is plotted in Figure 7.6. Penalty functions for other constraints can be defined in a similar way as

$$pelD_{sout} = \frac{(D_{sout} - D_{sout,\max})}{D_{sout,\max}} * d(D_{sout} - D_{sout,\max}) \tag{7.104}$$

$$pelD_{rin} = \frac{(D_{rin,\min} - D_{rin})}{D_{rin,\min}} * d(D_{rin,\min} - D_{rin}) \tag{7.105}$$

$$pelB_{r2} = \frac{(B_{r2,\min} - B_{r2})}{B_{r2,\min}} * d(B_{r2,\min} - B_{r2}) \tag{7.106}$$

$$pelT_{rw} = \frac{(T_{rw,\min} - T_{rw})}{T_{rw,\min}} * d(T_{rw,\min} - T_{rw}) \tag{7.107}$$

$$pelJ_{s} = \frac{(J_{s} - J_{s,\max})}{J_{s,\max}} * d(J_{s} - J_{s,\max}) \tag{7.108}$$

$$pelJ_{r} = \frac{(J_{r} - J_{r,\max})}{J_{r,\max}} * d(J_{r} - J_{r,\max}) \tag{7.109}$$

$$pelT_{st} = \frac{(T_{st,\min} - T_{st})}{T_{st,\min}} * d(T_{st,\min} - T_{st}) \tag{7.110}$$

$$pelT_{blc} = \frac{(T_{blc,\min} - T_{blc})}{T_{blc,\min}} * d(T_{blc,\min} - T_{blc}) \tag{7.111}$$

$$pelI_{st} = \frac{(I_{st} - I_{st,\max})}{I_{st,\max}} * d(I_{st} - I_{st,\max}) \tag{7.112}$$

$$pels_r = \frac{(s_r - s_{r,\max})}{s_{r,\max}} * d(s_r - s_{r,\max}) \tag{7.113}$$

The term *penalty* of (7.102) is the weighted sum of all the penalty functions for each of the constraints:

$$\begin{aligned} penalty = {} & k_1 * pelD_{sout} + k_2 * pelD_{rin} + k_3 * pelB_{r2} + k_4 * pelT_{sw} + k_5 * pelT_{rw} + k_6 * pelJ_s \\ & + k_7 * pelJ_r + k_8 * pelT_{st} + k_9 * pelT_{blc} + k_{10} * pelI_{st} + k_{11} * pels_r \end{aligned} \tag{7.114}$$

If all the design constraints are satisfied, the value of *penalty* is zero and the objective function *output* of (7.102) is the same as in (7.101). The coefficients k_i (i=1,2,3,4,...) represent the importance of violating certain constraints. First a set of values for k_i is chosen to scale each term in (7.114) to have a value of 1 when the limit is exceeded by 10% (110% of the maximum value or 90 % of the minimum value), which gives k_i (i=1,2,3,4,...)=10. Prior design experience gives an approximate range of *output* in (7.102) to be around 100. To make all design constraints relatively strict, when any of the constraints is violated, a value of 2 times of the *output* is assigned *penalty*. Hence, all the k_i's are increased by 100*2 = 200 from 10, which gives k_i (i=1,2,3,4,...)=2000.

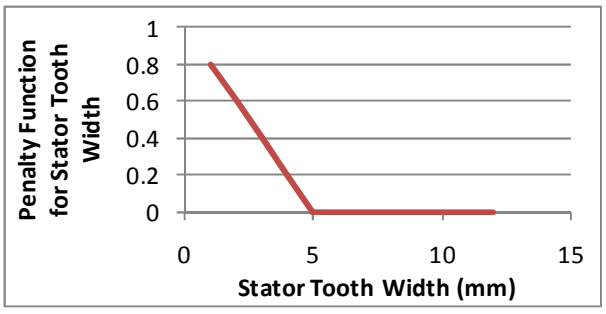

Figure 7.6: Penalty function for minimum stator tooth width

7.2.7.3 PSO implementation and optimization results

In the proposed induction machine design method, there are six prime design variables: $\overline{B}$, D, L, g, J_s, J_r. Hence, each particle is a six-dimensional vector. Since the number of design parameters increases from four in SMPM machine design to six in induction machine design, the number of particles used for the optimization also has to be increased.

The steel used for the stator and rotor lamination in this paper is non-oriented N007 from Cogent Steel[68]. The flux densities for the stator core, stator teeth, rotor core and rotor teeth are chosen to be 1.45 T, 1.45 T, 1.6 T and 1.6 T, respectively. The core loss is calculated from the manufacturer's catalog data given in [68]. The stator has 48 slots and the rotor has 42 slots.

Since there are more prime design variables in the proposed induction machine design method than for SMPM machines, more particles are needed. PSO is therefore run with a swarm of 40 particles and 100 iterations are needed to find the optimal design with the lowest value of *output* which also satisfies the design constraints defined in Table 7.2. The values of the six prime design variables and the performance of the optimal design found by PSO are shown in Table 7.3 and Table 7.4, respectively. The starting torque and breakdown torque of this optimal design just meet the design constraints(152.8 Nm over minimum starting torque of 150 Nm, and 209 Nm over minimum breakdown torque of 200 Nm), which agrees with the widely-known concept that starting performance is one of the primary limiting factors for mains-fed induction machine design.

Table 7.3: Values of the six prime design variables found by PSO

$\overline{B}$ (T)	D (mm)	L (mm)	g (mm)	J_s (A/mm^2)	J_r (A/mm^2)
0.5	154.2	122.2	0.38	5.36	4.56

Table 7.4: Performances of the optimal mains-fed induction machine found by PSO

Total machine weight	46.8 kg	Locked-rotor current	103.6 A
Efficiency	91.6 %	Breakdown torque	209 Nm
Power factor	88.3 %	Slip at rated output	0.04
Locked-rotor torque	152.8 Nm	*OFV*	87.1

7.3 Design optimization for inverter-fed induction machines

As described in Chapter 2, when induction machines are fed by variable-frequency inverters, the starting current and the starting torque are no longer design concerns. Furthermore, it is not necessary to select the machine rated frequency equal to that of the power grid, but it can be selected optimally based on power supply, operating environment, and design requirements. The proposed mains-fed induction machine design and optimization method is therefore modified for inverter-fed induction machine design in this section.

7.3.1 Design optimization and result

For inverter-driven induction machine design and optimizations, the constraints on the locked-rotor torque and current are removed, but the other constrains in Table 7.2 still apply. For comparison reasons, the same objective function of (7.102) is used (locked-rotor torque and current requirements removed from *penalty*). The same materials are used for the stator and the rotor. The flux densities for the stator core, stator teeth, rotor core and rotor teeth are also chosen to be the same as for the mains-fed induction machines, respectively. In addition, the stator winding layout, rotor bar number, and rotor slot shape are also the same as for the mains-fed induction machines. PSO is run with a swarm of 40 particles and 100 iterations and the optimal design result is shown in Table 7.5, where OFV is the objective function value (OFV) of the optimal design. The result shows that when the starting performance is not in the design constraints, better machine performances (83.2 of *OFV* compared to 87.1) are achieved.

Table 7.5: Performances of the optimal inverter-fed induction machine found by PSO

D (mm)	166	Weight (kg)	48.6
L (mm)	110	Efficiency	91.5 %
$\overline{B}$ (T)	0.46	Power factor	0.91
g (mm)	0.38	*OFV*	83.2
Js (A/mm2)	4.32	Penalty	0
Jr (A/mm2)	5.05		

7.3.2 Pole number selection

In a variable-speed motor design, the choice of pole number p and the resulting operating frequency f are important. With a smaller p and the same airgap flux density, the flux per pole is higher and the core thickness is thus larger. For the same stator outer diameter, less space is left for winding coils and the copper loss is higher. With a larger p, the f is higher and the core loss is higher. Moreover, the number of stator slots will also become larger with the same number of slot per pole phase, which results in increased manufacturing difficulty of the stator/rotor teeth. The overall effect is that the pole number is not determined by a single factor but varies for different material types, operating conditions, spatial constraints, and design objectives.

An effective approach proposed in this research to find the application-dependent optimal pole number is to design and optimize a series of machines with different pole numbers but with the same design constraints and same objective function. Since the proposed design method is able to find optimal designs effectively and fast, it is a good candidate for this task of generating a series of optimal designs. As an illustration, a series of induction machines are designed with constrains as shown in Table 7.2 and the objective function of (7.102). The stator/rotor slot number combinations and winding layout for each pole number are summarized in Table 7.6. The number of slot per pole per phase q for 2 pole and 4 pole designs are selected to be 4 because higher q helps to reduce the MMF harmonics produced by the stator winding. For 6 pole and 8 pole designs, q is reduced to 3 to avoid the tooth width to be too thin. As described on [8], the selection of stator and rotor slot combinations is based on many factors, particular due to the interactions of the stator and rotor MMF harmonics, and is a complicated topic with

numerous publications over several decades. In this research, the selection of rotor slot number is based on recommendations given by [8]. If a designer wishes to study the effect of slot numbers and winding configurations upon the efficiency and weight of the machine, then similar methods as the comparison of distributed and concentrated windings for SMPM machines in Chapter 4 can be used. In this research, certain other stator/rotor slot combinations have been tried but Table 7.6 yields the best optimization results. The machine performances of the optimal designs found by PSO for different pole numbers are shown in Table 7.7. With this proposed design and optimization method, optimal designs with different pole numbers can be found quickly and compared. Besides the machine topology, the choice of frequency also affects the power electronics design and the thermal design. By repeating such studies of optimal machine design with different pole numbers, design objectives, and design constraints, a large amount of quantitative results can be quickly produced by the proposed design and optimization method. These quantitative results contain detailed design information and provide important help to both machine designers and system designers, especially at an early design stage.

Table 7.6: Stator/rotor slot number and winding layout

Pole Number	Stator Slot Number	Rotor Slot Number	Winding Layout
2	24	18	Double layer, shorted-pitched by one stator slot
4	48	42	
6	54	48	
8	48	42	

Table 7.7: Comparison of different pole number designs

	2	4	6	8
Weight (kg)	86.8	48.6	41.7	35.8
Efficiency	90.9 %	91.5 %	92.2 %	92.2%
Power factor	0.85	0.91	0.88	0.85
Penalty	0	0	0	0
OFV	135.5	83.2	81.3	80.7

7.4 Comparison of PSO with Genetic Algorithms

Besides PSO, there are also other types of computational based optimization algorithms, for example, Genetic Algorithms (GA) is a popular alternative. It would be interesting to find out which algorithm is more suitable for machine design optimization problems. This section considers the 15 kW, 60 Hz, 1800 rpm induction machine design as an example and compares the performances of the PSO and GA methods. Some comparisons of GA and PSO have been reported by others, such as [41, 80], but this research uses a design method with a much larger dimension and hence a more challenging optimization problem. The comparison result is thus more informative.

7.4.1 Introduction and implementation of GA

Genetic Algorithm (GA) [81] is a search procedure that explores the solution space using mechanisms that emulates natural selection, including reproduction, crossover and

mutation. Steps of solving the induction machine design optimization problem using the analytical design method with GA can be summarized as follows:

1) *Encode any potential solution of the optimization problem into a binary string, called a chromosome.*

In this work, the six prime design variables $\overline{B}$, L, D, g, J_{rb} and J_s are converted into a binary string with 76 bits and a typical chromosome is shown in Figure 7.7. The bit string that describes a prime design variable in the chromosome is called a gene. This chromosome shown in Figure 7.7 is thus comprised of six genes. The number of bits assigned to each prime design variable depends on the typical range of this design variable for a 15 kW, 60 Hz, 1800 rpm induction machine. Scaling coefficients and offsets, which convert binary values to real values as illustrated in (7.115), are selected to make sure that typical values of the prime design variables are covered by the chromosomes. The values for scaling coefficients and offsets chosen in this research are shown in Table 7.8. For example, the binary value of D has 17 bits, which has a range of 0 to 2^{17}-1=131071. From past design experiences, too small a D will not yield a valid design. Hence, a value of 50 is assigned to *offset* to help reduce the search domain. Also from past design experiences, too large a D yields a too bulky design. Hence, a scaling coefficient of 500 is selected to reduce the upper bound of the search domain from (131071+50) to (131071/500+50)≈ 312.

$$(real\ value) = (binary\ value) / (scaling\ coefficient) + offset \tag{7.115}$$

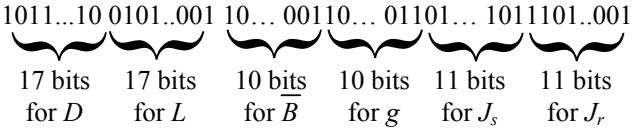

Figure 7.7: Illustration of a typical chromosome

Table 7.8: Scaling and offset coefficients

	Scaling Coefficients	Offset	Range of binary values	Range of real values
D (mm)	500	50	131071	50 ~ 312
L (mm)	500	50	131071	50 ~ 312
$\overline{B}$ (T)	1000	0	1023	0 ~ 1
g (mm)	1000	0	1023	0 ~ 1
Js (A/mm2)	200	2	2047	2 ~ 10
Jr (A/mm2)	200	2	2047	2 ~ 10

2) Create an initial population of chromosomes

The initial population is created by randomly populating each chromosome with zeros and ones.

3) Evaluate the chromosomes by the design objective function

Each chromosome represents an induction machine design candidate and the value of its objective function is calculated. For each candidate, the value of *output* is scaled using the mean and population of the total population, which is called Sigma scaling [82]. The advantage of sigma scaling is to help avoid premature convergence [82].

4) Select members from the current population to produce offspring

The chromosomes that have a low objective function value will have a larger probability of being selected to produce offspring. Stochastic universal sampling, which

is reported to exhibit no bias and minimal spread and ensure a selection of offspring [83], is used in this work.

5) Perform crossover

Among the chromosomes selected at step 4), pairs of parents are randomly picked and crossover is performed. To keep the population size constant for each generation, the number of parent pairs is equal to the population size and each pair produce one offspring. Uniform crossover is used, where each gene in the offspring is created by copying the corresponding gene from one or the other parent chosen according to a randomly generated binary crossover mask [81].

6) Perform mutation

Each bit in the chromosome is subject to mutation with a probability.

7) Repeat 3) to 6) until stop criterion is met

The maximum generation number is used as the stop criterion in this work.

7.4.2 Comparison result

PSO and GA are implemented with the induction machine design method to find the design that minimizes the objective function of (7.102). The two computational based optimization algorithms are compared in terms of their ability to find the correct optimal solution and the computational efficiency in solving the optimization problems.

7.4.2.1 Performance in finding the optimal solution

For both PSO and GA, the optimization processes are stochastic processes. For example, if PSO is run several times (even if each run starts with the same particles and the same iterations), the final solutions found by PSO each time may not be exactly the same, i.e., the algorithm does not guarantee to always find the correct optima. This

phenomenon is also true for GA and many other computational based optimization algorithms. Hence, the performance in finding the optimal solution for computational based optimization algorithms should be defined in a statistical sense and a good algorithm should be able to find the correct optima with a high probability. The optimal solutions for each run of the algorithm can be considered to be a random number with a mean and standard deviation. For minimization problems, if the optimal solutions found by an algorithm have a lower mean and smaller standard deviation than the solutions by another algorithm, then the first algorithm is considered to have a better performance.

In this work, PSO is run with a swarm of 40 particles and 100 iterations. For comparison proposes, GA is run with a population size of 40 chromosomes and 100 generations. Each algorithm is repeated 10 times and the optimal solutions are analyzed statistically. The result is compared in Table 7.9. For both GA and PSO, their running coefficients are carefully chosen and tuned for reasonably good performances. As calculated in the previous sections, the correct optimal design has an objective function value (OFV) of 83.2. Considering calculation tolerances, any design with an OFV of below 84 is considered to be a correct optimal design in Table 7.9. The comparison result of Table 7.9 shows that PSO and GA are both able to find the optimal solution within the 10 runs. PSO finds the correct optimal more times than GA (5 out of 10 versus 2 out of 10). PSO has a lower average of the optimal OFV (85.9) than GA (88.9) and also has a lower standard deviation of the optimal OFV. All the above comparison results indicate that PSO has a better ability to find the correct optima while GA is more likely to get trapped into local optima.

Table 7.9: Comparison of optimal Objective Function Value (OFV) for 10 runs by PSO and GA

	Best OFV	Worst OFV	Average of OFV	Standard deviation of OFV	Times to find correct optimal objective
PSO	83.2	93.9	85.8	3.61	5
GA	83.5	95.1	88.9	3.74	2

7.4.3 Computational efficiency

As described earlier, whether the correct optimum is found has some probability. In the actual implementation, the computational intelligence algorithm needs to be run several times to confirm that the best optimal solution is the correct one. The tuning of running coefficients used in the algorithms also requires running the algorithms a certain number of times. The overall number of candidates evaluated to find the correct solution is the product of the population size, the number of iterations or generations, and the times needed to run the algorithm in order to ensure a sufficiently good optimal solution (including tuning process). Since many machine design analysis methods, such as FEA, are computationally expensive, the optimization algorithm suitable for machine design should be able to find the correct optima with the least number of design candidates evaluated.

The number of iterations or generations needed to find optimal solutions depends on the convergence rate of the problem, which is determined primarily by the running coefficients and population size. For example, a higher value of the social acceleration constant in PSO or a lower sigma scaling coefficient will increase the convergence rate.

Hence, it would be reasonable to keep the number of iterations or generations constant and compare the ability to find optimal solutions with reduced population sizes.

In order to evaluate the algorithm's robustness to population size, PSO and GA are both run with reduced population sizes and their results are compared in Table 7.10. Again, the running coefficients for both algorithms are carefully tuned. With a population size significantly reduced to as low as 10, PSO still has relatively low average and standard deviation of OFV, which indicates that PSO still maintains acceptable performance (low average of OFV and standard deviation) while GA is much worse.

Table 7.10: Performance comparison of PSO and GA for reduced population size with running each algorithm 10 times

	Population size =20			
	Best OFV	**Worst OFV**	**Average of OFV**	**Standard deviation of OFV**
PSO	84.1	92.7	89.4	3.1
GA	83.8	96.2	90.7	5.2
	Population size =10			
	Best OFV	**Worst OFV**	**Average of OFV**	**Standard deviation of OFV**
PSO	83.2	106	91.2	7.7
GA	84.5	117	97.8	10.6

Another desirable property of a computationally efficient optimization algorithm is the robustness to its running coefficients so that computational effort is saved with less

tuning effort. The robustness of PSO and GA is compared with randomly selected running coefficients. For PSO, the inertia, local and global acceleration constants are selected randomly between 0 and 1. For GA, crossover probability and mutation probability are also selected between 0 and 1 and the sigma scaling coefficient is selected between 0 and 5. Each algorithm is run 5 times and the result is compared in Table 7.11. The results show clearly that PSO has a lower average and standard deviation and GA's worst solution of 106, is significantly higher than the 84.7 of PSO. The comparison shows that tuning of the parameters is important for GA while PSO requires less tuning, which saves time to find the optimal solution. Furthermore, this time saving in the tuning is pronounced as the modeling techniques become more intensive.

Table 7.11: Performance comparison of PSO and GA for randomly chosen coefficients with running each algorithm 5 times

	Best OFV	Worst OFV	Average of OFV	Standard deviation of OFV
PSO	84.9	93.5	87.2	3.2
GA	87.9	106	94	6.5

7.5 Chapter summary

In this chapter, a novel design and optimization method is proposed for both mains-fed and inverter-driven induction machines. The proposed method is more efficient than traditional design methods because it finds an optimal design with no heuristic approaches or design iterations. The computing time is almost negligible. The optimal

design results are verified by FEA. For mains-fed induction machine designs, the requirements of industry standards, such as NEMA design standards, are considered in the design and optimization. For inverter-driven induction machine designs, the advantage of supplying the machine with adjustable frequencies is reflected by the proposed design and optimization method. Better machine performances (lower value of *output*) are thus achieved for inverter-driven induction machines over mains-fed induction machine designs. The proposed method not only designs induction machines optimally, but is also a useful tool to help both machine designers and drive system designers to make system-level decisions at the initial design stage.

PSO and GA are compared in this chapter with the aim of finding which algorithm is more suitable for machine design optimization. The results show that PSO and GA both have the ability to find the correct optimal solution, but PSO has a better performance in finding the global optima. Furthermore, in terms of the computational efficiency, which is a key requirement for the algorithms in machine design, PSO outperforms GA significantly. PSO has a lower performance degrading with a smaller population size, and higher robustness to its algorithm coefficients. The comparison results indicate that PSO should be preferred over GA, particularly when time is a limiting factor.

CHAPTER 8
Conclusions, Contributions and Recommendations for Future Works

8.1 Summary

This dissertation has proposed a method for the design and optimization of Surface Mount Permanent Magnet (SMPM) machines, as influenced by the energy source, mechanical loads, thermal effects, and the up-to-date developments in materials and manufacturing capabilities. It has also proposed a method for the design and optimization of cage rotor induction machines.

Chapter one has introduced the background information regarding the design and optimization of electrical machines and stated the objective of this research.

Chapter two has presented a comprehensive review of previous work on the design and optimization of SMPM machines and induction machines. First, a summary of the traditional machine design approach has been presented and has come to a conclusion that the traditional design is strongly based on the heuristic selection of parameters and empirical curves and does not reflect the modern development in materials, power electronics, etc. Moreover, the traditional design process is an inefficient iterative process, which makes it difficult to optimize a design. Second, the more recent development of the SMPM machine and induction machine and optimization methods, including the CAD software tools, has been summarized. It has been concluded by this review that although the more recent machine design methods and tools can incorporate the modern techniques at some level, they are still far from ideal. The selection of key design parameters by the designer, such as the magnetic loading, electric loading, and current density, still plays an

important role in the design. Though thermal analysis is applied in some of the design processes, thermal design is typically treated separately and is only used to check the temperature distribution of a completed design. The literature review presented in this chapter has justified the need and novelty of the proposed research - developing a machine design and optimization method, which is able to reflect the effect of the energy source, power electronics, load profile, thermal constraints, and material properties.

In Chapter three, a new analytical design method of SMPM machines with good accuracy and considerations of the nonlinearity in the material has been developed. PSO has been applied in a novel way to find the optimal solutions with respect to a certain user defined objective function. The advantage with this proposed analytical design method and PSO optimization is that the heuristic selection of the design variables, including the electric loading, magnetic loading and aspect ratio, are no longer necessary. The PSO computing time is almost negligible. The results will provide useful insight for drive system designers or machine designers at the initial design stage.

Chapter four has studied the concentrated winding, a winding type that is becoming popular recently, and compared it to the traditional distributed winding for SMPM machines. An analytical design method has been developed for a SMPM motor with either distributed or concentrated stator windings and PSO has been applied to optimize the design of each motor for both weight sum multi-objective optimization and vector multi-objective optimization. The optimized designs with the two winding types have been compared quantitatively for certain user-defined objective functions. The Pareto front of the two winding designs have been found and compared. Optimization results

have shown that the concentrated winding machines generally have a better performance than the distributed winding machines, in terms of active volume and efficiency.

Chapter five has proposed a novel integrated Electromagnetic-Thermo-Mechanical design method for the design of Surface Mount Permanent Magnet (SMPM) machines. In this integrated approach the current density is no longer heuristically selected and the thermal and mechanical designs are no longer treated separately as is often done in traditional designs. The magnet protection has also been included in the proposed integrated design method. Particle Swarm Optimization has been used to find designs that minimize user defined cost functions. The optimization results have shown that the integrated design approach is able to find optimal designs with systematical consideration of both electromagnetic and mechanical design factors, cooling capability and thermal limits. The consideration of load profiles has also been incorporated in the proposed integrated design and optimization method. Particle Swarm Optimization has also been applied to optimize SMPM machine designs with certain specific load profiles and the gains of considering the load profiles have been illustrated.

In Chapter six, a sensitivity analysis has been carried out to study how the SMPM machine performance varies with variations of the machine parameters between the design calculation and the actual manufactured machine. Three sources of machine parameter variations have been identified: material properties, modeling errors, and manufacturing tolerances. Detailed sensitivity analysis results have been listed in Table 6.1. The sensitivity analysis has shown that although the machine parameters may vary from their original value used in the design calculation and optimization, the effect of such variations on the machine performance can be determined and can be used by

machine designers to decide which parameters should be given more attention and importance to reduce the effect of such variations. The sensitivity analysis result has also shown that the optimal solution can still hold if parameter variations are within a certain range.

Chapter seven has proposed a novel design and optimization methods for both mains-fed and inverter-driven induction machines. The proposed methods are more efficient than traditional design methods because they find an optimal design with no heuristic approaches or manual design iterations. The computing time is almost negligible. The optimal design results have been verified by FEA. For mains-fed induction machine designs, the requirements of industry standards, such as the NEMA design standard for example, have been considered in the design and optimization. For inverter-driven induction machine designs, the advantage of supplying the machine with adjustable frequencies has been reflected by the proposed design and optimization method. When the inverter-driven and mains-fed induction machines are both optimized by PSO and with the same objective function, inverter-driven induction machines have shown better performances than mains-fed induction machine designs (indicated by lower optimal value of the design objective function). The proposed method not only designs induction machines optimally, but is also a useful tool to help both machine designers and drive system designers to make system-level decisions at the initial design stage.

PSO and GA have been compared in this work with the aim of finding which algorithm is more suitable for machine design. The results show that PSO and GA both have the ability to find the correct optimal solution, and PSO has a better performance in finding the global optima. Furthermore, in terms of the computational efficiency, which

is a key requirement for the algorithms in the machine design, PSO outperforms GA significantly. PSO has a lower performance degrading with a smaller population size, and higher robustness to algorithm coefficients. The comparison results have indicated that PSO should be preferred over GA when time is a limiting factor. This conclusion is not only for induction machines, but also applies for SMPM machines and other types of machine design and optimizations.

8.2 Contributions

The main contributions of this research are summarized as follows:

1. A comprehensive literature survey of the traditional machine design methods and recent progresses in the design and optimization of Surface Mount Permanent Magnet (SMPM) machines and induction machines has been presented. In addition, the applications of optimization algorithms in electrical machine design have been summarized. These design and optimization methods have been evaluated with a focus on details of the accuracy of the design models, the computational efficiencies, and the abilities to reflect constraints and specifications.
2. A novel electromagnetic analytical design method of SMPM machines has been developed, which needs only three prime design variables but is able to design SMPM machines in fine details. A PSO based optimization algorithm is applied in a novel way to optimize the electromagnetic design of SMPM machines subject to a user-defined multi-objective optimization. The advantage over the traditional and other existing design methods is that this proposed method does not have the heuristic selection of the design variables and does not need manual

design iterations. The computing time is almost negligible and the design cycle is significantly reduced compared to the tradition machine design. Part of this has already been published in [84] and [85].

3. A new method for multi-objective designs of Surface Mount Permanent Magnet machines with distributed or concentrated windings has been developed. SMPM machines with the two winding types have been optimized and compared. The merits and disadvantages of the two winding types can thus be comprehensively understood from the quantitative comparison of results. Part of this has already been published in [41].
4. A novel electromagnetic-thermo-mechanical integrated design and optimization approach for SMPM machines has been proposed. A significant advantage over the traditional machine design method is that the proposed method is not based on rules-of-thumb or heuristical approaches, but is based on the physics of the electrical machines. A generic thermo-mechanical model of SMPM machines developed by the authors partner ground in mechanical engineering [61] [1] has been integrated with the electromagnetic design method of SMPM machines in this work.With the proposed method, the thermal and mechanical design is no longer treated separately and heuristically as in the traditional design, but has been systemically integrated with the electromagnetic design; the effect of power source, cooling capability, thermal limits, and up-to-date material capabilities are also reflected in the design and optimization. Superior designs compared to traditional designs can be achieved with PSO based multi-objective optimization. The proposed integrated design approach also has the merit of good

computational efficiency and provides a significant time reduction of the design cycle compared to FEA. Part of this had already been submitted to the IEEE Transactions of Industrial Electronics and is currently under review.

5. A novel sensitivity analysis has been developed for the design of SMPM machines to determine how the variations of certain machine parameters affect the machine performances. The proposed sensitivity analysis provides designers with useful information on how the optimal design is affected by variation of machine parameters.
6. A novel electromagnetic analytical design method of induction machines has been developed, which needs only six prime design variables but is able to design induction machines in fine details. The advantage over the traditional and other existing design method is that this proposed method does not have the heuristic selection of the design variables and does not need manual design iterations. The computing time is almost negligible and the design cycle is significantly reduced compared to the tradition machine design. Part of this has already been accepted to the 2010 Energy Conversion Congress and Exposition (ECCE 2010).

The research work presented in this dissertation has resulted in several publications, which are listed as follows:

Journal papers:

Y. Duan, A. Semidey, R. G. Harley, J.R. Mayor and T. G. Habetler, "Integrated Electromagnetic-Thermo-Mechanical Design and Optimization of Surface Mount Permanent Magnet Machines," submitted to IEEE Transactions on Industrial Electronics.

Y. Duan, R. G. Harley, and T. G. Habetler, "Method for Vector Multi-objective Optimized Designs of Surface Mount Permanent Magnet Motors with Concentrated or Distributed Stator Windings," submitted to IEEE Transactions on Energy Conversion.

Conference papers:

Y. Duan, R. Harley and T. Habetler, "Method for Multi-objective Optimized Designs of Surface Mount PM Motors with Concentrated or Distributed Stator Windings", IEEE International Electrical Machines and Drives Conference (IEMDC 2009), pp. 323-328, Miami, FL, May 3-6, 2009.

Y. Duan, R. Harley and T. Habetler, "A Useful Multi-objective Optimization Design Method for PM Motors Considering Nonlinear Material Properties", IEEE Energy Conversion Congress and Exposition (ECCE 2009), pp. 187-193, San Jose, CA, Sept. 20-24, 2009.

Y. Duan, R. Harley and T. Habetler, " Multi-objective Design Optimization of Surface Mount Permanent Magnet Machine with Particle Swarm Intelligence", IEEE Swarm Intelligence Symposium (SIS 2008), St. Louis, MO, pp. 1-5, Sept. 21-23, 2008.

Y. Duan, R. G. Harley and T. G. Habetler, "Comparison of Particle Swarm Optimization and Genetic Algorithm in the Design of Permanent Magnet Motors," IEEE International Conference on Power Electronics and Machine Drives (IPEMC 2009), pp. 822-825, Wuhan, China, 17-20, May 2009

Y. Duan and R. Harley, "Present and Future Trends in Wind Turbine Generator Designs", IEEE Symposium of Power Electronics and Machines in Wind Applications, pp. 1-6, Lincoln, NE, June 24-26, 2009.

Y. Duan, R. G. Harley, and T. Habetler, "Method for Multi-objective Optimization Designs of Three Phase Induction Motors", accepted to IEEE Energy Conversion Congress and Exposition (ECCE 2010), Atlanta, GA, Sept. 2010.

A. Semidey, **Y. Duan**, J.R. Mayor, and R.G. Harley, "Optimal Electromagnetic-Thermo-Mechanical Integrated Design for Surface Mount Permanent Magnet Machines Considering Load Profiles", accepted to IEEE Energy Conversion Congress and Exposition (ECCE 2010), Atlanta, GA, Sept. 2010.

In addition, several more journal and conference papers, based on the research of Electromagnetic-Thermo-Mechanical integrated design of SMPM machines, are being prepared.

8.3 Recommendations for Future Work

Although this work has presented contributions to various areas of electrical machine design and optimizations, there are several directions in which further research could build on the results presented in this work.

1. The proposed electromagnetic design method for induction machines can be integrated with thermal models (generic thermal model, not based on heuristic curves) to develop an Electromagnetic-Thermo-Mechanical integrated design method of induction machines. Presently the generic thermal model is only developed for SMPM machines, where the stator

copper loss and core loss are the major heat sources. Since the rotor bar Watt loss is another major heat source for induction machines, modeling the complicated heat transfer between the rotor and stator is a significant challenge. Once a generic thermal model is developed for induction machines, an integrated Electromagnetic-Thermo-Mechanical design method for induction machines can be developed, which will achieve similar features and advantages for the proposed integrated Electromagnetic-Thermo-Mechanical design method for SMPM machines

2. Modeling of different cooling media can be added to the integrated design method. Presently, the cooling capability is represented by the media type and flow speed. It would be interesting if a fan design were added in the integrated method. If the fan is installed on the same shaft as the rotor of the machine, at higher cooling gas flow speed and pressure, more shaft torque is needed for driving the fan. Hence, there is a trade-off between machine efficiency and cooling capability. If this trade-off is considered in the optimization, machines with superior performances may possibly be found.
3. Research can be carried out to increase accuracy of induction machine performance calculation, for example, the leakage inductance calculations. Because of the complicated interactions of the stator current, rotor bar current, and the magnetic field around the airgap, various assumptions have to be made to develop analytical equations for performance calculations, though the performance calculations in the present method have been verified by FEA to have reasonably good accuracy. With the development of modern

advanced electromagnetic theories, there may be possibilities to increase the accuracies of induction machine performance calculations. Models with better accuracies lead to design and performance calculations closer to the manufactured machines.

4. SMPM and induction machine prototypes can be built to verify the proposed design and optimization method for SMPM machines and induction machines. Nevertheless the proposed design methods have been extensively verified by FEA with good agreements. However, experimental measurements on a manufactured prototype machine that include the effect of manufacturing tolerances and material property variations can be carried out to further investigate the gains of the proposed method. The prototype machines should not only verify the performance of one optimally designed machine, but should be a series of machines with different design objectives and ratings.
5. A cost model can be developed for SMPM machines and induction machines and added into the design objective. The cost of the product is always one of the major concerns for manufacturers. Hence, the proposed method will find more applications if machine cost is included.
6. On the optimization side, research can be done regarding how to properly choose the coefficients attached to each performance index in the weighted-sum multi-objective optimization. It is recommended that a study of the machine design objectives and trade-offs in different applications should be first carried out. An approach that is able to convert such objectives and trade-offs into the numbers before each performance index is recommended.

In this way, the proposed machine design method will design machines to better fulfill the needs of specific applications.

7. For different applications, there might be special design considerations and requirements. For example, a good flux-weakening capability and a high torque burst capability are desired for traction motors in hybrid vehicle applications. Such special application-based challenges are presently solved by designer's experience and by trial-and-error. Since the proposed design method already designs machines in fine detail, these special considerations can be possibly added into the proposed design method. PSO may then possibly find designs that not only meet those additional challenges, but also have better performances (higher efficiency, cooler, less weight, etc.) than existing designs.

APPENDIX I

Typical Values for the Height of Stator Slot Tip and Wedge [12]

Items	Typical Values
B_{s0}	2.5 ~ 4.0 mm
H_{s1}	0.5 ~ 1.5 mm
α_1	30^o or 35^o

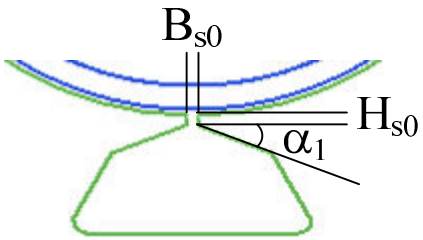

APPENDIX II

Matlab Program of the Electromagnetic Design Model of SMPM Machines (Distributed Winding)

1. Main Design Function

```
function output=SMPM_inte_fun_v8_transient(para)

global Nm Np DiaSGap ThickSYoke Lst ThickMag g Tsr f Kop Spp Kw Bf Lst
Pout kcarter miu0 miuR Hs Hs0 Hs1 Hs2 Bs0 Bs1 Bs2  Rs As Hs2 Tw PHImp
DiaRYoke DiaSYoke BFgap Ut Bg Bm Bair kj Br;

% Stator diameter at gap side
DiaSGap=para(1);
% Motor axial length /mm
Lst=para(2);
% Thick of magnet /mm
ThickMag=para(3);
% Current density A/mm2
J=para(4);


%% %%%%%%%%%%%%%%%%%%%%%%%%%%  Inputparameters   %%%%%%%%%%%%%%%%%%%%%%%%%%
% Frequency
f=60;
% Terminal Voltage
Ut=480/sqrt(3);

miu0=4*pi*1e-7;
miuR=1.05;


% Number of poles
Np=4;
% Slots/phase/pole
Spp=2;
% Number of slots
Nm=3*Spp*Np;

% Pole coverage coefficient
Embrace=0.83;

% Airgap length /mm
g=1;
Bs0=2;



%%%%%%%%%%%%%%%%%%%%%%%%%%%%%%%%%%%%%%%%%%%%%%%%%%%%%%%%%%%%%%%%%%%%%%%%%%%
%%
```

```
%% %%%%%%%%%%%%%%%%%%%%%%%%%  Airgap flux density %%%%%%%%%%%%%%%%%%%%%%

% % NdFe35, Parallel magnetized and operate at, Br, T; Hc A/m

% Magnitude of each harmonics of B profile in the airgap

BFgap=emfcal_zhu_fun3input([DiaSGap ThickMag]);

% Airgap flux density profile with mechanical degree for two poles
j=13; % the number of how many harmonics to be computed, 7 means from
1st to 13rd
for t=1:180
    for s=1:j
    Bairm(s,t)=BFgap(s)*cos((2*s-1)*Np*((t-45)/(Np/2)/180*pi));
    end
end
Bair=sum(Bairm);
t=1:180;

theta=(t)/(Np/2);   % theta is mechanical degree

Bair=Bair';
theta=theta';

% plot(theta,Bair);

% % Maximum value of flux density in the airgap
Bm=sum(Bair(23:67))/45;
% Bg=sum(abs(Bair))/length(Bair);
Bg=sum(Bair(6:86))/80;


%% %%%%%%%%%%%%%%Calculation of teeth width and yoke thickness%%%%

%Flux density in stator core
Bsc=1.45;
%Flux density in rotor core
Brc=1.45;
%Flux density in stator teeth
Bt=1.45;

% Stacking factor of the stator iron laminations
kj=0.95;
% Total magnetic flux per pole produced by the magnets
PHImp=Bg*pi*DiaSGap*Lst/Np;

% Maximum flux in the stator yoke
PHIsy=PHImp/2;
% Thickness of the stator yoke
ThickSYoke=PHIsy/(Bsc*kj*Lst);
% Thickness of the rotor yoke
ThickRYoke=PHIsy/(Brc*kj*Lst);

N=floor(360/Nm);
N0=floor(360/Nm/2);
```

```
Bairta(1)=sum(abs(Bair(1:N)))/N;
for kk=1:Nm/2-1
    Bairta(kk)=sum(abs(Bair(N0+(kk-1)*N+1:N0+kk*N)))/N;
end
Bairm=max(Bairta);
% Stator tooth width
Tw=Bm*(pi*DiaSGap/Nm)/kj/Bt;

DiaRGap=DiaSGap-2*g;
DiaRYoke = DiaRGap-2*(ThickMag+ThickRYoke);



%% %%%%%%%%%%%% Calculation of current and number of turns %%%%%%


% With full pitch winding, winding factor
Kw=1/Spp*sin(pi/6)/sin(pi/6/Spp);

% Rated power,  200W is mechanical loss
Pout=15200;

% Ampere Turns

%AmpT=Pout/3/4.44/Kw/f/(PHImp/1000^2);

% Slot type 3
Hs0 = 1;
Hs1 = 1;
Rs = 2;
%Hs2 = Hs-Hs0-Hs1-Rs;
Bs1 = pi*(DiaSGap+2*(Hs0+Hs1))/Nm-Tw;
%Bs2 = pi*(DiaSGap+2*(Hs0+Hs1+Hs2))/Nm-Tw;


% Number of total turns per phase
Nc=round(fsolve('ampturnDist',200));
NCoil_half=round(3*Nc*2/Nm/2); % Number of turns per half slot
NCoil=NCoil_half*2; % Number of turns per slot
Nc=NCoil*Nm/2/3;

% Phase Current
E=4.44*f*Nc*Kw*BFgap(1)*2/pi*pi*DiaSGap*Lst/Np/1000^2;
Ip=Pout/3/E;
% Ip=AmpT/Nc;
% E=Pout/3/Ip;


% Wire size determination
WireDia=sqrt(Ip/J/pi)*2; % Wire diameter
G=round(log(WireDia/8.24865)/log(0.890526)); % Wire gauge
WireDiaG=8.24865*(0.890526)^G;
AcuWire=pi*WireDiaG^2/4;
% Copper area per slot
Acu=AcuWire*Nc/Spp/(Np/2);
% Wire copper diameter
%Dwire=sqrt(Ip/J*4/pi);
```

```
% Recalculate current density
J=Ip/AcuWire;


%% %%%%%%%%%%% Calculation of number of turns and stator size %%%%%



% Copper Fill factor
Fl=0.4;
% Stator slot area per slot
As=Acu/Fl;

% Teeth length
Hs = fsolve('tlength',10);

DiaSYoke=DiaSGap+2*(Hs+ThickSYoke);
% DiaSYoke=2*(sqrt((Hs+DiaSGap/2+Rs)^2+(Bs2/2-Rs)^2)+ThickSYoke+Rs);
% Stator slot width at the gap side, at the core side/mm: Swg, Swc
Swg=pi*DiaSGap/Nm-Tw;
Swc=pi*(DiaSGap+2*Hs)/Nm-Tw;

% Slot type 3
% Hs0 = 1;
% Hs1 = 1;
% Rs = 2;
Hs2 = Hs-Hs0-Hs1-Rs;
% Bs1 = pi*(DiaSGap+2*(Hs0+Hs1))/Nm-Tw;
Bs2 = pi*(DiaSGap+2*(Hs0+Hs1+Hs2))/Nm-Tw;
% Bs0=1;



%% %%%%%%%%%%%%%%%%%%%%%%%%%%%%%%%%%Calculation of inductance  %%%%%%%%

%Magnetising inductance
% kcarter=1.1;
gp=g+ThickMag/miuR;
% Carter Coefficient
gamma=4/pi*(Bs0/2/gp*atan(Bs0/2/gp)-1/2*log(1+(Bs0/2/gp)^2));
taos=pi*DiaSGap/Nm;
kcarter=taos/(taos-gamma*gp);

Lm=3/pi*(Spp*Nc/Spp/(Np/2)*Kw)^2*miu0/(g*kcarter+ThickMag/miuR)*(DiaSGa
p-2*g)*Lst/1000;
Xm=2*pi*f*Lm;
wsb=(Bs1+Bs2)/2;
Llslot=Spp*Np*(Nc*3/Nm*2)^2*miu0*(Hs2*Lst/3/wsb+Hs1*Lst/((Bs1+Bs0)/2)+H
s0*Lst/Bs0)/1000;
% End inductance

Llend=Spp*Np*miu0*(Tw+wsb)*(Nc*3/Nm)^2/2*log((Tw+wsb)*sqrt(pi)/(sqrt(2*
As)))/1000;
% Total leakage inductance
Ll=Llslot+Llend;
Xl=2*pi*f*Ll;
```

```
%% %%%%%%%%%%%%%% Calculation of copper loss %%%%%%%%%%%%%%%%%

% Resistivity of copper
pcu=1.68*1e-8;
Lext=20;
% End length of one turn, assume full pitch winding
Lend=Lext*2+pi/2*(DiaSGap+2*(Hs0+Hs1)+Hs2)/Np; % Average of the maximum
and minimum end length
% Wire length of one turn
Lwireturn=Lst*2+Lend*2;
% Total wire length
Lwire=Nc*Lwireturn;


% Wire resistance
Rcu=pcu*Lwire/AcuWire*1000;

% ac resistance
m_layer=round(Hs2/WireDiaG);
skin_depth=1/sqrt(pi*miu0/pcu*f);
ep_depth=sqrt(AcuWire*1e-6)/4/skin_depth;
ac_ratio=1;
for k=2:m_layer
    ac_ratio=ac_ratio+2/3*(ac_ratio^2-1);
end
ac_ratio=ac_ratio*ep_depth/2*(sinh(ep_depth)+sin(ep_depth))/(cosh(ep_de
pth)+cos(ep_depth));
Racu=Rcu*ac_ratio;
% Armature copper loss
PCu=Ip^2*Rcu*3;


%% %%%%%%%%%%%%%%%% Calculation of active weight %%%%%%%%%%%%%%%%%%%
% Mass density of steel in kg/m3
Md=7.8*1e3;
% Weight of the stator bore in kilogram
WtSYoke=pi*(DiaSYoke^2-(DiaSYoke-2*ThickSYoke)^2)/4*Lst*Md*(1e-9);
% Weight of the stator teeth
WtSTeeth=Nm*Tw*Hs*Lst*Md*(1e-9);
% Weight of the rotor yoke
WtRYoke=pi*((DiaRYoke+2*ThickRYoke)^2-DiaRYoke^2)/4*Lst*Md*(1e-9);
% Mass density of copper in kg/m3
Mc=8.96*1e3;
% Weight of copper
%WtCopper=3*(Np*Lst+DiaSGap*pi*kcoil)*(Nc/Spp/(Np/2))*Spp*(Acu/(Nc/Spp/
(Np/2)))*Mc*(1e-9);
%WtCopper=3*(Lst+DiaSGap*pi*kcoil)*Nc*2*AcuWire*Mc*1e-9;
WtCopper=3*Lwire*AcuWire*Mc*1e-9;
% Weight of Permanent Magnet
Mpm=7474; % mass density of NdFeB in kg/m3
WtMagnet=(DiaRGap^2-(DiaRGap-ThickMag*2)^2)*pi/4*Embrace*Lst/1000^3*Mpm;
% Total weight
Weight=WtSYoke+WtSTeeth+WtRYoke+WtCopper+WtMagnet;
```

```
%% Calculation of core loss
% % Core loss estimation at no load condition
% % Loss density W/kg
LdTeeth=3.03;
LdCore=3.03;
Pcore=(WtSYoke*LdCore+WtSTeeth*LdTeeth)*kj;
StatorCoreLoss=Pcore;
WtStatorCore=WtSTeeth+WtSYoke; % Total weight of stator steel in kg
VolumeStator=WtStatorCore/Md; % Total volume of stator steel in kg/m3
SCoreDensity=StatorCoreLoss/(VolumeStator*1e9);% Stator core loss
density in W/mm3

%% Generate vector for thermal analysis


A_slot_tot = (((Bs1 + Bs2)/2 * Hs2) + ((Bs0 + Bs1)/2 * Hs1)) / 1000^2;
R_f_i = DiaSGap/2/1000; % inner radius of the foot / m
Theta_f = acos((2*R_f_i^2-(Bs0/1000)^2)/(2*R_f_i^2))/2; % half the
angle of the foot in radius
R_f_o = (DiaSGap/2+Hs0+(Hs1/2))/1000; % outer radius of the foot / m
% R_w = (DiaSGap/2+Hs0+Hs1)/1000;
R_avg = R_f_i + Hs0/1000 + Hs1/1000 + (Hs2/2000);
Theta_t = atan(((Bs1+Bs2)/4000)/R_avg);   % harlf the angle of the
tooth in radians
R_s_i =  sqrt(A_slot_tot/Theta_t + R_f_o^2); % inner radius of the
stator / m
R_s_o = DiaSYoke/2/1000;
Theta_o = 2*pi/(Nm*2); % Half the angle of the slot in radius
R_w_b=(DiaSGap+2*Hs0+2*Hs1)/2/1000;

%--------Boundary conditions

% Outer stator radius boundary
T_s_o_inf = 300; % [K]
h_s_o = 1; % [W/m^2-K]
q_s_o=0; %[W/m^2]

% Inner stator radius boundary
T_f_i_inf = 300; % [K]
h_f_i = 1; % [W/m^2-K]
q_f_i=0; %[W/m^2]


thermal_vector = [Lst/1000 Ip 3 SCoreDensity Rcu T_s_o_inf h_s_o q_s_o
T_f_i_inf h_f_i q_f_i];

thermal_geometries = [Theta_f Theta_t Theta_o R_f_i*1000 R_f_o*1000
R_w_b*1000 R_s_i*1000 R_s_o*1000];

Boundary_Type='smooth_natural_horizontal';% must be
smooth_natural_horizontal, smooth_natural_vertical, smooth_froced
                %  finned_natural_vertical, finned_natural_horizontal,
                %  finned_forced


Max_Winding_Temp=Motor_Thermal_Analysis_v8_2(thermal_geometries,thermal
_vector,Boundary_Type);
```

```
% load maxtemp.mat
% The transient time and temperature is stored under variable
"Winding_Temp_Transient"
% The first row is time vector in seconds
% The second row is the maximum winding tempature as a function of time



% Calculate penalty function for winding temperature
Life_ex=20000; % expected winding insulation life
L_TF140=20000; % winding insulation life for class F at 140 C
% % if transient
% Life_Temp=insulation_life(Winding_Temp_Transient);
% if steady state
Life_Temp=L_TF140*10^(-0.03*(Max_Winding_Temp-153));

pelTemp=max([0 (Life_ex-Life_Temp)/Life_ex]);




%% Frame Calculations

%----------Frame Spec
Material = 'steel'; % must be steel, cast_iron, or aluminum
Torque_max = 300; % [N-m]


n = 50; % safety factor

if strcmp(Material,'steel')
    T_Yeild = 120 * 10^6; %Pa
    k_frame = 60; %W/m-k
elseif strcmp(Material,'cast_iron')
    T_Yeild = 150 * 10^6; %Pa
    k_frame = 35; %W/m-k
elseif strcmp(Material,'aluminum')
    T_Yeild = 140 * 10^6; %Pa
    k_frame = 170; %W/m-k
else
    error('Material Type not valid')
end

a = 1;
b = 4 * R_s_o ;
c = 6 * (R_s_o )^2;
d = (4 * (R_s_o )^3) - (4 * n * Torque_max/(pi * T_Yeild));
e = - 4 * n * Torque_max * (R_s_o )/(pi * T_Yeild);

r = roots([a b c d e]);

t_frame = min(abs(r))*1000; % [mm]
Wtframe = pi*((DiaSYoke+t_frame*2)^2-DiaSYoke^2)/4*Lst*Md*(1e-9);
% Weight=Weight+Wtframe;

%% Calculation of performances
```

```
% weight
Weight=Weight+Wtframe;

% Volume
Volume=pi*(DiaSYoke+2*t_frame)^2/4*1.3*Lst/1000^3;
% Magnet Volume
VMagnet=(DiaRGap^2-(DiaRGap-ThickMag*2)^2)*pi/4*Embrace*Lst;


% Total Loss estimation
Ptotal=PCu+Pcore;

% Estimation of windage and friction loss
Pwf=200;
% Efficiency
Eff=15000/(Pout+Ptotal+Pwf);

% Power factor
pfactor=(E+Ip*Rcu)/Ut;
% Torque ampere
TperA=Pout/(f*2*pi/(Np/2))/Ip;

%% Calculate penalty function for saturation

% Penalty function for saturation
Btm=armature([DiaSGap ThickMag Ip]); % maximum flux density in the
stator teeth
BtL=1.7; % lower bound to trigger the saturation penalty
slBt=10; % increasing slope for saturation penalty
pelSat=linpenalty(Btm,[BtL slBt]);


%% Magnet protection from demagnetization

% Rated condition
B_dmg=0;
Is_dmg=Np*pi/(6*miu0*Kw*Nc)*(Br*ThickMag/1000-
B_dmg*(g+ThickMag)/1000); % maximum allowable rms stator phase current
before demagnetization
dmg_rated=Ip/Is_dmg; % demagnetization indicator. dmg_inc<1, no
demagnetization
dmgrL=0.9; % trigger of demagnetization at rated condition
sldmgr=10;
pelDmgr=linpenalty(dmg_rated,[dmgrL sldmgr]); % penalty function for
demagnetization at rated condition

% Short circuit
% short_exp=exp(-pi/(2*pi*f*(Lm+Ll)/Rcu));
% dmg_short=((8/pi*Embrace*short_exp-1)*Br*ThickMag/1000-
B_dmg*(g+ThickMag)/1000)/(Br*ThickMag/1000-B_dmg*(g+ThickMag)/1000);
dmg_short=(8/pi*Embrace*Br*ThickMag/1000)/(Br*ThickMag/1000-
B_dmg*(g+ThickMag)/1000)-1;
dmg_shortinc=dmg_short/(Xl/Xm); % the machine is safe when Xl/Xm is
larger than dmg_short, or dmg_shortinc<1
dmgsL=1; % lower bound to rigger
sldmgs=10; % slope
```

```
pelDmgs=linpenalty(dmg_shortinc, [dmgsL sldmgs]); % penalty function
for demagnetization at short circuit
pelDmgs=0;


%% Output
% sum of penalty function
penaltysum = 1000*(pelSat+pelDmgr+pelDmgs+pelTemp);
output = Weight+(1-Eff)*100-TperA*10+penaltysum;
% output=Weight+penaltysum;
% penaltysum
```

2. Function to calculate airgap flux density

```
function BF=emfcal_zhu_fun_3input(para)
global Bs0 Nm Br


DiaSGap=para(1);
ThickMag=para(2);

miu0=4*pi*1e-7;


%material NdFeB35
Br=1.04;
miur=1.05;
g=1e-3;
hm=ThickMag/1000; %5.5e-3;
%Kc=1.01;
gp=g+hm/miur;
% Carter Coefficient
gamma=4/pi*(Bs0/1000/2/gp*atan(Bs0/1000/2/gp)-
1/2*log(1+(Bs0/1000/2/gp)^2));
taos=pi*DiaSGap/Nm;
Kc=taos/(taos-gamma*gp);

% consider sloting
Rs=DiaSGap/1000/2+(Kc-1)*gp;
%Sizing
% Rs=75.6e-3;


Rm=DiaSGap/1000/2-g;
Rr=Rm-hm;
% Number of poles, in the paper, it's pole pairs
p=4;
% L=110e-3;
%b0=14.5e-3;

% The radius where the flux density is calculated
r=DiaSGap/1000/2;

%theta=0:(2*pi/p/90):(2*pi/p);
```

```
%embrace
alphap=0.83;
j=40;


for n=1:2*j-1;

%For radial magnetization
%Mr(n)=2*Br/miu0*alphap*sin(n*pi*alphap/2)/(n*pi*alphap/2);
%Mt(n)=0;

%For parallel magnetization
A1(n)=sin((n*p/2+1)*alphap*pi/(2*p/2))/((n*p/2+1)*alphap*pi/(2*p/2));

if n*p/2==1
    A2(n)=1;
else
A2(n)=sin((n*p/2-1)*alphap*pi/(2*p/2))./((n*p/2-1)*alphap*pi/(2*p/2));
end

Mr(n)=Br/miu0*alphap*(A1(n)+A2(n));
Mt(n)=Br/miu0*alphap*(A1(n)-A2(n));

Mn(n)=Mr(n)+n*p/2*Mt(n);

if n*p/2==1
    %For radial magnetization
%A3n=1;
%For parallel magnetization
A3(n)=2*Mr(1)/Mt(1)+1/n/p;
else
%For radial magnetization
%A3n=n*p
%For parallel magnetization
A3(n)=(p/2*n-1/n/(p/2))*Mr(n)/Mn(n)+1/n/(p/2);
end

if n*p/2==2
    Kb1(n)=A3(n).*(Rm/Rs)^2-A3(n).*(Rr/Rs)^2+(Rr/Rs)^2*log((Rm/Rr)^2);
    Kb2(n)=(miur+1)/miur*(1-(Rr/Rs)^2)-(miur-1)/miur*((Rm/Rs)^2-
(Rr/Rm)^2);
    KB(n)=miu0.*Mn(n)./2./miur.*Kb1(n)./Kb2(n);
    fBr(n)=1+(Rs/r)^2;
    fBt(n)=-1+(Rs/r)^2;
else
    Kb1(n)=A3(n)-1+2*(Rr/Rm)^(p/2*n+1)-(A3(n)+1)*(Rr/Rm)^(2*p/2*n);
    Kb2(n)=(miur+1)/miur*(1-(Rr/Rs)^(2*n*p/2))-(miur-
1)/miur*((Rm/Rs)^(2*n*p/2)-(Rr/Rm)^(2*n*p/2));
    Kb3(n)=p/2*n/((n*p/2)^2-1);
    KB(n)=miu0*Mn(n)/miur*Kb3(n)*Kb1(n)/Kb2(n);
    fBr(n)=(r/Rs)^(p/2*n-1)*(Rm/Rs)^(n*p/2+1)+(Rm/r)^(p/2*n+1);
    fBt(n)=-(r/Rs)^(p/2*n-1)*(Rm/Rs)^(n*p/2+1)+(Rm/r)^(p/2*n+1);
end
end
%theta=0:(2*pi/p/90):(2*pi/p);
for t=1:180
```

```
    for s=1:j
        BF(s)=KB(2*s-1)*fBr(2*s-1);
    Bairm(s,t)=KB(2*s-1)*fBr(2*s-1)*cos((2*s-1)*p/2*((t/180*pi)));
    end
end

Bair=sum(Bairm);
t=1:180;

theta=(t)/(p/2);    % theta is mechanical degree

Bair=Bair';
theta=theta';

%plot(theta,Bair)
```

3. Function to calculate number of stator turns

```
function Ub=ampturn(Nc)

global Nm Np DiaSGap ThickSYoke Lst ThickMag g Tsr f Kop Spp Kw Bf Lst
Pout kcarter miu0 miuR Hs0 Hs1 Bs0 Bs1 Bs2 Hs2 Tw As loss PHImp
DiaRYoke DiaSYoke BFgap Ut Bg Bm beta;
% This function only works for SMPM machines with field-oriented-
control, and needs to be modified with other control methods.

Kop=0.5;
%Nc=88;
% rms value of induced back emf
% E=4.44*f*Nc*Kw*BFgap(1)*pi*(DiaSGap-2*g)*Lst/Np/1000^2;
E=4.44*f*Nc*Kw*BFgap(1)*2/pi*pi*DiaSGap*Lst/Np/1000^2;
% rms value of armature current
I=Pout/3/E;

%Magnetising inductance
% kcarter=1.11;
gp=g+ThickMag/miuR;
% Carter Coefficient
gamma=4/pi*(Bs0/2/gp*atan(Bs0/2/gp)-1/2*log(1+(Bs0/2/gp)^2));
taos=pi*DiaSGap/Nm;
kcarter=taos/(taos-gamma*gp);


Lm=3/pi*(Spp*Nc/Spp/(Np/2)*Kw)^2*miu0/((g+ThickMag/miuR)*kcarter)*DiaSG
ap*Lst/1000; % Giras's book equation 5.23, or Lipo's book
% Specific permeance coefficient
hsw=Hs0+Hs1;
bss1=Bs1;
kl1=hsw/(2*bss1*Kop)+hsw/(2*bss1*(1-Kop))*(log(hsw/(2-2*Kop))-
log(hsw*Kop/(2-2*Kop)));
% % Leakage inductance, not accurate
% Ll=Np*Spp*(Nc/Spp/(Np/2))^2*Lst*miu0*kl1/1000;
% Temperary value for Bs2
Bs2=2*Bs1;
wsb=(Bs1+Bs2)/2;
```

```
% Temperary value for Hs2
Hs2=2*Tw;


Llslot=Spp*Np*(Nc*3/Nm*2)^2*miu0*(Hs2*Lst/3/wsb+Hs1*Lst/((Bs1+Bs0)/2)+H
s0*Lst/Bs0)/1000;
%
Llend=Spp*Np*miu0*(Tw+wsb)*(Nc*3/Nm)^2/2*log((Tw+wsb)*sqrt(pi)/(sqrt(2*
As)))/1000;
%Approximation of end slot leakage inductance
Llend=0.05*Llslot;
Ll=Llslot+Llend;



Ub=(E+I*0.2)^2+(2*pi*f)^2*(Lm+Ll)^2*I^2-Ut^2;
```

4. Function to calculate H_{s2}

```
function Aread = tlength(Hss)

global Nm Np DiaSGap ThickSYoke Lst ThickMag g Tsr f Kop Spp Kw Bf Lst
Pout kcarter miu0 miuR Hs Hs0 Hs1 Bs1 Bs2  Rs As Hs2  Tw loss DiaRYoke
DiaSYoke;



Hs2=Hss-Hs0-Hs1;
Bs2=((DiaSGap/2+Hs2+Hs1+Hs0)*tan(pi/Nm)-Tw/2/cos(pi/Nm))*2;
Bs1=((DiaSGap/2+Hs0+Hs1)*tan(pi/Nm)-Tw/2/cos(pi/Nm))*2;
Aslottotal=(Bs1+Bs2)*Hs2/2+(Bs2-2*Rs)*Rs+pi*Rs^2/2;

SlotLiner=0.5;
WedgeThick=0.5;
LayIns=0.5;
AslotWire=Aslottotal-Hs2*LayIns-Bs2*LayIns-
(2*Bs1+Bs2+2*Hs2/cos(pi/Nm))*SlotLiner-Bs1*WedgeThick;
Aread=AslotWire-As;
```

5. Function to calculate armature reaction magnetic field

```
function Barm=armature(para)
% para=[DiaSGap Thickmag Ip]
global Nm Np DiaSGap ThickSYoke Lst ThickMag g Tsr f Kop Spp Kw Bf Lst
Pout kcarter miu0 miuR Hs Hs0 Hs1 Hs2 Bs0 Bs1 Bs2  Rs As Hs2 Tw PHImp
DiaRYoke DiaSYoke BFgap Ut Bair kj;

Iprms=para(3);
% Ip=25/sqrt(2); % RMS value
% Rs=DiaSGap/2;
```

```
Rsi=para(1)/2;
% Rr=Rsi-g-ThickMag;
Rr=Rsi-g-para(2);
% slot opening/mm

miu0=4*pi*1e-7;
% Total number of turns per phase
Nc=144;
% Effective airgap length
gp=g+ThickMag/miuR;
% vpool=[1 5 7 11 13];
% vpool=[1 5 7 11 13 17 23 25 29 31 35 37 41 43 53 55 59 61 65 67];
vpool=[1 5 7 11 13 17 23 25 29 31];
for k=1:length(vpool)
    v=vpool(k);
    % Slot opening factor
    Ksov(v)=sin(v*Bs0/2/Rsi)/(v*Bs0/2/Rsi);
    % Function Fvr,
    r=Rsi-g;
    Fv(v)=gp*v/r*(r/Rsi)^v*(1+(Rr/r)^(2*v))/(1-(Rr/Rsi)^(2*v));
    % With full pitch winding, winding factor
    Kd(v)=1/Spp*sin(v*pi/6)/sin(v*pi/6/Spp);
    BarmMag(v)=Iprms*miu0*3*Nc/pi/(gp*1e-3)/v*Ksov(v)*Kd(v)*Fv(v)/2;
end

for t=1:360
    for s=1:length(vpool)
        v=vpool(s);
%     Barmmat(v,t)=BarmMag(v)*sin(v*(t*2/180*pi+pi/2));
    Barmmat(v,t)=BarmMag(v)*sin(t*2/180*pi+pi/2);
    end
end
Barm=sum(Barmmat);
%
Btotal=Barm'+[Bair;Bair];
% % Half of Botoal used in the excel
Bexcel=Btotal(1:180);


N=floor(360/Nm);
N0=floor(360/Nm/2);
Bta(1)=sum(abs(Bexcel(1:N0)))/N0;
for kk=1:Nm/2-1
    Bta(kk)=sum(abs(Bexcel(N0+(kk-1)*N+1:N0+kk*N)))/N;
end
Btm=max(Bta)*pi*(DiaSGap)/Nm/kj/Tw;

Barm=Btm;
```

6. Function for linear penalty function

```
function y=linpenalty(x,pel)
% linpenalty is a linear penalty function with lower bound 0 and upper
```

```
% bound 1
% FP is a two dimentional vector [FPl slope], which stores the lower
and upper triggering position in the x axis
FPl=pel(1);
slope=pel(2);
if x<FPl
    y=0;
else
    y=slope*(x-FPl);
end
```

APPENDIX III

Matlab Program of the PSO for SMPM Machine Design Optimization

```
clear all
close all
global Nm Np DiaSGap ThickSYoke Lst ThickMag g Tsr f Kop Spp Kw Bf Lst
Pout kcarter miu0 miuR Hs Hs0 Hs1 Bs1 Bs2 Rs As Hs2 Tw loss PHImp
DiaRYoke DiaSYoke Ut;


%% parameters setup
n_particle=10;  % numbers of particles
Vmax=[1 1 1 1];   %velocity band
inertia=[0.7 0.7 0.7 0.7];  %innertia constant
phi1=[0.4 0.4 0.4 0.4];  %self acceleration constant
phi2=[0.5 0.5 0.5 0.5];  %social acceleration constant
iteration_max=40; % maximum iterations
n_variable=4; % number of design variables

%% initialization
% d=10000*ones(round(n_variable*n_particle),round(iteration_max));
d(:,1) =
[100*rand(n_particle*2,1)+100;8*rand(n_particle,1)+2;5*rand(n_particle,
1)+1.5];


for k=1:n_particle
    input=[d(k,1) d(k+n_particle,1) d(k+2*n_particle,1)
d(k+3*n_particle,1)];
    S(k,1)=SMPM_inte_fun_v8_SS(input);

end
% for k=1:n_particle
%     input=[d(k,1) d(k+n_particle,1) d(k+2*n_particle,1)
d(k+3*n_particle,1)];
%     S(k,1)=TheoDesignFunDist_4input_v6(input);
%
% end
Smin=S;     %minimum for each particle
dmin=d;     %optimum position for each particle
v(1:n_particle,2)=2*Vmax(1)*(rand(n_particle,1)-0.5);     %initialize
velocity for DiaSGap
v(n_particle+1:n_particle*2,2)=2*Vmax(2)*(rand(n_particle,1)-
0.5);     %initialize velocity for Length
v(n_particle*2+1:n_particle*3,2)=2*Vmax(3)*(rand(n_particle,1)-
0.5);     %initialize velocity for ThickMag
v(n_particle*3+1:n_particle*4,2)=2*Vmax(4)*(rand(n_particle,1)-
0.5);     %initialize velocity for Current density
[Gmin i]=min(Smin);     %global minimum
dGmin=[d(i) d(i+n_particle) d(i+n_particle*2)
d(i+n_particle*3)];             %global optimum position
%% Searching
tic
```

```
for i=2:iteration_max;
    d(:,i)=d(:,i-1)+v(:,i);
    %S(:,i)=exp(d(:,i)).*sin(2*pi*d(:,i))+5e2*(2+sign(d(:,i)-5)-
sign(d(:,i)));
    parfor k=1:n_particle
        input=[d(k,i) d(k+n_particle,i) d(k+2*n_particle,i)
d(k+3*n_particle,i)];
         S(k,i)=SMPM_inte_fun_v8_SS(input);
    end
    %%update local minimum and position
    for k=1:n_particle
        if Smin(k)>S(k,i)
            Smin(k)=S(k,i);
            dmin(k)=d(k,i);
            dmin(k+n_particle)=d(k+n_particle,i);
            dmin(k+n_particle*2)=d(k+n_particle*2,i);
            dmin(k+n_particle*3)=d(k+n_particle*3,i);
                end;
                end;

    %%update global minimum and position
    if Gmin>min(Smin)
        [Gmin j]=min(Smin);
        dGmin(1)=dmin(j);
        dGmin(2)=dmin(j+n_particle);
        dGmin(3)=dmin(j+n_particle*2);
        dGmin(4)=dmin(j+n_particle*3);
    end
    %%update velocity

v(1:n_particle,i+1)=inertia(1)*v(1:n_particle,i)+phi1(1)*rand*(dmin(1:n
_particle)-d(1:n_particle,i))+phi2(1)*rand*(dGmin(1)-d(1:n_particle,i));

v(n_particle+1:n_particle*2,i+1)=inertia(2)*v(n_particle+1:n_particle*2
,i)+phi1(2)*rand*(dmin(n_particle+1:n_particle*2)-
d(n_particle+1:n_particle*2,i))+phi2(2)*rand*(dGmin(2)-
d(n_particle+1:n_particle*2,i));

v(n_particle*2+1:n_particle*3,i+1)=inertia(3)*v(n_particle*2+1:n_partic
le*3,i)+phi1(3)*rand*(dmin(n_particle*2+1:n_particle*3)-
d(n_particle*2+1:n_particle*3,i))+phi2(3)*rand*(dGmin(3)-
d(n_particle*2+1:n_particle*3,i));

v(n_particle*3+1:n_particle*4,i+1)=inertia(4)*v(n_particle*3+1:n_partic
le*4,i)+phi1(4)*rand*(dmin(n_particle*3+1:n_particle*4)-
d(n_particle*3+1:n_particle*4,i))+phi2(4)*rand*(dGmin(4)-
d(n_particle*3+1:n_particle*4,i));
    %%band of velocity
    v(1:n_particle,i+1)=min(v(1:n_particle,i+1),Vmax(1));
    v(1:n_particle,i+1)=max(v(1:n_particle,i+1),-Vmax(1));

v(n_particle+1:n_particle*2,i+1)=min(v(n_particle+1:n_particle*2,i+1),V
max(2));

v(n_particle+1:n_particle*2,i+1)=max(v(n_particle+1:n_particle*2,i+1),-
Vmax(2));
```

```
v(n_particle*2+1:n_particle*3,i+1)=min(v(n_particle*2+1:n_particle*3,i+
1),Vmax(3));

v(n_particle*2+1:n_particle*3,i+1)=max(v(n_particle*2+1:n_particle*3,i+
1),-Vmax(3));

v(n_particle*3+1:n_particle*4,i+1)=min(v(n_particle*3+1:n_particle*4,i+
1),Vmax(4));

v(n_particle*3+1:n_particle*4,i+1)=max(v(n_particle*3+1:n_particle*4,i+
1),-Vmax(4));
 end;

dGmin
Gmin

toc
%% Plot
t=1:iteration_max;
figure(1)
for n=2:n_particle
plot(t,d(n,:));
hold on;
end
for n=n_particle+1:n_particle*2
plot(t,d(n,:),'r-.');
hold on;
end
for n=n_particle*2+1:n_particle*3
plot(t,d(n,:),'g--');
hold on;
end
for n=n_particle*3+1:n_particle*4
plot(t,d(n,:),'y-o');
hold on;
end
hold off
xlabel('Number of iterations')
ylabel('Values of motor airgap diameter and axial Length(mm)')
title('Particle behavior(DiaSGap:-;Length:-.-)')

figure(2)
for n=1:n_particle
plot(t,S(n,:));
hold on;
end
hold off
xlabel('Number of iterations')
ylabel('motor total Weight(kg)')
title('Output of each particle')
```

APPENDIX IV

Matlab Program for Concentrated Winding SMPM Machine Design Model

1. Main Design Function

```
function output=TheoDesignFunCont_3input(para)
% Values of variables to be selected initially: DisSGap, ThickMag, J

global Nm Np DiaSGap ThickSYoke Lst ThickMag g Tsr f Kop Spp Kw Bf Lst
Pout kcarter miu0 miuR Hs Hs0 Hs1 Hs2 Bs0 Bs1 Bs2  Rs As Hs2 Tw PHImp
DiaRYoke DiaSYoke BFgap Ll Lm Ut;

% Stator diameter at gap side
DiaSGap=para(1);
% Motor axial length /mm
Lst=para(2);
% Raidal magnet length /mm
ThickMag=para(3);
%%
%%%%%%%%%%%%%%%%%%%%%%%%%%%%   Input parameters    %%%%%%%%%%%%%%%%%%%%%%%%%
% Frequency
f=60;
% Terminal voltage
Ut=480/sqrt(3);

miu0=4*pi*1e-7;
miuR=1.099779;




% Number of poles
Np=4;
% Slots/phase/pole
Spp=0.5;
% Number of slots
Nm=3*Spp*Np;

% Pole coverage coefficient
Embrace=0.83;

% Airgap length /mm
g=1;
% Slot opening
Bs0=3;
%%%%%%%%%%%%%%%%%%%%%%%%%%%%%%%%%%%%%%%%%%%%%%%%%%%%%%%%%%%%%%%%%%%%%%%%%%%
%%

%%
```

```
%%%%%%%%%%%%%%%%%%%%%%%%%%%  Airgap flux
density %%%%%%%%%%%%%%%%%%%%%%%%

% % NdFe35, Radially magnetized and operate at, Br, T; Hc A/m

% Magnitude of each harmonics of B profile in the airgap

% BFgap=emfcal_zhu_fun_Cont(DiaSGap);
BFgap=emfcal_zhu_fun3input([DiaSGap ThickMag]);

% Airgap flux density profile with mechanical degree for two poles
j=13; % the number of how many harmonics to be computed, 7 means from
1st to 13rd
for t=1:180
    for s=1:j
    Bairm(s,t)=BFgap(s)*cos((2*s-1)*Np*((t-45)/(Np/2)/180*pi));
    end
end
Bair=sum(Bairm);
t=1:180;

theta=(t)/(Np/2);   % theta is mechanical degree

Bair=Bair';
theta=theta';

%plot(theta,Bair);

% % Maximum value of flux density in the airgap
Bm=sum(Bair(16:75))/60;
Bg=sum(abs(Bair))/length(Bair);

%%

%%%%%%%%%%%%%%%%%%%%%%%%%%%%%%%%%%%%Calculation of teeth width and yoke
thickness%%%%%%%%%%%%%%%%%

%Flux density in stator core
Bsc=1.45;
%Flux density in rotor core
Brc=1.45;
%Flux density in stator teeth
Bt=1.45;

% Stacking factor of the stator iron laminations
kj=0.95;
% Total magnetic flux per pole produced by the magnets
PHImp=Bg*pi*(DiaSGap-2*g)*Lst/Np;
% Maximum flux in the stator yoke
PHIsy=PHImp/2;
% Thickness of the stator yoke
ThickSYoke=PHIsy/(Bsc*kj*Lst);
% Thickness of the rotor yoke
ThickRYoke=PHIsy/(Brc*kj*Lst);
```

```
% Stator tooth width
Tw=Bm*(pi*DiaSGap/Nm-Bs0)/kj/Bt;
DiaRGap=DiaSGap-2*g;
DiaRYoke = DiaRGap-2*(ThickMag+ThickRYoke);

%%

%%%%%%%%%%%%%%%%%%%%%%%%%%%%%% Calculation of current and number of
turns %%%%%%%%%%%%%%%%%


% With full pitch winding, winding factor
% alpha=pi/3/Spp;
% Kw=1/Spp*sin(Spp*alpha/2)/sin(alpha/2);
Kw=sin(2/3*pi);

% Rated power,  200W is mechanical loss
Pout=15200;

% Ampere Turns

AmpT=Pout/3/4.44/Kw/f/(PHImp/1000^2);

% Slot type 3
Hs0 = 2;
Hs1 = 6;
Rs = 3;
%Hs2 = Hs-Hs0-Hs1-Rs;
Bs1 = pi*(DiaSGap+2*(Hs0+Hs1))/Nm-Tw;
%Bs2 = pi*(DiaSGap+2*(Hs0+Hs1+Hs2))/Nm-Tw;


% Number of total turns per phase
Nc=round(fsolve('ampturnCont',100));

% Back EMF
E=4.44*f*Nc*Kw*BFgap(1)*2/pi*pi*(DiaSGap-2*g)*Lst/Np/1000^2;
%E=4.44*f*Nc*Kw*PHImp/1000^2;
%E=(E1+E2)/2;
% rms value of armature current
Ip=Pout/3/E;

% Current density A/mm2
J=4.9;

WireDia=sqrt(Ip/J/pi)*2; % Wire diameter
G=round(log(WireDia/8.24865)/log(0.890526)); % Wire gauge
WireDiaG=8.24865*(0.890526)^G;
AcuWire=pi*WireDiaG^2/4;
% Copper area per slot
Acu=AcuWire*Nc/Spp/(Np/2);
% Wire copper diameter
%Dwire=sqrt(Ip/J*4/pi);
%%

%%%%%%%%%%%%%%%%%%%%%%%%%%%%%% Calculation of number of turns and
stator size %%%%%%%%%%%%%
```

```
% %Specific current loading, RMS A/mm
% S1=3*2*Nc*Ip/pi/DiaSGap;
%
% % Copper area per slot
% Acu=S1*pi*DiaSGap/1000/Nm/J;

% Copper Fill factor
Fl=0.65;
% Stator slot area per slot
As=Acu/Fl;

% Teeth length
Hs = fsolve('tlength',10);
Hs2=Hs-Hs0-Hs1;
Bs2=((DiaSGap/2+Hs2+Hs1+Hs0)*tan(pi/Nm)-Tw/2/cos(pi/Nm))*2;
Bs1=((DiaSGap/2+Hs0+Hs1)*tan(pi/Nm)-Tw/2/cos(pi/Nm))*2;
DiaSYoke=2*((Hs+Rs+DiaSGap/2)/cos(pi/Nm)-Tw/2*tan(pi/Nm)+ThickSYoke);


%%%%%%%%%%%%%%%%%%%%%%%%%%%%%%%%%%%%Calculation of inductance  %%%%%%%%
%%%%%%%%%%%%%%%%%%%%%%%%%%%%%%%%%%%%Calculation of inductance  %%%%%%%%
gp=g+ThickMag/miuR;
% Carter Coefficient
gamma=4/pi*(Bs0/2/gp*atan(Bs0/2/gp)-1/2*log(1+(Bs0/2/gp)^2));
taos=pi*DiaSGap/Nm;
kcarter=taos/(taos-gamma*gp);
%Magnetising inductance
% kcarter=1.01;
Lm=3/pi*(Spp*Nc/Spp/(Np/2)*Kw)^2*miu0/(g*kcarter+ThickMag/miuR)*(DiaSGa
p-2*g)*Lst/1000;
Xm=2*pi*f*Lm;

% Calculation of slot leakage inductance from Zhu's paper
h0=Hs0+Hs1;
h=Hs2;
b=Bs1; % Approximation of Bs2
b0=Hs0;
for k=2:2:10
    lamdaLs3(k)=2/(k*pi)*(1+exp(-2*k*pi*h/b))/(1-exp(-
2*k*pi*h/b))*sin(k*pi*b0/2/b)^2/(k*pi*b0/2/b)^2;
end
lamdaLs=h0/b0+h/3/b+b/12/h+sum(lamdaLs3);
Lls=2*miu0*Lst*Nc^2/(2*Np)*lamdaLs/1000;
lamdaMs=h0/b0+h/3/b-b/12/h+sum(lamdaLs3);
Llm=2*miu0*Lst*Nc^2/(2*Np)*lamdaMs/1000;
Llslot=Lls+Llm/2;
%End inductance
Llend=Spp*Np*miu0*(Tw+b)*(Nc*3/Nm)^2/2*log((Tw+b)*sqrt(pi)/(sqrt(2*As))
)/1000;
% Total leakage inductance
Ll=Llslot+Llend;
% % Specific permeance coefficient
% hsw=Hs0+Hs1;
% bss1=Bs1;
```

```
% kl1=hsw/(2*bss1*Kop)+hsw/(2*bss1*(1-Kop))*(log(hsw/(2-2*Kop))-
log(hsw*Kop/(2-2*Kop)));
% % Leakage inductance, not accurate
% Ll=Np*Spp*(Nc/Spp/(Np/2))^2*Lst*miu0*kl1/1000;
Xl=2*pi*f*Ll;

%%
% %%%%%%%%%%%%%%%%%%%%%%%%%%%%%%%% Calculation of copper loss
%


% end windings arrangement constant
% kcoil=0.13;
% % Resistivity of copper
% pcu=1.68*1e-8;
% % copper resistivity of one phase, assuming serieal connection
% %Rcu=pcu*(Np*Lst+(DiaSGap+ThickSYoke)*pi*kcoil)/1000*(Nc/Spp/(Np/2))*
Spp/(Acu/(Nc/Spp/(Np/2))/1000^2);
% Rcu=pcu*(Lst+DiaSGap*pi*kcoil)*Nc*2/1000/(Ip/J/1000^2);
% % Copper losses, not accurate
% Pcu=3*Rcu*Ip^2;

% Resistivity of copper
pcu=1.68*1e-8;
% % End length of one turn
% Lend=(2*Tw+pi*(Tw+(Bs1+Bs2)/2))/2; % Average of the maximum and
minimum end length
% % Wire length of one turn
% Lwireturn=Lst*2+Lend;
% % Total wire length
% Lwire=Nc*Lwireturn;


% Wire Length
% WireIns=0.3;
% %FillDL=0.85;
% SlotLiner=0.5;
% DN1=floor((Bs1-SlotLiner)/2/(WireDiaG+WireIns));
% LN1=floor((Hs2+Rs-2*SlotLiner)/cos(pi/Nm)/(WireDiaG+WireIns));
% %DN2=(Nc/2-DN1*LN1)/LN1*2;
% WireLend=0;
% Ncslot=Nc/Spp/(Np/2);
% for k=1:DN1
%     WireLend=WireLend+2*pi*(Tw/2+SlotLiner+(k-
1)*(WireDiaG+WireIns)+(WireDiaG+WireIns)/2)*LN1;
% end
% % Length of end wire per tooth
% WireLend=WireLend+(Ncslot/2-
DN1*LN1)*2*pi*(Tw/2+SlotLiner+(Bs1/2+(Bs2+Rs)/2)/2*cos(pi/Nm));
% EndAd=2;
% Lwire=(WireLend+(Lst+EndAd*2)*Nc)*Nm;
Endadj=2;
Endclear=5;
slotangle=2*pi/Nm;
enddiameter=Endadj*2+(DiaSGap/2+Hs0+Hs1+Hs2/2)*slotangle-
((DiaSGap/2+Hs0+Hs1+Hs2/2)*slotangle-Tw)/2;
endlength=pi*enddiameter;
```

```
turnlength=endlength*2+2*Lst+2*Endclear;
Lwire=turnlength*Nc;

% % Wire copper area
% Acuwire=Ip/J;
% Wire resistance
Rcu=pcu*Lwire/AcuWire*1000;
% Armature copper loss
PCu=Ip^2*Rcu*3;

% % bare wire area
% Awb=Acu/Nc;
% dwb=sqrt(Awb/pi);
% % Wire gauge
% G=log(dwb/8.24865)/log(0.890526);



%%

%%%%%%%%%%%%%%%%%%%%%%%%%%%%%%%% Calculation of
weight %%%%%%%%%%%%%%%%%%%%
% Mass density of steel in kg/m3
Md=7.8*1e3;
% Weight of the stator bore in kilogram
WtSYoke=pi*(DiaSYoke^2-(DiaSYoke-2*ThickSYoke)^2)/4*Lst*Md*(1e-9);
% Weight of the stator teeth
WtSTeeth=Nm*Tw*Hs*Lst*Md*(1e-9);
% Weight of the rotor yoke
WtRYoke=pi*((DiaRYoke+2*ThickRYoke)^2-DiaRYoke^2)/4*Lst*Md*(1e-9);
% Mass density of copper in kg/m3
Mc=8.96*1e3;
% Weight of copper
%WtCopper=3*(Np*Lst+DiaSGap*pi*kcoil)*(Nc/Spp/(Np/2))*Spp*(Acu/(Nc/Spp/
(Np/2)))*Mc*(1e-9);
%WtCopper=3*(Lst+DiaSGap*pi*kcoil)*Nc*2*Ip/J*Mc*1e-9;
WtCopper=3*Lwire*AcuWire*Mc*1e-9;
% Weight of Permanent Magnet
WtMagnet=(DiaRGap^2-(DiaRGap-
ThickMag*2)^2)*pi/4*Embrace*Lst/1000^3*7400;
% Total weight
Weight=WtSYoke+WtSTeeth+WtRYoke+WtCopper+WtMagnet;
% Volume
Volume=pi*DiaSYoke^2/4*Lst/1000^3;

% % Core loss estimation at no load condition
% % Loss density W/kg
LdTeeth=3.14;
LdCore=2.2;
Pcore=(WtSYoke+WtRYoke)*LdCore+WtSTeeth*LdTeeth;

% Total Loss estimation
Ptotal=PCu+Pcore;

% Efficiency
Eff=15000/(Pout+Ptotal);
%
```

```
% Power factor
pfactor=E/Ut;
% Torque ampere
TperA=Pout/(f*2*pi/(Np/2))/Ip;
%%
%%%%%%%%%%%%%%%%%%%%%%%%
Output %%%%%%%%%%%%%%%%%%%%%%%%%%%%%%%%%%%%%%%%%%%%

% output=Volume*100000;
% output=Weight+Volume*10000+10*(100-Eff*100);
% output=10*(100-Eff*100);
output = Volume*20000+2*Weight+(1-Eff)*200+WtMagnet*5-TperA*5;
```

2. Function for calculate number of turns

```
function Ub=ampturn(Nc)

global Nm Np DiaSGap ThickSYoke Lst ThickMag g Tsr f Kop Spp Kw Bf Lst
Pout kcarter miu0 miuR Hs0 Hs1 Bs0 Bs1 Bs2 Hs2 Tw As loss PHImp
DiaRYoke DiaSYoke BFgap Ll Lm Ut;

Kop=0.5;
%Nc=88;
% rms value of induced back emf
E=4.44*f*Nc*Kw*BFgap(1)*2/pi*pi*(DiaSGap-2*g)*Lst/Np/1000^2;
% rms value of armature current
I=Pout/3/E;

%Magnetising inductance
% kcarter=1.1;
gp=g+ThickMag/miuR;
% Carter Coefficient
gamma=4/pi*(Bs0/2/gp*atan(Bs0/2/gp)-1/2*log(1+(Bs0/2/gp)^2));
taos=pi*DiaSGap/Nm;
kcarter=taos/(taos-gamma*gp);

Lm=3/pi*(Spp*Nc/Spp/(Np/2)*Kw)^2*miu0/(g*kcarter+ThickMag/miuR)*(DiaSGa
p-2*g)*Lst/1000;
% Specific permeance coefficient
hsw=Hs0+Hs1;
bss1=Bs1;
kl1=hsw/(2*bss1*Kop)+hsw/(2*bss1*(1-Kop))*(log(hsw/(2-2*Kop))-
log(hsw*Kop/(2-2*Kop)));
% % Leakage inductance, not accurate

% Ll=Np*Spp*(Nc/Spp/(Np/2))^2*Lst*miu0*kl1/1000;
% Temperary value for Bs2
Bs2t=3*Bs1;
wsb=(Bs1+Bs2)/2;

%
Llslot=Spp*Np*(Nc*3/Nm*2)^2*miu0*(Hs2*Lst/3/wsb+Hs1*Lst/((Bs1+Bs0)/2)+H
s0*Lst/Bs0)/1000;
%End inductance
```

```
%
Llend=Spp*Np*miu0*(Tw+wsb)*(Nc*3/Nm)^2/2*log((Tw+wsb)*sqrt(pi)/(sqrt(2*
As)))/1000;
% Ll=Llslot+Llend;



% Calculation of slot leakage inductance from Zhu's paper
h0=Hs0+Hs1;
h=10*h0;
b=Bs1*3; % Approximation of Bs2
b0=Hs0;
for k=2:2:6
    lamdaLs3(k)=2/(k*pi)*(1+exp(-2*k*pi*h/b))/(1-exp(-
2*k*pi*h/b))*sin(k*pi*b0/2/b)^2/(k*pi*b0/2/b)^2;
end
lamdaLs=h0/b0+h/3/b+b/12/h+sum(lamdaLs3);
Lls=2*miu0*Lst*Nc^2/(2*Np)*lamdaLs/1000;
lamdaMs=h0/b0+h/3/b-b/12/h+sum(lamdaLs3);
Llm=2*miu0*Lst*Nc^2/(2*Np)*lamdaLs/1000;
Llslot=Lls+Llm/2;
%Approximation of end slot leakage inductance
Llend=0.05*Llslot;
Ll=Llslot+Llend;


Ub=(E+I*0.2)^2+(2*pi*f)^2*(Lm+Ll)^2*I^2-Ut^2;
```

3. **The functions to calculate airgap flux density, tooth length, and armature reaction field are the same as distributed windings**

APPENDIX V

Matlab Program for Vector Multi-Objective PSO

```
clear all
close all
global Nm Np DiaSGap ThickSYoke Lst ThickMag g Tsr f Kop Spp Kw Bf Lst
Pout kcarter miu0 miuR Hs Hs0 Hs1 Bs1 Bs2 Rs As Hs2 Tw loss PHImp
DiaRYoke DiaSYoke Ut;


%% parameters setup
n_particle=100;  % numbers of particles
Vmax=[1.5 1.5 0.2];   %velocity band
inertia=[1 1 0.5];  %innertia constant
phi1=[0.3 0.3 0.1];  %self acceleration constant
phi2=[0.3 0.3 0.1];  %social acceleration constant
iteration_max=100; % maximum iterations
%% initialization
d(:,1)= [180*rand(n_particle*2,1)+20;5*rand(n_particle,1)+3];

magn=500;
%S(:,1)=exp(d(:,1)).*sin(2*pi*d(:,1));
for k=1:n_particle
    input(k,:)=[d(k,1) d(k+n_particle,1) d(k+2*n_particle,1)];
    p_mout=TheoDesignFunDist_3input(input(k,:));
    Sp(k,:)=p_mout;


end
for k=1:n_particle
    input(k,:)=[d(k,1) d(k+n_particle,1) d(k+2*n_particle,1)];
    input(1,:)=[70 80 3];
    p_mout=TheoDesignFunDist_3input(input(k,:));
    Sp(k,:)=p_mout;

end

v(1:n_particle,2)=2*Vmax(1)*(rand(n_particle,1)-0.5);     %initialize
velocity for DiaSGap
v(n_particle+1:n_particle*2,2)=2*Vmax(2)*(rand(n_particle,1)-
0.5);     %initialize velocity for Length
v(n_particle*2+1:n_particle*3,2)=2*Vmax(3)*(rand(n_particle,1)-
0.5);     %initialize velocity for ThickMag

% setup an archive for pareto front
front=paretofront(Sp);
archd=input(front,:); % setup an archive of pareto front
arch=Sp(front,:); % setup an archive of pareto front

ndSmin=round(rand*length(arch));
```

```
if ndSmin==0
    ndSmin=1;
end

ndGmin=round(rand*length(arch));
if ndGmin==0
    ndGmin=1;
end

dSmin=input(ndSmin,:);
dGmin=input(ndGmin,:);
% Smin=S;     %minimum for each particle
% dmin=d;     %optimum position for each particle
% [Gmin i]=min(Smin);     %global minimum
% dGmin=[d(i) d(i+n_particle) d(i+n_particle*2)];             %global
optimum position
%% Searching
for i=2:iteration_max;
    d(:,i)=d(:,i-1)+v(:,i);
    %S(:,i)=exp(d(:,i)).*sin(2*pi*d(:,i))+5e2*(2+sign(d(:,i)-5)-
sign(d(:,i)));
    for k=1:n_particle
        input(k,:)=[d(k,i) d(k+n_particle,i) d(k+2*n_particle,i)];
         p_mout=TheoDesignFunDist_3input(input(k,:));

        Sp(k,:)=p_mout;

    end
%     %%update local minimum and position
%     for k=1:n_particle
%         if Smin(k)>S(k,i)
%             Smin(k)=S(k,i);
%             dmin(k)=d(k,i);
%             dmin(k+n_particle)=d(k+n_particle,i);
%             dmin(k+n_particle*2)=d(k+n_particle*2,i);
%                 end;
%                 end;
%
%     %%update global minimum and position
%     if Gmin>min(Smin)
%         [Gmin j]=min(Smin);
%         dGmin(1)=dmin(j);
%         dGmin(2)=dmin(j+n_particle);
%         dGmin(3)=dmin(j+n_particle*2);
%     end

    % Update archive
    Sp1=[Sp;arch];
    input1=[input;archd];
    front=paretofront(Sp1);
    archd=input1(front,:); % setup an archive of pareto front, the
particle position
    arch=Sp1(front,:); % setup an archive of pareto front, the particle
output

    ndSmin=round(rand*length(arch));
        if ndSmin==0
```

```
            ndSmin=1;
        end

    ndGmin=round(rand*length(arch));
        if ndGmin==0
            ndGmin=1;
        end

    % update global and local minimum
    dSmin=archd(ndSmin,:);
    dGmin=archd(ndGmin,:);

    %%update velocity

v(1:n_particle,i+1)=inertia(1)*v(1:n_particle,i)+phi1(1)*rand*(dSmin(1)
-d(1:n_particle,i))+phi2(1)*rand*(dGmin(1)-d(1:n_particle,i));

v(n_particle+1:n_particle*2,i+1)=inertia(2)*v(n_particle+1:n_particle*2
,i)+phi1(2)*rand*(dSmin(2)-
d(n_particle+1:n_particle*2,i))+phi2(2)*rand*(dGmin(2)-
d(n_particle+1:n_particle*2,i));

v(n_particle*2+1:n_particle*3,i+1)=inertia(3)*v(n_particle*2+1:n_partic
le*3,i)+phi1(3)*rand*(dSmin(3)-
d(n_particle*2+1:n_particle*3,i))+phi2(3)*rand*(dGmin(3)-
d(n_particle*2+1:n_particle*3,i));
    %%band of velocity
    v(1:n_particle,i+1)=min(v(1:n_particle,i+1),Vmax(1));
    v(1:n_particle,i+1)=max(v(1:n_particle,i+1),-Vmax(1));

v(n_particle+1:n_particle*2,i+1)=min(v(n_particle+1:n_particle*2,i+1),V
max(2));

v(n_particle+1:n_particle*2,i+1)=max(v(n_particle+1:n_particle*2,i+1),-
Vmax(2));

v(n_particle*2+1:n_particle*3,i+1)=min(v(n_particle*2+1:n_particle*3,i+
1),Vmax(3));

v(n_particle*2+1:n_particle*3,i+1)=max(v(n_particle*2+1:n_particle*3,i+
1),-Vmax(3));
 end;



%% Plot
% t=1:iteration_max;
% figure(1)
% for n=2:n_particle
% plot(t,d(n,:));
% hold on;
% end
% for n=n_particle+1:n_particle*2
% plot(t,d(n,:),'r-.');
% hold on;
% end
```

```
% for n=n_particle*2+1:n_particle*3
% plot(t,d(n,:),'g--');
% hold on;
% end
% hold off
% xlabel('Number of iterations')
% ylabel('Values of motor airgap diameter and axial Length(mm)')
% title('Particle behavior(DiaSGap:-;Length:-.-)')
%
% figure(2)
% for n=1:n_particle
% plot(t,S(n,:));
% hold on;
% end
% hold off
% xlabel('Number of iterations')
% ylabel('motor total Weight(kg)')
% title('Output of each particle')

% t=1:iteration_max+1;
% true=[2-1/2*atan(2*pi)/pi 3-1/2*atan(2*pi)/pi 4-1/2*atan(2*pi)/pi 5-
1/2*atan(2*pi)/pi 6-1/2*atan(2*pi)/pi];
% Ref=true(:)*ones(1,iteration_max+1);
%
% figure(1)
% plot(t,Ref(1,:),'r-.');
% hold on;
% plot(d(1,:),'.-');
% hold on;
% for n=2:5
% plot(t,Ref(n,:),'r-.')
% hold on;
% end;
%
% for n=2:n_particle;
%     plot(d(n,:),'.-');
%     hold on;
% end;
% hold off;
%
%
% title('Particle trajectory')
% xlabel('Number of interations')
% ylabel('Position')
% legend('local optimum value','Particle trajectory')

%% Plot pareto front
plot(arch(:,1),1-arch(:,2),'.');
axis([0 0.008 0.8 1])
xlabel('Volume(m^3)')
ylabel('Efficiency')
hold;
% volume vs effciency
plot(0.0038,0.94,'o');
plot(0.0037,0.9368,'o');
plot(0.0048,0.9588,'o');
plot(0.0047,0.9585,'o');
```

```
% weight vs effciency
% plot(30,0.9469,'o');
% plot(29.4,0.9368,'o');
% plot(32.02,0.9588,'o');
% plot(33.23,0.9585,'o');
```

APPENDIX VI

Matlab Program for Mains-Fed Induction Machine Design Model

1. Main design program

```
function output=induction_motor_main_6input_fun(motorinput)
global T_rated Bavg p D L g Kc Kw Vph miu0 Kw f Bs1 AreaSlot Nslot Tw
Area_bar phi_stator Nrslot Dr  B_rt slotliner wedge lip rwt Br0
%% constants
miu0=4*pi*1e-7;

%% machine specifications
Prout=15000; % machine output power
n=1800; % rated rotor rpm
f=60; % electrical frequency
p=60*f/n*2; % number of poles
T_rated=Prout/(2*pi*f)*p/2; % rated output shaft torque
Vph=460/sqrt(3); % phase excitation voltage

%% input design variables

D= motorinput(1); % airgap diameter in mm
L= motorinput(2); % machine axial length in mm
Bavg=motorinput(3); % average airgap flux density
g= motorinput(4); % airgap length in mm

CurDensity=motorinput(5); % selected stator current density in A/mm2
barCurDensity=motorinput(6); % rotor bar current density in A/mm2
ringCurDensity=barCurDensity*1.2; % rotor ring current density in A/mm2
Bt_peak=1.45; % tooth flux density peak value
B_sc=1.45; % stator core peak flux density
B_rt=1.6; % desired rotor tooth average flux density
B_rc=1.6; % desired rotor core magnet flux density
Nrslot=42; % Number of rotor slot
Spp = 4; % slot per pole per phase
spitch=1; % short pitch number

%% machine stator winding pattern

Nslot=Spp*p*3; % Number of stator slots

% With full pitch winding, winding factor
alpha=pi/3/Spp;
Kw_f=1/Spp*sin(Spp*alpha/2)/sin(alpha/2);


beta=(Nslot/p-spitch)/(Nslot/p);
Kw_s=abs(sin(beta*pi/2)); % short pitch factor
Kw=Kw_f*Kw_s; % winding factor considering short pitch
```

```
%% Carter coefficient
Bs0=1; % stator slot opening in mm
Br0=2; % rotor slot opening
Dr=D-2*g; % rotor outer diameter
yr=pi*Dr/Nrslot; % rotor slot pitch
ys=D*pi/Nslot; % slot pitch
gamma1=Bs0^2/(5*g+Bs0);
gamma2=Br0^2/(5*g+Br0);
Kc1=ys/(ys-gamma1);
Kc2=yr/(yr-gamma2);
Kc=Kc1*Kc2;

%% Electromagnetic design: calculation of number of turns based on
vector
%% control
Tph0=fsolve('windingturns',100); % number of stator turns per phase,
initial value
T_hfslot=ceil(Tph0/(Nslot/3)); % number of coil turns per half slot
Tph1=T_hfslot*Nslot/3; % number of turns per phase for integer number
of coil turns, recalculate
Bavg1=Bavg*Tph0/Tph1; % recalculate Bavg to meet integeter number of
coil turns

%% stator current and flux linkage
lambda_dre=Bavg1*pi*(D/1000)*(L/1000)/p*Tph1; % rotor d-axis flux
linkage in synchronous frame
I_qse=T_rated/(3*p/4*lambda_dre); % stator q-axis current
Fmg=Kc*g/1000*Bavg1/miu0; % airgap mmf drop
mmf_ratio=1.5; % the ratio of the mmf drop on airgap to the ratio on
the whole path
Imag=mmf_ratio*Fmg*2*p/2/(1.35*Kw*Tph1); % magnetizing current,
assuming no mmf drop on steel
I_dse=Imag*sqrt(2); % stator d-axis current
I_rated=sqrt(I_qse^2+I_dse^2)/sqrt(2);
ac=T_hfslot*Nslot*2*I_rated/(pi*D/1000);

%% Stator slot design
Y=pi*D/p; % stator pole pitch in mm
alpha_i=1; % flux density shape factor, determined by teeth saturation
phi_stator=Bavg1*Y*L/1e6; % stator winding flux per pole

FluxTooth=pi/2*Bavg1*L*Y/1e6/(Spp*3); % maximum flux density per tooth
if uniformly distributed flux
lamfactor=0.95; %lamination factor
saturation_factor=1;

B_st=Bt_peak/saturation_factor;
Tw=FluxTooth/(L*lamfactor/1000)/(Bt_peak/saturation_factor)*1000; %
stator tooth width


slotliner=1; % slot liner thickness
wedge=2; % wedge thickness
lip=1; % lip thickness
Bs1=pi*(D+2*(wedge+lip))/Nslot-Tw; % slot width at airgap

%% rotor slot design
```

```
Hr0=1; % rotor lip thickness
Hr1=1; % rotor wedge thickness


%% continue stator design

CondArea=I_rated/CurDensity; % coil conductor area in mm2
WireDia=sqrt(CondArea/pi)*2;

% select standard wire gauge
G=round(log(WireDia/8.24865)/log(0.890526)); % Wire gauge
WireDiaG=8.24865*(0.890526)^G;
AcuWire=pi*WireDiaG^2/4; % copper cross section area per coil

fl=0.65; % stator slot fill factor
ins_thck=0.05; % insulation thickness
AreaSlot=pi/4*(WireDiaG+ins_thck*2)^2*T_hfslot*2/fl; % slot area need

ds=fsolve('slot_depth',20); % stator slot depth including wedge, lip
and liner
Hs2=ds-wedge-lip; % effective slot depth excluding wedge and lip
Bs2=pi/Nslot*(D+2*ds)-Tw; % slot width at bottom


hscore=phi_stator/2/(L/1000*lamfactor)/B_sc*1000; % stator core
thickness
Ds_out=D+ds*2+hscore*2; % stator outer diameter

Lcoilend=2*pi*(D/2+Hs2/2+lip+wedge)/p*beta*1.15; %end lenth per coil
Lmc=L+Lcoilend+20; % estimated mean length per harf coil
Lphase=Lmc*Tph1*2+120; % estimated length per phase
% Resistivity of copper
pcu=1.78*1e-8;
% resistance per phase
Rcu=pcu*Lphase/AcuWire*1000;

%% continue rotor design
I_dre=0;
Lrm_ratio=0.95; % assume a ratio of Lm/Lr
I_qre=-I_qse*Lrm_ratio;
I2_p=sqrt(I_dre^2+I_qre^2)/sqrt(2); % rotor current in the equivalent
circuit

Nsp=Nrslot/p; % rotor slot per pole
Ibar=Kw*Nslot/Nrslot*(T_hfslot*2)*I2_p; % rotor bar current
%I_ring=0.3*Nslot/p*(T_hfslot*2)*I2_p; % endring current, not sure of
0.3
I_ring=Ibar/2/sin(pi*p/Nrslot/2);

Area_bar=Ibar/barCurDensity; % rotor bar area

rwt=pi/2*Bavg1*L*Y/1e6/(Nrslot/p)/(L*lamfactor/1000)/(B_rt)*1000; %
rotor tooth width
Br0=2; % rotor lip depth
Br1=pi*(Dr-2*Hr0-2*Hr1)/Nrslot-rwt; % rotor bar width at top
```

```
% Hr2=fsolve('bar_depth',10); % solving for rotor slot width at top,
assuming parallel slot
Hr2=BarDepth([Br1 Dr Hr0+Hr1 rwt Nrslot Area_bar]);

Br2=pi*(Dr-2*Hr0-2*Hr1-2*Hr2)/Nrslot-rwt; % rotor bar width at bottom


L_barend=15; % rotor bar end length
L_bar=L+L_barend*2; % total rotor bar length
% Resistivity of aluminum
pal=2.82*1e-8;
% % skin effect resistance coefficient
% beta_s=sqrt(2*pi*f*miu0/2/pal*Br1/Br2);
% epsilon=beta_s*Hr2/1000*sqrt(0.02); % assume a slip of 0.02
% K_R=epsilon*(sinh(2*epsilon)+sin(2*epsilon))/(cosh(2*epsilon)-
cos(2*epsilon));
K_R=1;
% rotor resistance considering skin effect
R_bar=pal*(L_bar/1000)/(Area_bar/1e6)*K_R; % resistance per rotor bar
Pal_bar=Nrslot*Ibar^2*R_bar; % rotor bar loss

Db=Dr-2*Hr2; % rotor endring outer diameter

Area_ring=I_ring/ringCurDensity;
ringH=sqrt(Area_ring); % assuming square cross sectional area
ringW=ringH;
De=Db-ringW; % endring centerline diameter
R_ring=pal*(pi*De/1000)/(Area_ring/1e6); % end ring resistance
Pal_ring=2*I_ring^2*R_ring;

Pal_rotor=Pal_bar+Pal_ring; % Total rotor copper loss
Rr=Pal_rotor/(3*I2_p^2); % Rotor resistance in the equivalent circuit



hrcore=phi_stator/2/(L/1000*lamfactor)/B_rc*1000; % rotor core
thickness
Dr_in=Dr-2*Hr0-2*Hr2-2*hrcore; % rotor inner diameter

%% steel B-H curve
% B_steel=0.05:0.05:2;
% H_steel=[22.8 35 45 49 57 65 70 76 83 90 98 106 115 124 135 148 162
177 198 220 237 273 310 356 417 482 585 760 1050 1340 1760 2460 3460
4800 6160 8270 11170 15220 22000 34000];
% Material Cogent Power NO007
B_steel=0.1:0.1:1.8;
H_steel=[25 32 39 44 51 57 64 73 84 99 124 160 248 470 1290 3550 7070
13000];

%% Magnetization current calculation
H_st=interp1(B_steel,H_steel,B_st);
H_sc=interp1(B_steel,H_steel,B_sc);
H_rt=interp1(B_steel,H_steel,B_rt);
H_rc=interp1(B_steel,H_steel,B_rc);
Fmg=Kc*g/1000*Bavg1/miu0; % airgap mmf drop
Fmts=H_st*ds/1000; % mmf drop on stator teeth
Fmtr=H_rt*(Hr2+Hr0)/1000; % mmf drop on rotor teeth
```

```
Fmcs=H_sc*(pi*(Ds_out-hscore)/p*2/3)/1000; % mmf drop on stator core
Fmcr=H_sc*(pi*(Dr_in+hrcore/2)/p*2/3)/1000; % mmf drop on rotor core
Flm=2*(Fmg+Fmts+Fmtr)+Fmcs+Fmcr; % total mmf drop
K_st=(Fmts+Fmtr)/Fmg; % teeth saturation factor

Imag=Flm*p/2/(1.35*Kw*Tph1);
Im_pu=Imag/I_rated;

%% Stator leakage reactance
% coefficients
Kslot2=1/4+3/4*beta;
Kslot1=1/4+3/4*Kslot2;
% permeance for stator slot leakage
lambda_sslot=2/3*Hs2/(Bs2+Bs2)*Kslot1+(lip/Bs0+wedge/Bs1-
Bs0/2/Bs1+0.785)*Kslot2;
% permeance for stator end leakage

lambda_send=0.34*Spp/L*(Lcoilend*2-0.64*Y);
% permeance for stator differential leakage
C_sdiff=1-0.033*Bs0^2/g/ys;
gamma_sdiff=(0.18*sin(pi*(6*beta-5.5))+1.24)/100;
lambda_sdiff=0.9*ys*Spp^2*Kw^2*C_sdiff*gamma_sdiff/Kc/g/(1+K_st);

X_sl=miu0*2*pi*f*L/1000*Tph1^2/p/Spp*(lambda_sslot+lambda_send+lambda_s
diff);

%% Magnetizating inductance
X_mg=Vph/Imag-X_sl;

%% Rotor leakage reactance
%permeance for rotor slot leakage
lambda_rslot=2/3*Hr2/(Br1+Br2)*Kslot1+(Hr0/Br0+Hr1/Br1-
Hr0/2/Br1+0.785)*Kslot2;
% permeance for rotor end leakage
lambda_rend=2.3*De/1000/Nrslot/4/(sin(pi*p/2/Nrslot))^2*log(4.7*De/ring
W*3);
% permeance for rotor differential leakage
gamma_rdiff=9*(3*p/Nrslot)^2/100;
lambda_rdiff=0.9*pi*Dr/Nrslot*gamma_rdiff/Kc/g*(Nrslot/3/p)^2;

X_rbe=2*pi*60*miu0*L/1000*(lambda_rslot+lambda_rend+lambda_rdiff);%
rotor leakage reactance actual value
X_rl=4*3*(Tph1*Kw)^2/Nrslot*X_rbe; % rotor leakage inductance in
equivalent circuit

%% Weight estimation
md_steel=8120; % mass density of hiperco 50A in kg/m3
md_copper = 8940; % mass density of copper in kg/m3
md_aluminum = 2700; % mass density of aluminum in kg/m3

B_rc=B_sc; % desired rotor core magnet flux density
hrcore=phi_stator/2/(L/1000*lamfactor)/B_rc*1000; % rotor core
thickness
Dr_in=Dr-2*Hr0-2*Hr2-2*hrcore; % rotor inner diameter

V_STeeth=Tw*ds*Nslot*L/(1e9); % stator teeth total volume in m3
Wt_STeeth=md_steel*V_STeeth; % stator teeth total weigth in kg
```

```
V_SCore=pi/4*L*(Ds_out^2-(Ds_out-2*hscore)^2)/(1e9); % stator core
total volume in m3
Wt_SCore=md_steel*V_SCore; % stator core total weigth in kg

V_RTeeth=(pi*((Dr/2)^2-(Dr_in/2+hrcore)^2)-Area_bar*Nrslot)*L/(1e9); %
rotor teeth total volume in m3
Wt_RTeeth=md_steel*V_RTeeth; % rotor teeth total weigth in kg
V_RCore=pi/4*L*((Dr_in+2*hrcore)^2-Dr_in^2)/(1e9); % rotor core total
volume in m3
Wt_RCore=md_steel*V_RCore; % rotor core total weigth in kg

V_RBar = Area_bar*Nrslot*L_bar/(1e9);% rotor bar total volume in m3
Wt_RBar = md_copper*V_RBar;%md_aluminum*V_RBar;% rotor bar total weight
in kg
V_Ring = 2*Area_ring*pi*De/(1e9);% rotor end ring total volume in m3
Wt_Ring = md_copper*V_Ring;%md_aluminum*V_Ring;% rotor end ring total
weight in m3

V_SWinding = 3*AcuWire*Lphase/(1e9); %stator winding total volume in m3
Wt_SWinding = md_copper*V_SWinding;%stator winding total weight in m3

Wt_total=Wt_STeeth+Wt_SCore+Wt_RTeeth+Wt_RCore+...
    Wt_RBar+Wt_Ring+...
    Wt_SWinding;

%% Core loss estimation
% Core loss data at 60 Hz
% B = 0.1  0.2  0.3  0.4  0.5 0.6  0.7  0.8  0.9 1.0 1.1  1.2  1.3  1.4
% 1.5 1.6  1.7  1.8
% L = 0.01 0.04 0.09 0.14 0.2 0.26 0.33 0.41 0.5 0.6 0.70 0.85 1.03
1.25
% 1.5 1.74 1.97 2.18 W/lb
closs_t=1.5/0.45359; % core loss density in teeth in W/kg
closs_b=1.5/0.45359; % core loss density in yoke in W/kg
K_caug=1; % core loss augumentation
Pcore=K_caug*(closs_t*Wt_STeeth+closs_b*Wt_SCore); % core loss by
fundamental

%% friction and stray loss estimation
P_fct=0.012*Prout;
P_stray=0.01*Prout;

%% Performance calculation at rated condition

I_dse1=Imag*sqrt(2); % recalculate stator d-axis current
s_inv=Rr/(X_rl+X_mg)*I_qse/I_dse; % slip frequency at rated load when
inverter driven
I_qse1=I_qse;
Is1=sqrt(I_dse1^2+I_qse1^2)/sqrt(2);
V_qse1=Rcu*I_qse1+(X_sl+X_mg)*I_dse1;
V_dse1=Rcu*I_dse1+((X_sl+X_mg)-X_mg^2/(X_rl+X_mg))*I_qse1;
Vph1=sqrt(V_qse1^2+V_dse1^2)/sqrt(2); % applied phase voltage
I_qre1=-X_mg/(X_mg+X_rl)*I_qse1;
I_dre1=0;
Ir1=sqrt(I_qre1^2+I_dre1^2)/sqrt(2);
P_cu1=3*Is1^2*Rcu;
P_al1=3*Ir1^2*Rr;
```

```
P_loss1=P_cu1+P_al1+Pcore+P_fct+P_stray; % total loss at full load
eff1=Prout/(P_loss1+Prout); % efficiency at full load
nrspeed1=(1-s_inv)*n;
Sinput=3*sqrt(V_qse1^2+V_dse1^2)/sqrt(2)*sqrt(I_qse1^2+I_dse1^2)/sqrt(2
); % input apparent power
pfactor=Prout/Sinput;


%% Starting performance
% skin effect resistance coefficient
beta_s=sqrt(2*pi*f*miu0/2/pal*Br1/Br2);
% Start up rotor resistance
epsilon=beta_s*Hr2/1000*sqrt(1); % assume a slip of 0.02
K_R_st=epsilon*(sinh(2*epsilon)+sin(2*epsilon))/(cosh(2*epsilon)-
cos(2*epsilon));
% rotor resistance considering skin effect
R_bar_st=pal*(L_bar/1000)/(Area_bar/1e6)*K_R_st; % resistance per rotor
bar
Rr_st=(R_bar_st+R_ring)*4*3/Nrslot*(Tph1*Kw)^2;
% Starting current
I_st=Vph/sqrt((Rr_st+Rcu)^2+(X_rl+X_sl)^2);
% Starting current per unit value
per_I_st=I_st/I_rated;
% Starting torque
T_st=3*Rr_st*I_st^2*p/2/(2*pi*f);
% Starting torque ratio
per_T_st=T_st/T_rated;

%% Breakdown
% Breakdown slip
s_bk=Rr/sqrt(Rcu^2+(X_rl+X_sl)^2);
% Breakdown current
I_bk=Vph/sqrt((Rcu+Rr/s_bk)^2+(X_rl+X_sl)^2);
% Breakdown current per unit value
per_I_bk=I_bk/I_rated;
% Breakdown torque
T_bk=3/2*Vph^2/(Rcu+sqrt(Rcu^2+(X_rl+X_sl)^2))*p/2/(2*pi*f);
% Breakdown torque per unit value
per_T_bk=T_bk/T_rated;


%% Calculate objective function

% Penalty function for minimum shaft diameter
if Dr_in<20
    pel_Dr_in=100;
else
    pel_Dr_in=0;
end

% Penalty function for airgap length
if g<0.3
    pel_g=100;
elseif g>1.5
    pel_g=100;
else
    pel_g=0;
```

```
end

% Penalty function for minimum tooth width and slot opening
if Tw<5 || Bs1<2
    pel_Tw_Bs1=100;
else
    pel_Tw_Bs1=0;
end

% penalty funciton for minimum bar bottom width
if Br2<1 || Hr2<2
    pel_Br2_Hr2=100;
else
    pel_Br2_Hr2=0;
end

if CurDensity>6 || barCurDensity>7
    pel_CurDensity=100;
else
    pel_CurDensity=0;
end

% penaly function for maximum slip
s_NEMAB=0.05;
pel_s=linpenalty(s_inv, [s_NEMAB 10]);

% penalty funciton for maximum stator outer diameter
Dsoutmax=440;
pel_Dsout=linpenalty(Ds_out, [Dsoutmax 10]);


% penalty function for maximum starting current
I_st_NEMAB=580;
pel_Ist=linpenalty(I_st, [I_st_NEMAB 100]);

% penalty function for minimum starting torque
T_st_NEMAB=150;
pelT_st=linpenalty(-T_st, [-T_st_NEMAB 100]);

% penalty function for minimum breakdown torque
T_bk_NEMAB=200;
pelT_bk=linpenalty(-T_bk, [-T_bk_NEMAB 100]);



penalty=pel_Dr_in+pel_g+pel_Tw_Bs1+pel_Br2_Hr2+pel_Dsout+pel_Ist+pelT_s
t+pelT_bk+pel_CurDensity+pel_s;
output=Wt_total+(1-eff1)*200+(1-pfactor)*200+penalty;
```

2. Function to calculate the number of stator turns

```
function y = windingturns(Tph1)

global T_rated Bavg p D L g Kc Kw Vph miu0 Kw f
```

```
lambda_dre=Bavg*pi*(D/1000)*(L/1000)/p*Tph1; % rotor d-axis flux
linkage in synchronous frame
I_qse=T_rated/(3*p/4*lambda_dre); % stator q-axis current
Fmg=Kc*g/1000*Bavg/miu0; % airgap mmf drop
mmf_ratio=1.5; % the ratio of the mmf drop on airgap to the ratio on
the whole path
Imag=mmf_ratio*Fmg*2*p/2/(1.35*Kw*Tph1); % magnetizing inductance,
assuming no mmf drop on steel
I_dse=Imag*sqrt(2); % stator d-axis current
X_mg=Vph/Imag; % magnetizing inductance, neglecting stator leakage
inductance
lambda_dre1=X_mg/(2*pi*f)*I_dse;
y=lambda_dre-lambda_dre1;
```

3. Function to calculate the stator slot depth

```
function aread=slot_depth(slotd)

global D Bs1 AreaSlot Nslot Tw slotliner wedge lip


slack=0.5;
d1_d2=slotd-(slotliner*6+wedge+lip+slack);
ws2=pi/Nslot*(D+2*slotd)-Tw;
areap=(ws2-slotliner*2+Bs1-slotliner*2)*d1_d2/2;
aread=areap-AreaSlot;
```

4. Function to calculate the rotor slot depth

```
function f=BarDepth(x)
% x(1)=Br1;
% x(2)=Dr;
% x(3)=Hr0+Hr1;
% x(4)=rwt;
% x(5)=Nrslot;
% x(6)=Area_Bar;
% b=Br1+pi*(Dr-2*Hr0)/Nrslot-rwt;
% a=2*pi/Nrslot;
b=x(1)+pi*(x(2)-2*x(3))/x(5)-x(4);
a=2*pi/x(5);
c=2*x(6);
delta=b^2-4*a*c;
if delta<0
    f=0;
else
    f=(b-sqrt(delta))/2/a;
end
```

APPENDIX VII

Matlab Program for Inverter-fed Induction Machine Design Model

```
function output=induction_motor_main_6input_fun(motorinput)
global T_rated Bavg p D L g Kc Kw Vph miu0 Kw f Bs1 AreaSlot Nslot Tw
Area_bar phi_stator Nrslot Dr  B_rt slotliner wedge lip rwt Br0
%% constants
miu0=4*pi*1e-7;

%% machine specifications
Prout=15000; % machine output power
n=1800; % rated rotor rpm
p=4; % number of poles
f=p*n/60/2; % electrical frequency
T_rated=Prout/(2*pi*f)*p/2; % rated output shaft torque
Vph=460/sqrt(3); % phase excitation voltage

%% input design variables

D= motorinput(1); % airgap diameter in mm
L= motorinput(2); % machine axial length in mm
Bavg=motorinput(3); % average airgap flux density
if Bavg<0
    Bavg=rand;
end
g= motorinput(4); % airgap length in mm

CurDensity=motorinput(5); % selected stator current density in A/mm2
barCurDensity=motorinput(6); % rotor bar current density in A/mm2
ringCurDensity=barCurDensity*1.2; % rotor ring current density in A/mm2
Bt_peak=1.45; % tooth flux density peak value
B_sc=1.45; % stator core peak flux density
B_rt=1.6; % desired rotor tooth average flux density
B_rc=1.6; % desired rotor core magnet flux density
Nrslot=42; % Number of rotor slot
Spp = 4; % slot per pole per phase
spitch=1; % short pitch number

%% machine stator winding pattern

Nslot=Spp*p*3; % Number of stator slots

% With full pitch winding, winding factor
alpha=pi/3/Spp;
Kw_f=1/Spp*sin(Spp*alpha/2)/sin(alpha/2);


beta=(Nslot/p-spitch)/(Nslot/p);
Kw_s=abs(sin(beta*pi/2)); % short pitch factor
Kw=Kw_f*Kw_s; % winding factor considering short pitch

%% Carter coefficient
Bs0=1; % stator slot opening in mm
```

```
Br0=2; % rotor slot opening
Dr=D-2*g; % rotor outer diameter
yr=pi*Dr/Nrslot; % rotor slot pitch
ys=D*pi/Nslot; % slot pitch
gamma1=Bs0^2/(5*g+Bs0);
gamma2=Br0^2/(5*g+Br0);
Kc1=ys/(ys-gamma1);
Kc2=yr/(yr-gamma2);
Kc=Kc1*Kc2;

%% Electromagnetic design: calculation of number of turns based on
vector
%% control
Tph0=fsolve('windingturns',100); % number of stator turns per phase,
initial value
T_hfslot=ceil(Tph0/(Nslot/3)); % number of coil turns per half slot
Tph1=T_hfslot*Nslot/3; % number of turns per phase for integer number
of coil turns, recalculate
Bavg1=Bavg*Tph0/Tph1; % recalculate Bavg to meet integeter number of
coil turns

%% stator current and flux linkage
lambda_dre=Bavg1*pi*(D/1000)*(L/1000)/p*Tph1; % rotor d-axis flux
linkage in synchronous frame
I_qse=T_rated/(3*p/4*lambda_dre); % stator q-axis current
Fmg=Kc*g/1000*Bavg1/miu0; % airgap mmf drop
mmf_ratio=1.5; % the ratio of the mmf drop on airgap to the ratio on
the whole path
Imag=mmf_ratio*Fmg*2*p/2/(1.35*Kw*Tph1); % magnetizing current,
assuming no mmf drop on steel
I_dse=Imag*sqrt(2); % stator d-axis current
I_rated=sqrt(I_qse^2+I_dse^2)/sqrt(2);
ac=T_hfslot*Nslot*2*I_rated/(pi*D/1000);

%% Stator slot design
Y=pi*D/p; % stator pole pitch in mm
alpha_i=1; % flux density shape factor, determined by teeth saturation
phi_stator=Bavg1*Y*L/1e6; % stator winding flux per pole

FluxTooth=pi/2*Bavg1*L*Y/1e6/(Spp*3); % maximum flux density per tooth
if uniformly distributed flux
lamfactor=0.95; %lamination factor
saturation_factor=1;

B_st=Bt_peak/saturation_factor;
Tw=FluxTooth/(L*lamfactor/1000)/(Bt_peak/saturation_factor)*1000; %
stator tooth width


slotliner=1; % slot liner thickness
wedge=2; % wedge thickness
lip=1; % lip thickness
Bs1=pi*(D+2*(wedge+lip))/Nslot-Tw; % slot width at airgap

%% rotor slot design

Hr0=1; % rotor lip thickness
```

```
Hr1=1; % rotor wedge thickness


%% continue stator design

CondArea=I_rated/CurDensity; % coil conductor area in mm2
WireDia=sqrt(CondArea/pi)*2;

% select standard wire gauge
G=round(log(WireDia/8.24865)/log(0.890526)); % Wire gauge
WireDiaG=8.24865*(0.890526)^G;
AcuWire=pi*WireDiaG^2/4; % copper cross section area per coil

fl=0.65; % stator slot fill factor
ins_thck=0.05; % insulation thickness
AreaSlot=pi/4*(WireDiaG+ins_thck*2)^2*T_hfslot*2/fl; % slot area need

ds=fsolve('slot_depth',20); % stator slot depth including wedge, lip
and liner
Hs2=ds-wedge-lip; % effective slot depth excluding wedge and lip
Bs2=pi/Nslot*(D+2*ds)-Tw; % slot width at bottom


hscore=phi_stator/2/(L/1000*lamfactor)/B_sc*1000; % stator core
thickness
Ds_out=D+ds*2+hscore*2; % stator outer diameter

Lcoilend=2*pi*(D/2+Hs2/2+lip+wedge)/p*beta*1.15; %end lenth per coil
Lmc=L+Lcoilend+20; % estimated mean length per harf coil
Lphase=Lmc*Tph1*2+120; % estimated length per phase
% Resistivity of copper
pcu=1.78*1e-8;
% resistance per phase
Rcu=pcu*Lphase/AcuWire*1000;

%% continue rotor design
I_dre=0;
Lrm_ratio=0.95; % assume a ratio of Lm/Lr
I_qre=-I_qse*Lrm_ratio;
I2_p=sqrt(I_dre^2+I_qre^2)/sqrt(2); % rotor current in the equivalent
circuit

Nsp=Nrslot/p; % rotor slot per pole
Ibar=Kw*Nslot/Nrslot*(T_hfslot*2)*I2_p; % rotor bar current
%I_ring=0.3*Nslot/p*(T_hfslot*2)*I2_p; % endring current, not sure of
0.3
I_ring=Ibar/2/sin(pi*p/Nrslot/2);

Area_bar=Ibar/barCurDensity; % rotor bar area

rwt=pi/2*Bavg1*L*Y/1e6/(Nrslot/p)/(L*lamfactor/1000)/(B_rt)*1000; %
rotor tooth width
Br0=2; % rotor lip depth
Br1=pi*(Dr-2*Hr0-2*Hr1)/Nrslot-rwt; % rotor bar width at top
% Hr2=fsolve('bar_depth',10); % solving for rotor slot width at top,
assuming parallel slot
Hr2=BarDepth([Br1 Dr Hr0+Hr1 rwt Nrslot Area_bar]);
```

```
Br2=pi*(Dr-2*Hr0-2*Hr1-2*Hr2)/Nrslot-rwt; % rotor bar width at bottom


L_barend=15; % rotor bar end length
L_bar=L+L_barend*2; % total rotor bar length
% Resistivity of aluminum
pal=2.82*1e-8;
% % skin effect resistance coefficient
% beta_s=sqrt(2*pi*f*miu0/2/pal*Br1/Br2);
% epsilon=beta_s*Hr2/1000*sqrt(0.02); % assume a slip of 0.02
% K_R=epsilon*(sinh(2*epsilon)+sin(2*epsilon))/(cosh(2*epsilon)-
cos(2*epsilon));
K_R=1;
% rotor resistance considering skin effect
R_bar=pal*(L_bar/1000)/(Area_bar/1e6)*K_R; % resistance per rotor bar
Pal_bar=Nrslot*Ibar^2*R_bar; % rotor bar loss

Db=Dr-2*Hr2; % rotor endring outer diameter

Area_ring=I_ring/ringCurDensity;
ringH=sqrt(Area_ring); % assuming square cross sectional area
ringW=ringH;
De=Db-ringW; % endring centerline diameter
R_ring=pal*(pi*De/1000)/(Area_ring/1e6); % end ring resistance
Pal_ring=2*I_ring^2*R_ring;

Pal_rotor=Pal_bar+Pal_ring; % Total rotor copper loss
Rr=Pal_rotor/(3*I2_p^2); % Rotor resistance in the equivalent circuit



hrcore=phi_stator/2/(L/1000*lamfactor)/B_rc*1000; % rotor core
thickness
Dr_in=Dr-2*Hr0-2*Hr2-2*hrcore; % rotor inner diameter

%% steel B-H curve
% B_steel=0.05:0.05:2;
% H_steel=[22.8 35 45 49 57 65 70 76 83 90 98 106 115 124 135 148 162
177 198 220 237 273 310 356 417 482 585 760 1050 1340 1760 2460 3460
4800 6160 8270 11170 15220 22000 34000];
% Material Cogent Power NO007
B_steel=0.1:0.1:1.8;
H_steel=[25 32 39 44 51 57 64 73 84 99 124 160 248 470 1290 3550 7070
13000];

%% Magnetization current calculation
H_st=interp1(B_steel,H_steel,B_st);
H_sc=interp1(B_steel,H_steel,B_sc);
H_rt=interp1(B_steel,H_steel,B_rt);
H_rc=interp1(B_steel,H_steel,B_rc);
Fmg=Kc*g/1000*Bavg1/miu0; % airgap mmf drop
Fmts=H_st*ds/1000; % mmf drop on stator teeth
Fmtr=H_rt*(Hr2+Hr0)/1000; % mmf drop on rotor teeth
Fmcs=H_sc*(pi*(Ds_out-hscore)/p*2/3)/1000; % mmf drop on stator core
Fmcr=H_sc*(pi*(Dr_in+hrcore/2)/p*2/3)/1000; % mmf drop on rotor core
Flm=2*(Fmg+Fmts+Fmtr)+Fmcs+Fmcr; % total mmf drop
```

```
K_st=(Fmts+Fmtr)/Fmg; % teeth saturation factor

Imag=Flm*p/2/(1.35*Kw*Tph1);
Im_pu=Imag/I_rated;

%% Stator leakage reactance
% coefficients
Kslot2=1/4+3/4*beta;
Kslot1=1/4+3/4*Kslot2;
% permeance for stator slot leakage
lambda_sslot=2/3*Hs2/(Bs2+Bs2)*Kslot1+(lip/Bs0+wedge/Bs1-
Bs0/2/Bs1+0.785)*Kslot2;
% permeance for stator end leakage

lambda_send=0.34*Spp/L*(Lcoilend*2-0.64*Y);
% permeance for stator differential leakage
C_sdiff=1-0.033*Bs0^2/g/ys;
gamma_sdiff=(0.18*sin(pi*(6*beta-5.5))+1.24)/100;
lambda_sdiff=0.9*ys*Spp^2*Kw^2*C_sdiff*gamma_sdiff/Kc/g/(1+K_st);

X_sl=miu0*2*pi*f*L/1000*Tph1^2/p/Spp*(lambda_sslot+lambda_send+lambda_s
diff);

%% Magnetizating inductance
X_mg=Vph/Imag-X_sl;

%% Rotor leakage reactance
%permeance for rotor slot leakage
lambda_rslot=2/3*Hr2/(Br1+Br2)*Kslot1+(Hr0/Br0+Hr1/Br1-
Hr0/2/Br1+0.785)*Kslot2;
% permeance for rotor end leakage
lambda_rend=2.3*De/1000/Nrslot/4/(sin(pi*p/2/Nrslot))^2*log(4.7*De/ring
W*3);
% permeance for rotor differential leakage
gamma_rdiff=9*(3*p/Nrslot)^2/100;
lambda_rdiff=0.9*pi*Dr/Nrslot*gamma_rdiff/Kc/g*(Nrslot/3/p)^2;

X_rbe=2*pi*60*miu0*L/1000*(lambda_rslot+lambda_rend+lambda_rdiff);%
rotor leakage reactance actual value
X_rl=4*3*(Tph1*Kw)^2/Nrslot*X_rbe; % rotor leakage inductance in
equivalent circuit

%% Weight estimation
md_steel=8120; % mass density of hiperco 50A in kg/m3
md_copper = 8940; % mass density of copper in kg/m3
md_aluminum = 2700; % mass density of aluminum in kg/m3

B_rc=B_sc; % desired rotor core magnet flux density
hrcore=phi_stator/2/(L/1000*lamfactor)/B_rc*1000; % rotor core
thickness
Dr_in=Dr-2*Hr0-2*Hr2-2*hrcore; % rotor inner diameter

V_STeeth=Tw*ds*Nslot*L/(1e9); % stator teeth total volume in m3
Wt_STeeth=md_steel*V_STeeth; % stator teeth total weigth in kg
V_SCore=pi/4*L*(Ds_out^2-(Ds_out-2*hscore)^2)/(1e9); % stator core
total volume in m3
Wt_SCore=md_steel*V_SCore; % stator core total weigth in kg
```

```
V_RTeeth=(pi*((Dr/2)^2-(Dr_in/2+hrcore)^2)-Area_bar*Nrslot)*L/(1e9); %
rotor teeth total volume in m3
Wt_RTeeth=md_steel*V_RTeeth; % rotor teeth total weigth in kg
V_RCore=pi/4*L*((Dr_in+2*hrcore)^2-Dr_in^2)/(1e9); % rotor core total
volume in m3
Wt_RCore=md_steel*V_RCore; % rotor core total weigth in kg

V_RBar = Area_bar*Nrslot*L_bar/(1e9);% rotor bar total volume in m3
Wt_RBar = md_copper*V_RBar;%md_aluminum*V_RBar;% rotor bar total weight
in kg
V_Ring = 2*Area_ring*pi*De/(1e9);% rotor end ring total volume in m3
Wt_Ring = md_copper*V_Ring;%md_aluminum*V_Ring;% rotor end ring total
weight in m3

V_SWinding = 3*AcuWire*Lphase/(1e9); %stator winding total volume in m3
Wt_SWinding = md_copper*V_SWinding;%stator winding total weight in m3

Wt_total=Wt_STeeth+Wt_SCore+Wt_RTeeth+Wt_RCore+...
    Wt_RBar+Wt_Ring+...
    Wt_SWinding;

%% Core loss estimation
% Core loss data at 60 Hz
% B = 0.1  0.2  0.3  0.4  0.5 0.6  0.7  0.8  0.9 1.0 1.1  1.2  1.3  1.4
% 1.5 1.6  1.7  1.8
% L = 0.01 0.04 0.09 0.14 0.2 0.26 0.33 0.41 0.5 0.6 0.70 0.85 1.03
1.25
% 1.5 1.74 1.97 2.18 W/lb
closs_t=1.5/0.45359*(f/60)^1.5; % core loss density in teeth in W/kg
closs_b=1.5/0.45359*(f/60)^1.5; % core loss density in yoke in W/kg
K_caug=1; % core loss augumentation
Pcore=K_caug*(closs_t*Wt_STeeth+closs_b*Wt_SCore); % core loss by
fundamental

%% friction and stray loss estimation
P_fct=0.012*Prout;
P_stray=0.01*Prout;

%% Performance calculation at rated condition

I_dse1=Imag*sqrt(2); % recalculate stator d-axis current
s_inv=Rr/(X_rl+X_mg)*I_qse/I_dse; % slip frequency at rated load when
inverter driven
I_qse1=I_qse;
Is1=sqrt(I_dse1^2+I_qse1^2)/sqrt(2);
V_qse1=Rcu*I_qse1+(X_sl+X_mg)*I_dse1;
V_dse1=Rcu*I_dse1+((X_sl+X_mg)-X_mg^2/(X_rl+X_mg))*I_qse1;
Vph1=sqrt(V_qse1^2+V_dse1^2)/sqrt(2); % applied phase voltage
I_qre1=-X_mg/(X_mg+X_rl)*I_qse1;
I_dre1=0;
Ir1=sqrt(I_qre1^2+I_dre1^2)/sqrt(2);
P_cu1=3*Is1^2*Rcu;
P_al1=3*Ir1^2*Rr;
P_loss1=P_cu1+P_al1+Pcore+P_fct+P_stray; % total loss at full load
eff1=Prout/(P_loss1+Prout); % efficiency at full load
nrspeed1=(1-s_inv)*n;
```

```
Sinput=3*sqrt(V_qse1^2+V_dse1^2)/sqrt(2)*sqrt(I_qse1^2+I_dse1^2)/sqrt(2
); % input apparent power
pfactor=Prout/Sinput;


%% Starting performance
% skin effect resistance coefficient
beta_s=sqrt(2*pi*f*miu0/2/pal*Br1/Br2);
% Start up rotor resistance
epsilon=beta_s*Hr2/1000*sqrt(1); % assume a slip of 0.02
K_R_st=epsilon*(sinh(2*epsilon)+sin(2*epsilon))/(cosh(2*epsilon)-
cos(2*epsilon));
% rotor resistance considering skin effect
R_bar_st=pal*(L_bar/1000)/(Area_bar/1e6)*K_R_st; % resistance per rotor
bar
Rr_st=(R_bar_st+R_ring)*4*3/Nrslot*(Tph1*Kw)^2;
% Starting current
I_st=Vph/sqrt((Rr_st+Rcu)^2+(X_rl+X_sl)^2);
% Starting current per unit value
per_I_st=I_st/I_rated;
% Starting torque
T_st=3*Rr_st*I_st^2*p/2/(2*pi*f);
% Starting torque ratio
per_T_st=T_st/T_rated;

%% Breakdown
% Breakdown slip
s_bk=Rr/sqrt(Rcu^2+(X_rl+X_sl)^2);
% Breakdown current
I_bk=Vph/sqrt((Rcu+Rr/s_bk)^2+(X_rl+X_sl)^2);
% Breakdown current per unit value
per_I_bk=I_bk/I_rated;
% Breakdown torque
T_bk=3/2*Vph^2/(Rcu+sqrt(Rcu^2+(X_rl+X_sl)^2))*p/2/(2*pi*f);
% Breakdown torque per unit value
per_T_bk=T_bk/T_rated;


%% Calculate objective function

% Penalty function for minimum shaft diameter
if Dr_in<20
    pel_Dr_in=100;
else
    pel_Dr_in=0;
end

% Penalty function for airgap length
if g<0.3
    pel_g=100;
elseif g>1.5
    pel_g=100;
else
    pel_g=0;
end

% Penalty function for minimum tooth width and slot opening
```

```
if Tw<5 || Bs1<1
    pel_Tw_Bs1=100;
else
    pel_Tw_Bs1=0;
end

% penalty funciton for minimum bar bottom width
if Br2<1 || Hr2<2
    pel_Br2_Hr2=100;
else
    pel_Br2_Hr2=0;
end

if CurDensity>6 || barCurDensity>7
    pel_CurDensity=100;
else
    pel_CurDensity=0;
end

% % penaly function for maximum slip
% s_NEMAB=0.05;
% pel_s=linpenalty(s_inv, [s_NEMAB 10]);

% penalty funciton for maximum stator outer diameter
Dsoutmax=440;
pel_Dsout=linpenalty(Ds_out, [Dsoutmax 10]);


% % penalty function for maximum starting current
% I_st_NEMAB=580;
% pel_Ist=linpenalty(I_st, [I_st_NEMAB 100]);
%
% % penalty function for minimum starting torque
% T_st_NEMAB=150;
% pelT_st=linpenalty(-T_st, [-T_st_NEMAB 100]);

% penalty function for minimum breakdown torque
T_bk_NEMAB=200;
pelT_bk=linpenalty(-T_bk, [-T_bk_NEMAB 100]);



penalty=pel_Dr_in+pel_g+pel_Tw_Bs1+pel_Br2_Hr2+pel_Dsout+pelT_bk+pel_Cu
rDensity;
output=Wt_total+(1-eff1)*200+(1-pfactor)*200+penalty;
if abs(imag(output))>0
    output=500;
end
% output
% Wt_total
% (1-eff1)*200
% (1-pfactor)*200
```

APPENDIX VIII

Matlab Program for Induction Machine Design with Genetic Algorithm

```
clear all
close all
global T_rated Bavg p D L g Kc Kw Vph miu0 Kw f Bs1 AreaSlot Nslot Tw
Area_bar phi_stator Nrslot Dr  B_rt slotliner wedge lip rwt Br0;


% D L Bavg g CurDensity barCurDensity
%% parameters setup
n_particle=40;  % numbers of particles
Vmax=[1 1 1 1 1 1];   %velocity band
inertia=[0.7 0.7 0.6 0.6 0.7 0.7];  %innertia constant
phi1=[0.4 0.4 0.4 0.4 0.4 0.4];  %self acceleration constant
phi2=[0.5 0.5 0.5 0.5 0.5 0.5];  %social acceleration constant
iteration_max=100; % maximum iterations
n_variable=6; % number of design variables
%% initialization
% d=10000*ones(round(n_variable*n_particle),round(iteration_max));
d(:,1) =
[100*rand(n_particle*2,1)+100;0.8*rand(n_particle,1)+0.2;0.7*rand(n_par
ticle,1)+0.3;5*rand(n_particle*2,1)+1];


for k=1:n_particle
    input=[d(k,1) d(k+n_particle,1) d(k+2*n_particle,1)
d(k+3*n_particle,1) d(k+4*n_particle,1) d(k+5*n_particle,1)];
    S(k,1)=induction_motor_inverter_6input_fun(input);

end

Smin=S;     %minimum for each particle
dmin=d;     %optimum position for each particle
v(1:n_particle,2)=2*Vmax(1)*(rand(n_particle,1)-0.5);     %initialize
velocity for DiaSGap
v(n_particle+1:n_particle*2,2)=2*Vmax(2)*(rand(n_particle,1)-
0.5);     %initialize velocity for Length
v(n_particle*2+1:n_particle*3,2)=2*Vmax(3)*(rand(n_particle,1)-
0.5);     %initialize velocity for ThickMag
v(n_particle*3+1:n_particle*4,2)=2*Vmax(4)*(rand(n_particle,1)-
0.5);     %initialize velocity for Current density
v(n_particle*4+1:n_particle*5,2)=2*Vmax(5)*(rand(n_particle,1)-
0.5);     %initialize velocity for turns
v(n_particle*5+1:n_particle*6,2)=2*Vmax(6)*(rand(n_particle,1)-0.5);
[Gmin i]=min(Smin);     %global minimum
dGmin=[d(i) d(i+n_particle) d(i+n_particle*2) d(i+n_particle*3)
d(i+n_particle*4) d(i+n_particle*5)];             %global optimum
position
%% Searching
tic
for i=2:iteration_max;
    d(:,i)=d(:,i-1)+v(:,i);
```

```
    %S(:,i)=exp(d(:,i)).*sin(2*pi*d(:,i))+5e2*(2+sign(d(:,i)-5)-
sign(d(:,i)));
    parfor k=1:n_particle
        input=[d(k,i) d(k+n_particle,i) d(k+2*n_particle,i)
d(k+3*n_particle,i) d(k+4*n_particle,i) d(k+5*n_particle,i)];
         S(k,i)=induction_motor_inverter_6input_fun(input);
    end
    %%update local minimum and position
    for k=1:n_particle
        if Smin(k)>S(k,i)
            Smin(k)=S(k,i);
            dmin(k)=d(k,i);
            dmin(k+n_particle)=d(k+n_particle,i);
            dmin(k+n_particle*2)=d(k+n_particle*2,i);
            dmin(k+n_particle*3)=d(k+n_particle*3,i);
            dmin(k+n_particle*4)=d(k+n_particle*4,i);
            dmin(k+n_particle*5)=d(k+n_particle*5,i);
                end;
                end;

    %%update global minimum and position
    if Gmin>min(Smin)
        [Gmin j]=min(Smin);
        dGmin(1)=dmin(j);
        dGmin(2)=dmin(j+n_particle);
        dGmin(3)=dmin(j+n_particle*2);
        dGmin(4)=dmin(j+n_particle*3);
        dGmin(5)=dmin(j+n_particle*4);
        dGmin(6)=dmin(j+n_particle*5);
    end
    %%update velocity

v(1:n_particle,i+1)=inertia(1)*v(1:n_particle,i)+phi1(1)*rand*(dmin(1:n
_particle)-d(1:n_particle,i))+phi2(1)*rand*(dGmin(1)-d(1:n_particle,i));

v(n_particle+1:n_particle*2,i+1)=inertia(2)*v(n_particle+1:n_particle*2
,i)+phi1(2)*rand*(dmin(n_particle+1:n_particle*2)-
d(n_particle+1:n_particle*2,i))+phi2(2)*rand*(dGmin(2)-
d(n_particle+1:n_particle*2,i));

v(n_particle*2+1:n_particle*3,i+1)=inertia(3)*v(n_particle*2+1:n_partic
le*3,i)+phi1(3)*rand*(dmin(n_particle*2+1:n_particle*3)-
d(n_particle*2+1:n_particle*3,i))+phi2(3)*rand*(dGmin(3)-
d(n_particle*2+1:n_particle*3,i));

v(n_particle*3+1:n_particle*4,i+1)=inertia(4)*v(n_particle*3+1:n_partic
le*4,i)+phi1(4)*rand*(dmin(n_particle*3+1:n_particle*4)-
d(n_particle*3+1:n_particle*4,i))+phi2(4)*rand*(dGmin(4)-
d(n_particle*3+1:n_particle*4,i));

v(n_particle*4+1:n_particle*5,i+1)=inertia(5)*v(n_particle*4+1:n_partic
le*5,i)+phi1(5)*rand*(dmin(n_particle*4+1:n_particle*5)-
d(n_particle*4+1:n_particle*5,i))+phi2(5)*rand*(dGmin(5)-
d(n_particle*4+1:n_particle*5,i));

v(n_particle*5+1:n_particle*6,i+1)=inertia(6)*v(n_particle*5+1:n_partic
le*6,i)+phi1(6)*rand*(dmin(n_particle*5+1:n_particle*6)-
```

```
d(n_particle*5+1:n_particle*6,i))+phi2(6)*rand*(dGmin(6)-
d(n_particle*5+1:n_particle*6,i));
    %%band of velocity
    v(1:n_particle,i+1)=min(v(1:n_particle,i+1),Vmax(1));
    v(1:n_particle,i+1)=max(v(1:n_particle,i+1),-Vmax(1));

v(n_particle+1:n_particle*2,i+1)=min(v(n_particle+1:n_particle*2,i+1),V
max(2));

v(n_particle+1:n_particle*2,i+1)=max(v(n_particle+1:n_particle*2,i+1),-
Vmax(2));

v(n_particle*2+1:n_particle*3,i+1)=min(v(n_particle*2+1:n_particle*3,i+
1),Vmax(3));

v(n_particle*2+1:n_particle*3,i+1)=max(v(n_particle*2+1:n_particle*3,i+
1),-Vmax(3));

v(n_particle*3+1:n_particle*4,i+1)=min(v(n_particle*3+1:n_particle*4,i+
1),Vmax(4));

v(n_particle*3+1:n_particle*4,i+1)=max(v(n_particle*3+1:n_particle*4,i+
1),-Vmax(4));

v(n_particle*4+1:n_particle*5,i+1)=min(v(n_particle*4+1:n_particle*5,i+
1),Vmax(5));

v(n_particle*4+1:n_particle*5,i+1)=max(v(n_particle*4+1:n_particle*5,i+
1),-Vmax(5));

v(n_particle*5+1:n_particle*6,i+1)=min(v(n_particle*5+1:n_particle*6,i+
1),Vmax(6));

v(n_particle*5+1:n_particle*6,i+1)=max(v(n_particle*5+1:n_particle*6,i+
1),-Vmax(6));
 end;

dGmin
Gmin

toc
%% Plot
t=1:iteration_max;
figure(1)
for n=2:n_particle
plot(t,d(n,:));
hold on;
end
for n=n_particle+1:n_particle*2
plot(t,d(n,:),'r-.');
hold on;
end
for n=n_particle*2+1:n_particle*3
plot(t,d(n,:),'g--');
hold on;
end
for n=n_particle*3+1:n_particle*4
```

```
plot(t,d(n,:),'y-o');
hold on;
end
for n=n_particle*4+1:n_particle*5
plot(t,d(n,:),'m-x');
hold on;
end
hold off
xlabel('Number of iterations')
ylabel('Values of motor airgap diameter and axial Length(mm)')
title('Particle behavior(DiaSGap:-;Length:-.-)')

figure(2)
for n=1:n_particle
plot(t,S(n,:));
hold on;
end
hold off
xlabel('Number of iterations')
ylabel('motor total Weight(kg)')
title('Output of each particle')

% t=1:iteration_max+1;
% true=[2-1/2*atan(2*pi)/pi 3-1/2*atan(2*pi)/pi 4-1/2*atan(2*pi)/pi 5-
1/2*atan(2*pi)/pi 6-1/2*atan(2*pi)/pi];
% Ref=true(:)*ones(1,iteration_max+1);
%
% figure(1)
% plot(t,Ref(1,:),'r-.');
% hold on;
% plot(d(1,:),'.-');
% hold on;
% for n=2:5
% plot(t,Ref(n,:),'r-.')
% hold on;
% end;
%
% for n=2:n_particle;
%     plot(d(n,:),'.-');
%     hold on;
% end;
% hold off;
%
%
% title('Particle trajectory')
% xlabel('Number of interations')
% ylabel('Position')
% legend('local optimum value','Particle trajectory')


  % onemax
function fitness=oneMax(chromosome)
global T_rated Bavg p D L g Kc Kw Vph miu0 Kw f Bs1 AreaSlot Nslot Tw
Area_bar phi_stator Nrslot Dr  B_rt slotliner wedge lip rwt Br0

chD=num2str(chromosome(1:17));
```

```
chL=num2str(chromosome(18:34));
chB=num2str(chromosome(35:44));
chg=num2str(chromosome(45:54));
chJs=num2str(chromosome(55:65));
chJr=num2str(chromosome(66:76));
D=bin2dec(chD)/500+50;
L=bin2dec(chL)/500+50;
B=bin2dec(chB)/1000;
g=bin2dec(chg)/1000;
Js=bin2dec(chJs)/200+2;
Jr=bin2dec(chJr)/200+2;
fitness=-induction_motor_inverter_6input_fun([D L B g Js Jr]);
```

BIBLIOGRAPHY

[1] A. Semidy and J. R. Mayor, "Generic Electric Machine Thermal Model Development using an Automated Finite Difference Approach," *IEEE International Conference on Electric Machines and Drives*, Miami, FL, May. 2009.

[2] P. Bertoldi and B. Atanasiu. Electrical Consumption and Efficiency Trends in the Enlarged European Union [Online]. Available: http://re.jrc.ec.europa.eu/energyefficiency/pdf/EnEff%20Report%202006.pdf

[3] O. Wasynczuk, S. D. Sudhoff, K. A. Corzine, J. L. Tichenor, P. C. Krause, I. G. Hansen, and L. M. Taylor, "A maximum torque per ampere control strategy for induction motor drives," *IEEE Transactions on Energy Conversion,* vol. 13, pp. 163-9, 1998.

[4] D. L. Logue and P. T. Krein, "Machine efficiency optimization using ripple correlation control," in *IEEE Applied Power Electronics Conference and Exposition*, Piscataway, NJ, USA, 2001, pp. 642-8.

[5] P. L. Chapman, S. D. Sudhoff and C. A. Whitcomb, "Optimal current control strategies for surface-mounted permanent-magnet synchronous machine drives," *IEEE Transactions on Energy Conversion,* vol. 14, pp. 1043-50, 1999.

[6] A. G. Jack, B. C. Mecrow, P. G. Dickinson, D. Stephenson, J. S. Burdess, N. Fawcett, and J. T. Evans, "Permanent-magnet machines with powdered iron cores and prepressed windings," *IEEE Transactions on Industry Applications,* vol. 36, pp. 1077-84, 2000.

[7] M. Persson, P. Jansson, A. G. Jack and B. C. Mecrow, "Soft magnetic composite materials-use for electrical machines," in *IEEE International Conference on Electrical Machines and Drives (IEMDC 95)*, London, UK, 1995, pp. 242-6.

[8] T. A. Lipo, *Introduction to AC machine design*, 2 ed.: University of Wisconsin-Madison, 2004, ISBN: 13: 978-0974547022.

[9] I. Boldea and S. A. Nasar, *The induciton machine handbook*, 1 ed.: CRC express, 2001, ISBN: 0-8493-0004-5.

[10] J. Robinson and Y. Rahmat-Samii, "Particle Swarm Optimization in Electromagnetics," *IEEE Transactions on Antennas and Propagation,* vol. 52, pp. 397-407, February 2004.

[11] M. G. Say, *Performance and design of AC machines*: Pitman, London, 1970, ISBN: 273 40199 8.

[12] F. Fu and X. Tang, *Induction machine design handbook*: China Machine Press, 2002, ISBN: 7-111-09078-0.

[13] Cartech, "Hiperco," http://cartech.ides.com/datasheet.aspx?i=101&E=197, last cited, 19 April 2007.

[14] M. Comanescu, A. Keyhani and M. Dai, "Design and analysis of 42v permanent magnet generator for automotive applications," *IEEE Transactions on Energy Conversion,* vol. 18, pp. 107-112, March 2003.

[15] N. Bianchi, S. Bolognani and P. Frare, "Design criteria of high efficiency SPM synchronous motors," *IEEE Transactions on Energy Conversion,* vol. 21, pp. 396-404, June 2006.

[16] C. Espanet, A. Miraoui and J. M. Kauffmann, "Optimal Design of an High Torque DC Brushless In-Wheel Motor," *IEEE Internation Electric Machines and Drives Conferences*, pp. 1402-1409, Madison,WI, 2003.

[17] R. Wrobel and P. H. Mellor, "The use of a genetic algorithm in the design optimization of a brushless DC permanent magnet machine rotor," *Second International Conference on Power Electronics, Machines and Drives*, pp. 823-827, Edinburgh,UK, 2004.

[18] W. Ouyang, D. Zarko and T. A. Lipo, "Permanent Magent Machine Design Practice and Optimization," *2006 IEEE conference on Industrial Applications*, pp. 1905-11, Tampa,FL, 2006.

[19] Y. Li, J. Zou and Y. Lu, "Optimum design of magnet shape in permanent-magnet synchronous motor," *IEEE Transactions on Magnets,* vol. 39, pp. 300-304, 2003.

[20] Z. M. Zhao, S. Meng, C. C. Chan and E. W. C. Lo, "A novel induction machine design suitable for inverter-driven variable speed systems," *IEEE Transactions on Energy Conversion,* vol. 15 pp. 413-420, Dec. 2000.

[21] S. Williamson and C. I.McClay, "Optimization of the geometry of closed rotor slot for cage induction motors," *IEEE Transactions on Industry Applications,* vol. 32, pp. 560-568, May/June 1996.

[22] M. Amrhein and P. T. Krein, "Rotor designs for small inverter-dedicated induction machines," *IEEE International Electric Machines and Drives Conference (IEMDC 03)*, pp. 1279-85, Madison, WI, 2003.

[23] L. Feng, D. W. Novotny, R. W. Fei and X. Xingyi, "Selection of the pole number of induction machines for variable speed applications," *IEEE Transactions on Industry Applications,* vol. 31, pp. 304-10, May/April, 1995.

[24] V. B. Honsinger, "Sizing equations for electrical machinery," *IEEE Transactions on Energy Conversion,* vol. 2, pp. 116-121, May 1987.

[25] K. S. R. Rao and M. Ramamoorty, " Design optimization of inverter fed 3-phase squirrel cage induction motor," *IEEE Conference on Convergent Technologies for the Asia-Pacific Region*, pp. 1303-7, Pulau Pinang, Malaysia, 2003.

[26] H.-P. Nee and C. Sadarangani, "The influence of load and rotor slot design on harmonic losses of inverter-fed induction motors," *Sixth International Conference on Electrical Machines and Drives*, pp. 173-178, Athens, Greek, 1993.

[27] D. Jackson, "Reliability through increased safety insulation systems: the effect of high-speed switching on the motor insulation system," *Power Engineering Journal,* vol. 14, pp. 174-181, 2000.

[28] T. Ozaki, T. Imai, F. Sawa, T. Shimizu and F. Kanemitsu, "Partial discharge resistant enameled wire," *International Symposium on Electrical Insulating Materials (ISEIM 2005)*, pp. 184-187, Kitakyushu, Japan, 2005.

[29] M. J. Melfi and R. T. Hart, "Considerations for the use of AC induction motors on variable frequency controllers in high performance applications," *IEEE Annual Textile, Fiber and Film Industry Technical Conference*, pp. 1-9, Charlotte, NC, 1998.

[30] G. Madescu, I. Boldea and T. J. E. Miller, "An analytical iterative model (AIM) for induction motor design," *Thirty-First IAS Annual Meeting, IAS '96*, pp. 566-573, San Diego, USA, Oct. 1996.

[31] G. Pugsley, C. Chillet, A. Fonseca and A. L. Bui-Van, "New modeling methodology for induction machine efficiency mapping for hybrid vehicles," in *IEEE International Electric Machines and Drives Conference (IEMDC'03)*, 2003, pp. 776-781 vol.2.

[32] G. Pugsley, C. Chillet and A. Fonseca, "Cost - performance - size optimization for automotive induction machines: A fast and accurate FEM, analytical model and optimization mixed procedure," *COMPEL - The International Journal for Computation and Mathematics in Electrical and Electronic Engineering,* vol. 25, pp. 297-308, 2006.

[33] M. Cunkas, R. Akkaya and O. Bilgin, "Cost optimization of submersible motors using a genetic algorithm and a finite element method," *International Journal of Advanced Manufacturing Technology,* vol. 33, pp. 223-32, 2007.

[34] Ansoft. *RMxprt - Design software for electric machines*. Available: http://www.ansoft.com/products/em/rmxprt/

[35] D. A. Staton, M. I. McGilp, T. J. E. Miller and G. Gray, "High-speed PC-based CAD for motor drives," *Fifth European Conference on Power Electronics and Applications,*, pp. 26-31, Brighton, Great Britain, Sep. 1993.

[36] J. A. Moses, J. L. Kinley, J. H. Lang, R. D. Tabors and F. de Caudra Garcia, "A Computer-Based Design Assistant for Induction Motors," *IEEE Transactions on Industry Applications,* vol. 30, pp. 1616-23, 1994.

[37] C. Blache and D. Paccard, "Magnetic structure design method," *IEEE Transactions on Magnetics,* vol. 29, pp. 2228-31, Sep. 1993.

[38] N. Bianchi and S. Bolognani, "Brushless DC Motor Design: An Optimization Procedure Based on Genetic Algorithms," *Eighth International Conference on Electric Machines and Drives (IEMD)*, pp. 16-20, Cambridge, Great Britain, Sep. 1997.

[39] J. Wang, W. Wang, G. W. Jewell and D. Howe, "Design Optimization of a Miniature Multi-Pole Permanent Magnet Generator," *Ninth International Conference on Electrical Machines and Drives (IEMD)*, pp. 128-32, 1999.

[40] G. K. V. Y. del Valle, S. Mohagheghi, J.-C Hernandez and R.G Harley, "Particle Swarm Optimization: Basic Concepts, Variants and Applications in Power Systems," *IEEE Transactions on Evolutionary Computation,* vol. 12, Apr. 2008.

[41] Y. Duan, R. G. Harley and T. G. Habetler, "Comparison of Particle Swarm Optimization and Genetic Algorithm in the Design of Permanent Magnet Motors," *IEEE International Conferenceo on Power Electronics and Machine Drives (IPEMC)*, Wuhan, China, May 2009.

[42] Y. Duan, R. G. Harley and T. G. Habetler, "A Useful Multi-objective Optimization Design Method for PM Motors Considering Nonlinear Material Properties," *IEEE Energy Coversion Congress and Exposition*, San Jose, CA, 2009.

[43] Z. Q. Zhu and D. Howe, "Instantaneous Magnetic Field Distribution in Permanent Magnet Brushless DC Motors, Part I: Open-Circuit Field," *IEEE Tranactions on Magnetics,* vol. 29, pp. 124-135, Jan. 1993.

[44] T. M. Jahns, Soong, W.L., "Pulsating torque minimization techniques for permanent magnet AC motor drives-a review," *IEEE Transactions on Industrial Electronics,* vol. 43, pp. 791-794, April 1996.

[45] Z. Q. Zhu, Howe, D, "Influence of design parameters on cogging torque in permanent magnet machines," *IEEE Transactions on Energy Conversion,* vol. 15, pp. 920-925, Dec. 2000.

[46] Z. Q. Zhu and D. Howe, "Instantaneous Magnetic Field Distribution in Permanent Magnet Brushless DC Motors, Part III: Effect of Stator Sloting," *IEEE Tranactions on Magnetics,* vol. 29, pp. 143-151, Jan. 1993.

[47] D. C. Hanselman, *Brushless Permanent Magnet Motor Design*: McGraw-Hill, 2006, ISBN: 0070260257.

[48] A. Reatti and M. K. Kazimierczuk, "Comparison of Varous Methods for Calculating the AC Resistance of Inductors," *IEEE Transactions on Magnetics,* vol. 38, pp. 1512-8, May, 2002.

[49] Carpenter. Hiperco Alloy 50 Product Information [Online]. Available: http://www.cartech.com/ssalloysprod.aspx?id=2360

[50] Z. Q. Zhu and D. Howe, "Instantaneous Magnetic Field Distribution in Brushless Permanent Magnet dc Motors, Part II: Armature-Reaction Field," *IEEE Transactions on Magnetics,* vol. 29, pp. 136-142, January 1993 1993.

[51] MCE. Materials / Neodymium Iron Boron (Sintered) / N3575 [Online]. Available: http://www.mceproducts.com/materials/material-details.asp?id=1008&MaterialTypeCode=1003

[52] T. Sebastian and G. Slemon, "Transient torque and short circuit capabilities of variable speed permanent magnet motors," *IEEE Transactions on Magnetics,* vol. 23, pp. 3619-3621, 1987.

[53] Bazaraa, M. S. and C. M. Shetty, *Nonlinear programming: Theory and algorithms*, 2 ed.: John Wiley & Sons, 1993, ISBN: 0-471-78610-1.

[54] Y. Wang, Y. Cheung and H. Liu, *Computational Intelligence and Security*: Springer, 2007, ISBN: 3540743766.

[55] F. Magnussen, P. Thelin and C. Sadarangani, "Performance evaluation of permanent magnet synchronous machines with concentrated and distributed windings including the effect of field-weakening," *2nd IEE International Conference on Power Electronics, Machines and Drives (ICEM)*, pp. 679-85, Edinburgh, UK, 2004.

[56] A. M. El-Refaie, T. M. Jahns and D. W. Novotny, "Analysis of Surface Permanent Magnet Machines with Fractional-Slot Concentrated Windings," *IEEE Transactions on Energy Conversion,* vol. 21, pp. 34-43, Mar. 2006.

[57] J. Cros and P. Viarouge, "Synthesis of Highe Performance PM Motors With Concentrated Windings," *IEEE Tranactions Energy Conversion,* vol. 17, pp. 248-254, 2002.

[58] C. A. Coello, G. B. Lamont and D. A. V. Veldhuizen, *Evolutionary Algorithms for Solving Multi-Objective Problems*, 2 ed. Boston: Springer, 2007, ISBN: 0306467623.

[59] S. K. Huang, K. Koo and J. S. Lee, "Homogeneous Particle Swarm Optimizer for Multi-Objective Optimization Problem," *International Conference on Artificial Intelligence and Machine Learning*, Cairo, Egypt, 2005.

[60] A. Semidey and J. R. Mayor, "Generic Electric Machine Thermal Model Development using an Automated Finite Difference Approach," *IEEE International Conference on Electric Machines and Drives*, Miami, FL, May. 2009.

[61] A. Semidey and J. R. Mayor, "MURI project report on "Multi-Disciplinary 4D Design Tools for Naval Electromechanical Devices," internal report Aug. 2009.

[62] A. Boglietti and A. Cavagnino, "TEFC Induction Motors Thermal Models: A Parameter Sensitivity Analysis," *IEEE Transactions on Industry Applications,* vol. 41, pp. 756-763, May/June 2005.

[63] C. Liao, C.-L. Chen and T. Katcher, "Thermal management of AC induction motors using computational fluid dynamics modeling," *International Conference on Electric Machines and Drives (IEMD),* vol. 99, pp. 189-91, May 1999.

[64] F. P. Incropera, D. P. Dewitt, T. L. Bergman and A. S. Lavine, *Fundamentals of Heat and Mass Transfer*, 2007, ISBN: 0-471-76115-X.

[65] IEEE, "IEEE Guide for the Statistical Analysis of Thermal Life Test Date," *ANSI/IEEE standard,* Dec 1988.

[66] AK Steel Product Data Bulletin, “Selection of Electrical Steels for Magnetic Cores” [Online]. Available: http://www.aksteel.com/pdf/markets_products/electrical/Mag_Cores_Data_Bulletin.pdf

[67] S. Dellinger, R. Harley and Y. Duan, "Interview with industry experts on permanent magnet and induction machine design," *unpublished work,* May 2010.

[68] Cogent Steel: Electrical Steel Thin Non Oriented American Grades [Online]. Available: http://www.sura.se/Sura/hp_products.nsf/vOpendocument/03A8B2433FAE16C4C1256AA8002280E6/$FILE/Thin%20NOFP%20America.pdf?OpenElement

[69] D. H. Braymer, *Armature Winding and Motor Repair*: General Books LLC, 2009, ISBN: 1151736457.

[70] J. M. Gere and B. J. Goodno, *Mechanics of Materials*, 7 ed.: CL-Engineering, 2008, ISBN: 0534553974.

[71] Y. Duan, R. G. Harley and T. G. Habetler, "A Useful Multi-objective Optimization Design Method for PM Motors Considering Nonlinear Material Properties," *IEEE Energy Coversion Congress and Exposition*, San Jose, CA, Sept. 20-24, 2009.

[72] A. Steel. Product Data Bulletin, "Selection of Electrical Steels for Magnetic Cores" [Online].

[73] NEMA, "NEMA MG1: Motors and Generators," ed, 2010.

[74] conversation with Stephen Dellinger, director of engineering in A.O. Smith, May 2010.

[75] J. H. Dableh, R. D. Findlay, B. Szabados, R. Belmans and S. Lie, "Investigation of the air gap influence on the performance and cost optimization of a squirrel cage induction motor," London, UK, 1993, pp. 32-7.

[76] N. Mohan, *Advanced Electric Drives*. Minneapolis: MNPERE, 2001, ISBN: 0-9715292-0-5.

[77] S. Williamson, L. H. Lim and M. J. Robinson, "Finite-element models for cage induction motor analysis," *IEEE Transactions on Industry Applications,* vol. 26, pp. 1007-1017, 1990.

[78] M. Amrhein and P. T. Krein, "Induction machine performance improvements - design-oriented approach with extension to 3-D," *IEEE International Electric Machines and Drives Conference (IEMDC)*, pp. 1557-1563, Antalya, Turkey, 2007.

[79] A. E. Smith and D. W. Coit, "Penalty Functions," in *Section C 5.2 of Handbook of Evolutionary Computation*, 1 ed: Oxford University Press and Institute of Physics Publishing, Sept. 1995.

[80] S. Panda and N. P.Padhy, "Comparison of Particle Swarm Optimization and Genetic Algorithm for FACTS-based controller design," *Applied Soft Computing,* vol. 8, pp. 1418-27, 2008.

[81] S. N. Sivanandam and S. N. Deepa, *Introduction to Genetic Algorithms*, 1 ed.: Springer, 2008, ISBN: 978-3-540-73189-4.

[82] M. Mitchell, *An Introduction to Genetic Algorithms*, 3 ed.: MIT Press, 1998, ISBN: 9780262631853.

[83] J. E. Baker, "Reducing Bias and Inefficiency in the Selection Algorithm," *Second International Conference on Genetic Algorithms and their Application*, pp. 14-21, Hillsdale, NJ, USA, 1987.

[84] Y. Duan, R. G. Harley and T. G. Habetler, "Multi-objective Design Optimization of Surface Mount Permanent Magnet Machine with Particle Swarm Intelligence," *IEEE Swarm Intelligence Symposium*, pp. 1-5, St. Louis, MO, 21-23 September 2008.

[85] Y. Duan, R. G. Harley and T. G. Habetler, "A Useful Multi-objective Optimization Design Method for PM Motors Considering Nonlinear Material Properties," *IEEE Energy Coversion Congress and Exposition*, pp. 187-193, San Jose, CA, September 20-24, 2009.

VITA

Yao Duan was born in China in 1984. He received a Bachelor of Engineering degree from Tsinghua University, Beijing, China, in 2006 and a Master of Engineering degree from Georgia Institute of Technology at Atlanta, Georgia, in 2008, both in Electrical Engineering.

Since July 2006, he has been working on the design and optimization of electrical machines, as a graduate Research Assistant in the electric power group of the Georgia Institute of Technology. In 2008 summer, he worked at the Electric Machines and Drives Laboratory, General Electric (GE) Global Research Center, Schenectady, NY, as a graduate intern.

His research interests include design and control of electrical machines in different applications.